Continuous Wave Frequency Modulated Optical Feedback (CWFM-OF): Theory and Applications

For obtaining the joint academic degree

Erasmus Mundus Doctor in Photonics Engineering, Nanophotonics and Biophotonics

from

Center for Sensors, Instruments and Systems Development

Technical University of Catalonia, UPC-BarcelonaTech

and

Dr.-Ing.

from

The Faculty of Mechanical Engineering

Karlsruhe Institute of Technology

Accepted

Dissertation

from

Ajit Jha

Day of Oral Exam: 25 November, 2016

KIT committee:

Referent: Prof. Dr.-Ing. Christoph Stiller

Coreferent: Prof. Dr. Santiago Royo

Committee member: Prof. Dr.-Ing. Fernando Puente Leon

UPC committee:

Supervisor: Prof. Dr. Santiago Royo

Co-Supervisor: Prof. Dr.-Ing. Christoph Stiller

Committee member: Prof. Maurizio Dabbicco

ABSTRACT

Paradoxically optical feedback (OF) (the phenomenon in which a fraction of the optical field emitted by a laser is fed back into its cavity), that was once considered an undesired phenomenon in the context of optical fibre communications because it introduces instabilities in the laser, has proven to be extremely useful in different real world photonic sensing applications. The optical feedback affects the internal parameters of the laser, such as the facet reflection coefficient, the laser gain, the photon and carrier density, and ultimately the emitted intensity from the laser. This direct relationship among the OF, intensity and frequency modulation is appealing because it transfigures the laser into a complete interferometric set-up where the laser itself acts as source, detector and interfering media all in one, suited for non-contact, non-destructive photonic sensing. The study in this Thesis contributes to different areas of optical feedback interferometry (OFI): from the theoretical formalization of understanding the transfer function of the laser under OF based on scattering theory, to signal processing of the optical feedback signal (OFS) in time and frequency domain simultaneously using the wavelet transform for combating noise, speckle management and extraction of the vibration related parameters of periodic and transient vibrations all in a single processing step. Furthermore, based on the Lang-Kobayashi formulation, experimental evidences are shown of the ability of injection modulation to stabilize the laser even under strong feedback conditions, taking advantage of the fact that the frequency deviation produced in the laser emission by OF is in opposite direction to that of injection modulation. To add on, however, the main contribution of this Thesis has been to develop yet another variant of OFI, continuous wave frequency modulated differential optical feedback (CWFM-DOF), that combines the non-linear dynamics due to OF and that due to injection modulation to measure the optical path difference (OPD) below half the emission wavelength with resolution way below the classical optical feedback (C-OF), while keeping the experimental setup the same as that of C-OF. Among the broad range applications which would benefit from such a sensor, such as Photo-acoustic tomography (PAT) or laser ultrasonic (LUS), the proposed methodology is tested to characterize the vibration of membrane of an acoustic

i

transducer and to measure the displacement of a metallic target due to the acoustic pressure. Thus, the Thesis extends the performance of OFI sensors and covers in detail the theoretical and experimental aspects of CWFM-DOF, and its application to the detection of very small perturbations.

Declaration

I hereby declare that the work in hand is from me independently and I have used nothing other than the given sources and aids and made all adopted forms, contents and references recognizable as such required by the statutes of the University of Karlsruhe and respectively in assurance of scientific practice and valid contents according to the recent relevant version thereof.

Ajit Jha

I hereby declare, that I have no pending or failed PhD examination procedures outside and beyond the Faculty of Mechanical Engineering of the Karlsruhe Institute of Technology (KIT).

Ajit Jha

ACKNOWLEDGEMENT

First of all I would like to express my deepest gratitude to Prof. Dr. Santiago Royo for believing in me and my qualifications and providing me with the opportunity to work with him. The continuous interaction, not only helped me develop academically but also build the confidence and prepare me to accept the challenges academically and personally. I would also like to thank him for his hours of insight discussions with me, giving me the liberty to express myself without doubt and above all listening to me repeatedly. These interactions not only helped me to be comfortable, free and confident, but also to understand the topic better, to develop my interest and to build the basis of all the research carried out along this PhD. Among the other activities, his vision in deciding "what to do", "when to do" and "how to do" and sometimes forcing me to do what was necessary rather than what I wanted has been the key to success. Without that I would not have had made such progress. In addition to his support academically, I also express my indebtness for standing by me in my difficult personal times. He has been a great mentor, guide, supervisor and a leader.

I also express my gratitude to my co-supervisor Dr. Ing. Christoph Stiller for his immense knowledge, co-operation and setting me at my liberty, in the best way to carry on my research activities towards my PhD. I take this opportunity to thank Dr. rer. nat. Martin Lauer for introducing to the research team with in Institute of Measurement and Control Engineering at Karlsruhe Institute of Technology.

Beside my advisers, I would like to thank Prof. Maurizio Dabbicco, Prof. Amir Rosenthal, Prof. Joseba Zubia, Assoc. Prof. Julien Perchoux, Prof. Jaume Pujol, Assoc. Prof. Jordi Mompart Penina, Prof. Jose Arasa Marti and Prof. Fernando Puente Leon who kindly accepted to review my research work, providing useful feedback and suggestions. I also would like to thank all the anonymous reviewers of my publications for the same reason. I believe their contributions have made this research better, and helped to significantly raise its standards.

I also would like to gratefully acknowledge European Union through Erasmus Mundus Joint Doctorate (EMJD) Programme in Photonics Engineering, Nanophotonics and Biophotonics

pencil but could not see me graduate; and for making me what I am today. Hope I have made you proud.

Contents

List of Figures

xiv

List of Tables

Acronyms

pp peak to peak.

AC alternating current.
Al Aluminium.
AlGaAs Aluminium Gallium Arsenide.
AlGaAsP Aluminium Gallium Arsenide Phosphite.
APW acoustic pressure wave.
AW acoustic wave.
AWGN additive white Gaussian noise.

CD compact disc.
CO₂ carbon dioxide.
C-OF classical optical feedback.
CWFM continuous wave frequency modulation.
CWFM-OF continuous wave frequency modulated optical feedback.
CWFM-DOF continuous wave frequency modulated differential optical feedback.
CWT continuous wavelet transform.

DC direct current.
DFB distributed feedback laser.
DH double hetrostructure.
DSMI differential SMI.
DVD digital versatile disc.

EOM electro optic modualtor.

FC fringe counting.
FEL free electron laser.
FIR finite impulse response.
FM frequency modulation.
FMCW frequency modulated continuous wave.
fMRI functional magnetic resonance imaging.

FP Fabry-Perot.
FWHM full width at half maximum.

GaAs Gallium-Arsenide.
GBP gain bandwidth product.

HCCP hollow cube corner prism.
He-Ne Helium-Neon.

IM intensity modulation.
InGaAs Indium Gallium Arsenide.
InGaAsP Indium Gallium Arsenide Phosphite.
IPUM improved phase unwrap method.

LASER light amplification by stimulated emission of radiation.
LD laser diode.
LDV laser Doppler velocimetry.
LEF linewidth enhancement factor.
LFF low frequency fluctuations.
LUS laser ultrasonic.

MASER microwave amplification by stimulated emission of radiation.
MBE molecular beam epitaxy.
MEMS micro electro mechanical systems.
MWQ multi quantum well.

Nd-YAG Neodymium-doped Yttrium Aluminium Garnet.
NIR near infrared.

OF optical feedback.
OFI optical feedback interferometry.
OFS optical feedback signal.

OPD optical path difference.

OPL optical path length.

PAT Photo-acoustic tomography.

PD photodiode.

PSD power spectral density.

PUM phase unwrap method.

QCL quantum cascade laser.

RF radio frequency.

RMSE root mean square error.

SAW surface acoustic wave.

SCL semiconductor laser.

SMI self-mixing interferometry.

SNOM scanning near-field optical microscopy.

SNR signal to noise ratio.

THz Tera Hertz.

UV ultraviolet.

VCSEL vertical cavity surface emitting laser.

List of Symbols

$1/\tau_p'$ photon decay rate.

$1/\tau_p^{of}$ rate of photon re-injection due to OF.

A_t amplitude of target vibration.

A_m modulation current amplitude.

A surface and defect recombination coefficient.

B_L electrical bandwidth.

B bimolecular recombination coefficient.

C feedback strength.

C Auger coefficient.

D_0 amplitude of differential displacement waveform.

E_c Conduction band.

E_g energy band gap.

E_v Valance band.

E electric field.

$F(\phi)$ function of feedback phase.

G_{gen} rate of injected electrons per unit volume.

$H(\omega_m)$ transfer function as a function of frequency.

$H_1(e^{j\omega})$ transfer function of first filter.

$H_1^*(e^{j\omega})$ complex conjugate of transfer function of first filter .

$H_2(e^{j\omega})$ transfer function of second filter .

I_0 bias current.

I_m modulation current amplitude.

I_{op} operating point of laser.

I_{th} threshold current.

I DC current.

J number of scale.

L_1 length of first external cavity.

L_2 length of second external cavity.

L_{ext0} peak modulation of OPL.

$L_{ext}(t)$ distance of the external vibrating target as a function of time.

L_{ext} separation of external target from laser.

L distance of external target from laser.

M frequency modulation index.

N_0 number of octave.

N_f number of fringes.

N_s number of measurement sample.

N_0 carrier density bias point.

N_1 number of electrons in the valance band.

N_2 number of electrons in the conduction band.

N_m peak carrier density subjected to modulation current.

N_m number of mode.

N_{p0} photon density at bias current.

N_{pm} peak photon density subjected to modulation current.

N_p number of photon per unit volume.

N_{th} threshold carrier density.

N_{tr} electron density at transparency.

N number of cavity.

N number of electrons per unit volume (carrier density).

N total number of sample.

P_{02}' power emitted from laser under feedback having reflection coefficient r_{eq}.

P_{01} power emitted from laser's mirror having reflection coefficient r_1.

P_{02} power emitted from laser's mirror having reflection coefficient r_2.

P_0 power emitted from solitary laser.

P_1 peak power emitted from laser under injection modulation.

P_{ac} power emission of laser under injection modulation.

P_m power waveform emitted from laser under CWFM-OF.

P_s power waveform emitted from laser under OF.

P emission power .

Q' quality factor of laser cavity in presence of feedback.

Q quality factor of laser cavity.

R_t pulse repetition rate of transducer emission .

R_{12} absorption.

R_{21} stimulated emission.

R_l leakage current rate.

R_{nr} non-radiative combination rate.

R_{rec} recombination rate per unit volume.

R_{sp} spontaneous emission rate.

R_{st} stimlated emission rate.

R range difference between reference mirror and the object.

SNR_f signal to noise ration under feedback.

T'_t period of secondary AW emission .

T_t pulse repetition time of transducer emission .

T_m modulation period.

T Temperature.

V'_m modulation voltage across laser (pp).

V'_{t0} calculated peak velocity of target vibration.

V_m modulation voltage from signal generator (pp).

V_v voltage applied to the piezo.

V_0 peak voltage of pulse.

V_p volume occupied by optical field / photon.

V_{t0} peak velocity of target vibration.

V volume of active region.

W_e squared amplitude of wavelet coefficient.

W_i imaginary part of wavelet coefficient.

W_r real part of wavelet coefficient.

W wavelet coefficient.

ΔB_{chirp} frequency response of laser in presence of chirp.

ΔN_{th} change in threshold carrier density.

ΔN change in carrier density.

$\Delta \beta_{FWHM}$ resonance frequency of laser in rad/s.

$\Delta \beta$ change in phase constant.

$\Delta \lambda$ change in wavelength.

$\Delta \nu_s$ spectral width under feedback.

$\Delta \nu$ frequency shift.

$\Delta \omega_{FWHM}$ resonance frequency of laser in rad/s.

$\Delta \omega_N$ change in frequency emission due to change in carrier density.

$\Delta \omega_\beta$ change in frequency emission due to change in phase constant.

$\Delta \omega$ change in emission frequency in rad/s.

$\Delta \phi_{ext}$ change in phase under feedback.

$\Delta \tau$ time delay between transmitted and received laser pulse.

Δf_r change in frequency.

Δg_{th} change in threshold gain.

Δg change in gain.

Δn_l change in real part of refractive index.

Δf maximum frequency deviation.

Δf change in frequency.

Γ confinement factor.

Ω_λ frequency modulation coefficient of laser in nm/mA.

Ω_f frequency modulation coefficient of laser in Hz/mA.

Ψ mother wavelet in frequency domain.

α_1 attenuation coefficient of the material forming the first external cavity.

α_s significance level.

α_2 attenuation coefficient of the medium forming the second cavity.

α_i internal loss per unit length.

α_m mirror loss.

α line width enhancement factor.

α attenuation coefficient of the material forming the laser cavity.

β_1 phase constant of the laser emission in the first external cavity .

β_2 phase constant in the second cavity.

β_{sp} spontaneous emission rate.

β_s phase constant under feedback.

β phase constant.

$\delta \lambda$ linewidth (spectral) broadening in nm.

$\delta \nu_0$ spectral width of solitary laser in Hz.

$\delta \nu_1$ spectral width of laser under IM in Hz.

$\delta \nu_f$ linewidth (spectral) broadening in Hz.

$\delta \nu_i$ linewidth (spectral) broadening due to IM in Hz.

$\delta \nu$ linewidth (spectral) broadening in Hz.

δl_{coh} change in coherence length of laser under IM as compared to solitary case.

η_{cpd} coupling efficiency of photodiode.

η_d differential quantum efficiency of laser.

η_i internal quantum efficiency of laser.

η_{pd} efficiency of photodiode.

η_{qpd} quantum efficiency of photodiode.

γ_1 propagation constant in the first external cavity .

γ_2 propagation constant in the second cavity.

γ_{fb} feedback rate.

γ_{pp} effective life time in photon.

κ coupling coefficient.

λ_0 emission wavelength at bias (center wavelength).

λ wavelength.

ν frequency.

$\omega_{\mathbf{m}}$ modulation frequency.

ω_0 frequency of Morlet wavelet in rad/s.

ω_0 solitary laser emission frequency.

ω_{3dB} modulation bandwidth of laser in rad/s.

ω_R resonance frequency of laser in rad/s.

ω_s frequency of laser emission under feedback in rad/s.

ω angular frequency.

$\phi_0{}'$ phase without feedback.

ϕ_0 feedback phase.

ϕ_{ext} phase of the equivalent reflectivity.

$\phi_m(t)$ feedback phase for CWFM-OF case.

ϕ_s phase of OFS under feedback.

ϕ phase of OFS.

π ratio of circumference to diameter of circle.

ψ mother wavelet.

τ_0' calculated time corresponding to the peak of pulse.

τ_1' calculated first 3 dB time of pulse.

τ_2' calculated second 3 dB time of pulse.

τ_{3dB}' calculated pulse width.

$\tau_t{}'$ secondary AW pulses width.

τ_p^{ext} mirror loss rate.

τ_p^{int} mirror loss rate.

τ_t pulse width of transducer emission .

τ_0 time corresponding to the peak of pulse.

τ_1 first 3 dB time.

τ_2 second 3 dB time.

τ_{3dB} pulse width.

τ_ϕ delay introduced by filter .

$\tau_{ext}(t)$ round trip delay as a function of time duet to external vibrating target.

τ_{ext} round trip time in the external cavity.

τ_i cavity loss rate.

τ_l laser's cavity round trip time .

τ_m mirror loss rate.

τ_p photon lifetime.

τ_{tm} measure secondary AW pulses width using CWFM-DOF.

τ carrier life time.

θ angle between laser beam and the target vibration.

$\tilde{n}_l$ group refractive index.

$\vec{E}$ optical field.

$\vec{I}$ incidence matrix.

$\vec{R}$ reflection matrix.

$\vec{S}$ scattering matrix.

$\vec{T}$ transmittance matrix.

$a(t)$ target vibration waveform.

a_0 smallest scale.

a_{ofi} dominant scale in the OFS.

a_p change in gain due to photon density.

a differential gain.

a scale parameter.

b shift parameter.

c velocity of light in vacuum.

$d(t)$ differential displacement waveform.

$d\lambda$ change in wavelength.

df degree of freedom.

dj increment in scale.

dt sampling time.

$f_{\mathbf{m}}$ modulation frequency in Hz.

f_0 frequency emission from solitary laser.

f_0 frequency of Morlet wavelet in Hz.

f_R frequency range.

f_a frequency corresponding to scale a.

f_c cut-off frequency.

f_s frequency emission from laser under OF.

f_s sampling frequency.

f_t frequency of target vibration.

f_{3dB} modulation bandwidth of laser in Hz.

f_D Doppler shift.

f_{if} intermediate frequency.

f_l effective cut-off frequency of filter that allows the constant phase .

f_{max} maximum frequency.

f_{min} minimum frequency.

f_{ofi} frequency corresponding to the dominant scale in the OFS.

f_r resonance frequency of laser in Hz.

f frequency emission from laser under feedback.

g_2 gain in the second cavity.

g_{th} threshold gain of laser.

g gain per unit length.

$h_1[n]$ impulse response of first fitler.

$h_2[n]$ impulse response of second fitler.

h Plank constant.

i_n shot noise current.

i_{dc} DC current from photodiode.

$i_m(t)$ modulation current.

i_s peak current under feedback.

k Boltzmann constant.

l laser cavity length .

m_i intensity modulation index.

m intensity modulation index under feedback.

$n"_l$ imaginary part of refractive index.

n_1 refractive index of the material in the first cavity.

n_2 refractive index of the medium forming the second cavity.

n_l real part of refractive index.

n refractive index of the material forming the laser cavity.

p laser longitudinal mode (an integer).

p probability that null hypothesis is true.

q electronic charge.

$r^{\mathbf{i}}_{\mathbf{eq}}$ imaginary part of equivalent reflection coefficient.

$r^{\mathbf{r}}_{eq}$ real part of equivalent reflection coefficient.

r_3 reflection coefficient at interface 2 and 3.

r_4 reflection coefficient at any poin twith in the second external cavity .

r_1 field amplitude reflection coefficient of first (left) laser facet.

r_2 field amplitude reflection coefficient of second (right) laser facet.

r_{eq3} equivalent reflection coefficient at interface 3.

r_{eq} equivalent reflection coefficient).

r_{eq} equivalent reflection coefficeint at interface 2.

r_{ext} reflection coefficient of external target).

r_{pb} pass band ripple.

r resolution.

t_1 transmission coefficient of the left (first) laser facet.

t_2 transmission coefficient of the right (second) laser facet.

t_s sampling time.

t time.

$v'_m(t)$ modulation voltage across laser.

$v_m(t)$ modulation voltage across laser.

v_g group velocity of photon.

v_t Velocity of remote vibrating target.

$x(t)$ arbitary signal as a function of time.

$x[n]$ discrete time domain signal.

z position in space.

E_0 initial optical field.

I_j incidence wave at port j.

R_i reflected wave at port i.

df_0 mode spacing.

n_N refractive index of the material forming k^{th} cavity.

s_{ij} scattering coefficient.

t_{ij} transmittance coefficient.

1. Introduction

The origin of light amplification by stimulated emission of radiation (LASER) can be traced back to the concept of spontaneous and stimulated emission, well known from Einstein's quantum theory of radiation in 1917 [15]. There it was explained that the interaction of a photon of specific frequency with an excited atom under population inversion causes the emission of another photon of the same frequency, phase, polarization and direction as the incident one. Three ingredients are thus fundamental to any laser: an (active) medium providing gain/amplification, a pump method enabling population inversion, and a cavity confining the optical field. In the quest to invent the laser, the first population inversion was demonstrated in ammonia atoms passing through an electrostatic focuser by Gordon et al. in 1955, in the first successful demonstration of the microwave amplification by stimulated emission of radiation (MASER), which emitted radiation in the microwave region [16]. The first successful laser that emitted radiation in the visible/infrared region was demonstrated by Maimam using ruby as the active medium, with population inversion obtained by optical excitation (shining a flash lamp on a ruby used as active medium) and the cavity formed by enclosing the active medium within highly polished mirrors [17]. Since then different types of laser families have been developed - chemical lasers, dye lasers, solid-state lasers, metal-vapor lasers, free electron laser (FEL), fibre lasers, etc., all of them emitting radiation of different wavelengths and powers. Of special interest to us is the fact that in 1962, Hall et. al reported emission of radiation using Gallium-Arsenide (GaAs) as a p-n junction, and at the same time transmission of light over a considerable distance [18]. This was a major breakthrough, as it meant the start of the development of SCLs, also known as LD. Since then SCLs are the frontier in laser industries and the choice for many important applications because of their small size, low cost, high reliability, spectral and modulation characteristics, and its capability of mass production and integration. SCLs are widely used in modern life and appliances, in fields as diverse as telecommunications, compact disc (CD), digital versatile disc (DVD), Blu-ray, printing, pointers, bar code readers, surgery, material processing, biophotonics, metrology, or sensors, to name a few [19, 20]. Current technological applications demand the miniaturization and integration of low-consumption optoelectronic devices, a feature which reinforces SCLs as the referential coherence source in many fields. At the same time, faster devices are needed to process and transmit the information. Hence, SCLs have become the technology of choice in the laser field and extensive research to stabilize its operation in terms of emission frequency and power for longer duration and harsh conditions are under way. For example, multi quantum well (MWQ) SCLs, quantum wire, quantum dot lasers and quantum cascade laser (QCL) have been currently developed to meet the requirements of the upcoming

technologies. [21–24].

In spite of today's extensive use of SCLs[1] in diverse applications, its performance has also shown some instabilities when subjected to different external perturbations. Situations like OF, the phenomenon in which a fraction of the field radiated from the laser is fed back into its own cavity, or modulation of the injection current of the laser, the condition induced by controlled changes in the intensity that feeds the laser, and also combinations of both, create different interesting behaviours in the laser. The effect of OF on the laser dynamics and stability was observed first by King and Stewart in 1963 [25]. It was observed that an external perturbation (in their case, the motion of a remote target) caused an intensity fluctuation of the laser emission comparable to that of classical interferometry. Since then, widespread research to explain the dynamics of the laser under feedback has been undertaken. Heil et. al proposed a successful delay difference equation for the phenomena [26–28]. Lang, Kobayashi and Petermann proposed a compound cavity model to explain the dynamics of the laser under feedback [29, 30]. In all the cases, an equivalent reflection coefficient set as a function of the reflection coefficient of the individual boundaries forming the cavity is taken into account, leaving the absorption (explained by attenuation coefficient, α) of the medium in between the boundaries unaccounted. One direct implication of the presence of OF is the use of expensive optical isolators in telecommunication systems, in order to prevent instabilities in the laser cavity resulting from OF effects. Beyond this very direct practical aspects, OF has gained considerable attention in the last few decades because it introduces a very rich and complex dynamical behaviour which enhances or degrades the performance of the laser significantly. On one hand, OF can cause important improvements in given aspects of the laser's performance (like decreasing the linewidth, or enhancing the modulation bandwidth) whereas on the other hand, the same phenomenon may severely degrade the performance of the laser (providing wide linewidth broadening and coherence collapse), depending upon the feedback strength (C) [31]. The list of phenomena induced is very extense, in particular, when used in conjugation with IM, causing quasi periodicity, period doubling, tripling and chaotic output, [32–34]. Further, modal instability [35–37], mode-locked pulses [38–43], frequency locked states [44], and low frequency fluctuations (LFF) [45, 46] have also been reported. Since OF cause such a rich dynamics in a laser, characterizes its properties, and causes instabilities in an otherwise very stable system, a better understanding of the dynamical behaviour of the laser in presence of OF is required to set the conditions to avoid or use the instabilities for real world applications. The study of these instabilities in the laser helps to eliminate them stabilizing the laser, and, at the same time, can be used to take advantage of the instability for real world applications. For example, such an analysis of laser dynamics can help to eliminate LFF [45, 46], which is undesirable for fibre optic communications, but on the other hand the same LFF is useful if applied to model and understand neural activities, or to map functional networks like the visual, auditory, or memory functions in the human brain using

---

[1]Hereafter, throughout the text, the term SCLs is replaced generally by *laser* unless explicitly stated.

functional magnetic resonance imaging (fMRI) [47]. Several other fields including climatology, biology, or communication find useful explanations and tools from the behavior of the non-linear dynamics and instabilities in the laser. OF, thus, has attracted interest to harness the instabilities of the laser for new applications, to explain complex nonlinear phenomena, and/or to eliminate existing instabilities, as required by the considered applications.

Further, OF has also been used to characterize different parameters of the laser under test. Destrez et al. used OF to characterize the spectral linewidth of single and multimode lasers as a function of feedback strength [48]. Yu et al. demonstrated the use of OF to measure the linewidth enhancement factor (LEF) (also called phase-amplitude coupling) of the considered laser [49]. In addition, OF also has found a very important application in the field of non-destructive testing in the form of non-contact optical sensors, first observed in [25], and explained in detail by Lang and Kobayashi [30]. In the case of OF-based optical sensors, normally referred to as OFI[2] sensors, the field emitted from the laser incides upon a remote target under test, where it is partially scattered. A small fraction of this scattered beam is re-injected back into the laser cavity, and the beating of the delayed optical field with that of the field emanating from the laser introduces a modulation in the optical frequency and power emitted from the laser. This modulation of optical power contains the signature of the properties of the remote target to be measured through the delayed field (e.g. vibration parameters, reflectivity etc.), and is detected using the built-in monitor PD implemented at the backside of the laser cavity. Since then, it has been used in a wide variety of diverse applications such as chaotic communication [32], displacement and velocity measurement [50,51], distance measurement, imaging [52,53], surface profiling [54], strain measurement [55], or characterization of the reflectivity of materials [56], to name a few. The main advantage of the use of OF in optical sensors and metrology for different real world applications lies in the fact that the laser is not only used as the light source, but at the same time it is also the interfering medium and the detector. This "all-in-one" approach makes the set-up extremely compact, economic, self-aligned and efficient. Further, the resolution and accuracy with the use of OF is comparable to that of classical optical interferometry.

In the use of OFI for the above mentioned sensing applications, the basic principle underlying is the detection of change in OPD in the external cavity, formed by the facet of the laser and the target under test, with an accuracy and precision as high as possible. Two approaches have been normally undertaken. One is the use of extensive setups including external modulators [57], dual frequency lasers [58], wave plates [59] and mis-alignment of components [60]; and another approach has been the use of extensive signal processing. Signal processing for the extraction of the desired parameters with a high level of accuracy is desirable for all kind of sensors, as it keeps the experimental setup simple and compact. Different approaches such as FC [50], Fourier transform [61], PUM [14], and Hilbert transform [62] have been implemented to extract the parameters under measurement (amplitude, velocity, strain, flow, etc.) with increased

---

[2]Also called self-mixing interferometry (SMI), or optical autodyne

accuracy. So far, in the various applications mentioned above, OF has been used to detect the OPD changes greater than half the emission wavelength, thus limiting the resolution of the applications to that value. This is due to the need to induce and detect fringes in the OFS. Breaking this legacy and increasing the resolution below half the emission wavelength, it was demonstrated that the use of OF to measure displacements lower than half the emission wavelength was also possible [63, 64].

A number of different variations of OF are described in the community and will be distinguished in this Thesis. The first one is what we will call C-OF, where the current fed to the laser is constant and the optical path difference between the laser and the remote target forming the external cavity is varied so a measurable perturbation is induced in the field within the cavity [30]. The second one is CWFM-OF, where the current to the laser is modulated and the optical path difference of the external cavity is kept constant [52]. A third variation, which we named CWFM-DOF will be introduced along this Thesis, where the current to laser *and* the external cavity length are modulated [65, 66]. A last variation, the case where the injection current to the laser and the external cavity are both maintained unmodulated has laso been described [45]. In this thesis, however, only the first three variants of OF are analyzed, and the last variant is left outside of scope.

Let's briefly comment also the two main impairments which degrade the OFS and make OF-based sensors difficult to implement in practice are the presence of noise and speckle. Different signal processing techniques have been implemented to combat the different types of noise including AWGN and impulsive noise [67, 68] to improve the performance and robustness of the OFI sensor. Speckle causes random intensity modulation of OFS, causing it to degrade and making the extraction of the parameters related to the vibration very difficult in some situations. Methods such as spatial division multiplexing [10] and the sliding window approach [69] to deal with it have been proposed, but they require multiple measurements and are computationally expensive, respectively.

The main research activities and novelties contributed in this Thesis, which form the subsequent Chapters, are briefly detailed in the following. In Chapter 2, we will introduce the basic theory of the laser and of OF, beginning with the traditional compound cavity, the Lang-Kobayashi and delay difference models to explain the OF phenomenology [26–30] and the instabilities which it introduces in the laser performance. Following the description of the theoretical model, a review of the various applications described for the OFI sensor is performed, including its uses in laser characterization, as a vibrometer to measure displacement and velocity, and in various other applications. A review of the different signal processing techniques used to combat the different types of noise, or speckle, in order to extract the vibrational parameters from the OFS with improved accuracy is then presented. All these aspects are both the basis and the state of the art of the developments performed in the different Chapters of this Thesis.

Chapter 3 is dedicated to an in-depth analysis of C-OF. In spite of the different existing

theories to calculate equivalent reflectivity in presence of external or multiple cavities, a novel theory based on the scattering matrix method is introduced and developed in detail. Such a development introduces a novelty from the classical compound cavity model [29], which only takes into account the phase constant (β) of the optical field travelling through the cavities, but not its attenuation coefficient (α), which considers how the media degrades and attenuates the optical field which propagates through it. A modified mathematical model for equivalent reflectivity for single and double cavities including attenuation, later on generalized to N external cavities is presented. Based on this novel concept of the equivalent reflectivity, the characteristics of the laser under OF are reviewed in detail under different conditions. It is generally accepted that the laser dynamics under OF are dependent on the feedback strength and the external cavity length. However, this theory we propose shows also that the attenuation constant of the medium in which the optical field propagates must be taken into account. A complete theoretical model based on the scattering matrix method [70] will be developed to include the effect of the attenuation constant of each "individual" cavity in the system in which the optical field propagates, so the effects of α in each cavity are included into the equivalent reflectivity of the whole external cacvity system.

It will be shown how the role of the attenuation constant becomes significant in several practical cases, in particular when the field emanating from the laser has to travel a path length through a diffusive medium enclosed by diffusive boundaries, such as measuring blood flow in skin or tissue. It will be shown (and quantified) that the attenuation constant of the medium has a direct relationship to the fringe visibility of the OFS. An increase in the attenuation constant causes losses of optical field such that the beating of the returned field with the field in the cavity produces fringes with very reduced visibility, making the signal processing step of OFS quite difficult. It is found that there exists a deterministic relationship between attenuation (determined in general by the thickness of the external cavity or cavities) which allows to optimize fringe visibility if external attenuation is controllable.

Continuing the legacy of other authors in the contribution to the improvement of OF, the use of the CWT [71] to process OFS in the time and frequency domains simultaneously is covered along Chapter 4. The use of CWT for extracting parameters related to the vibration of the target simultaneously in the time and frequency domain (e.g. displacement, frequency, velocity), remove AWGN and impulsive noise, and manage speckle all in a single processing step is demonstrated in detail. While the information in the time domain is used to determine the instantaneous displacement of the target, the information in the frequency domain is used to determine its frequency and velocity. Next, with the choice of complex Morlet transform as the analyzing wavelet, the phase of the complex wavelet coefficients is also used to extract the amplitude of vibration of the target with increased resolution and accuracy PUM as compared to that computed just with the information from the time domain. Still within Chapter 4, a novel approach to detect the envelope of OFS and keep track of speckle based on CWT will be

also proposed. Such a methodology has advantages in terms of simplicity and computational cost over previous methods described in the literature [10] [69]. Finally, the algorithm proposed here is tested upon a transient vibration to extract its dynamic vibrational parameters, which would not have been possible to extract using standard PUM and Fourier-based methods, as they are applicable to periodic signals only. To the best of our knowledge, this is the first application of C-OF to transient signals, enabling to quantify not only the parameters of the vibration but also *when* they happen.

Having described the instabilities and non-linearities in the laser due of OF, injection modulation or both in previous Chapters, it is worth to further study the static, dynamic and spectral characteristics of the laser in presence of these external perturbations simultaneously. In Chapter 5, the dynamics of laser the when subjected to C-OF and CWFM-OF based on the Lang-Kobayashi rate equation [30] are studied. Evidence of its theoretical predictions concerning the dynamics, and, in particular, the presentation of the use of injection modulation to stabilize the laser and to attain a monomodal state even in presence of strong feedback conditions is experimentally demonstrated. In this context, since the frequency coefficient Ω_f[3] (GHz/mA) of the laser plays a significant role in determining the stability of the laser under strong feedback, an experiment is designed to measure Ω_f experimentally. The main novelty of the proposal, however, lies in using the non-linearities in phase introduced by injection modulation to compensate that other ones introduced by strong OF. It is shown that the non-linearities in phase introduced by both phenomena contribute in opposite directions, enabling to compensate each other and keeping the laser in a quasi stationary state even in presence of strong feedback. It is worth pointing out that both OF and injection modulation are reported to independently produces instabilities and non-linearities in the laser [31–34,45,46], but it will be shown how when acting together in a precise manner they may compensate each other.

So far OF has been mainly used to measure the amplitude of vibrating targets whose amplitude is larger than half the emission wavelength. In Chapter 6, the non-linear dynamics of a semiconductor laser in presence of OF combined with injection modulation will be demonstrated to suffice for the measurement of sub wavelength changes in the position of a vibrating object. A novel method (CWFM-DOF) combining C-OF and CWFM-OF is proposed. The proposed method is defined based on the Lang-Kobayashi rate equation in presence [52] and absence of injection modulation [30]. The details of the method are explained using different simulations, and then experimental results showing the performance of the method are presented. CWFM-DOF is shown to be able to measure amplitudes smaller than $\lambda/2$ with resolutions in the magnitude of a few nanometers. Thus, CWFM-DOF extends the typical performance of OFI sensors to the measurement of very small amplitudes using a very simple setup, and with an increased bandwidth when compared to previous versions of differential OFI based on

---

[3]The property of laser which determines the change in emission frequency (wavelength) with the injection current

mechanical modulation and a double laser arrangement [63,64]. A detailed mathematical model of the proposed sensor in terms of bandwidth, sensitivity, resolution, range of detectable amplitudes and trade off among the different adjustable parameters is illustrated, and experiments on periodic and nonperiodic vibrations presented.

In our final Chapter 7, CWFM-DOF is tested in a real world application. With the recent interest in the use of acoustic transducers and acoustic waves in diverse applications (such as biomedicine, non destructive testing, or acoustic holography), it is of utmost importance for the manufacturer to monitor and control the vibration of the membrane of the transducer to provide proper acoustic fidelity. CWFM-DOF is used in this Chapter to characterize electromechanical transducers in terms of amplitude, frequency and repetition rate of the vibration of the membrane of the transducer. This characterization is significant for the manufacturer to understand and validate the dynamics of acoustic transducers. Further, CWFM-DOF is shown to satisfy the need of sensitive methods to detect and visualize acoustic surface perturbations on remote targets, by properly measuring the instantaneous surface displacement of an Aluminium plate due to acoustic radiation pressure.

Finally, a summary of the main conclusions of this research work, and comments on proposed future works related to findings of this Thesis is presented in Chapter 8, followed by the list of publications, patents and conference presentations achieved during the research work.

As a summary, the main contributions of the research in this Thesis are thought to be

- **Scattering Theory**: A developed a mathematical model for equivalent reflection coefficient taking into account both the phase and the attenuation constant of the media in the different cavities has been developed. Based on this equivalent reflectivity, the characteristics of laser under OF is studied. The model developed is suitable to optimize the performance of OFI sensors in multiple cavity systems.

- **Laser stability**: A methodology to keep the laser in mono modal and quasi stationary state is presented, even at strong feedback conditions, taking advantage of the phase effects introduced by injection modulation. Further, based on the methodology CWFM-OF a technique for the measurement of the frequency modulation coefficient of the laser is experimentally demonstrated.

- **Signal processing**: Signal processing of C-OF signal using the wavelet transform has been developed and applied, showing it efficiently combats noise, manages speckle and extracts vibrational parameters all at one single processing step. The method also enables the measurement of pulsed perturbations and the characterization of the moment in time when they occur.

- **CWFM-DOF as a photonic sensor**: A photonic sensor based on OF to measure amplitudes of vibration smaller than $\lambda/2$ with resolutions of a few nanometers is presented.

Such a tecnique has a bandwidth depending upon the amplitude and frequency modulation of the laser injection current and the separation of target from laser, wider than current methods.

- **CWFM-DOF applied to acoustic wave characterization**: The proposed photonic sensor has been tested for real world applications, in particular for the characterization of the electro-mechanical vibration of the membrane of an acoustic transducer and for the determination of the instantaneous surface displacement of a remote target under acoustic wave pressure.

2. Optical Feedback

2.1 INTRODUCTION

The laser, which was once supposed to be "a solution without a problem" soon after its invention in 1960, finds itself as "solution to several existing and future problems". At present, laser finds itself used in a variety of applications from basic consumer electronics to telecommunications, medical imaging, environmental monitoring or other advanced future applications including spectroscopy, microscopy and cosmology to name a few. Among the different types of lasers, which include solid state lasers (based on Neodymium-doped Yttrium Aluminium Garnet (Nd-YAG)), gas lasers (carbon dioxide (CO_2)), FEL, or liquid lasers, the SCL is very widely used. SCL distinguishes from other types of lasers primarily because of its ability to be directly pumped by an electric current, making it more power efficient than other laser families. The efficiency of SCL is in general around ~ 50 % while solid state or gas lasers stay around$\sim$ 1-10 % , due to the fact that they need be pumped by plasma excitation or an incoherent flash lamp [72]. Furthermore, it is small and compact, integrable, cheap, high power, and has a longer lifetime and a wider range of tunability in wavelength, which can go from near infrared (NIR) to ultraviolet (UV) depending upon the material used in the cavity (III-V material and Nitrides). The future of SCL and its applications is bright and strengthened by its multiple and diverse applications.

However, the performance of SCL may be significantly affected by external perturbations, being some of the most relevant optical feedback (OF), IM or combinations of both. This effects may occur, for instance, from reflection of the optical field from the end of a fibre (in data transmission in fibre optics communication), or from reflection from an arbitrary surface during laser operation, among other cases. This small optical field re-injected inside the laser's cavity has shown a very rich spectral and temporal dynamics. Different models, such as the compound cavity, the delay difference equation, or the Lang-Kobayashi model have been proposed. Such studies help to analyze in depth the working principle of the laser, and make it more efficient and effective for upcoming future applications.

This chapter is devoted to the review of the state of the art regarding the SCL, its dynamics under OF and IM, its potential applications and the present pitfalls which need to be overcomed to enhance its performance. In the sections to follow, starting with Sec. 2.2, the basic working principle of laser[1] is introduced. Particular attention is given to the analysis of small signals in laser performance, and to introduce some properties which will be relevant in upcoming Chapters

---

[1]From now onwards, SCL is replaced by laser unless otherwise stated

of this work, like modulation bandwidth, frequency chirp, and the relationship between IM and FM. Such phenomena form the basis for the development of the OF-based sensor developed in this thesis, and ultimately determine its bandwidth. In Sec. 2.3, the systematic derivation of the equations of laser under feedback for C-OF, and CWFM-OF is presented. They are derived from the two most popular models, the Petermann's compound cavity model [73] and the Lang-Kobayashi's model [30]. Such derivation enables to study the laser's temporal and spectral behaviour. Following this modelling, some of the real world applications of OF as a photonic sensor are presented in Sec. 2.4, showing the advantages of OF-based sensors. Next in Sec. 2.5, a review of the main signal processing techniques used in OF based sensors is presented. Finally, Sec. 2.6 ends the chapter with a brief conclusion of this review on lasers and OF.

2.2 THE SEMICONDUCTOR LASER

From quantum theory, the electrons within an atom are restricted to occupy a set of discrete energy levels. The same is true for electrons in solids, as well. However, in the case of solids, the electrons have a band of energy levels to occupy, instead of a set of discrete energy levels, which is the case in isolated atoms. Solids are formed by the bonding forces between individual atoms. When one or many isolated atoms are brought in close proximity, the wave functions of electrons in the neighbouring atoms overlap, altering the overall wave function which, in turn, affects the boundary conditions of Schrödinger wave equation. Under these conditions, the solution of the wave equation has different allowed energies, so the electrons in solids have a range or band of energy allowed to them. Usually, the influence of an atom upon the energy level of its neighbouring atom can be treated as a small perturbation, and causes the splitting of the discrete energy levels to bands separated by an energy band gap E_g, containing no energy level for the electrons to occupy [1, 2, 72, 74].

The upper band, with the larger energy levels E_c, is called the conduction band and the lower band, with the smaller energy levels E_v, is called the valence band, so $E_c > E_v$. As an example, the discrete energy levels in an isolated Si atom are shown in Fig. 2.1. The formation of energy bands in a semiconductor silicon crystal is shown in Fig. 2.2. In perfect equilibrium state, at $T = 0$ K, the electrons in an atom occupy the valence band leaving the conduction band empty. However, in a non-equilibrium state, when $T > 0$ K, electrons make transitions from the valence band to the conduction band, partially filling the conduction band and leaving holes[2] in the valence band. The number of electrons present in a particular energy level is given by Boltzmann statistics [2].

$$\frac{N_2}{N_1} = e^{-\frac{E_c - E_v}{kT}} = e^{-\frac{E_g}{kT}}, \tag{2.1}$$

---

[2]A "hole" is an empty state in the valence band. It is customary to treat such empty state as a charge carrier with unit positive charge and unit mass.
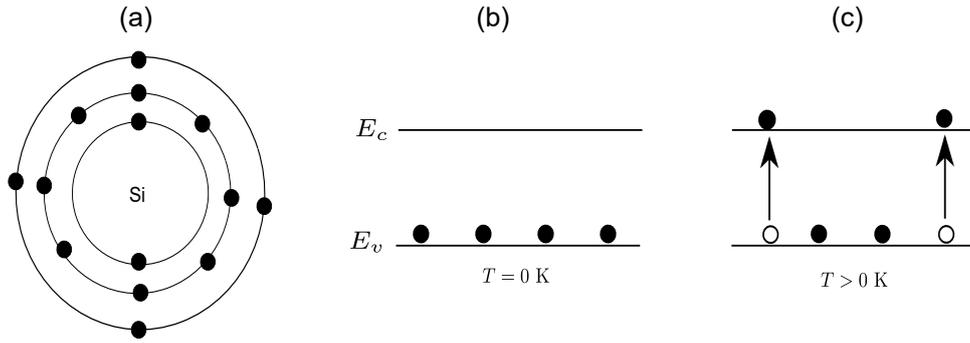
Figure 2.1: Discrete energy levels of an isolated Si atom. (a) Conduction and valence energy levels are discrete. (b) At temperature $T = 0$ K, electrons (shown by filled circle) occupy the valence band and conduction band is empty. (c) At $T > 0$ K, electrons can transition from valence to conduction band leaving a hole (open circle) behind.
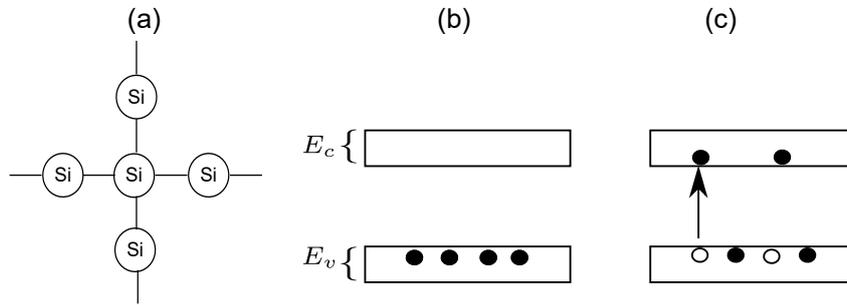
Figure 2.2: Energy band diagram of a Si crystal. (a) At temperature $T = 0$ K, electrons occupy the valence band and conduction band is empty. (b) At $T > 0$ K, electrons can transition from valence band to conduction band leaving a hole behind.

where N_1 and N_2 are the number of electrons in the valence and conduction bands, respectively; $E_g = E_c - E_v$, k is the Boltzmann constant, and T is the temperature. It is evident from Eq. (2.1) that for most of the cases $N_2 < N_1$, and electrons occupy mostly the valence band, as it corresponds to the lower energy levels. At best, when $T = \infty$, the population at both the level equals ($N_2 = N_1$), but the population inversion condition ($N_2 > N_1$) which will be key to laser performance never will be attained under equilibrium conditions. However, Einstein [15] showed that the necessary working condition for a laser is to have population inversion in a material, and to introduce gain, coherence monochromaticity and directionality via stimulated emission.

Having explained the concept of energy levels and energy bands in semiconductor materials, we are ready to review the different potential electronic transitions, and its relationship with photon emission. Fig. 2.3 shows the different potential electronic transitions that involve absorption and emission of photons. As illustrated, three different transition mechanisms are relevant. The first case is spontaneous emission (R_{sp}). Eq. (2.1) shows that at $T \neq 0$ K, some electrons can absorb enough thermal energy to cross the energy gap and make a transition to the conduction band. However, electrons tend naturally to occupy the minimum energy
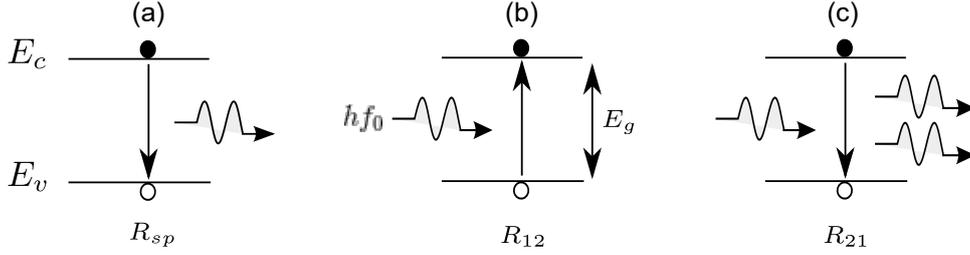
Figure 2.3: Electronic transitions between conduction and valence bands. (a) Spontaneous emission; (b) Absorption; (c) Stimulated emission. Adapted from [1].

level, so each electron in the conduction band can occupy it only for a limited time, described by its lifetime [3]. Beyond the duration of its lifetime, the electron makes a transition back to the valence band to spontaneously recombine with a hole, emitting a photon of frequency f_0, corresponding to E_g (Fig. 2.3 (a)). Since different electrons recombine at different time instances, after recombination photons of different phase are emitted in all possible directions and phase states, contributing to incoherent emission [1]. The second relevant case to analyze is absorption (R_{12}), where electrons in the valence band absorb radiation and make a transition to the conduction band, leaving a hole behind (Fig. 2.3 (b)) [1]. Absorption can be accomplished by some pumping mechanism, e.g. shining a flash lamp as a source of photons of frequency f_0 larger than the energy band gap (i.e $hf_0 >= E_g$) or injecting direct current. A continuous pump effect causes the electrons to make transitions from lower to higher energy levels. Given the lifetime of electrons in the higher energy level is longer than the absorption rate, after a certain time population inversion may be achieved [2]. The final case shown in Fig. 2.3 is stimulated emission (R_{21}), where the electrons are mostly in the excited state, and before the spontaneous emission of any photon another photon of frequency f_0 corresponding to the energy gap incides on the atom, causing the excited electron to relax to its ground state, while another photon of same frequency f_0, phase, and direction of propagation [1] is emitted. The probability in an atom of an individual electron to absorb a photon is the same as that of the excited electron to emit a photon via stimulated emission. Thus, the set of electrons in equilibrium will be a net absorber and amplification will not be possible. Under population inversion conditions, however, as there are a large number of pre-excited electrons, the atoms become net emitters of coherent photons [2].

Beyond accomplishment of the stimulated emission condition just described, it is seen that in a single pass of the beam the gain attained is normally very small. To enhance the gain, a large number of emission processes are required, which are obtained by placing a medium with gain in an optical resonator with positive feedback. Under these conditions, lasers are able to create relevant stimulated emission, to produce intense beams of light which are monochromatic, coherent, and highly collimated. In particular, the wavelength of laser light is extremely

---

[3]The lifetime of the electron is dependent on energy level and material.
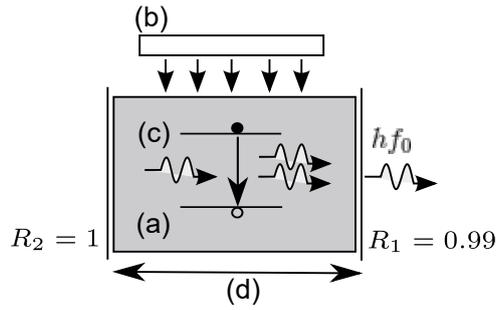
Figure 2.4: Components and mechanism involved in a laser: (a) Active medium; (b) Pump; (c) Stimulated emission; (d) Optical resonator.

monochromatic when compared to other sources of light, and all of the photons that compose the laser beam have a fixed phase relationship relative to one another, called coherence [1, 2].

Looking at the situation from another physical point of view, an excited atom acts as a small electric dipole which oscillates with the external field provided by the incident photon. One of the consequences of this oscillation is that it causes the electrons to decay to the lowest energy state, enabling the atom to return to its ground state. When this happens, a photon is released with same frequency, phase and direction as the "stimulating" photon, giving rise to "stimulated emission". At the end of the process two coherent photons are produced, enabling cascaded optical amplification (Fig. 2.3(c)). Generally speaking, when favourable conditions are created for stimulated emission in a system with inversion population, more and more atoms are forced to release photons, initiating a kind of chain reaction which releases a large amount of energy. This favourable conditions are achieved by placing the gain medium in a optical resonant cavity with positive feedback [2]. In this way, incoherent photons generated in the active medium by spontaneous emission travel in all possible directions, but when incident upon the excited atoms in the medium cause stimulated emission of another photon. This increases the number of photons and so introduces gain. As the single pass gain is very small, the entire process is performed inside an optical resonator, enclosing the active media between highly reflective mirrors [74]. The large number of photons in the cavity escape from one side, the one with a lower reflectivity, providing directionality to the beam. The process results in a rapid build up of energy emitting in a single particular wavelength (monochromatic light), and travelling coherently in a precise, fixed direction.

Thus, a laser requires for its operation four main components: (a) an active medium, where the population inversion can take place; (b) a pump mechanism, which creates population inversion in the active medium; (c) a stimulated emission process to cause gain in the active medium; and (d) a resonant cavity to enhance the gain, that is, an optical resonator. All these components are shown in Fig. 2.4.

Once the fundamental principles of laser functioning have been described, now the details on how such phenomenology is achieved within a semiconductor material, yielding a SCL are

E

$n-$AlGaAs $p-$AlGaAs

(a)

V

GaAs

$E_{gcl}=1.85\,\text{eV}$

$E_g=1.43\,\text{eV}$

$hf_0 = E_g$

(b)

(c)

(d)
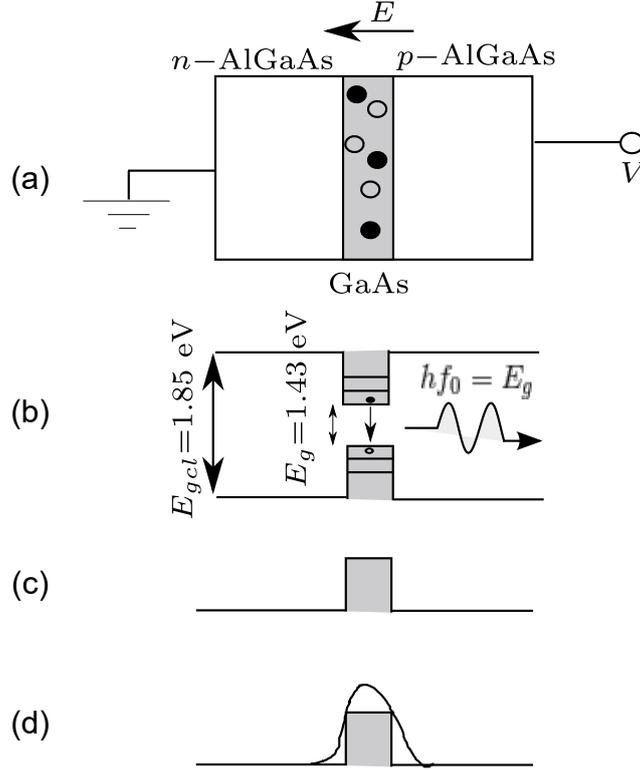
Figure 2.5: Working principle of the SCL. (a) $p-n$ DH diode; (b) Carrier confinement to increase the probability of effective recombination; (c) Optical field confinement resulting from difference in refractive index profile between active region and cladding; (d) Generated optical field, proportional to photon density in the active region, or $|E|^2$ confined in the wave guide resulting from (c). Adapted from [1, 2].

presented. A SCL is basically a double DH $p-n$ diode which effectively confines the carriers (electrons and holes) in a small active region, so increasing the probability of effective recombination and enabling stimulated emission to happen [2]. Current state of the art technology enables crystals with different bandgap values and small variations in lattice constants to be grown adjacent to one other, using techniques like e.g. molecular beam epitaxy (MBE). Fig 2.5 shows the schematics of a DH laser together with its energy band diagram, refractive index profile, field emission, and how carrier and field confinement are induced.

As illustrated in Fig 2.5, a thin (0.1-0.2 μm) layer of active material (typically GaAs) is sandwiched between a p and n Aluminium Gallium Arsenide (AlGaAs) cladding layer (Fig. 2.5(a)). The cladding layer has a greater bandgap than the active region. Under forward bias, the electric field exerts a force on the electrons and holes in the AlGaAs cladding to move them towards the sandwiched GaAs active region. When carriers are confined in the thin active region they behave as the classical "particle in a potential well" problem in quantum physics [2]. Therefore, the carriers occupy discrete energy levels in the quantum well (Fig. 2.5(b)). The formation of discrete energy levels changes the energies at which photons can be emitted from the material. For instance, (Fig. 2.5(b)), electrons in the discrete energy levels in the conduction band may make transition to the empty discrete levels in the valence band, to produce a photon

of energy (wavelength) of 1.43 eV (868 nm). Similarly, engineering the energy bandgap, GaAs has been used in semiconductor lasers to emit from infrared to red regions of the spectrum. For confining the emitted emission, the principle of refractive index mismatch is used. The refractive index of the active region is in general larger than that of the adjacent cladding (Fig. 2.5(c)), so a waveguide in transverse direction is formed, which confines the optical energy created by the recombination. The optical energy generated is proportional to the photon density or the squared amplitude of the electric field ($|E|^2$), as shown in Fig. 2.5(d) [1].

2.2.1 RATE EQUATION

As explained in Fig. 2.5(a), biasing the DH arrangement generates carriers in the active region. Various mechanisms, including radiative and non-radiative emission and carrier leakage provide recombination processes. The rate equation can thus be written as [1, 15, 72]

$$\frac{dN}{dt} = G_{gen} - R_{rec}, \tag{2.2}$$

where N is the carrier concentration (number of carriers per unit volume), G_{gen} is the rate of injected electrons and R_{rec} is the rate of recombination per unit volume within the active region. There is a loss of electrons in the active region due to different phenomena, including diffusion processes, the effect of the electric field, or thermal effects, which cause some electrons to be swept away from the active region. Taking into account this leakage current, the net electron generation is given by [1]

$$G_{gen} = \frac{\eta_i I}{qV}, \tag{2.3}$$

where η_i is the internal quantum efficiency of laser [4], V is the volume of the active region, q is the electron charge and I is the current flowing through the laser terminals. The recombination process is complex to describe as it involves different types of phenomena. The net recombination rate R_{rec} may be described as [1]

$$R_{rec} = R_{sp} + R_{nr} + R_l + R_{st}, \tag{2.4}$$

where R_{nr} is the non radiative recombination, and R_{sp}, R_{st}, R_l correspond to spontaneous, stimulated, and leakage recombination rates, respectively. One example of non-radiative radiation is Auger recombination, where electrons recombine with the hole to radiate an emission, but the emitted energy is transferred to another electron, instead of creating a photon. The first three terms correspond to natural decay phenomena, and it is customary to describe them through a carrier life time, τ. Thus, Eq. (2.4) can be rewritten as [1]

$$R_{rec} = \frac{N}{\tau} + R_{st}, \tag{2.5}$$

---

[4]Defined as the ratio of carriers injected in the active region rated to the total carriers pumped

where

$$\frac{N}{\tau} = R_{sp} + R_{nr} + R_l. \tag{2.6}$$

Using power series expansion for spontaneous, non radiative recombination and leakage current, and using $R_{sp} = NN^2$ and $R_{nr} + R_l = AN + CN^3$, Eq. (2.5) can be written as

$$R_{rec} = BN^2 + (AN + CN^3) + R_{st}, \tag{2.7}$$

where A is the surface and defect recombination coefficient, B is the bimolecular recombination coefficient, and C is the Auger coefficient [75]. Similarly, the photon rate generated in the cavity is

$$\frac{dN_p}{dt} = \Gamma R_{st} + \Gamma \beta_{sp} R_{sp} - \frac{N_p}{\tau_p}, \tag{2.8}$$

where Γ is the confinement factor[5], β_{sp} is the spontaneous emission rate, N_p is the number of photons in the cavity, and τ_p is the photon lifetime, also known as the cavity lifetime . The first two terms on the right represent the rate of photons generated by stimulated and spontaneous emission, respectively. The third term represents the photon loss within the cavity, as an effect of optical absorption, propagation of optical field within the cavity, and coupling of the optical field out of the cavity. It is shown in [1] that photon-stimulated electron-hole recombination (stimulated recombination) has an effect on gain which is given by

$$R_{st} = v_g g N_p = v_g a(N - N_{tr})N_p, \tag{2.9}$$

where v_g[6] corresponds to the group velocity of the photon within the cavity, g the gain per unit length, a the differential gain, and N_{tr} the electron density when at transparency[7]. It is worth mentioning that gain in a laser is related directly to the electron density. Hence, the coupled carrier and photon density rate in the case of the laser, obtained from Eq. (2.2), (2.3), (2.5), (2.8), (2.9) are given as

$$\frac{dN}{dt} = \frac{\eta_i I}{qV} - \frac{N}{\tau} - v_g g N_p. \tag{2.10}$$

$$\frac{dN_p}{dt} = \Gamma v_g g N_p + \Gamma \beta_{sp} R_{sp} - \frac{N_p}{\tau_p}. \tag{2.11}$$

2.2.2   STEADY STATE GAIN IN A LASER

As explained earlier, the optical mode in a SCL is confined within the cavity. In this section we will describe and characterize the cavity losses associated with optical field absorption and propagation inside a cavity, and its relationship to the cavity mirrors. It should be remembered

---

[5]Since the volume occupied by a single photon, V_p is larger than that of the actual volume of the active region (V), the photon density rate is $\frac{V}{V_p}R_{21} = \Gamma R_{21}$

[6]v_g is the group velocity related to the effective refractive index of the considered material, as $\tilde{n}_l = c/v_g$, with c the velocity of the field in vacuum

[7]The condition when absorption equals emission i.e, when $R_{sp} = R_{st}$ (Fig. 2.3)
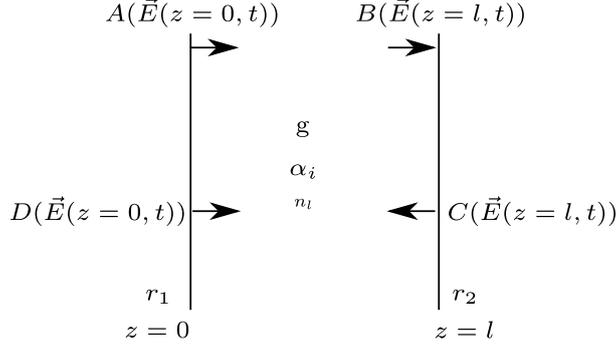
Figure 2.6: Working principle of laser. An active medium enclosed in between two reflective surfaces.

that we are using a quantum well to describe the DH which defines the laser cavity. For the cavity to work as a resonator and introduce gain, the losses associated with propagation need be overcomed, which essentially means that the dimension of the cavity has to be properly chosen to provide the desired gain to a particular mode. In this section, the condition to lase is derived from the semiconductor parameters. Referring to Fig. 2.6, a typical arrangement with an active media enclosed in between the cleaved semiconductor material is presented. In such arrangement the field amplitude reflection coefficients are described by r_1 and r_2 at each side of the internal cavity, respectively, The optical field $\vec{E}(z,t) = E_0 e^{-j(\beta z - \omega_0 t)}$ generated at point A, B, C and D is thus given by

$$\vec{E}(z = 0, t) = E_0 e^{\omega_0 t}, \tag{2.12a}$$

$$\vec{E}(z = l, t) = E_0 e^{-j(\beta l - \omega_0 t)} e^{\Gamma \frac{g}{2} l} e^{-\frac{\alpha_i}{2} l}, \tag{2.12b}$$

$$\vec{E}(z = l, t) = r_2 E_0 e^{-j(\beta l - \omega_0 t)} e^{\Gamma \frac{g}{2} l} e^{-\frac{\alpha_i}{2} l}, \tag{2.12c}$$

$$\vec{E}(z = 0, t) = r_1 r_2 E_0 e^{-j(2\beta l - \omega_0 t)} e^{\Gamma g l} e^{-\alpha_i l}, \tag{2.12d}$$

where l is the laser cavity length, E_0 is the initial optical field, ω_0 is the emission angular frequency, α_i is the internal loss per unit length, and $\beta = \omega_0/c$ is the phase constant of the optical field (explained in detail in Eqs. (2.17) and (2.18)). In order to impose the condition that the optical field within the cavity is not attenuated, it needs to keep the same amplitude after the round trip time, i.e. the optical field at point A and D, must be equivalent. It should be noticed that the factor of $1/2$ associated to α_i and g comes from the fact that the optical field $\vec{E}$ is the magnitude being considered, instead of power P, as $|\vec{E}|^2 = P$. Hence equating Eq. (2.12a) and (2.12d), the steady state condition is

$$r_1 r_2 e^{(\Gamma g - \alpha_i) l} e^{-j2\beta l} = 1. \tag{2.13}$$

Eq. (2.13), describes the equation of the threshold gain required for lasing, defined by

$$\Gamma g_{th} = \alpha_i + \frac{1}{l} ln(\frac{1}{r_1 r_2}) = \alpha_i + \alpha_m, \tag{2.14}$$

where α_m is the mirror loss. The subscript associated with the gain (g_{th}) is to demonstrate the fact that this is the minimum amount of gain required to compensate the losses and provide an effective gain mechanism within the cavity. Alternately, using the photon decay rate in the cavity ($1/\tau_p$), which is the sum of the cavity loss rate ($1/\tau_i$) and the mirror loss rate ($1/\tau_m$)[8], one gets.

$$1/\tau_p = 1/\tau_i + 1/\tau_m = v_g(\alpha_i + \alpha_m), \tag{2.15}$$

The threshold gain required to lase is thus described in terms of cavity (photon) lifetime as

$$\Gamma g_{th} = \alpha_i + \alpha_m = \frac{1}{v_g \tau_p} = \frac{\omega}{Q v_g}, \tag{2.16}$$

where Q is the quality factor of the cavity. It should be noted that Eq. (2.14) and (2.16) only relate the gain and loss of the system, and are independent from the stimulated emission rate.

Since gain is the main mechanism for lasing, slight alterations of the cavity losses or of the properties of the cavity result in different properties of the emitted laser radiation and the lased field. Eq. (2.13) sets the equation for the valid lasing frequency, which will be of special significance afterwords when we consider OF. Equating the phase at both sides of Eq. (2.13) we get to

$$\beta l = m\pi, \tag{2.17}$$

where p is the number of the longitudinal mode. The phase constant is dependent upon the frequency (ω_0) of the optical field (Eq. (2.18)), so Eq. (2.17) the allowed lasing frequencies in the resonator are bound and linked to the value of the longitudinal size of the cavity l.

$$\beta = \frac{\tilde{n}_l \omega_0}{c} = \frac{2\pi f_0 \tilde{n}_l}{c}, \tag{2.18}$$

where $\tilde{n}_l$ is the group refractive index of the material which forms the laser cavity. Equating Eqs. (2.17) and (2.18), the emission frequency needs be

$$f_0 = p \frac{c}{2\tilde{n}_l l}. \tag{2.19}$$

where p is the longitudinal mode. Since there can be multiple modes allowed depending upon the cavity length, the frequency (mode) spacing (df_0) corresponding to the round trip time delay (τ_l) is given by

$$df_0 = \frac{c}{2\tilde{n}_l l} = \frac{1}{\tau_l}. \tag{2.20}$$

It is evident, then, that both the lasing mode and its spacing are dependent upon the cavity round trip time, and subsequently upon the cavity length. As an example, taking a typical realistic value of $\tilde{n}_l$=3.5 and l=300 μm, then τ_l=2.3 ps and df_0=420 GHz. It should be noted

---

[8]Understood as the rate at which photons escape from the cavity to the outer world

that if the cavity length is perturbed periodically (by placing an external vibrating target, as in some cases within our experiments), the emission frequency also changes periodically. This has profound implications in the use of SCL as vibrometers, which will be covered in detail in Sec. 2.3.

Finally, let us consider that at steady state above threshold there exist a certain value of gain and carrier clamping, so that they do not increase monotonically [1]. This happens because as the current increases beyond the threshold value, it introduces population inversion. For a fraction of time (ns), the carrier concentration at the higher energy levels increases. Due to the stimulated recombination this concentration drops gradually, but at the same time the photon density grows causing an increase in gain. In the end, carrier concentration reaches the value it had under threshold conditions, causing the photon density and gain to fall, so a sustained cycle takes place [1]. So, per Eq. (2.14)

$$g(I > I_{th}) = g_{th} \tag{2.21}$$

$$N(I > I_{th}) = N_{th} \tag{2.22}$$

Similarly, in steady state conditions above threshold Eq. (2.10) becomes

$$\frac{dN}{dt} = \frac{\eta_i(I - I_{th})}{qV} - v_g g N_p, \quad I > I_{th} \tag{2.23}$$

From Eq. (2.23), the photon density at steady state above threshold is calculated using

$$N_p = \frac{\eta_i(I - I_{th})}{qV v_g g_{th}}, \quad I > I_{th} \tag{2.24}$$

where I_{th}, g_{th} and N_{th} are the current, gain and carrier concentration at the emission threshold. Since the power is proportional to the number of photons, the power out of cavity may now be calculated. The photon density N_p is multiplied by the energy of each emitted photon hf_0, and by the volume occupied by the photons in the cavity V_p, where they gather their optical energy. This optical energy is then multiplied by the loss factor due to the outcoming mirror $v_g \alpha_m = 1/\tau_m$, giving the optical power out of the cavity, P_0 as

$$P_0 = hf_0 N_p V_p v_g \alpha_m, \quad I > I_{th} \tag{2.25}$$

From Eqs. (2.25), (2.24) (2.14) and using $\Gamma = V/V_p$ we get

$$P_0 = \eta_i \frac{\alpha_m}{\alpha_i + \alpha_m} \frac{hf_0}{q}(I - I_{th}), \quad I > I_{th} \tag{2.26}$$

$$= \eta_d \frac{hf_0}{q}(I - I_{th}), \quad I > I_{th} \tag{2.27}$$

where η_d is the differential quantum efficiency that defines the number of photons generated per injected electron. Eq. (2.27) defines the total power P_0 out of the cavity. If both mirrors have the same reflection coefficients, then the power out of each mirror is $P_0/2$. However, in
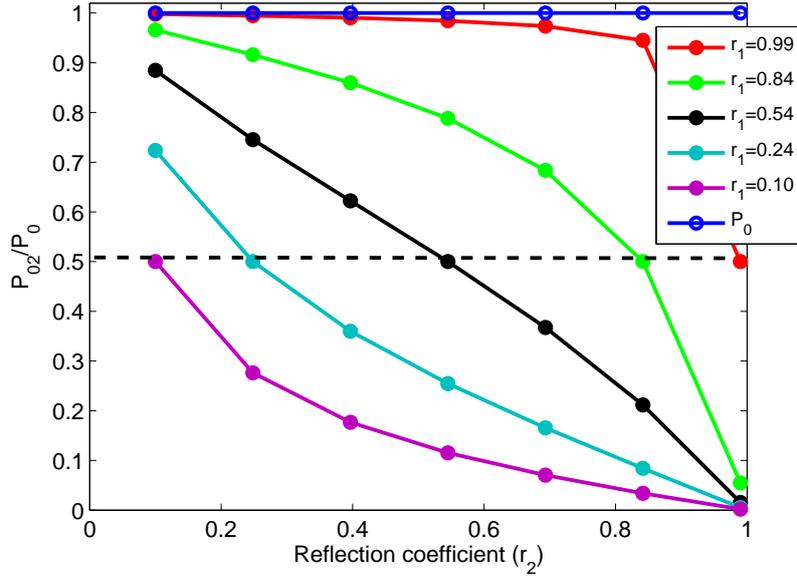
Figure 2.7: Effect of reflectivity of the mirror at $z = l$ (r_2) on power emission (P_{02}), for different values of r_1. The power emitted from laser facet normalized to total power (P_{02}/P_0)varies with the reflection coefficient of the laser facet. The dashed line corresponds to the ideal situation with $r_1 = r_2$ confirming that the emitted power becomes halved whenever the above condition is met.

the general case, the mirrors will have unequal reflection coefficients, so the emission will take place only in one direction. Let P_{01} be the power out of the mirror having reflection coefficient r_1 (which corresponds to the left mirror, $z = 0$ in Fig. 2.6), and P_{02} that leaving the mirror with a reflectivity r_2 (the right surface, $z = l$ in Fig. 2.6). Obviously $P_0 = P_{01} + P_{02}$. The ratio of both P_{01} and P_{02} is given by Eq. (2.28), and similarly the fraction of total power emitted from each surface is given by Eqs. (2.29) and (2.30), respectively. It is evident that the power emitted from one mirror is dependent upon the reflection coefficient of both of them.

$$\frac{P_{01}}{P_{02}} = \frac{r_2(1 - r_1^2)}{r_1(1 - r_2^2)}. \tag{2.28}$$

$$\frac{P_{01}}{P_0} = \frac{(1 - r_1^2)}{(1 - r_1^2) + \frac{r_1}{r_2}(1 - r_2^2)}. \tag{2.29}$$

$$\frac{P_{02}}{P_0} = \frac{(1 - r_2^2)}{(1 - r_2^2) + \frac{r_2}{r_1}(1 - r_1^2)}. \tag{2.30}$$

Fig. 2.7 explains the effect of the reflectivity of both mirrors upon the optical power emitted (P_0) by the right mirror at $z = l$, P_{02}. Initially the optical power generated in the cavity is a function of the pump current, the internal cavity losses and the mirror losses (Eq. (2.27)). The rest of the curves show the dependence of P_{02} upon r_1 and r_2. Keeping r_1 constant and increasing r_2, P_{02} decreases. In addition, whenever $r_1 = r_2$, P_{02} is exactly halved as compared to P_0, as expected (shown by the dashed line).

This strong dependence of the laser's power and its stability on the reflection coefficient

of the cavity mirrors is an important mechanism with profound implications. If the reflection coefficient is perturbed periodically, for instance by coupling the reflected field from an external vibrating target, so an equivalent cavity may be formed, the optical output power will change periodically, containing the signature of the vibrating parameters. This is exploited in depth when we use the laser as a sensor. This is further detailed in Sec. 2.3, where it is shown that by just placing a reflective surface in front of the laser, the equivalent reflectivity and ultimately the emission power is changed.

2.2.3   SMALL SIGNAL FREQUENCY RESPONSE OF THE LASER

In this section, the laser rate equation presented in (2.10) and (2.11) is used to determine the relaxation resonance frequency and its relationship to the modulation bandwidth when an AC component is applied to the current feeding the laser. Let us consider that the laser is biased at I_0 and an additional AC current $i_m(t) = A_m e^{j\omega_\mathrm{m} t}$ is applied. In steady state, this new current changes the carrier and photon density in a similar way to the AC current. Using complex frequency notation,

$$I = I_0 + A_m e^{j\omega_m t}. \tag{2.31}$$

$$N = N_0 + N_m e^{j\omega_m t}. \tag{2.32}$$

$$N_p = N_{p0} + N_{pm} e^{j\omega_m t}. \tag{2.33}$$

where $i_m(t)$ is the modulation current with modulation frequency ω_m and amplitude A_m. Similarly, $N_0(N_{p0})$ is the carrier (photon) density at the bias point; and N_m (N_{pm}) is the peak carrier (photon) density subjected to modulation current $i_m(t)$. Rewriting Eqs. (2.10) and (2.8) using (2.9) and neglecting the spontaneous emission term, we get

$$\frac{dN}{dt} = \frac{\eta_i I}{qV} - \frac{N}{\tau} - v_g a(N - N_{tr})N_p. \tag{2.34}$$

$$\frac{dN_p}{dt} = \Gamma v_g a(N - N_{tr})N_p - \frac{N_p}{\tau_p}. \tag{2.35}$$

Using the values of I (Eq. (2.31)), N (Eq. (2.31)) and N_p (Eq. (2.31)) in Eqs. (2.34) and (2.35), and after some manipulation (shown in appendix A) the response in the frequency domain of the carrier concentration and photon density are

$$j\omega_m N_m = \frac{\eta_i A_m}{qV} - \frac{N_m}{\tau} - \frac{N_{pm}}{\Gamma \tau_p} - v_g a N_m N_{p0}. \tag{2.36}$$

$$j\omega_m N_{pm} = \Gamma v_g a N_m N_{p0}. \tag{2.37}$$

Eqs. (2.36) and (2.37) describe the coupling of the carrier density N_m and the photon density N_{pm} induced by the added small AC current. From Eq. (2.36) we see how as N_m increases, N_{pm} also increases, meaning that the small AC current causes population inversion and creates the mechanism for gain and for an increase in photon density. However, from the third term on
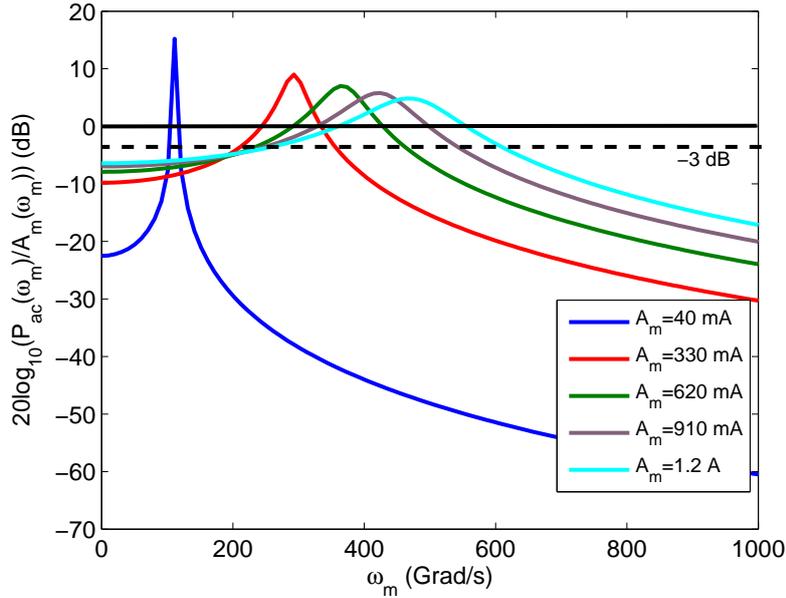
Figure 2.8: Frequency response of a laser under small AC signal modulation. The resonance frequency shifts to higher frequency values at increased bias current. The parameters used in the simulation were $\Gamma = 0.6$; $v_g = 0.75 \times 10^{10}$ cm/s; $a = 5 \times 10^{-16}/$ cm^2; $\eta_i = 1$; $V = 5 \times 0.25 \times 200$ μm^3; $\lambda = 692.5$ nm; $I_{th} = 30$ mA; $\tau_p = 2$ ps; $\tau = 3$ ns; $\alpha_m = 60$/cm; $\alpha_i = 5$/cm [1]. The $20log_{10}(*)$ scale is used because optical power is proportional to current and, for most of the cases, we are concerned about electrical power.

the right of Eq. (2.36), as N_{pm} increases N_m needs to decrease, as stimulated emission results in a decrease in the carrier concentration. Once N_m starts to decrease, N_{pm} also decreases (Eq.(2.37)), as there are less carriers to introduce recombination and emit a photon. Furthermore, as N_{pm} decreases, this causes N_m to increase (Eq.(2.36)). This completes one full cycle which is then repeated. This coupling of carrier and photon density produces a natural resonance in the laser's cavity. The frequency ω_R describing this natural resonance of oscillation in the cavity (the relaxation frequency) is found by multiplying Eq.(2.36) and (2.37), and adding some manipulation (shown in appendix A).

$$\omega_R^2 = \frac{v_g a N_{p0}}{\tau_p}. \tag{2.38}$$

The overall frequency response of the laser under a small signal modulation is determined by the optical-electrical transfer function, which is the ratio of the output optical power to the current input. It is obtained by solving Eqs. (2.36) and (2.37) and the detailed derivation is given in appendix B)

$$\frac{P_{ac}(\omega_m)}{A_m(\omega_m)} = \eta_d \frac{hf_0}{q} \frac{1}{(1 - \frac{\omega_m^2}{\omega_R^2}) + j\frac{\omega_m}{\omega_R}(\frac{1}{\omega_R \tau} + \omega_R \tau_p)}. \tag{2.39}$$

Fig. 2.8 shows the resonance frequency of the semiconductor laser at different AC current modulation frequencies ω_m, and for different values of the bias current. The detailed simulation

parameters are indicated in the figure caption. It is observed how keeping A_m constant, an increase in ω_m increases the magnitude of the transfer function. When $\omega_m = \omega_R$ a resonance occurs, and further increasing ω_m degrades significantly the transfer function. Thus, there is a limited range of frequencies over which the laser can be modulated. It is also observed that the resonance increases when the bias current is increased. It is also observed that the higher the bias current, the higher the resonance frequency and hence the higher the modulation bandwidth. This relationship is explicitly explained in Eq. (2.41) Using Eqs. (2.25) and (2.16), the definition of $\Gamma = V/V_p$ and the expression for η_d from Eq. (2.27) (detailed in appendix A) , the equation which expresses the relaxation frequency in terms of output optical power is

$$\omega_R = [\frac{\Gamma v_g a}{h f_0 V} \frac{\eta_i}{\eta_d}]^{\frac{1}{2}} \sqrt{P_0}. \tag{2.40}$$

Similarly, using Eq. (2.27) and Eq. (2.40), the relaxation frequency is expressed in terms of threshold current as

$$\omega_R = [\frac{\Gamma v_g a}{q V} \eta_i]^{\frac{1}{2}} \sqrt{I - I_{th}}. \tag{2.41}$$

Equation (2.40) and (2.41) demonstrate the fact that the relaxation frequency is proportional to the output optical power or, equivalently, that it will be key to keep the bias of the laser well above the threshold value. This has a direct implication, as it will be shown in Sec. 6.2.2 that the bandwidth of proposed CWFM-DOF sensor is dependent upon the modulation frequency of the laser and hence it is desirable to modulate the laser as high as possible. This requires that the laser to be biased away from threshold, but this in turn has a trade-off that for the OFI to be efficient, it should be biased close to the threshold [76]. For most of the cases it is of interest to find the modulation bandwidth of laser, ω_{3dB}, defined as the frequency at which the electrical power reduces to half its value at direct current (DC) value. Using Eq. (2.39), it is determined by [1]

$$\omega_{3dB} = \sqrt{1 + \sqrt{2}} \omega_R \approx 1.55 \omega_R, \tag{2.42}$$

using typical values in a semiconductor laser, like $\Gamma = 0.6$, $v_g = 0.75 \times 10^{10}$ cm/s, $a = 5 \times 10^{-16}/\text{cm}^2$, $q = 1.6 \times 10^{-19}$ C, $V = 5 \times 0.25 \times 200$ μm^3, $\eta_i = 1$, $I = 80$ mA, $I_{th} = 30$ mA, the calculated ω_R (f_r) is 53 Grad/s (8.4 GHz) (Eq. (2.41)) and ω_{3dB} (f_{3dB}) is 82 Grad/s (13 GHz) (Eq. (2.42)). Authors in [77] experimentally measured the resonance frequency of Indium Gallium Arsenide (InGaAs) lasers to be 6 GHz when a 4 mA bias current was used. The modulation bandwidth of laser is thus in the order of a few GHz. This relationship will be very important in the cases when wideband frequency modulation of the laser is desired, e.g. in high speed data communication using optical fibre. In addition, it is shown in Sec. 6.2.2 of this Thesis how the bandwidth of the proposed sensor based on OF is proportional to the modulation frequency of laser, so a high relaxation frequency is very desirable so the laser may be modulated to high frequencies, and ultimately to increase the bandwidth of the proposed sensor, which is part of the goals of this PhD.

2.2.4 FM RESPONSE OR FREQUENCY CHIRP

It was shown in Eqs. (2.36) and (2.37) that injection modulation changes both the carrier density and the photon density in the gain medium. Since carrier density is related to both gain and refractive index, its modulation affects both of them. Eq. (2.19) shows that the frequency of the emitted photons depend upon the effective refractive index of the material forming the cavity, and the cavity length. The effective refractive index depends upon the lasing frequency (the wavelength dispersion, defined as $dn/d\lambda$) and the carrier concentration (the plasma loading, defined as dn/dN) [1].

In addition, refractive index of the active medium forming the laser cavity is a complex quantity consisting of real (n_l) and imaginary parts ($n"_l$), with the imaginary part directly related to gain through

$$\tilde{n}_l = n_l + jn_l''. \tag{2.43}$$

$$g = \frac{4\pi}{\lambda}n_l''. \tag{2.44}$$

On one hand, the modulation of the gain due to the AC current causes IM, while, on the other hand, the modulation of refractive index causes a modulation in the optical path length of the cavity, which introduces FM. The parameter that relates IM to the FM is the linewidth enhancement factor (α), described by

$$\alpha = -\frac{dn_l/dN}{dn_l''/dN} = -\frac{4\pi}{\lambda}\frac{dn_l/dN}{dg/dN} = -\frac{4\pi}{\lambda a}\frac{dn_l}{dN}. \tag{2.45}$$

From Eq. (2.45), with a change in carrier density defined by ΔN, the change in refractive index Δn_l is

$$\Delta n_l = \frac{\lambda}{4\pi}a\alpha\Delta N. \tag{2.46}$$

Further, it is shown in [72] that the frequency shift (also called the frequency chirp, $\Delta\nu$) in the emission is related to α so ΔN is written as

$$\Delta\nu = \frac{\alpha}{4\pi}\Gamma v_g a\Delta N. \tag{2.47}$$

It is observed that frequency chirp is directly proportional to the linewidth enhancement factor. For instance, consider an Indium Gallium Arsenide Phosphite (InGaAsP) laser with emission frequency at 692 nm which is modulated as $\Delta N = 5 \times 10^{17}/$ cm^3. Let us also consider the other parameters to be $\alpha = 4$, $\Gamma = 0.6$, $v_g = 0.75 \times 10^{10}$ cm/s, $a = 5 \times 10^{-16}$ cm^2. Under these conditions, the frequency chirp is $\Delta\nu = 358$ GHz, which corresponds to a change in wavelength $\Delta\lambda = 0.57$ nm. Similarly, if the carrier concentration is periodically swept using injection modulation by an AC current, the frequency shift introduced varies periodically. This mechanism is the basis of the concept behind the high frequency vibrometry sensor described later in Ch. 6 of this memory. Fig. 2.9 shows the linear chirp introduced in the laser by varying
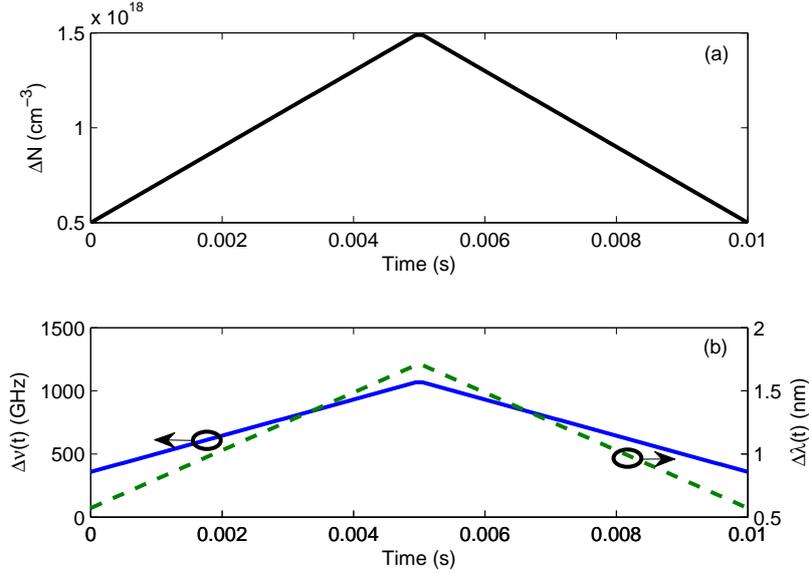
Figure 2.9: Frequency chirp in laser emission due to IM: (a) Carrier concentration changed due to injection current; (b) Change in frequency (wavelength) of the emission due to the change in carrier concentration.

the carrier density using a triangular modulation current. It should be noted that the Fig. 2.9 shows the magnitude of chirp, and the sign has not been taken into account.

In the general case, the frequency (wavelength) decreases (increases) following the increase in carrier concentration. In most of the cases, it is desirable to relate the frequency chirp to the power output of the laser, so the relation between IM and FM can be established. Authors in [78] have shown that the frequency chirp is related to power emission by

$$\Delta\nu = \frac{\alpha}{4\pi}[\frac{\mathrm{d}}{\mathrm{d}t}ln(P_0(t)) + \frac{2\Gamma}{Vhf_0}P_0(t)]. \tag{2.48}$$

The first term of Eq. (2.48) corresponds to the chirp caused by electron-hole resonance, while the second term is the adiabatic chirp. It is clear from Eq. (2.48) that the amount of chirp introduced in a semiconductor laser depends strongly upon the power emission. So, the higher is the bias point relative to the threshold, the larger will be the power and, subsequantly, the larger will be the chirp introduced. As a consequence, in the case where a large chirp in the emission is desired, the operating point should be set well above the threshold of the laser. Secondly, the amplitude of the current modulation should be large enough to produce significant changes in the power emission from the laser. Eq. (2.48) is plotted in Fig. 2.10 showing the effect of the change in optical power on the frequency chirp. Here the emitted power is modulated by an injection current with different amplitudes but a with constant frequency $f_\mathrm{m} = 1$ kHz. It is observed that with an increase in modulation current, the emitted power increases (Fig. 2.10 (a)) and simultaneously the frequency chirp also increases (Fig. 2.10 (b)).

Along Ch. 6 of this Thesis the feasibility of the use of the phenomena of frequency chirp for high frequency vibrometry is demonstrated. There the effect of IM, upon the chirp is exploited

25
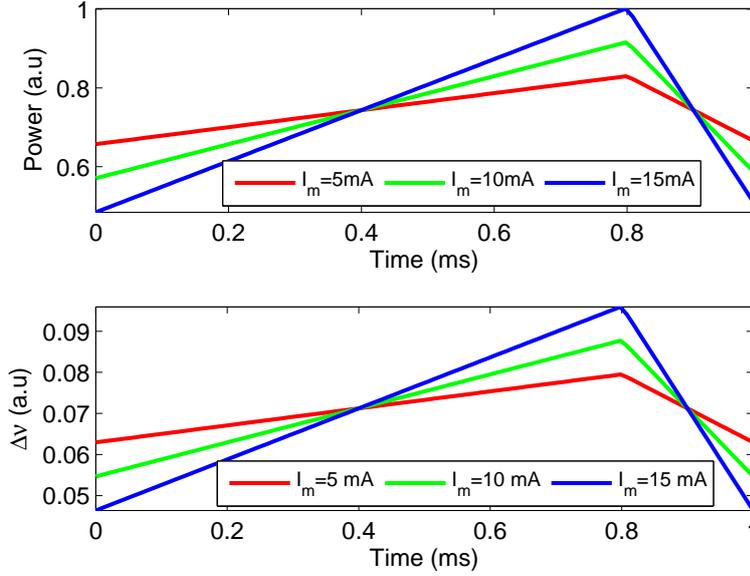
Figure 2.10: Frequency chirp in laser emission depending upon the emission power (Eq. (2.48)). With the increase in amplitude of the modulation current (a sawtooth waveform), the emission power increases (a) and ultimately the chirp also increases (b).

for the development of a laser based vibrometer. However, chirp has some secondary effects as it causes spectrum and linewidth broadening, which are not desirable features for a laser-based sensor. While spectrum broadening introduces the need of wideband detectors and amplifiers, linewidth broadening causes the laser beam to be incoherent and thus to reduce fringe visibility. For the use of the SCL as an interferometric sensor, there exists a trade-off between the amount of chirp and the bandwidth, which is analyzed next.

The frequency response of the laser in the presence of chirp is described in [1] as

$$\Delta B_{chirp} = \frac{\alpha}{4\pi}(\gamma_{pp} + j\omega_m)\frac{P_1}{P_0} = \frac{\alpha}{4\pi}m_1(\gamma_{pp} + j\omega_m), \tag{2.49}$$

where ΔB_{chirp} is the chirp of the signal emitted from the laser, $\gamma_{pp} = \Gamma v_g a_p N_p$ is a parameter related to effective photon life time with a typical value of 1.32×10^9/s, $a_p = \partial g/\partial N_p$ is the change in gain due to changes in photon density, P_1 is the peak power emitted from laser under modulation, and $m_i = P_1/P_0$ is the intensity modulation index. It should be noted that although m_i is the ratio of power, however normalizing the power to the emitted beam area, we get intensity and it is desirable to express it in terms of intensity rather than the power. In most of the cases, it is also desirable to express the frequency spectrum in terms of the bias current, as it is the main factor controlling the power emitted from the laser. The modulation in the emission power P_1 is related to the transfer function of the laser $H(\omega_m)$ and the modulation current A_m as

$$P_1 = \frac{hf_0}{q}H(\omega_m)A_m. \tag{2.50}$$

26
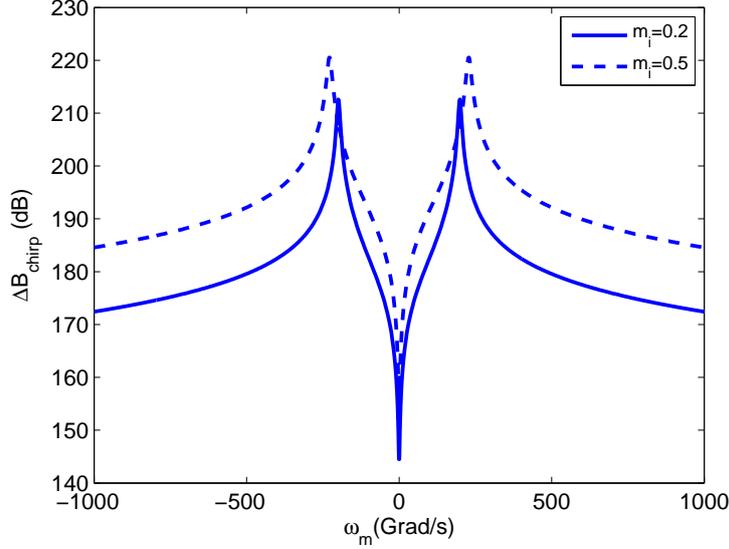
Figure 2.11: Effect of chirp IM on spectrum of laser emission (Eq. (2.49)). 3 dB spectrum of laser emission increases from 3.1 Grad/s to 8.5 Grad/s with increase in m from 0.2 to 0.5. The parameters used in the simulation were $\Gamma = 0.6$, $v_g = 0.75 \times 10^8$ m/s, $a = 5 \times 10^{-20}$ m^2, $\eta_i = 0.5$, $q = 1.6 \times 10^{-19}$ C, $V = 3.75 \times 10^{-14}$ m^3, $h = 6.62 \times 10^{-34}$ Js, $c = 3 \times 10^8$ m/s, $\lambda = 692.5 \times 10^{-9}$ m, $f_0 = 4.3 \times 10^{14}$ Hz, $\tau_p = 2 \times 10^{-12}$ s, $\tau = 3 \times 10^{-9}$ s, $\alpha_m = 6000$/m, $\alpha_i = 2000$/m, $\eta_d = 0.75$, $\alpha = 4$, $\gamma_{pp} = 1.32 \times 10^9$/s.

Using Eqs. (2.49), (2.50), and (2.27), one may find out the frequency response of the laser in presence of chirp in terms of the modulation current as

$$\Delta B_{chirp} = \frac{\alpha}{4\pi}(\gamma_{pp} + j\omega_m)\frac{A_m}{\eta_d(I - I_{th})}H(\omega_m), \tag{2.51}$$

Dividing both sides of Eq. (2.49) by $f_{\mathrm{m}} = \omega_{\mathrm{m}}/(2\pi)$, we get

$$M = \frac{\alpha}{2}m_i(\frac{\gamma_{pp}}{\omega_m} + j1), \tag{2.52}$$

where $M = \Delta B_{chirp}/\omega_m$ is the FM modulation index of the laser. Equation (2.52) is important as it demonstrates the fact that IM and FM have complex relationships, and both their magnitude and phase need be taken into account to determine the general behaviour of the laser. In addition, the magnitude of FM is proportional to the magnitude of IM, and is related to the LEF. Fig. 2.11 shows the effect of m_i on the frequency chirp. It is observed how the chirp in the laser increases when IM does. This confirms the fact that higher modulation currents induce larger chirps in the laser.

Figure 2.12 shows the detailed magnitude and phase relationships between IM and FM, as a function of the modulation frequency at a fixed $m_i = 0.2$. It is observed that keeping the m_i constant at 0.2, while increasing the modulation frequency ω_{m}, the relationship between IM and FM is modified substantially. When $\omega_{\mathrm{m}} << \omega_R$ the magnitude response of FM is dominant over IM (Fig. 2.12 (a)) and both have the same phase (Fig. 2.12 (b)). When the modulation frequency increases ($\omega_{\mathrm{m}} < \omega_R$), the magnitude response of FM is still dominant over that of IM

(Fig. 2.12 (c)), however a phase difference between them starts to appear, which increases with an increase in the modulation frequency ω_m (Fig. 2.12 (d)). Such phase change is equivalent to a delay between IM and FM in the time domain. Further increasing the modulation frequency so it becomes close to the resonance frequency of the laser ($\omega_\mathrm{m} \approx \omega_R$) makes the magnitude response of IM to increase very significantly and approach the magnitude of FM (Fig. 2.12 (e)), and also a sharp transition appears near the resonant frequency ω_R in both phase terms (Fig. 2.12 (f)). Finally, when modulating the laser beyond the resonance frequency $\omega_\mathrm{m} > \omega_R$, the magnitude response of both terms does not significantly change (Fig. 2.12 (g)), but a constant phase difference between them appears (Fig. 2.12 (h)) (in opposition to what happened in Fig. 2.12 (d), where the phase difference increased with increase in modulation frequency).

Let us now briefly look at the role of the value of m, the amplitude modulation index defined in Eq. 2.49 . It is observed that equivalent results are found when m_i is increased to 0.5 (Fig. 2.13). A more useful descriptor is the ratio of FM to IM response, (M/m_i). From Eq. (2.52), it is clear that such ratio is dependent upon the internal parameters of the laser γ_{pp} and α. The ratio of FM to IM at different values of the linewidth enhancement factor α is shown in Fig. 2.14. It is observed that keeping α constant and increasing the modulation frequency, the ratio decreases. However, the ratio increases with the increase in α as expected from Eq. (2.52). The ratio of FM to IM for an InGaAsP DFB laser has been measured experimentally [79] showing values as high as 3 in a linear scale for a modulation frequency of $f_\mathrm{m} = 3$ GHz.

2.2.5 LINEWIDTH BROADENING

The quantitative broadening of the spectral width of the laser due to the induced chirp can be calculated considering the spectral broadening ($\delta\nu_i$) due to sinusoidal frequency modulation. The spectral broadening in response to FM, in this case, defined as the difference in spectral width of laser under IM ($\delta\nu_1$) and solitary laser ($\delta\nu_0$) is given as [72]

$$\delta\nu_i = \delta\nu_1 - \delta\nu_0 = 2(M+1)f_m. \tag{2.53}$$

Equation (2.53) states simply that the linewidth of the laser increases linearly with the increase in modulation frequency f_m. Further, given the source has a Gaussian emission spectrum, the spectral width of the laser is inversely proportional to the coherence length of the beam (Eq. (2.54)) [72]. Thus, the chirp introduced by injection modulation has on influence on coherence, and subsequently on the inherent internal properties of the laser as well. Coherence is related to spectral broadening through

$$\delta l_{coh} \approx \frac{c}{\delta\nu_i}, \tag{2.54}$$

where δl_{coh} is the change in coherence length of laser under IM as compared to solitary case. Figure 2.15 shows the effect of the modulation frequency on the spectral width and coherence length of the field emitted, for different values of the amplitude modulation index. It is seen

that the larger the value of m_i, the larger the spectral broadening and the smaller the coherence length. Further, it may be appreciated how the most relevant effects are found for values close to $f_{\mathrm{m}} = 0$.
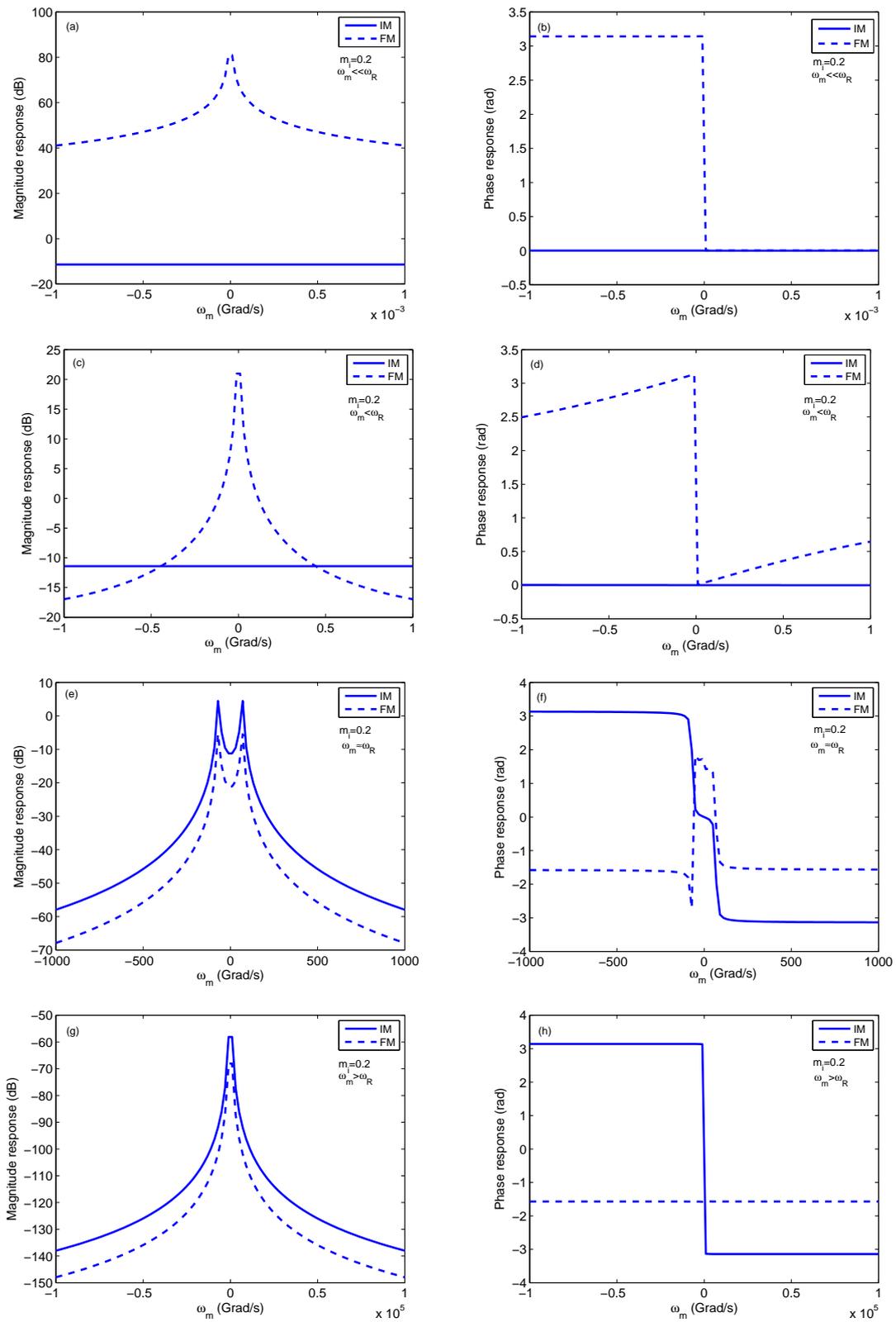
Figure 2.12: Magnitude and phase relationships between IM and FM in a laser subject to a modulation with $m_i = 0.2$, at different ω_m. ω_R is the resonance frequency defined by Eq. 2.41.

30
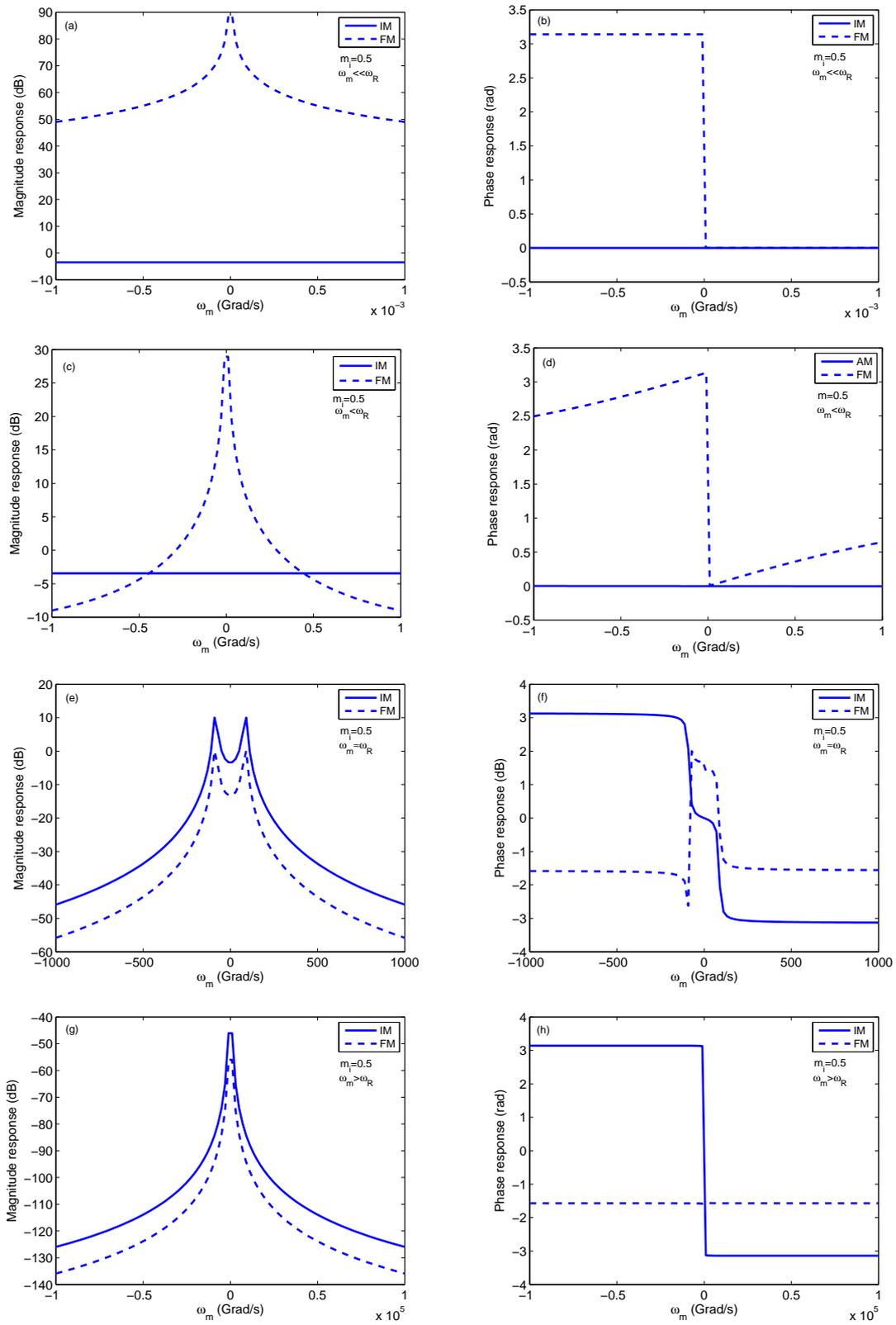
Figure 2.13: Magnitude and phase relationships between IM and FM in a laser subject to a modulation with $m_i = 0.5$ at different ω_m. ω_R is resonance frequency defined by Eq. 2.41.
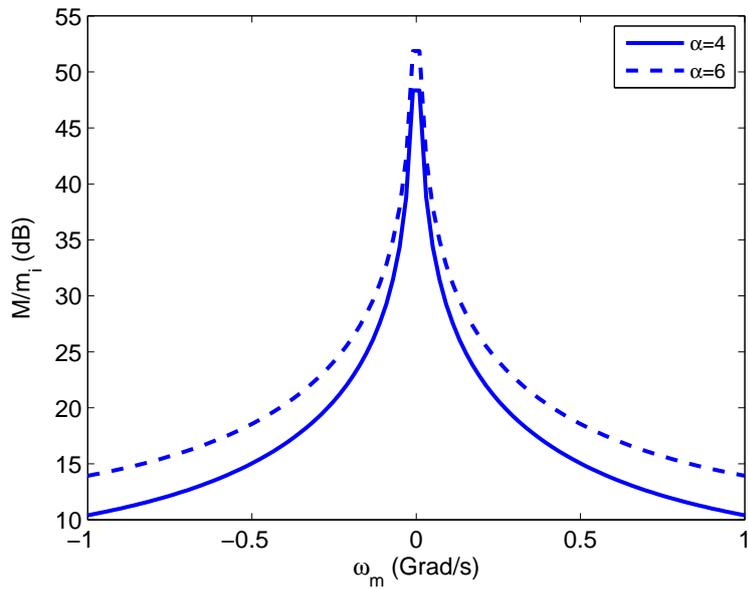
Figure 2.14: Ratio between frequency modulation index (M) and intensity modulation index (m_i). The ratio decreases with increase in modulation frequency ω_m but increases with the increase in linewidth enhancement factor α.
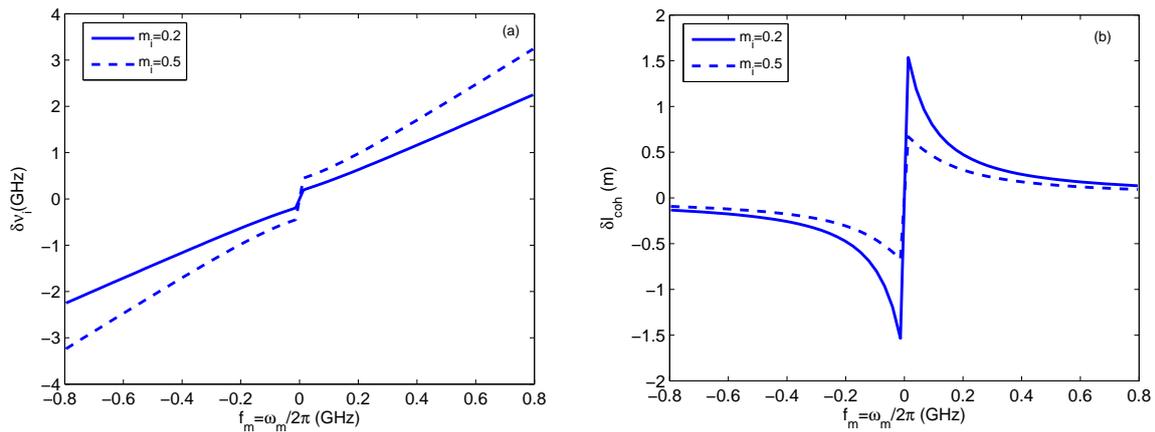
Figure 2.15: Effect of IM on the spectral width and coherence length of the laser. An increase in the modulation index (m_i) brings on an increase in spectral width and a decrease of the coherence length

2.3 OPTICAL FEEDBACK

Because of their high-gain active medium, low-Q optical cavity, and extraordinarily small size, SCL are extremely sensitive to OF [80]. In addition, as a result of the change in reflectivity in the facets of SCL, they are extremely sensitive to spurious reflections, which cause a fraction of the light emitted by the laser to re-enter the laser cavity. Surprisingly, levels of emitted field fed back into the cavity below -90 dB, which correspond to reflected powers in the 1 pW range for emitted powers in the 1 mW range, are enough to significantly change the spectral and temporal characteristics of the laser [3]. It was shown in Eq. (2.20) that the mode emission from the laser was dependent upon the length of the cavity in which the gain medium was placed. Hence, altering the cavity length the mode emission is significantly changed, which for example happens when placing an external reflective mirror at a given distance from the emitting facet of the laser. In typical laser-based applications, like for instance in fibre optics communications, OF causes a serious degradation of the laser behaviour when a small fraction of the emitted power is sent back to the cavity from the laser-fibre interface. It is well known that lasers are used in a wide variety of applications, including spectroscopy, biomedical imaging, aeronautics, environmental sensing, or optical metrology, where the stability and reliability of the laser performance is of utmost importance, so the influence of OF on laser performance has gained considerable attention in the late years, as it causes a very rich and complex dynamical behaviour which alters significantly the properties of the laser and gives rise to different applications. Therefore, a deeper understanding of the dynamical behaviour of the semiconductor laser is required in order to avoid, or to take advantage, of such instabilities in real world applications. This will be covered in this Section.

The history of OF dates to 1970 when Broom et al. reported, for the first time, the observation of some dynamical effects arising in SCL coupled to an external resonator [81]. Later, Morikawa et al. discussed the appearance of oscillations in the output of SCL subject to optical reflections [82]. Hirota and Suematsu [83] theoretically demonstrated that conditions of OF introduced noise in the laser. They also demonstrated that the laser's dynamic properties, in the presence of OF, were strongly dependent upon the distance of the external reflector from the laser. Specifically, the behaviour was classified as being either that of a "double cavity state" or that of an "external injection state", depending on whether the distance to the external reflector was smaller or greater than the coherence length of the laser. One of the most important effects of OF described in this paper was that induced noise would be expected to play a central role in many applications of semiconductor lasers.

Paradoxically, very soon it was realized that OF could have a beneficial effect for laser applications. Authors in [84] used OF to enhance the longitudinal mode selection and for narrowing the linewidth of the laser. Chinone et al. [85] showed an improvement of the relaxation oscillations when the external reflector was placed at large distances from the laser, while the

contrary, that is, a reduction in the relaxation oscillations was achieved when such distance was less than a few centimetres from the laser. Lang and Kobayashi [30] presented a complete theoretical model to explain the various complex phenomena arising due to the presence of OF. Moreover, they explained several of the aspects of the basic physics of semiconductor laser gain media which led to complex behaviour under conditions of external feedback, including the description of the broad gain spectrum which appeared. The paper included experimental measurements of the behaviour of the semiconductor laser subject to optical reflections from an external mirror placed a few centimetres away from the laser. Among a number of different interesting features of the behaviour of the device, the authors reported experimental observation of bistability, and of hysteresis effects in light output power against the drive current characteristics of the lasers. In addition, they experimentally demonstrated that OF from an external vibrating reflector changed the optical output power periodically (where each period represented an amplitude of half the emission wavelength), which paved the way to use the laser as a sensor to detect the vibration of remote external reflectors [30]. Thus, studying the OF effects in semiconductor lasers is key due to the confluence of a number of significant features arising from both practical and theoretical considerations if we are to develop and understand SCL-based sensors. In particular, it is key to understand the compound cavity effects, [72] and the Lang-Kobayashi model [30] which are discussed further in the following.

2.3.1   COMPOUND CAVITY MODEL

To consider the effect of OF, the model of the laser cavity in Fig. 2.6 is modified to include a third external cavity, as shown in Fig. 2.16(a). In the presence of a partially reflective target at distance L_{ext}, an external cavity is formed in addition to the laser's internal cavity. The equivalent reflection coefficient (r_{eq})[9] resulting from the laser's facet r_2 and the external target r_{ext} is a complex term given by [72].

$$r_{eq} = r_2 + (1 - |r_2|^2)r_{ext}e^{-j\omega_s\tau_{ext}}, \tag{2.55}$$

$$= |r_{eq}|e^{-j\phi_{eq}}, \tag{2.56}$$

where ω_s is the angular frequency of emission under OF, $\tau_{ext} = 2L_{ext}/c$ is the round-trip time of the field in the external cavity, often called the external round-trip delay, and $|r_{eq}|$ and $\phi_{ext} = \omega_s\tau_{ext}$ are the magnitude and phase of the equivalent reflection coefficient, respectively. Using this concept of equivalent reflection coefficient, the model now reduces to an "equivalent" internal cavity of the laser provided that the facet reflection coefficients are chosen to be r_1 and r_{eq} (Fig. 2.16(b)). Under these conditions, the phase equation (2.17) becomes

$$2\beta l + \phi_{ext} = 2q\pi, \tag{2.57}$$

---

[9]A more detailed derivation of the equation for equivalent reflectivity is described in Ch. 3, where this compound cavity model will be expanded to include absorption and consider multiple cavities.
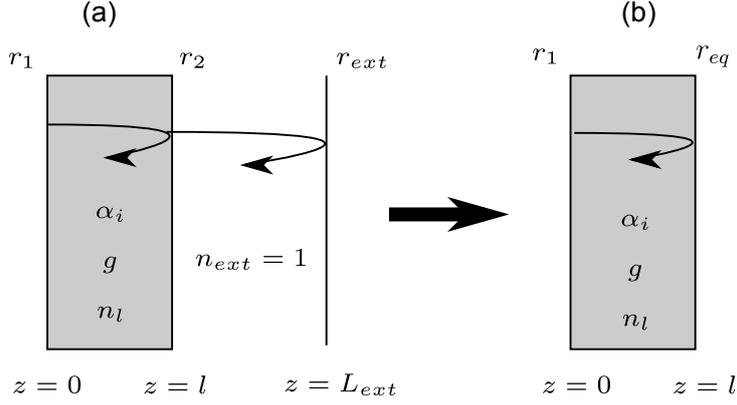
Figure 2.16: Compound cavity model used to explain the effect of OF in the laser cavity. (a) Internal cavity of the laser plus external cavity formed with the target at distance L_{ext}; (b) Equivalent cavity.

where p is an integer, and is the round trip phase of the external cavity (that is, the phase of the reflected field). Without loss of generality, the reflection coefficient of the facet of the laser and the external target can be considered as a positive real number. Equating the real and imaginary parts of Eq. (2.55), we get the in-phase (and quadrature phase components of equivalent reflectivity, given by [72]

$$\text{Re}(r_{eq}) = r_{eq}^r = r_2 + r_2 \kappa cos(\omega_s \tau_{ext}), \qquad (2.58)$$

$$\text{Im}(r_{eq}) = r_{eq}^i = -r_2 \kappa sin(\omega_s \tau_{ext}), \qquad (2.59)$$

with r^r_{eq} being the real part and r^i_{eq} the imaginary part of reflection coefficient, and with the coupling coefficient κ determining the fractional increase in the optical field due to the reflection from the external target, described by

$$\kappa = \frac{(1 - |r_2|^2) r_{ext}}{r_2}. \qquad (2.60)$$

Assuming the reflection coefficients of the facet of the laser and the external target to be real and positive, r^r_{eq} is seen to directly affect the gain of the laser. Using Eqs. (2.14) and (2.58); and $ln(1 + x) \sim x$ (ignoring higher order terms), the change in the threshold gain of the laser due to OF relative to the original gain, Δg_{th} is given as

$$\Delta g_{th} = \frac{-2k}{\Gamma v_g \tau_l} cos(\omega_s \tau_{ext}). \qquad (2.61)$$

which implies that the change in gain of the laser under OF varies as the cosine of the round-trip delay, a very relevant effect for using the laser under OF as a sensor. While r^r_{eq} affects the performance of the gain in the laser, both r^i_{eq} and r^r_{eq} contribute to the change in the emission frequency. r^i_{eq}, on its side, changes the phase of net reflection at mirror ($z = l$ in Fig. 2.16) from zero to $\phi_{ext} = r^r_{eq}$, influencing on the cavity resonant frequency. Without OF, the resonance condition is given by $2\beta l = 2p\pi$ (Eq. (2.17)). In the presence of OF, however, the new phase condition taking into account the phase change due to the quadrature components of

the effective reflection coefficient is $2\beta l + \phi_{ext} = 2p\pi = 2\beta_s l$ (Eq. (2.57)). This implies that the phase constant needs to adjust itself such that $\phi_{ext} = 2(\beta_s - \beta)l = 2\Delta\beta l$. Using $\Delta\beta = \Delta\omega/v_g$, we get

$$\phi_{ext} = 2\frac{\Delta\omega}{v_g}l. \tag{2.62}$$

Rewriting Eq. (2.62) in terms of the laser's cavity round trip time, the change in emission frequency due to the change in the propagation constant, $\Delta\omega_\beta$, is given by

$$\Delta\omega_\beta = \frac{\phi_{ext}}{\tau_l} = \frac{-\kappa}{\tau_l}sin(\omega_s\tau_{ext}). \tag{2.63}$$

In addition to the phase change introduced in the external cavity through r^i_{eq}, the in-phase component r^r_{eq} that changes the threshold gain of laser (Eq. (2.61)) has its own relationship with the threshold carrier density, described through α. This change in the threshold of the carrier density contributes to an additional phase change, and hence shifts the emitted frequency. For small changes, the differential gain is approximated as $a \sim \Delta g/\Delta N$ [1]. Using Eq. (2.61), the change in carrier density at threshold, ΔN_{th}, is determined as

$$\Delta N_{th} = \frac{-2\kappa}{\Gamma v_g \tau_l a}cos(\omega_s\tau_{ext}). \tag{2.64}$$

Using Eq. (2.47), the induced change in frequency emission due to carrier concentration $\Delta\omega_N$ becomes

$$\Delta\omega_N = -\alpha\frac{\kappa}{\tau_l}cos(\omega_s\tau_{ext}). \tag{2.65}$$

Adding Eqs. (2.63) and (2.65) and using $asin\theta + bsin\theta = \sqrt{(a^2 + b^2)}sin[\theta + tan^{-1}(b/a)]$, the total change in emission frequency due to the presence of OF is written as

$$\Delta\omega = \frac{-\kappa}{\tau_l}\sqrt{1 + \alpha^2}sin(\omega_s\tau_{ext} + tan^{-1}\alpha), \tag{2.66}$$

where $\Delta\omega = \omega_s - \omega_0$ is the change in emission frequency due to the presence of OF. It is convenient to rewrite Eq. (2.66) in terms of the change in frequency in the argument of the *sin* function as well, yielding

$$\Delta\omega = \frac{-\kappa}{\tau_l}\sqrt{1 + \alpha^2}sin(\Delta\omega\tau_{ext} + \omega_0\tau_{ext} + tan^{-1}\alpha). \tag{2.67}$$

Multiplying Eq. (2.67) by τ_{ext}, we get the expression for the excess phase introduced in the system due to OF,

$$\Delta\phi_{ext} = -Csin((\omega_s - \omega_0)\tau_{ext} + \phi_0), \tag{2.68}$$

where $\Delta\phi_{ext} = \phi_s - \phi_0'$, and $\phi_s = \omega_s\tau_{ext}$ and $\phi_0' = \omega_0\tau_{ext}$ are the phases of the OFS under feedback, and in absence of OF[10], respectively. The feedback coefficient C and the feedback

---

[10] A condition often called the free running state of the laser, or the standalone laser
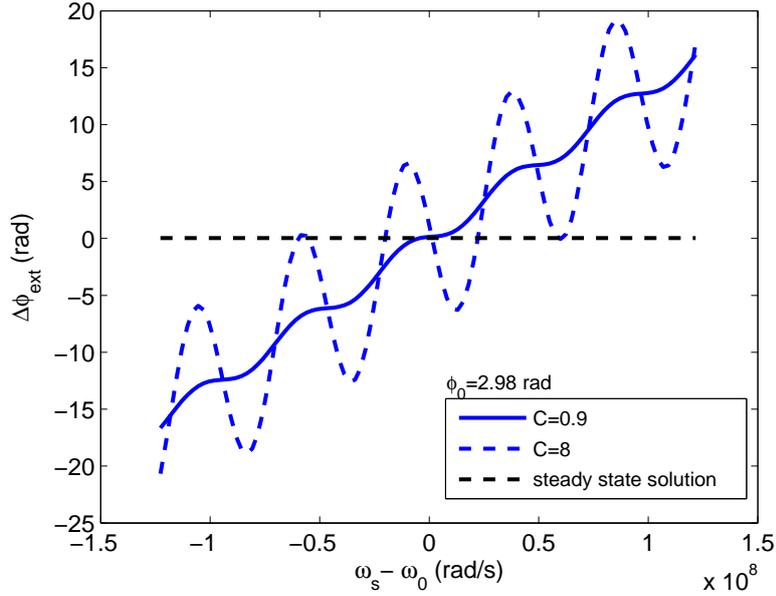
Figure 2.17: Effect of the feedback coefficient C on the number of modes allowed in a cavity under feedback.

phase ϕ_0 [86] are given by

$$C = -\kappa \frac{\tau_{ext}}{\tau_l} \sqrt{1 + \alpha^2} = -\frac{(1 - |r_2|^2)r_{ext}}{r_2} \frac{\tau_{ext}}{\tau_l} \sqrt{1 + \alpha^2}. \tag{2.69}$$

$$\phi_0 = \omega_0 \tau_{ext} + tan^{-1}\alpha. \tag{2.70}$$

Eq. (2.68) is thus a nonlinear equation, and its graphical solution is the value of the abscissa where the ordinate becomes zero. The variation of excess round trip phase $\Delta\phi_{ext}$ as a function of the change in emission frequency $(\omega_s - \omega_0)$ due to OF is shown in Fig. 2.17. It is observed that the solution of Eq. (2.68) determines a very limited number of allowed steady state solutions, corresponding to the number of possible emission frequencies ω_s, which are conventionally referred to as the "modes" in the cavity. The number of solutions of Eq. (2.68) is thus strongly dependent upon the feedback parameter C and the initial phase ϕ_0 [87]. For $C < 1$, there is only one solution to Eq. (2.68) and only one mode exists in the cavity, but as the value of C becomes greater than 1, multiple solutions to Eq. (2.68) may appear, making the laser to behave as a multimodal system. Such multimodal behaviour gives rise to relevant experimental phenomena, being the most important in practice the presence of mode competition, so the mode having highest gain and/or minimum linewidth becomes the dominant one [72]. The existence of feedback levels where two or more modes can simultaneously exist leads also to different nonlinear phenomena, such as mode beating or hystheresis. These are the conditions for C-OF.

Proceeding similarly, when under the presence of *both* IM and OF, there is an additional frequency shift due to injection modulation, which is added to Eq. 2.66 in order to get the

equation for frequency emission for CWFM-OF [52], which stands as

$$\omega_s - (\omega_0 + 2\pi\Omega_f i_m(t))\tau_{ext} = -Csin(\omega_s\tau_{ext} + \phi_0), \qquad (2.71)$$

where Ω_f is the frequency modulation coefficient of the laser in (Hz/mA), and $i_m(t)$ is the modulation current. It should be emphasized that the phase equation in the case of CWFM-OF (Eq. 2.71) has significant differences when compared to that of C-OF (Eq. 2.71), due to the additional term containing Ω_f. Such phase equation has thus different boundary conditions and different laser response as compared to C-OF. The entire Chapter 5 of this Thesis is dedicated to perform a thorough analysis of the laser dynamics for the case of CWFM-OF, and to compare them to the temporal and spectral properties of the laser with C-OF. Such comparison, to the best of our knowledge, is performed for the first time from the laser sensor point of view.

Even though the above detailed analysis was made for a laser of a Fabry-Perot (FP) type, it holds equally true for vertical cavity surface emitting laser (VCSEL) and DFB lasers as well [88, 89]. The detailed analysis of the effect of OF in DFB lasers has been studied in [90]. The sensitivity of these lasers to OF is dependent upon the coupling coefficient (κ) and feedback strength (C). If lasers are to present low sensitivity to OF, the reflection coefficient of the exit facet r_2 of the cavity must be large. This is justified from Eq. (2.60), which suggests that as r_2 increases, the coupling coefficient κ decreases. Such low sensitivity can also be attained by making the laser cavity longer (given the external round trip delay is fixed) hence decreasing the feedback coefficient C (Eq.(2.69)). Since the effective internal round trip delay within the laser cavity in the case of a DFB laser is smaller than in a FP laser of the same cavity length (l), this gives a higher feedback coefficient in DFB lasers. In the case of VCSEL, on one hand, its short cavity length make it sensitive to the OF, but on the other hand, its high reflective facet degrades its response to OF. In addition, as VCSELs are grown on (001) substrate, they lack strong polarization anisotropy and may undergo polarization switching and degrade its performance when subjected to OF [91]. Thus DFBs are more sensitive to OF when compared to FP and VCSEL.

2.3.2 THE LANG-KOBAYASHI MODEL

Although the effects of OF on the operation of a semiconductor laser had been studied earlier [81, 92], the 1980 paper by Lang and Kobayashi [30] is generally considered a milestone in the sense that it settled the basis for the initiation of enormous research efforts devoted to studying in depth optical-feedback effects from both theoretical and experimental sides. Essentially, Lang and Kobayashi showed that a semiconductor laser, when subject to external OF, can show multi-stability as well as hystheresis features, analogous to those occurring in a nonlinear Fabry-Perot resonator. The presence of a reflecting surface outside the laser cavity creates an external cavity, which has its own longitudinal modes with a frequency separation $1/\tau_{ext}$. The existence of two sets of longitudinal modes leads to a competition between the laser cavity (with

a much larger mode spacing) and a passive cavity (no gain in the external cavity), each having its own resonances. Although the results obtained by the Lang-Kobayashi model are exactly the ones obtained using the compound cavity model (Sec. 2.3), this model better describes the situation in a SCL, and it additionally helps to explain other non-linear phenomenons in the cavity such as LFF, period doubling and chaos, to name a few. However, all these phenomena lie outside the scope of this PhD.

The basic concept of the Lang-Kobayashi model lies in studying the non-linearity induced in the laser due to OF by modifying the rate equations of the standalone laser ((2.10) and (2.11)) to accommodate OF.

$$\frac{dE(t)}{dt} = \frac{1}{2}(1 - j\alpha)\Gamma v_g a(N - N_{tr})E(t) + \gamma_{fb}E(t - \tau_{ext})e^{j\omega_0\tau_{ext}}, \tag{2.72}$$

$$\frac{dN(t)}{dt} = \frac{\eta_i I}{qV} - \frac{N(t)}{\tau} - [\frac{1}{\tau_p} + \Gamma v_g a(N - N_{tr})]E(t)^2, \tag{2.73}$$

where $\gamma_{fb} = \kappa/\tau_l$ is the feedback rate, understood as the increase in the optical field per unit round trip time of the internal laser cavity due to feedback. The steady state solution is obtained by equating the Eqs. (2.72) and (2.73) to zero. It is shown in [93] that the phase equation obtained is the same presented in Eq. (2.68). Further, the phase modulation resulting from OF causes the intensity modulation as well, [93, 94]

$$P_s(t) = P_0(1 + m(F(\omega_s\tau_{ext}))), \tag{2.74}$$

where $P_s(t)$ is the power emission from the laser under feedback; P_0 is the power emission from the solitary laser, m is the modulation index as a result of OF effect, and $F(\phi)$ is a function of the feedback phase, whose shape depends upon the feedback strength. For low feedback strengths $C << 1$ (very weak feedback regime), the shape of OFS is a cosine. Increasing the feedback strength to $C < 1$ (weak feedback regime), the shape of OFS starts to deviate from a pure cosine as some inclination appears during the transitions. Further increasing the feedback coefficient to $1 < C < 4.6$ (moderate feedback regime) the inclination increases to eventually become triangular and exhibits hystheresis. At $C > 4.6$ (strong feedback regime), mode hopping is observed and the OFS becomes chaotic. [86, 95].

2.3.3 CLASSIFICATION OF OPTICAL FEEDBACK

Authors in [3] studied the effect of OF on $1.5\mu m$ DFB lasers. It was observed that there exist five regimes of the laser behavior with clear transitions from one to another, depending upon the feedback power ratio and the distance of the laser to the external reflector. The five regimes are schematically depicted in Fig. 2.18. Regime I corresponds to low feedback levels, and is characterized by $C < 1$. The spectral broadening and narrowing of the emission occurs depending upon the phase of the reflected optical field. A change in spectral width of 30%

was observed at a distance of 40 cm with feedback power being -80 dB. This corresponds to a reflected power of 10 pW when the emitted power out of laser is 1 mW. It should be noted that, the further the external reflector, the smaller should be the feedback level, so that the laser will be expected to lie in this regime. For most of the metrological applications of our interest, it is desirable to work in this regime [50].

Regime II is characterized by ($C > 1$), where in principle multiple modes in the cavity may be allowed to exist. The observable phenomenon includes the presence of hopping between the different modes which solve the excess phase equation. However, the external cavity length can be adjusted so a particular mode attains the minimum spectral width, or the minimum threshold gain compared to other competing mode, so with the maximum reduction in spectral width it will become the dominant stable mode. It is shown in [72] that the mode with minimum spectral width is more stable than the one with minimum threshold gain. In addition to mode hopping, mode splitting was also observed depending upon the feedback level and the distance to external reflector. If we further increase the feedback level (from -39 dB to -45 dB), mode hopping is supressed, and the laser operates in a stable mode whose characteristics do not change with the distance to the target. These phenomena are characerized by regime III. Regime IV is the region of coherence collapse. The spectral width becomes so wide that the laser is no longer coherent, and emits radiation of different wavelengths. This regime is not affected by the change in the distance from the laser to the target, and is only dependent upon the feedback level. Finally, regime V is observed when the feedback dominates the field inside the cavity. This is achieved when $r_{ext} >> r_2$. Similarly to Regimes III and IV, the characteristics of the laser in this regime are independent of the distance to the external reflector, and is solely determined by the feedback level.

2.4 APPLICATIONS OF OPTICAL FEEDBACK

The effect of OF on the laser dynamics was studied as early as the invention of the laser itself. This was first discovered by King and Steward as early as in 1963 to induce intensity modulations of the laser. It was found that each modulation period corresponded to a $\lambda/2$ optical displacement of the external reflector [25]. In 1968 Rudd reported detection of the Doppler shift due to the displacement of the remote reflector in gas lasers [96]. Later on, a complete self-aligned interferometer for measurement purposes was presented by Donati in 1978 [97]. OF injection causes rapid intensity modulations of the laser through the interference between the incident lasing field and the frequency shifted (due to target motion), extremely weak reflected field injected back into the laser cavity. Such modulations and are detected by either a built in monitor photodiode or the junction voltage fluctuations [97]. Since then a lot of theoretical and experimental work has been done to use OF in diverse fields of application. In electrical engineering, it has been used to measure the motor shaft runout in an electric motor [98], and
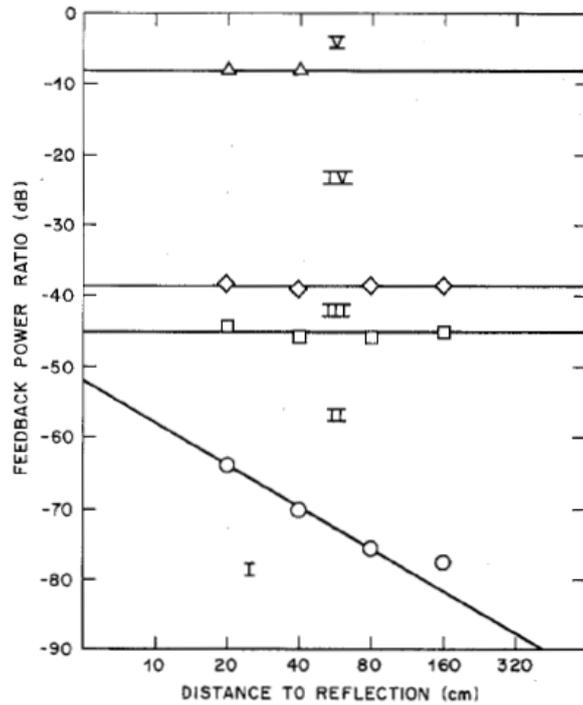
Figure 2.18: Feedback regime of $1.5\mu m$ DFB lasers (after [3]).

the shaft trajectory in synchronous motors [99]; in civil engineering, it has been used to measure beam deformation [100]; in biology, for tissue imaging [101] and tomography [102, 103], or for non-invasive measurements of blood flow rates [8, 61]; it has also been used for the determination of the parameters of lasers [104–106]. Generally speaking, it has been used for the measurement of a large number of other different quantities and applications, inclusing distance [107–110], displacement [111], vibration [112], velocity [113], pressure [114], strain [55], hole depth during laser-based ablation [115]; imaging [52], or acoustic field measurements [7]. A comprehensive list of applications of OF in real world applications can be found in [89], among other sources. In the following we will briefly overview some of the most general parameters, that is, measurements of displacement, velocity, absolute distance, and the applications of the technique more close to the ones in this Thesis, including acoustic fields, biomedical applications, and laser characterization, reviewing the main features of the sensing technique in each case.
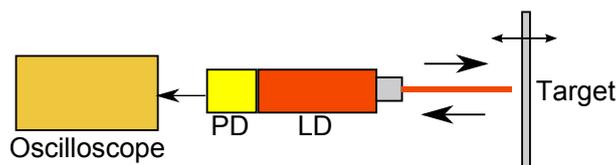
Figure 2.19: Block diagram for OF based Displacement. LD; PD.

41

2.4.1 DISPLACEMENT

It was shown in Sec. 2.3.2, Eq. (2.74) that the OF causes the frequency of the laser, its phase and ultimately its emitted power to modulate. This property is used easily to measure the displacement of a remote vibrating target with just an laser diode. The block diagram to use OF to measure displacement is shown in Fig. 2.19. Suppose the target is vibrating i.e. that the external cavity is no longer constant but a function of time $L_{ext}(t)$. Then the round-trip delay in the external cavity is no longer a constant but a function of time $\tau_{ext}(t)$. Thus, the continuously delayed reflected field causes an interference pattern when it beats with the stationary field inside the laser cavity. The condition for maxima and minima corresponding to the phase change of 2π can be found by equating the argument of Eq. (2.74) to 2π, we get

$$\omega_s \tau_{ext} = 2\pi, \tag{2.75}$$

since the frequency change due to OF is very small $(\omega_s - \omega_0)/\omega_0 << 1$, we can assume for simplicity that $\omega_s \sim \omega_0$. Then the above equation becomes,

$$L_{ext} = \frac{\lambda_0}{2}. \tag{2.76}$$

It is evident from Eq. (2.76), that for every displacement of the target equal to half the emission wavelength, the phase of the OF signal will change by 2π, which will be seen as a fringe in the OFS. Thus, by counting the fringes, the target displacement can be easily retrieved. This methodology of FC to measure the target displacement was first proposed by Donati [97].

The experimental set-up to measure the displacement is normally similar to the one presented in Fig. 2.19. As an example of typical performance, one simple experimental measurement to show the method is presented. A Hitachi HL6501 0.65 μm band Aluminium Gallium Arsenide Phosphite (AlGaAsP) LD with a MWQ structure is used, although several other laser families and geometries could equally serve for our purpose. For this laser, the emission wavelength (λ_0) was 692 nm. The light emitted from the LD was then focused on the target using a Thorlabs 352240 lens with focal length of 8 mm and numerical aperture of 0.5. A piezoelectric linear stage (PI-LISA P-753.3CD) was used as target [4]. The conversion ratio from voltage to displacement for this transducer is 3.8 μm/V. A triangular-shaped voltage of amplitude 1V pp is applied to the piezo resulting in a displacement of 3.8 μm pp (Fig. 2.20 (b), solid line). The OFS resulting from the target motion is shown in Fig. 2.20 (a). From Eq. (2.76), each fringe corresponds to $\lambda_0/2$ of target displacement, so a total of ten fringes in one ramp gives the amplitude of target vibration is $10 \times \lambda_0/2$, which results in 3.8 μm pp as expected, and a complete displacement reconstruction presented in Fig. 2.20 (b), dashed line.

This is thus a very a direct method to measure the target displacement, or any equivalent change in OPD between the laser and the external target. The method is, however, limited by the resolution and accuracy of $\lambda/2$. Very important research efforts have been devoted to improve this limited resolution, which are briefly overviewed along section 2.5.1 and 2.5.2. This

thesis is, partially, devoted to present a method to increase the resolution of the OFI sensor beyond this limit of half the emission wavelength.
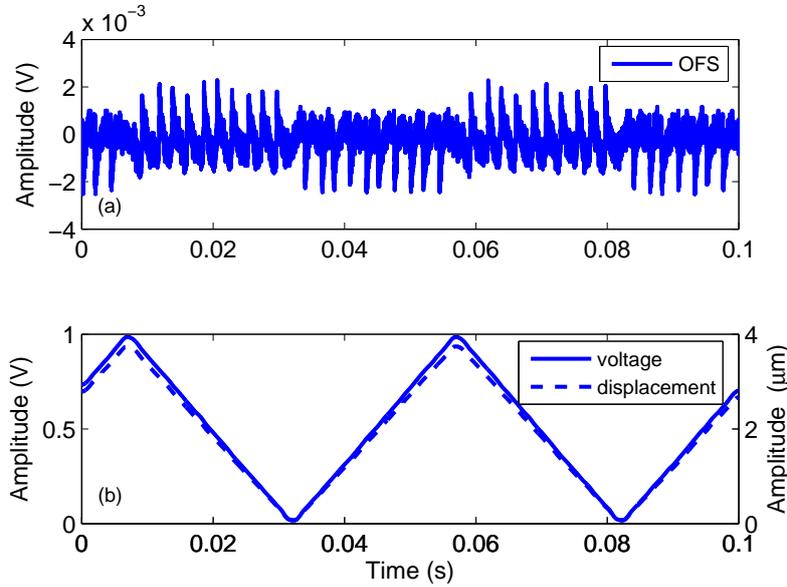
Figure 2.20: Displacement measured using a general OFI sensor; (a) Experimental results for displacement in the example described in the text. (b) Displacement of the piezo (dash) resulting from applied voltage [4].

2.4.2 VELOCITY

Several sensors based on a myriad of measurement principles are used today in industry. Inductive, magnetic, capacitive, or photoelectric sensors are good examples of this [116]. Accelerometers are a type of sensors widely used to measure the vibration of an object in terms of its acceleration, which later can be converted into velocity or displacement by integration when required. However, accelerometers are contact based sensors, which distort the measurements of acceleration due to its presence, an effect which is critical in several applications. Non-contact sensors are required to overcome this problem, and obviously laser Doppler velocimetrys (LD-Vs) are one of the best suited candidates for it. In addition to being non-contact, LDV can be directed at objects under test which are difficult to access, or which are either too small or too hot to attach a physical sensor. LDVs, then, do not cause mass loading of objects under test, which is especially important for micro electro mechanical systems (MEMS) devices. LDV are basically interferometers which measure the Doppler shift of light when reflected back from vibrating objects [117]. A variety of LDV systems have been developed to measure vibration parameters, typically displacement, velocity or acceleration under single point, scanning, 3-D, rotational, multi beam, differential, and continuous scan LDVs arrangements. OF based interferometry adds on to this list, as OFI based LDVs has been demonstrated by a number of scholars and researchers [96, 118–124].

43

The same set up we built in the former paragraph to demonstrate displacement measurement (Fig. 2.19) is used for OF based laser velocimetry as well. The basic principle of measuring the target velocity is based on the principle of Doppler shift in the emission frequency resulting from a moving target. The optical field emitted by the laser, when reflecting onto the non-stationary target is subject to a Doppler shift proportional to the velocity of target. This reflected and Doppler-shifted field interferes with the "stationary" field inside the laser cavity, resulting in an OFS whose frequency is shifted by the Doppler frequency. The resulting OFS is detected by the PD embedded at the rear of laser, as in the case of displacement measurement or the junction voltage changes, which when processed in the frequency domain outlines clearly the Doppler frequency, proportional to the velocity of the target through

$$f_D = \frac{2v_t}{\lambda_0} cos(\theta). \tag{2.77}$$

where f_D, v_t, λ_0, and θ are the Doppler frequency, the velocity of the target, the emission wavelength and is the angle between the laser beam and the target motion (in this case it is set to $\pi/2$) respectively. Using the OFS presented in Fig. 2.20 (a), the velocity of target vibration is directly found by performing its Fourier transform and results are presented in Fig. 2.21). The sharp peak at the Doppler frequency, $f_D = 440$ Hz is clearly observable (stressed using the
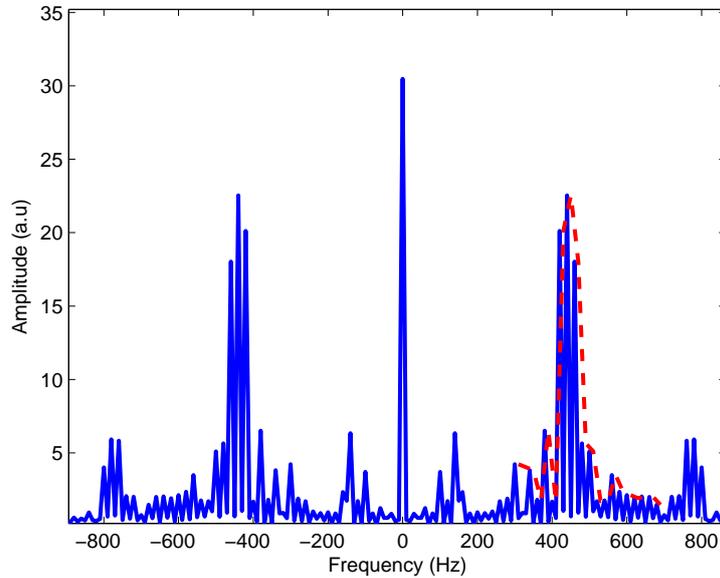
Figure 2.21: Experimental results of OF based velocimetry. A sharp peak in the spectrum of OFS correspond to the Doppler shift due to relative velocity between the laser and the target. The dashed line demonstrates the experimental width of the spectrum.

dashed line in 2.21). Using Eq. (2.77), the velocity of target motion is found to be 152 μm/s. This is in exact match with the one recovered from the measured displacement in Fig. 2.20 (b) (since the target moves 3.8 μm in 0.025 s, the velocity is 152 μm/s).

2.4.3 ABSOLUTE DISTANCE

The basic principle behind distance or range calculation is to project some type of electromagnetic field (either optical, radio or ultrasonic waves) on a distant target and then process the field back-reflected from the target in order to estimate the range to the target. Among the other types of electromagnetic field used in the measurement of absolute distance, th optical field presents added advantages in terms of its resolution (because of its shorter wavelength), and its relatively longer range (because of long coherence length, and the ability to focus sharply using lenses) [125]. Absolute distance measurements based on optical methods can be categorized essentially in in three main types: time-of-flight, triangulation and interferometry [5].

Fig. 2.22 (a) shows the block diagram of a time-of-flight set-up. This method os based on detection of time delay between the emitted pulse and reflected pulse from the distant target. The distance is then calculated by $R = c\Delta\tau/2$, where R is the distance to the target, or range; $\Delta\tau$ is the time interval between the transmitted and reflected pulses; and c is the and velocity of light in medium (normally air, but also water and other media, depending upon the application).

The optical power in the reflected signal in the case of the time-of-flight technique decreases rapidly, specially under highly scattering media. In order to increase the dynamic range and resolution, other approaches such as FMCW radar are used. The basic principle of FMCW radar is shown in Fig. 2.22 (b). The method is based on the FM of the radar signal introduced by the modulation of injection current (Fig. 2.9).

Referring to Fig. 2.22(b), frequency sweeping of the emitted optical field is accomplished by modulating the injection current of a tunable laser, which results in a frequency modulated continuous signal. The reflected optical field from the reference mirror and the object (the distance between the beam splitter and mirror being a known quantity) causes beats in the external photodiode at an intermediate frequency (f_{if}) which is related to the distance of object compared to the known reference mirror (R) as

$$f_{if} = \frac{\Delta f_r \tau}{T_m} = \frac{2\Delta f_r R}{cT_m},$$
(2.78)

where Δf_r is the change in the frequency and T_m is the modulation period. These interferometric signal, typically set in a Michelson configuration, carries information on the difference in length of the reference and measuring arms of the interferometer. This method can have a high accuracy, but at the expense of a quite complex experimental set-up [5].

Based on the principle of FMCW radar, and taking advantage of OF, the set-up for an OF based range finder is shown in Fig. 2.23. The setup is obviously much more compact, without need of any isolator, beam-splitter, or the rest of optical elements required for FMCW radar (Fig. 2.22 (b)). The working principle of a OF based range finder is based on the modulation of the frequency of the emitted optical field by a sawtooth (or triangular) waveform, which results in a frequency modulated signal, equivalent to that in the FMCW radar. This FMCW signal is incident upon the distant target. The reflected and delayed FMCW signal is then fed back
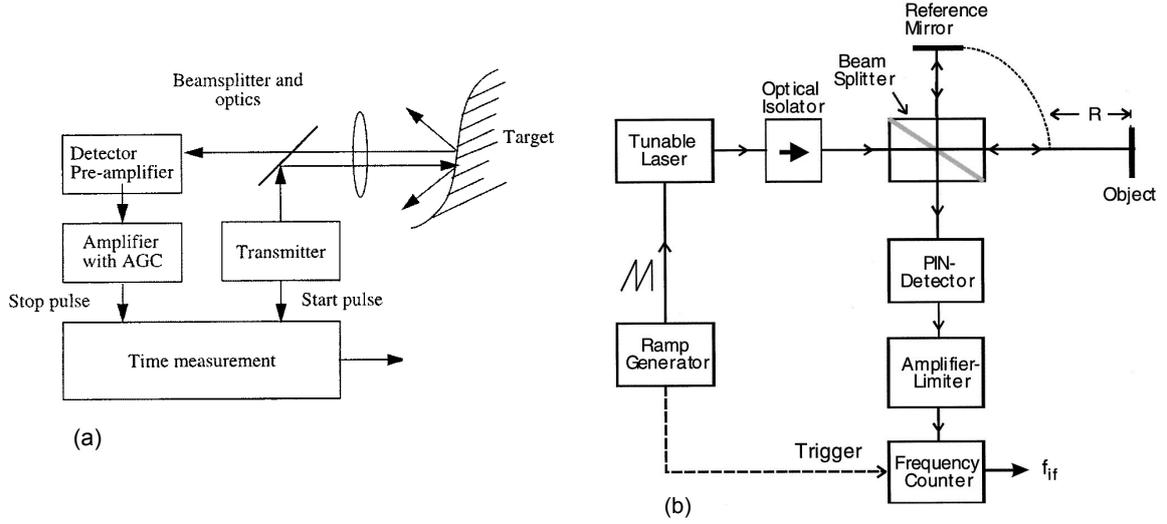
Figure 2.22: Block diagram of optical method to measure the distance of target. (a) time-of-flight (b) FMCW radar [5].
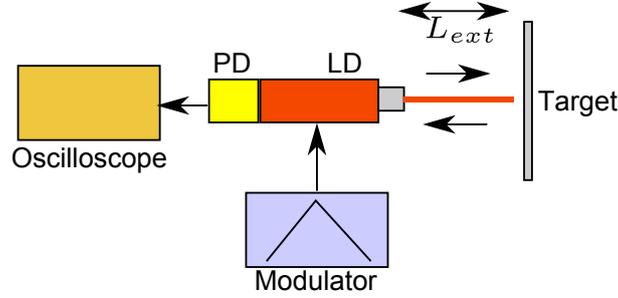
Figure 2.23: Block diagram of OF based range finder.

to the laser cavity where it beats together with the optical field in the cavity. This, of course, differs with the FMCW radar principle, where the reference and object beam are separate and interfere on an external photodiode. Such beat in the cavity causes an interference pattern and a number of fringes appear, which are detected by the either internal monitor photodiode of the laser package or the variations in the junction voltage. Let us suppose that N_f fringes are produced in the interference pattern we just described. Referring to Sec. 2.3.2 (Eq. (2.74)), the change in phase of the OFS due to the change in wavelength described by injection modulation is [6, 120, 126]

$$\frac{\mathrm{d}N_f\phi_s}{\mathrm{d}\lambda} = \frac{\mathrm{d}}{\mathrm{d}\lambda}\left(\frac{4\pi N_f}{\lambda_0}L_{ext}\right) = \frac{-4\pi}{\lambda^2}L_{ext}. \tag{2.79}$$

Since the phase difference between consecutive fringes is 2π, it can be equated to 2π in Eq. (2.79). The distance to the external target L_{ext} is

$$L_{ext} = \frac{\lambda_0^2}{2d\lambda}N_f = \frac{\lambda_0^2}{2\Omega_\lambda A_m(pp)}N_f, \tag{2.80}$$

where λ_0 is the emission wavelength, $d\lambda$ is the change in wavelength emission, Ω_λ is the wavelength modulation coefficient of the laser, and $A_m(pp)$ is the amplitude of the modulation

46

current. The resolution (r) of this measurement method is thus

$$r = \frac{\lambda_0^2}{2d\lambda}.$$ (2.81)

Similarly, in terms of the frequency sweep Δf_r, and the frequency modulation coefficient Ω_f, L_{ext} is given by

$$L_{ext} = \frac{c}{2\Delta f} N_f = \frac{c}{2\Omega_f A_m(pp)} N_f.$$ (2.82)

Beheim and Frietch in 1986 laid the theoretical and experimental results which demonstrated the use of OF combined with FM to measure the distance [6]. Groot et al. implemented the sensor experimentally and measured the range of a distant target at distances from 0.25m to 2.35m with an accuracy of 2 cm [120]. Norgia et al. in 2007 improved the resolution to 0.3 mm by working under a closed feedback loop [110].

As in previous sections, an experiment based on the set-up in Fig. 2.23 with parameters $\lambda_0 = 826.2$ nm, $L_{ext} = 7$ cm, $\Omega_\lambda = 0.005$ nm/mA, $A_m = 13.36$ mA is performed as an example. Results are presented in Fig. 2.24 (a). The number of fringes in each ramp $N_f = 13$ is clearly visible. Using Eq. (2.81), the resolution of this sensor is calculated to be 5 mm, and using Eq. (2.80), the calculated distance is 6.64 cm (compared to an actual value of 7 cm), giving an error of 3.6 mm. For comparison purpose only, the equivalent waveform obtained in the original paper is presented in Fig. 2.24 (b) [6].

(a) (b)
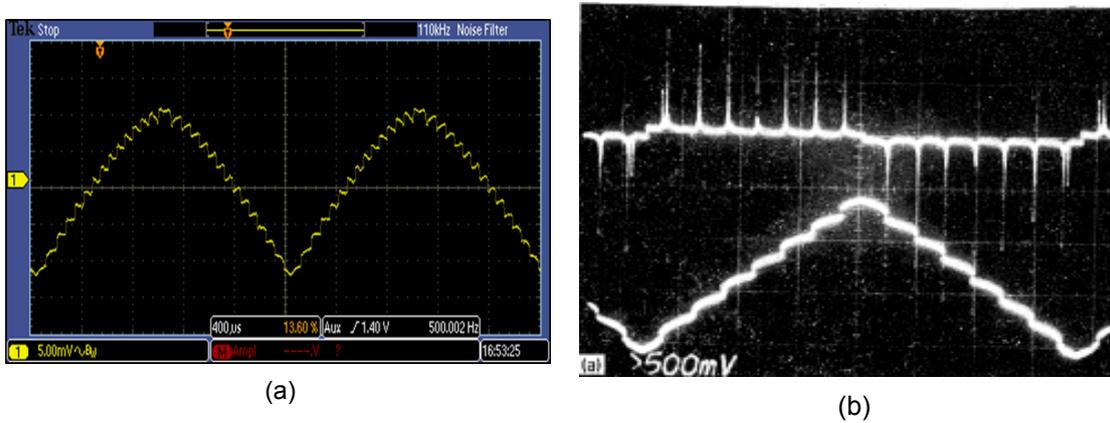
Figure 2.24: Experimental results for OF-based absolute distance measurement: (a) Experimental results described in the text; (b) Original experiment at [6] .

2.4.4 IMAGING OF ACOUSTIC FIELDS

The need for sensitive methods of detection and visualization of acoustic surface perturbations has grown with the increasing interest of fields such as acoustic holography [127, 128], ultrasonics or acoustic surface wave devices [129], acoustic trapped energy resonators [127], or laser ultrasonics [130]. In acoustic holography, the bulk wave emanating from the transducer incides

upon the surface of the target. Such incident acoustic pressure wave causes instantaneous surface displacement, transferring the acoustic pattern to the interrogating optical beam, which when processed reveals the acoustic hologram. For ultrasonic or acoustic surface devices, the vinration of the membrane reveals important information, as power flow or attenuation, which is important to design and manufacture transducers and detectors. In trapped energy resonators, the surface perturbations reflect the pattern of acoustical localization, which is essential to them. In special advanced methods for dynamics testing, e.g. dynamic displacement and/or vibration of membranes of MEMS devices , ultrasound or acoustic transducers are necessary to develop reliable, marketable products. The purpose of testing is to provide a feedback to design and manufacture process. In order to fully understand the behaviour of many devices e.g. micromachined mechanical devices, such as those used to generate and detect acoustic or ultrasound is thus necessary to be able to measure their dynamic displacement behaviour [131, 132]. Further, laser-induced ultrasound (laser ultrasonics) is currently an state-of-the art method for non-destructive testing of weldings and materials, where the detection of surface acoustic waves induced by a ns laser pulse is used to investigate inner structural defects [130].

Optical methods permit to study the acoustic waves at any point in or on the specimen in al the cases cited, without either absorbing or interfering with the acoustic waves in any way.The use of lasers or optical methods to detect acoustic waves is an emerging area of research. There are various techniques used to detect the effect of the acoustic perturbations on the light beam and to relate the results to the acoustic field parameters. One of the optical methodologies to detect the membrane vibration is the use of coherent laser sources as a probe to measure the amplitude or phase of the displacements induced by the acoustic wave. If the cross section of the sampling beam, or the spot size of the probing beam is small compared to the wavelength of the acoustic field as it appears on the sampled surface, the acoustically induced temporal and spatial variations are coupled to the phase of the reflected beam, and the information related to the amplitude variations normal to the surface can be deduced by simple phase demodulation techniques or phase to intensity modulation interferometric techniques. Several optical methods have been used to characterize the acoustically perturbed surfaces. Optical interferometry has been used for the accurate detection of displacements in microscale devices, in particular, interdigital phase sensitive diffraction gratings enabled the implementation of interferometric detection in atomic force microscopy units and in very sensitive accelerometers [133]. The displacement of the membrane of the micromachined capacitive acoustic transducers has been performed with interferometric detection techniques [134]. Authors in [135] used the optical heterodyne technique to measure and characterize surface acoustic wave (SAW) devices. The classical knife-edge technique has been also used to measure the tilt of the surface [129]. An amplitude grating technique for detecting the phase and the amplitude of a particular spatial frequency component in the perturbation [136]. Optical superheterodyning techniques have also been used to measure the displacement directly [137–139]. A review of the available optical

48
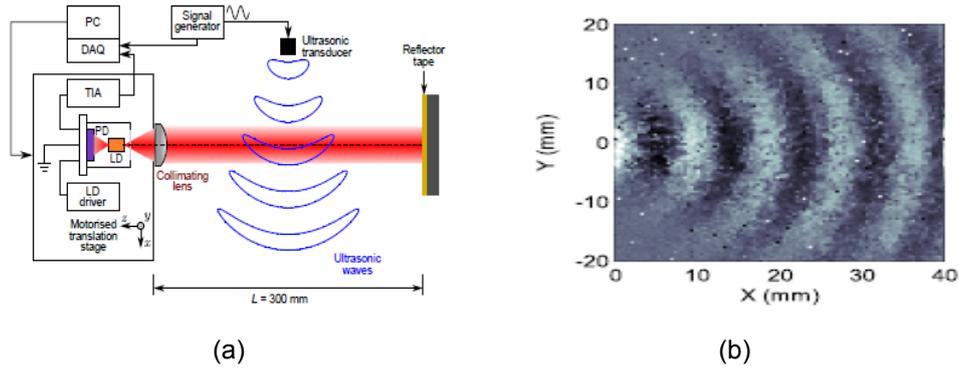
Figure 2.25: Imaging an acoustic field using OF. (a) Schematic diagram; (b) Experimental image of the detected acoustic field [7].

methods to extract acoustic related parameters is provided in [139]. However, despite the many techniques available to probe the acoustic parameters optically, most of them are complex, bulky, use several electrical and optical components, which present issues related to the alignment, robustness and performance of setups. For instance, the problem with the optical heterodyne technique is the complexity, extensive use of optical and electrical devices and components in the experimental set-up followed by a signal processing step. The experimental set up consists of a frequency shifter (an acoustic-optic modulator) and a lock-in amplifier to lock the output signal at a particular frequency and so increase signal to noise ratio (SNR).

Quite recently, Bertling et al. [7] used OF to measure the variation in the local pressure associated to the acoustic wave, permitting its reconstruction as a 2D image without the requirements of the complex setups typical of the methods mentioned above. They used the principle of optical path change (in particular, the change in refractive index) due to compression and rarefaction of a media when a sound or acoustic wave propagates through it. Fig. 2.25 (a) shows the schematics of an experimental set-up for imaging an acoustic wave. The ultrasonic transmitter was placed midway ($z = 150$ mm) between the laser ($z = 0$ mm) and the retro-reflective screen ($z = 300$ mm), at a height of 110 mm above the surface of the optical table, in order to produce a sound wave propagating in free-space which travels perpendicular to the axis of propagation of the optical beam. The acoustic wave propagating through the medium between the laser and the reflective surface changes the effective refractive index of the medium, and also the phase of the OFS, and ultimately its amplitude. The field distribution resulting from a 101×101 pixel scan area in a 40 mm$\times$40 mm area is show in Fig. 2.25 (b).

2.4.5 BIOMEDICAL APPLICATIONS

Owing to its simple, self-aligned, and compact structure, OF has been widely used in the biomedical field to measure the blood flow noninvasively since some years ago [8, 61, 101, 102, 140, 141]. The flow measurements are based on the same principle of velocity measurement already discussed (Sec. 4.26). Fig. 2.26 (a) shows the principle of blood flow measurement
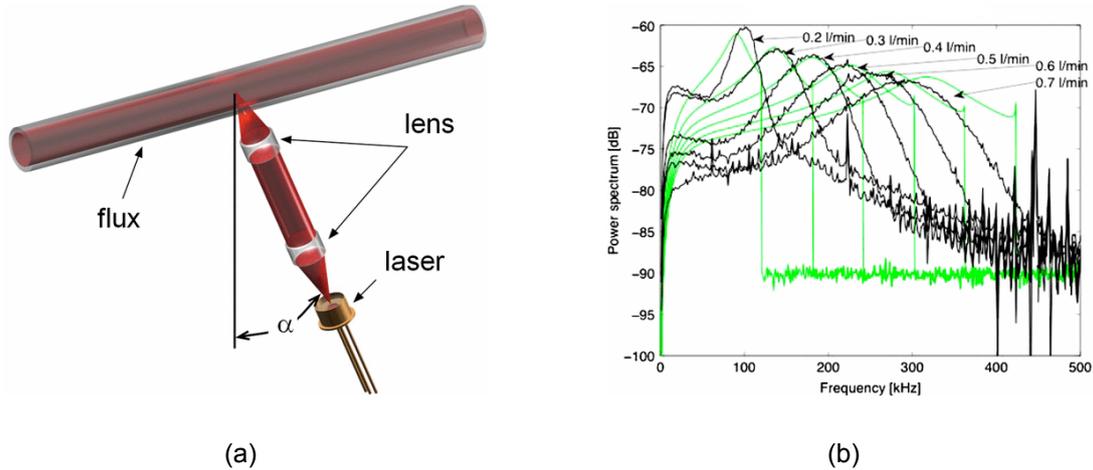
Figure 2.26: Principle of blood flow measurement using OFI. (a) Schematicsof the setup; (b) Experimental results: with the increase in blood flow, the Doppler frequency increases corresponding to larger velocity. [8].

and 2.26 (b) the Doppler shift in OFS due to blood flow, where information about the blood flow velocity may be retrieved [8]. Using a single-channel OF laser vibrometer, Hast et al. [141] measured the Doppler signal of the cardiovascular pulse in radial arteries of the forearm. Norgia et al. used a single channel OF based sensor to measure the transfer impedance of the respiratory system by a forced oscillation technique [142]. The transfer impedance is important in the sense that it provides information on tissues and airways, and is useful for assessing the mechanical properties of lungs and a number of associated disorders. Dean [143] has proposed OFI detection of T-waves. The application is about sensing with a QCL (in Tera Hertz (THz) regime), with the prospect of using them as an optical radar on living tissue, targeting the detection of skin cancer. Alternatively, Kayaozdemir et al. used the speckle phenomenon in an OF to measure the blood flow non-invasively [144]. Norgia et. al used OF to measure blood flow in an extracorporeal circulator [145]. Milesi et al. used OF to measure the displacement of chest walls for the monitoring of respiration, with a resolution as small as 400 nm, and validated the results both in vitro and in vivo on seven healthy volunteers [146]. A thorough review of a number of current research activities around OFI in biosensing is found in [76].

OF has also been used in conjugation with several other techniques in the field of microscopy, in a very promising combined approach. Blaize et al. proposed OF based laser imaging for scattering type scanning near-field optical microscopy (SNOM). They implemented an ultra sensitive imaging method by combining a SNOM with optical heterodyne interferometry and the dynamic properties of the laser under feedback [147]. Authors in [148], taking advantage of the high sensitivity of the frequency-shifted feedback laser and the axial positioning ability of confocal microscopy developed cross-sectional imaging in highly scattered media with an axial resolution better than 2 nm.

2.4.6 LASER CHARACTERIZATION

Amongst the diverse applications of OF, it is also quite relevant and frequent its use to measure and characterize different parameters of the laser itself. Several authors have demonstrated measurements of the LEF α using OFI [104–106,149–153]. In a recent approach, Fan et al. [154] proposed a simple solution independent of C to measure α, using two independent OFS. In that approach, it was shown that the phase of the OFS under feedback and that of the free-running laser intersect when the condition $\phi_s = p\pi - tan^{-1}\alpha$ is met. By further investigating the relationship between light phase and emitted power, α could be measured from the combination of the power values of two OFS, acquired under two different optical feedback strengths. The intersection point of the two OFS was computed by checking the zero crossing point and then Eq. (2.83) was used to compute α from OFS P_s as

$$\alpha = \sqrt{\frac{1}{P_f^2} - 1}. \tag{2.83}$$

So at each zero crossing of OFS, α was measured. In case of multiple zero crossings, the arithmetic mean gave the value of α of the laser under test.

2.5 IMPROVING THE PERFORMANCE OF OFI

The extraction of the measured physical parameters with the utmost accuracy and resolution is a desirable property of all instrumentation and sensors; so it is for OF-based sensors. Generally speaking, two approaches are taken to increase resolution and accuracy of the measured parameters: (a) using external hardware and devices to improve the setup and (b) signal processing. Both are briefly overviewed in the coming paragraphs. The former causes set-ups to be more bulky, expensive and difficult to operate and align, while the latter attains improved results keeping the setup simple and compact, normally at the price of increased processing time. Since a relevant part of this thesis is devoted to OFI sensors of improved resolution, and to enhanced signal processing procedures of the OFS, a brief overview of the state of the art regarding experimental setup with extended properties, and of signal processing techniques applied to OFS is presented. The main trends within signal processing in OFS involve managing noise in the signal, dealing with speckle effects, and increasing the resolution and/or the accuracy of the measurements, hence extending the range of applications of OFI-based sensors.

2.5.1 EXTENDED EXPERIMENTAL SETUP

Addy et al. [60] in 1996 reported that the frequency of the fringes of an OFS can be doubled because of the misalignment of the external reflector to attain a resolution to $\lambda/4$. However, the doubled fringe was observed to be independent of the external cavity length on a scale of approximately 1 mm only, so it could not be used for a displacement measurement beyond that.

Servagent at al. in 2000 used an electro optic modualtor (EOM) to introduce an additional phase change in OFS to that produced by the target vibration. The comparison between the OFS before and after the phase shift allowed to measure the displacement with resolution of $\lambda/4$ and with an error of 65 nm. In addition, using five sets of phase-shifted OFS, and comparing among them, the error was reduced to $\lambda/20 \approx 40$ nm [155]. Liu et al. [156] in 2003 also demonstrated doubling the fringe frequency by putting a quartz crystal plate in the external cavity at a specific angle between the crystalline axis and the laser beam, getting displacement measurements with a resolution of $\lambda/4$. Mao et al. in 2006 [58] doubled the fringe frequency using a folded feedback cavity formed by a hollow cube corner prism (HCCP), decreasing resolution to $\lambda/4$. Tan at el. in 2007 [59] used single-mode Nd-YAG laser with a birefringent waveplate in the external cavity. Because of the birefringent effect, two kinds of light could be fed back into the laser cavity by an external feedback mirror and modulate the laser intensities in two orthogonal directions resulting in a resolution of $\lambda/8$ in the measurement of target displacement. Further, using orthogonally polarized dual frequency Helium-Neon (He-Ne) lasers, a resolution of $\lambda/16$ in target displacement was attained. Fei at el. in 2006 [157] used a He-Ne laser and tilted the target (in this case, a mirror) to reconstruct the displacement with resolutions down to $\lambda/80 \approx 7.91$ nm resolution. They observed that by tilting a highly reflective target, the fringe count could be made 40 times larger than the normally available fringes, so as a result each fringe corresponded to $\lambda/80$. The drawback of this last method was the fact that the number of fringes was dependent upon the separation of the laser and the target, so when keeping the tilt angle of the target fixed, an increase in the separation of the laser and the target meant that the fringe count decreased.

So far, the techniques mentioned above increase the resolution of displacement calculation provided that the amplitude of the target displacement is greater than half the wavelength of emission. A different approach based on the active heterodyne technique [11] was proposed to measure displacements of the target smaller than half the emission wavelength [158]. In that technique, the authors used a pair of laser diodes, each with its own external cavity. The first was used as a reference having a fixed cavity length, whereas the external cavity of the second LD (the one used for measurement) was perturbed resulting in a shift in frequency due to OF (Eq. (2.66)). This shift is then determined experimentally using an heterodyne approach. With this approach the authors were able to measure a displacement of 160-170 nm ($\approx \lambda/5$), with an error of just ± 5 nm [158]. However, the main disadvantage of this technique was that it used two lasers, and its accuracy was dependent upon the precise measurement of the spectral emission frequency and the frequency shift. Since the shift in emission frequency in the laser due to nanometric displacements is very small ($\approx$ MHz as compared to the conventional THz range in emission frequency), it implied the need of a very high resolution spectrum analyzer. In

---

[11]The process of detuning the emission frequency of the laser due to the displacement of the remote target, to then determine the shift using an heterodyne technique [158]

addition to that, this method could only translate the beat frequency to give the peak amplitude of the displacement, not to measure the entire waveform. Finally, using a double laser setup, Azcona et al. in 2013 [63] retrieved the entire displacement waveform of a target wich vibrated with amplitude smaller than half the emission wavelength, at nanometric resolution. This methodology, which set the basis for the works in this PhD, had a number of inconveniences which is enhanced in this work. A first discussion on this method was introduced in Chapter 1, and will be detailed in depth in Chapter 6.

2.5.2 SIGNAL PROCESSING

The use of mathematics, statistics and algorithms to extract the information desired from the data outcome of a physical system is a common practice to improve the results of experimental measurements. This not only may remove the need of extensive and expensive components in the setup, but also help the global system to perform better. This general principle also applies to OF based sensors. On one side, OFI sensors consist of a single laser capable of measuring a variety of physical phenomena; on the other side, signal processing of the OFS helps to make it applicable in a number of wide and diverse fields effectively and efficiently, while maintaining its simplicity and compactness. Thus, a great deal of research effort has been devoted to signal processing of the OFS.

2.5.2 NOISE IN OFI

Among the different types of noise (shot noise, thermal noise, AWGN, impulsive noise, or amplification noise to name a few), three major types are dominant in the OFS: shot noise [159, 160], AWGN and impulsive noise [9, 161].

Shot noise is an inherent property of optoelectronic devices that results from the quantum nature of photons arriving to the photodiode. It is directly related to the amount of light incident upon the detector. The mean squared shot noise current from a photodiode is given by [162]

$$< i_n^2 > = 2qI_{dc}B_L, \tag{2.84}$$

where i_n is the shot noise current and B_L is the electrical bandwidth under consideration (which typically refers to the bandwidth of the photodiode or the amplifier that follows it). In the particular case of an OF based sensor, the power of the shot noise in the weak feedback regime has been described in [93] as

$$P_{sn} = 2\eta_{cpd}\eta_{qpd}\frac{q}{hf_s}m < P_f > B_L = 2\eta_{pd}\frac{q}{hf_s}mP_0B_L, \tag{2.85}$$

where η_{cpd}, η_{qpd} and η_{pd} are the coupling, quantum, and the overall efficiency of the photodiode, respectively; f_s is the frequency emission of laser under OF; and $\eta_{pd} = \eta_{cpd}\eta_{qpd}$, and $i_{dc} =$

$\eta_{pd}mP_0q/(hf_s)$. Further, the peak current ($i_s(t)$) and power ($P_s(t)$) obtained from the PD embedded in the rear of LD under OF in the weak feedback regime is given by Eqs. (2.86) and (2.87) respectively [93]

$$i_s = \eta_{pd}\frac{q}{hf_0}mP_0, \tag{2.86}$$

$$P_s = i_f^2 = [\eta_{pd}\frac{q}{hf_0}mP_0]^2, \tag{2.87}$$

where the modulation index m is

$$m = 2\kappa\tau_p/\tau_l. \tag{2.88}$$

The SNR in the case of an OF based sensor (SNR_f) with noise dominated by the shot noise is obtained by dividing Eq. (2.87) by Eq. (2.85) so

$$SNR_f = \frac{1}{2}\eta_{pd}\frac{q}{hf_sB_L}P_0m^2. \tag{2.89}$$

Placing the value of κ from Eq. (2.60) in Eq. (2.88), the signal to noise ratio under feedback of Eq. (2.89)) may be obtained in terms of the reflection coefficient of the target, and then given by

$$SNR_f = 2\eta_{pd}\frac{q}{hf_sB_L}P_0\frac{(1-r_2^2)r_{ext}^2}{r_2^2}\frac{\tau_p^2}{\tau_l^2}. \tag{2.90}$$

Eq. (2.89) shows that keeping the emission power constant, the SNR improves with an increase in the modulation index. Thus, a large modulation index is desirable for OF-based sensors. This is also intuitive because the modulation index is related to fringe visibility, so the higher the modulation index, the larger the contrast of the interference fringes, so they can be easily detected. Fig. 2.27 demonstrates the effect of the reflection coefficient of the external target on the shot noise (SNR due to shot noise) on an OF based system. It is seen that increasing r_{ext} the SNR and m both increase. However, m increases continuously with r_{ext}, but the SNR attains saturation ($SNR_f \sim -88$ dB) as $m \to 1$. This gives the minimum value of SNR that must be maintained so the OFS can be separated from noise. To put it in another way, the signal to noise ratio of the OFS must always be greater than -88 dB in order to be separated from noise, and any signal below this value remains undetectable.

Let us now take a look onto the other noise classes dominant in OFI. AWGN results from two or many stochastic processes which occur in nature, and is additive to any other noise present in the system. AWGN is known to spreas across the frequency spectrum according to a Gaussian function. Impulsive noise, on the contrary, appears as sharp random fluctuations consisting of random occurrences of energy spikes of random amplitude, with an spectral content caused by a variety of sources, such as electromagnetic interference, ill synchronization between data acquisition devices, or even typing on the keyboard of a compute [163]. Because of its impulse nature, impulsive noise has a wide spectrum very much dependent upon its duration and cause.
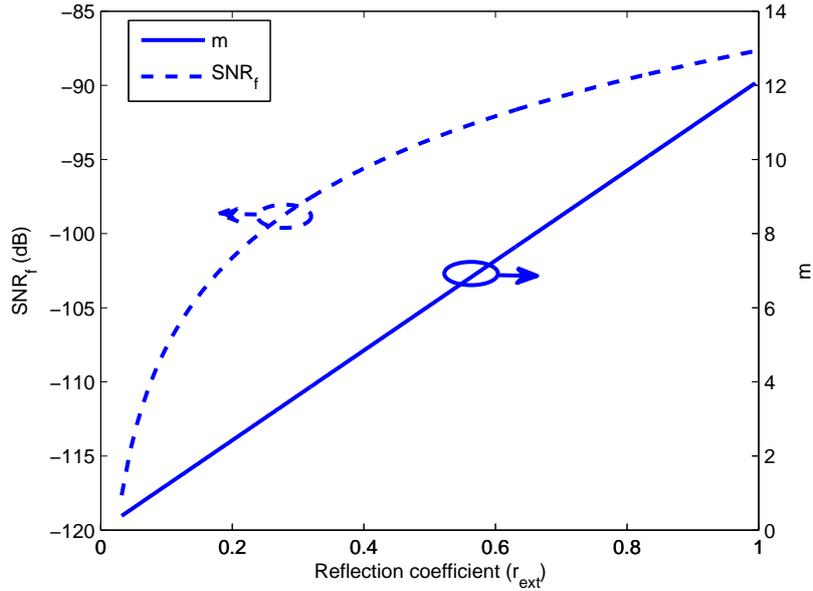
Figure 2.27: Effect of refectivity of external target on shot noise the signal to noise ratio induce dby show noise and the modulation index. The parameters used in the simulation are $\eta_{pd} = 0.35$, $\lambda = 830$ nm, $B_L = 10$ MHz, $\tau_p = 2$ ps, $r_2 = \sqrt{0.5}$; $P_0 = 1$ mW, $L_{ext} = 10$ cm, $l = 10$ μm, $\tilde{n}_l = 3.5$.

In general, the bandwidth of impulsive noise in the frequency domain is inverse to its duration in the time domain. Fig. 2.28 shows the AWGN and the impulsive noise in an experimental OFS compared to that presented in [9].

Several signal pre-processing solutions have been proposed in order to efficiently remove these different sources of noise and so improve the SNR of the OFS. The most common has been the use of a low-pass filter to remove AWGN. Zabit et al. in [164] proposed a moving-average filter to remove the AWGN. A Kaiser-based FIR filter combined with a median filter was implemented by Yu at el. [165]. Wei proposed the use of neural network interpolation [161], and Sun, a filter based on the wavelet transform combined with a median filter [9].

2.5.2 SPECKLE IN OFI

Speckle is an intensity pattern produced by interference of multiple coherent waveforms after scattering at a rough object. It is a result of the interference of multiple waves with the same frequency but different amplitude and phase, which add up to produce an intensity of random amplitude depending upon the distribution of the interfering waves, which is generally unknown and only can be managed statistically. When a surface is illuminated by a coherent beam of light, such that of a laser, from the theory of diffraction each point on the surface acts as a secondary source of emission. In this case, if the separation between two points on the target is greater than half the emission wavelength, then numerous reflected fields from distinct points on the target reach each detector with different amplitude and phase, equivalent to different
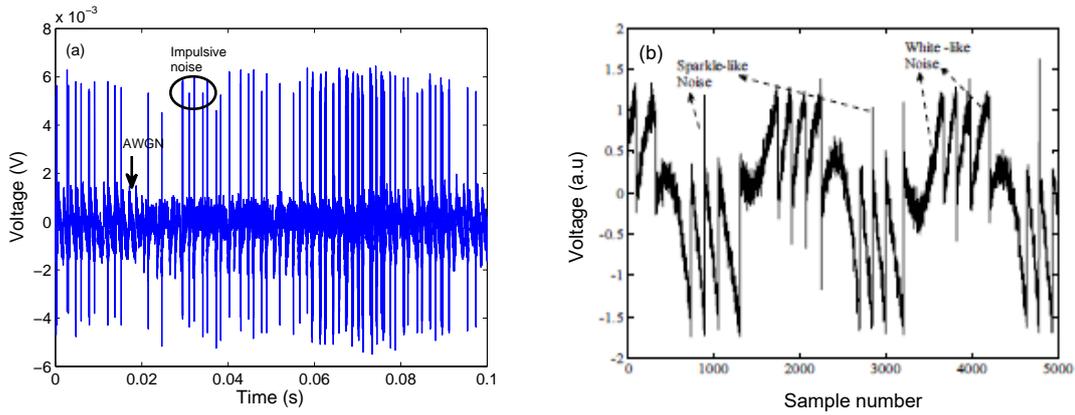
Figure 2.28: AWGN and impulsive noise in an OFS. (a) Experimental data acquisition; (b) Compared with that in [9].

delays in the time domain. Such coherent reflected fields randomly interfere among themselves and cause random fluctuations in the observed intensity. Figure 2.29 shows the irregularities in the surface of a piezoelectric target compared with the laser spot size incident upon it. Fig. 2.30 (a) shows the resulting experimental OFS. The sharp fluctuation in intensity captured by the photodiode results in random sharp fluctuations of the amplitude envelope of the OF signal, which are clearly visible. Similar results were observed by [10, 166]. Since OF based sensors are phase sensitive (basically phase modulation is turned into intensity modulation), the phase error resulting because of the speckle effect affects the measurement as well. Comprehensive details on how the speckle introduces error in displacement measurement has been explained by Donati in [167], and since then different methodologies based on signal processing [62, 69] and extensive set-up approaches [10] have been proposed.

2.5.2 RESOLUTION AND ACCURACY IN OFI

Displacement measurement is one of the most important applications of OFI-based sensing, and has been briefly described before. In 1995, Donati et al. [50] developed a fringe counting method based on the fact that each fringe on an OFS waveform corresponds to a half-wavelength shift
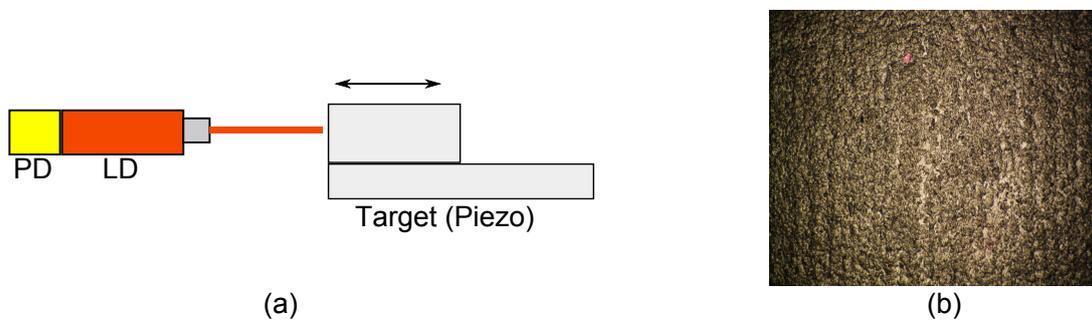
Figure 2.29: Speckle in an OF based sensor. (a) Schematics of the OF based sensor. (b) Surface irregularities in the target (a piezo [4]) seen under a microscope and compared to the laser spot (central above).

56
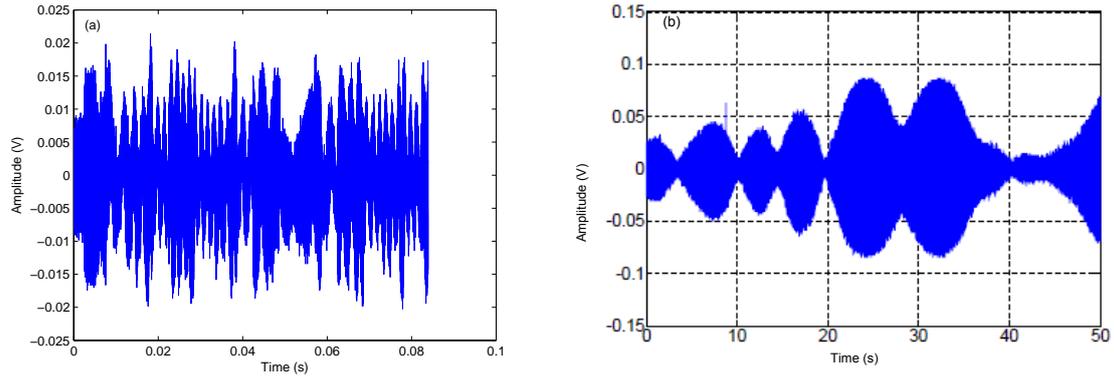
Figure 2.30: Speckle effects in an OFS. (a) Experimental ; (b) Presented in [10].
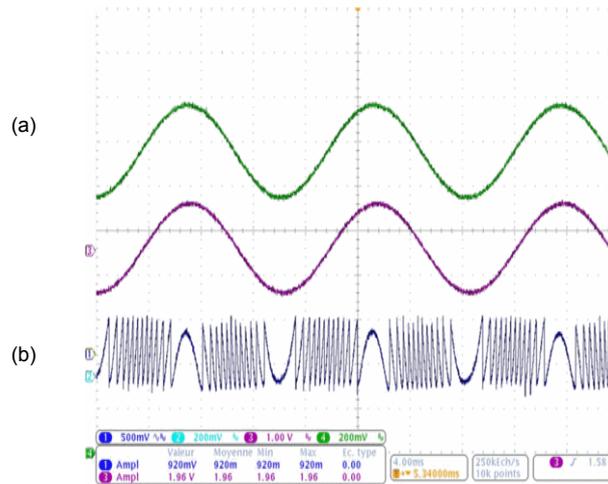
Figure 2.31: FC method to reconstruct displacement with resolution and accuracy of half emission wavelength [11]. (a) OF based and reference displacement (b) Acquired OFS.

of a moving target (also described in Sec. 4.11). Fig. 2.31 demonstrates graphically how the FC method works [11]. It is also a method easy to automate by software. The method is simple and powerful, but only achieves a resolution of half-wavelength for displacement measurements. Since then, a lot of the activity in the field has been oriented to increase the resolution of this measurements, and to decrease its error.

In one of the first attempts to improve the method, Servagent et al. in 1998 linearised the normalized optical power approximating it to an ideal sawtooth signal, demonstrating a resolution of $\lambda/12$ [168]. In order to further increase the resolution Merlo and Donati [169] in 1997 proposed PUM which reduced the error to only $\lambda/67$. This algorithm, however, was limited only to $C < 1$. To extend this, Bes at al. in 2006 [13] extended the phase unwrapping algorithm to values of $C > 1$ as well.

Zabit et. al in 2010 [12] proposed for the first time a fringe loss compensation algorithm which allowed to compensate for fringe losses under moderate feedback conditions, where hysteresis is present, and decreased the error in the reconstruction of displacement to $\lambda/20 = 40$ nm.

57
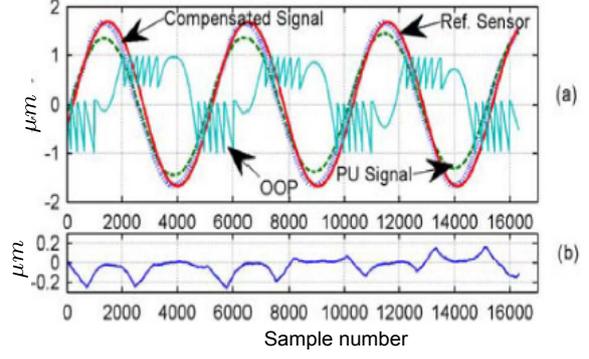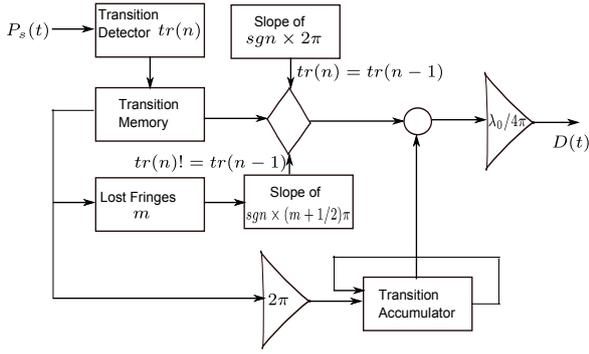
Figure 2.32: Fringe compensation algorithm. (left) Schematics. (a) Experimental displacement retrieval; (b) difference between the compensated signal and the reference signal [12].
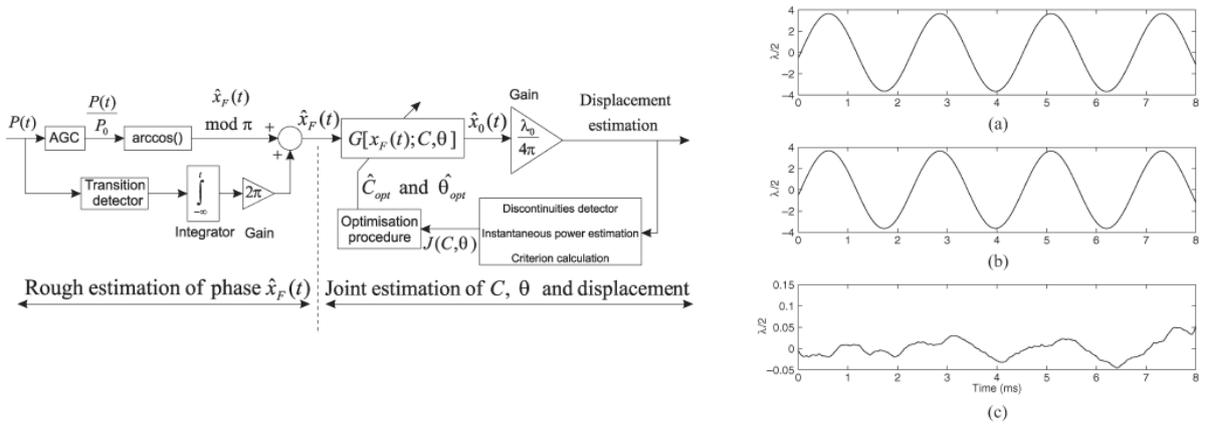
Figure 2.33: Phase unwraping method. (left) Schematics. (a) Experimental displacement retrieval; (b) reference displacement; (c) difference between them (lower) [13].

The schematics of the algorithm is shown in Fig. 2.32 (a). It is based on the principle of comparing the sign of consecutive fringes to determine the moment when the transition takes place. If the fringes have the same sign, this should correspond to a no transition condition, so the slope segment 2π is chosen. Otherwise, if there is a change in the sign, a transition must occur and a slope segment of $\pi/2$ is chosen. This has a twofold effect. First, it provides the compensation of displacement by adding $\pi/2$ at the maximum and at the minimum of the phase reconstructions. Second, for harmonic vibrations, it compensate the fringe-loss effect which appears at the edges of the harmonic displacement, when the target changes its direction of motion. The displacement retrieval based on this signal processing algorithm is superior in terms of peak to peak error to the PUM, and as commented reduces error to 40 nm (2.32 (b)).

Bes et al. in 2006 proposed the PUM, which enabled joint estimation of feedback strength [13] and reconstruction of the displacement, decreasing the error down to $\lambda/20 \approx 40$ nm. The principle of the signal processing method is illustrated in Fig. 2.33 and can be split up into two principal steps. The first step is to make a rough estimation of the phase of the OFS, from the standard phase equation (Eq. (2.68)), and then the phase value obtained is refined

58
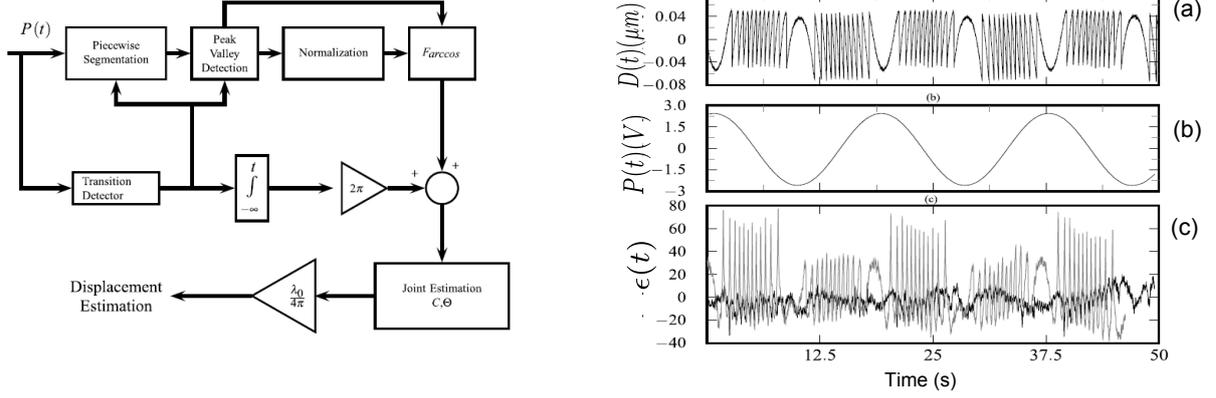
Figure 2.34: Improved phase unwrap method. (left) Schematics. (a) OFS; (b) Experimental displacement retrieval using IPUM; (c) Error using IPUM (black) compared with error in PUM (grey). [14].

based on the joint estimation of the feedback strength and the feedback phase to optimize the reconstructed phase, which contains detailed information about the target displacement. The schematics of the signal processing technique are shown in Fig. 2.33 (left) with results in Fig. 2.33 (a) compared with the reference in 2.33 (b) and the error resulting in 2.33 (c).

In the last approach we are aware of in order to improve resolution and accuracy by signal processing of the OFS, Bernal et al. in 2013 [14] introduced IPUM, which optimized the PUM method we just described to decrease the peak to peak error down to just 37 nm. This improvement was achieved based on modifications of the PUM method, which were essentially (a) taking into account both the peak and the valley of a given fringe before normalizing; (b) inverting the displacement obtained by PUM for correcting the phase; and (c) the joint estimation of feedback strength and feedback phase is now used to improve the calculation of the phase. The detailed schematics of the signal processing scheme are shown in Fig. 2.34 (left) with the results in 2.34 (a), compared to reference in 2.34 (b) and the resulting error in 2.34 (c).

2.6 CONCLUSION

In this Chapter an overview, which combined the main theoretical aspects of the laser together with the state of the art related to OFI measurements was presented. Starting with the very basic principles of the SCL, the Chapter progressed towards the rate equation and the fundamental properties which lay the foundations of this PhD work. Among different relevant properties of SCL studied, much attention was given to the small signal analysis of laser, the relationship of the frequency emission and the length of the cavity, and the modulation bandwidth of laser and, specially, the frequency chirp introduced in the laser due to injection modulation, used extensively in subsequent Chapters. Further, the relation between IM and FM resulting from injection modulation was studied. These properties form the basic theory which builds

the wideband, sub nanometric displacement sensor based on OF which is developed in chapters to follow.

Next, among the different models used to explain OF, the two best known approaches were analyzed in detail. Both the Petermann's compound cavity model, and a model based on the Lang-Kobayashi equations were explained. Among the rich dynamical behaviour observed in the laser under OF, literature review concentrated on the works related to harnessing the OF for developing non-contact and non-destructive photonic sensors. The comparison of OF based sensor with that with other optical / radio frequency (RF) sensors was introduced to reflect the advantages in terms of cost (basically converting a single SCL to source, detector and interfering media all in one) and ease of implementation (without needing of bulky components and necessity to align them). It was also shown that the OFI is used in a wide variety of applications in various field e.g. absolute distance (range), displacement, imaging to name a few. Examples of appplication of the main parameters measured were presented, and a review of the applications more directly related to this PhD was also presented together with a thorough review of the associated literature. In our last section, we discussed the late approaches for improving the performance of OFI sensors, including hardware and signal processing strategies. This sets the framework to present the main contributions of this Thesis in its proper context.

3. Optical Feedback Based on Scattering Theory

3.1 INTRODUCTION

In Chapter 2 (Sec. 2.3.1, Eq. (2.55)), it was mentioned that, in the case of reflection from an external target, the equivalent reflection coefficient of the laser facet is a function of phase delay, or equivalently of the round trip delay. However, the attenuation of the optical field, determined by the attenuation coefficient (α) of the medium forming the external cavity was not taken into account [72]. The attenuation of the optical field in the external cavity, among many others, is an important parameter as it determines the fringe visibility of the OFS and ultimately enables its detection. The dependence of the attenuation coefficient of the material forming the external cavity (or cavities) and the reflection coefficient at the boundaries is important, in particular, in the case of diffusive materials which need to be characterized, or when

In this Chapter, starting with the concept of scattering theory and its tool scattering (S) matrix to represent the laser cavity with gain and loss, and the external cavities with only losses, the associated transmission matrix (T matrix) is also presented in parallel in Sec. 3.2. The difference between S and T matrices is that the former relates the reflected field to the incidence field at any interface; however, the later relates the fields of one side of the interface to the other. Both matrices are equivalently used depending upon the desired analysis of the parameters under study. Next, the S and T matrix formalism just introduced is applied to the laser to obtain its characteristic gain equation (Chapter 2, Eq. (2.14)) in Sec. 3.3. In Sec. 3.4, the concept is extended to OF from single cavity and the standard equation of equivalent reflection coefficient (Chapter 2, Eq. (2.56)) is modified taking into account the attenuation coefficient of the material found within the cavity. The detailed joint effect of the reflection and attenuation coefficients, and their contribution to the resonance under feedback is then studied. Next, utilizing the cascade properties of S and T matrix, the effect of OF from a single external cavity is extended to situations where multiple cavities are involved, by just changing the boundary conditions in a recursive way. The optimal condition for the effective coupling of the reflected optical field from multiple cavities in terms of *individual* cavity parameters such as cavity length, attenuation and reflection coefficients, or losses is studied in Sec. 3.5. Finally, a conclusion in Sec. 3.6 ends the Chapter.
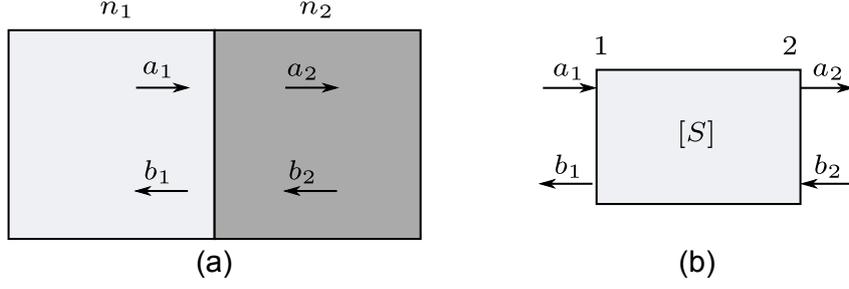
Figure 3.1: Formalization of scattering matrix. (a) Wave propagation through medium of different refractive index. (b) Conversion to two port system.

3.2 BASICS OF SCATTERING THEORY

The scattering matrix (S matrix) relates the amplitude of the reflected and incident waves. The scattering matrix ($\vec{S}$) relates the reflected ($\vec{R}$) and incident ($\vec{I}$) field as $\vec{R} = \vec{S}\vec{I}$. Scattering matrix theory is widely used in describing the travelling wave in electrical networks with multiple impedance mismatch. It has widely been used e.g. in microwave circuits [70]. The same concept may be applied to explaining the optical wave propagation in the laser, and OF as well. It was first used by Wang et al. for analysis of interferometric and ring lasers [170]. Lau et. al used it to describe a three junction triangular ring wave guide laser [171]. [172] analysed scattering loss in DFB lasers due to the presence of the grating. Coldren et al. used S and T matrix both to determine the equivalent reflection and transmission coefficients in groove coupled lasers, and two section coupled resonator systems [173, 174]. In general, for a two port system like the one shown in Fig. 3.1 (a), the reflected and incident field are related the to scattering coefficient as

$$
\begin{bmatrix} b_1 \\ a_2 \end{bmatrix} = \begin{bmatrix} s_{11} & s_{12} \\ s_{21} & s_{22} \end{bmatrix} \begin{bmatrix} a_1 \\ b_2 \end{bmatrix},
\tag{3.1}
$$

where s_{ij} are the scattering coefficients that determine the amplitude of the field at port i due to the incident field at port j, and are the coefficients which constitute matrix $\vec{S}$, so $s_{ij} \in \vec{S}$, $b_1, a_2 \in \vec{R}$ and $a_1, b_2 \in \vec{I}$. Further, each scattering coefficient s_{ij} is defined as

$$
s_{ij} = \frac{R_i}{I_j}|_{I_k=0; k \neq j},
\tag{3.2}
$$

where R_i is the amplitude of the reflected wave at port i, and I_j is the incident wave at port j. For example, consider $i = 1, 2$ and $j = 1, 2$ for a two port system (Fig. 3.1 (b)) Using Eq. (3.2), the scattering coefficient for the two port system (Fig. 3.1 (b)) in which we have converted Fig.

3.1 (a) is [1, 70, 171]

$$s_{11} = \frac{b_1}{a_1}\big|_{b_2=0} = r = \frac{n_1 - n_2}{n_1 + n_2},$$
$$s_{21} = \frac{a_2}{a_1}\big|_{b_2=0} = t = \frac{2n_1}{n_1 + n_2},$$
$$s_{12} = \frac{b_1}{b_2}\big|_{a_1=0} = t' = \frac{2n_2}{n_1 + n_2},$$
$$s_{22} = \frac{a_2}{b_2}\big|_{a_1=0} = -r,$$

(3.3)

where n_N is the refractive index of the medium forming the medium N, r and t are the reflection and transmission coefficients at interface 1; and t' is the transmission coefficient at interface 2. It is clear that using the scattering matrix, the transmission and reflection coefficient are determined in a single shot. s_{11} and s_{21} give information about the reflection and transmission coefficient for a field incident from the left and s_{22} and s_{12} give information about the reflection and transmission coefficient for a field incident from the right. Hence, using Eqs. (3.3) and (3.1), the relation between the reflected and incident fields is given by S matrix as

$$\text{S matrix}: \quad \begin{bmatrix} b_1 \\ a_2 \end{bmatrix} = \begin{bmatrix} r & t' \\ t & -r \end{bmatrix} \begin{bmatrix} a_1 \\ b_2 \end{bmatrix}. \tag{3.4}$$

There is another important and related matrix which relates the quantity on the left side (the forward wave) of the port to the quantity on the right side (the backward wave), which is the transmission matrix $\vec{T}$, mathematically explained as

$$\begin{bmatrix} a_1 \\ b_1 \end{bmatrix} = \begin{bmatrix} t_{11} & t_{12} \\ t_{21} & t_{22} \end{bmatrix} \begin{bmatrix} a_2 \\ b_2 \end{bmatrix}, \tag{3.5}$$

where $t_{ij} \in \vec{T}$. One important feature of the T matrix is that it allows cascading of the systems in a chain and its implementation in explaining the effect of OF on laser dynamics (explained shortly). Further the T matrix is related to the S matrix [1] according to

$$t_{11} = \frac{1}{s_{21}}, \quad t_{12} = -\frac{s_{22}}{s_{21}}$$
$$t_{21} = \frac{s_{11}}{s_{21}}, \quad t_{22} = s_{12} - \frac{s_{11}s_{22}}{s_{21}}$$

(3.6)

and, equivalently,

$$s_{11} = \frac{t_{21}}{t_{11}}, \quad s_{12} = t_{22} - \frac{t_{12}t_{21}}{t_{11}}$$
$$s_{21} = \frac{1}{t_{11}}, \quad s_{22} = -\frac{t_{12}}{t_{11}}$$

(3.7)

Placing the value of s_{ij} from Eq. (3.3) in Eq. (3.6) to obtain t_{ij}, then Eq. (3.5) becomes

$$\text{T matrix}: \quad \begin{bmatrix} a_1 \\ b_1 \end{bmatrix} = \begin{bmatrix} \frac{1}{t} & \frac{r}{t} \\ \frac{r}{t} & \frac{1}{t} \end{bmatrix} \begin{bmatrix} a_2 \\ b_2 \end{bmatrix}. \tag{3.8}$$
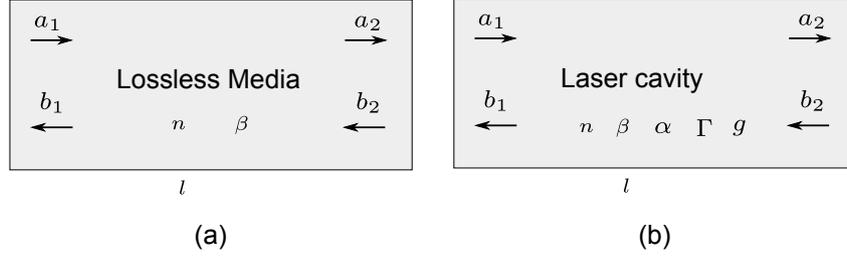
Figure 3.2: Schematic diagram to obtain S and T matrix for different media. (a) Lossless and continuum media; (b) Laser cavity with gain and attenuation.

For the basic case of transmission in lossless medium without discontinuities (Fig. 3.2 (a)), the S and T matrix are given by [1]

$$\text{S matrix :} \quad \begin{bmatrix} b_1 \\ a_2 \end{bmatrix} = \begin{bmatrix} 0 & e^{j\beta l} \\ e^{j\beta l} & 0 \end{bmatrix} \begin{bmatrix} a_1 \\ b_2 \end{bmatrix}. \tag{3.9}$$

$$\text{T matrix :} \quad \begin{bmatrix} a_1 \\ b_1 \end{bmatrix} = \begin{bmatrix} e^{-j\beta l} & 0 \\ 0 & e^{j\beta l} \end{bmatrix} \begin{bmatrix} a_2 \\ b_2 \end{bmatrix}, \tag{3.10}$$

where β and l are respectively the phase constant and the cavity length. It should be noted that, since the media does not have discontinuities, the coefficients s_{ij} and t_{ij} related to reflection are set to zero in Eqs. (3.4) and (3.8) to obtain Eqs. (3.9) and (3.10), respectively. Similarly, for the laser cavity (Fig. 3.2 (b)) the associated loss and gain are introduced and the S and T matrix are given by

$$\text{S matrix :} \quad \begin{bmatrix} b_1 \\ a_2 \end{bmatrix} = \begin{bmatrix} 0 & e^{j\beta l}e^{(\Gamma\frac{g}{2}-\frac{\alpha}{2})l} \\ e^{j\beta l}e^{(\Gamma\frac{g}{2}-\frac{\alpha}{2})l} & 0 \end{bmatrix} \begin{bmatrix} a_1 \\ b_2 \end{bmatrix}, \tag{3.11}$$

$$\text{T matrix :} \quad \begin{bmatrix} a_1 \\ b_1 \end{bmatrix} = \begin{bmatrix} e^{-j\beta l}e^{-(\Gamma\frac{g}{2}-\frac{\alpha}{2})l} & 0 \\ 0 & e^{j\beta l}e^{(\Gamma\frac{g}{2}-\frac{\alpha}{2})l} \end{bmatrix} \begin{bmatrix} a_2 \\ b_2 \end{bmatrix}, \tag{3.12}$$

where Γ is the confinement factor.

3.3 LASER MODEL USING S AND T MATRICES

Following the definitions in Sec. 3.3, in this section the basic laser gain equation is derived using the S and T matrix formalism just introduced, and compared to that in Chapter 2 (Eq. (2.14)). To do so, first the laser cavity is analyzed from the point of view of scattering theory. Then, the corresponding gain equation is compared with the one obtained using the standard methods available in the literature [1, 72].

Fig. 3.3 shows a laser cavity enclosed by two surfaces named as 1 and 2. At interface 1, T matrix (Eq. (3.8)) equals

$$\begin{bmatrix} a_1 \\ b_1 \end{bmatrix} = \begin{bmatrix} \frac{1}{t_1} & \frac{r_1}{t_1} \\ \frac{r_1}{t_1} & \frac{1}{t_1} \end{bmatrix} \begin{bmatrix} a_2 \\ b_2 \end{bmatrix}. \tag{3.13}$$

Between interface 1 and 2, T matrix (Eq. (3.12)) equals

$$\begin{bmatrix} a_2 \\ b_2 \end{bmatrix} = \begin{bmatrix} e^{-j\beta l} e^{-(\Gamma\frac{g}{2}-\frac{\alpha}{2})l} & 0 \\ 0 & e^{j\beta l} e^{(\Gamma\frac{g}{2}-\frac{\alpha}{2})l} \end{bmatrix} \begin{bmatrix} a_3 \\ b_3 \end{bmatrix}. \tag{3.14}$$

Finally, at interface 2, T matrix (Eq. (3.8)) equals

$$\begin{bmatrix} a_3 \\ b_3 \end{bmatrix} = \begin{bmatrix} \frac{1}{t_2} & \frac{r_1}{t_2} \\ \frac{r_2}{t_2} & \frac{1}{t_2} \end{bmatrix} \begin{bmatrix} a_4 \\ b_4 \end{bmatrix}. \tag{3.15}$$

From Eqs. (3.13), (3.14) and (3.15), the relationships between the waves entering the laser cavity and leaving it, and the overall transmission characteristics, are grouped as

$$\begin{bmatrix} a_1 \\ b_1 \end{bmatrix} = \begin{bmatrix} \frac{1}{t_1} & \frac{r_1}{t_1} \\ \frac{r_1}{t_1} & \frac{1}{t_1} \end{bmatrix} \begin{bmatrix} e^{-j\beta l} e^{-(\Gamma g-\alpha)\frac{l}{2}} & 0 \\ 0 & e^{j\beta l} e^{(\Gamma g-\alpha)\frac{l}{2}} \end{bmatrix} \begin{bmatrix} \frac{1}{t_2} & \frac{r_2}{t_2} \\ \frac{r_2}{t_2} & \frac{1}{t_2} \end{bmatrix} \begin{bmatrix} a_4 \\ b_4 \end{bmatrix}. \tag{3.16}$$

$$= \begin{bmatrix} \frac{1}{t_1 t_2} e^{-j\beta l} e^{-(\Gamma g-\alpha)\frac{l}{2}} + \frac{r_1 r_2}{t_1 t_2} e^{j\beta l} e^{(\Gamma g-\alpha)\frac{l}{2}} & \frac{r_2}{t_1 t_2} e^{-j\beta l} e^{-(\Gamma g-\alpha)\frac{l}{2}} + \frac{r_1 r_2}{t_1 t_2} e^{j\beta l} e^{(\Gamma g-\alpha)\frac{l}{2}} \\ \frac{r_1 r_2}{t_1 t_2} e^{-j\beta l} e^{-(\Gamma g-\alpha)\frac{l}{2}} + \frac{r_1}{t_1 t_2} e^{j\beta l} e^{(\Gamma g-\alpha)\frac{l}{2}} & \frac{r_1 r_2}{t_1 t_2} e^{-j\beta l} e^{-(\Gamma g-\alpha)\frac{l}{2}} + \frac{1}{t_1 t_2} e^{j\beta l} e^{(\Gamma g-\alpha)\frac{l}{2}} \end{bmatrix} \begin{bmatrix} a_4 \\ b_4 \end{bmatrix}. \tag{3.17}$$

$$= \begin{bmatrix} t_{11} & t_{12} \\ t_{21} & t_{22} \end{bmatrix} \begin{bmatrix} a_4 \\ b_4 \end{bmatrix}. \tag{3.18}$$

Using the boundary conditions under steady state, the standalone laser emits without light input from the outside i.e. a_4 and $b_1 \neq 0$ even though a_1 and $b_4 = 0$, i.e.

$$a_4, b_1 \neq 0 \mid a_1, b_4 = 0. \tag{3.19}$$
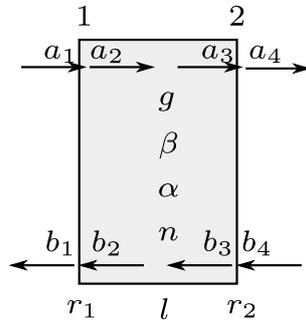
Figure 3.3: Schematic diagram of laser cavity as a two port system. Γ, β, α, n, r_1, r_2, have the usual meaning defined in Ch. 2; t_1 (t_2) is the transmission coefficient of the first (second) laser facet (not shown in the figure).

Using condition (3.19) in Eq.(3.18), we get

$$
\begin{bmatrix} 0 \\ b_1 \end{bmatrix} = \begin{bmatrix} t_{11} & t_{12} \\ t_{21} & t_{22} \end{bmatrix} \begin{bmatrix} a_4 \\ 0 \end{bmatrix}.
\tag{3.20}
$$

From Eq. (3.20), we get a pair of coupled equations

$$
0 = t_{11} a_4.
\tag{3.21}
$$

$$
b_1 = t_{21} a_4.
\tag{3.22}
$$

where substituting the value of t_{11} from Eq. (3.17) into Eq.(3.21), we get

$$
\frac{e^{-j\beta l} e^{-(\Gamma g - \alpha)\frac{l}{2}} + r_1 r_2 e^{j\beta l} e^{(\Gamma g - \alpha)\frac{l}{2}}}{t_1 t_2} a_4 = 0.
\tag{3.23}
$$

Since, $a_4, t_1, t_2 \neq 0$, Eq. (3.23) reduces to

$$
e^{-j\beta l} e^{-(\Gamma g - \alpha)\frac{l}{2}} + r_1 r_2 e^{j\beta l} e^{(\Gamma g - \alpha)\frac{l}{2}} = 0.
\tag{3.24}
$$

$$
e^{-j\beta l} e^{-(\Gamma g - \alpha)\frac{l}{2}} \left(1 + r_1 r_2 e^{2j\beta l} e^{2(\Gamma g - \alpha)\frac{l}{2}} \right) = 0.
\tag{3.25}
$$

Either,

$$
1 + r_1 r_2 e^{2j\beta l} e^{2(\Gamma g - \alpha)\frac{l}{2}} = 0.
\tag{3.26}
$$

Or,

$$
e^{-j\beta l} e^{-(\Gamma g - \alpha)\frac{l}{2}} = 0.
\tag{3.27}
$$

From Eq. (3.26),

$$
r_1 r_2 e^{2j\beta l} e^{2(\Gamma g - \alpha)\frac{l}{2}} = -1.
\tag{3.28}
$$

And equating the magnitudes on both sides,

$$
e^{2(\Gamma g - \alpha)\frac{l}{2}} = \frac{1}{r_1 r_2}.
\tag{3.29}
$$

$$
\Gamma g = \alpha + \frac{1}{l} ln \frac{1}{r_1 r_2}.
\tag{3.30}
$$

$$
\Gamma g = \alpha_i + \alpha_m,
\tag{3.31}
$$

where α_i is the internal cavity loss and α_m is the mirror loss. This equation is equivalent to the one obtained in Chapter 2 (Eq. (2.14)). Further, equating the phase of Eq. (3.28) on both

sides i.e. equating the phase after the round-trip to be zero (or an integral multiple of 2π)

$$e^{2j\beta l} = e^{2jq\pi}, \tag{3.32}$$

$$\beta = \frac{q\pi}{l}, \tag{3.33}$$

$$\Delta\beta = \frac{\pi}{l}, \tag{3.34}$$

$$\Delta f = \frac{c}{2ln}, \tag{3.35}$$

$$\Delta\lambda = \frac{\lambda^2}{2ln}, \tag{3.36}$$

where q is the mode number (an integer) i.e. $q =1,2 ...$ Eq. (3.34) states that the laser cavity acts as a waveguide which allows electromagnetic waves that differ by π/l to propagate through it.

The different elements of the T matrix have different meanings. For instance, the parameter t_{11} (t_{11}^2) (Eq. (3.6)) is related to the reflection coefficient (reflectance). Further, it also gives the information about the cavity modes allowed in the laser cavity. To better visualize the meaning of the parameter, Fig. 3.4 is the plot of $|s_{21}| = 1/t_{11}$ obtained from Eq. (3.18) for different phase and attenuation constants. It is observed that only those modes that are integral multiples of $\beta l/\pi$ are promoted in the cavity, while the rest are attenuated.

Besides, the effect of the attenuation coefficient in mode competition is also shown. It is observed that the strength of the propagating mode is directly proportional to the product of the cavity length and the attenuation coefficient of the material forming the laser cavity (αl). Hence, to the losses incurred in the cavity during propagation. In addition, the FWHM of the lased field, $\Delta\beta_{FWHM}$ ($\Delta\omega_{FWHM}$), and the photon life time (τ_p) are related to the attenuation coefficient and to losses in the cavity as [72]

$$\Delta\beta_{FWHM} = \frac{1}{l}\left[\frac{1 - r_1 r_2 e^{-\alpha l}}{r_1 r_2 e^{-\alpha l}}\right]. \tag{3.37}$$

$$\Delta\omega_{FWHM} = \frac{v_g}{l}\left[\frac{1 - r_1 r_2 e^{-\alpha l}}{r_1 r_2 e^{-\alpha l}}\right] = \frac{1}{\tau_p}, \tag{3.38}$$

where the total lifetime of the photon in the cavity is the sum of photon losses due to the mirror loss rate (escaping to outer world), τ_p^{ext} and the internal loss rate due to absorption, τ_p^{int}. Mathematically,

$$\frac{1}{\tau_p} = \frac{1}{\tau_p^{ext}} + \frac{1}{\tau_p^{int}}. \tag{3.39}$$

The quality factor (Q) of the laser, which determines the sharpness of the mode emitted by the laser is given by [72]

$$Q = \frac{\omega}{\Delta\omega_{FWHM}} = \frac{1}{\tau_p}. \tag{3.40}$$

Fig. 3.5 shows the effect of losses in the laser cavity on mode broadening, obtained from Eq. (3.37). It is evident that an increase in losses broadens the spectral width of the lasing field.
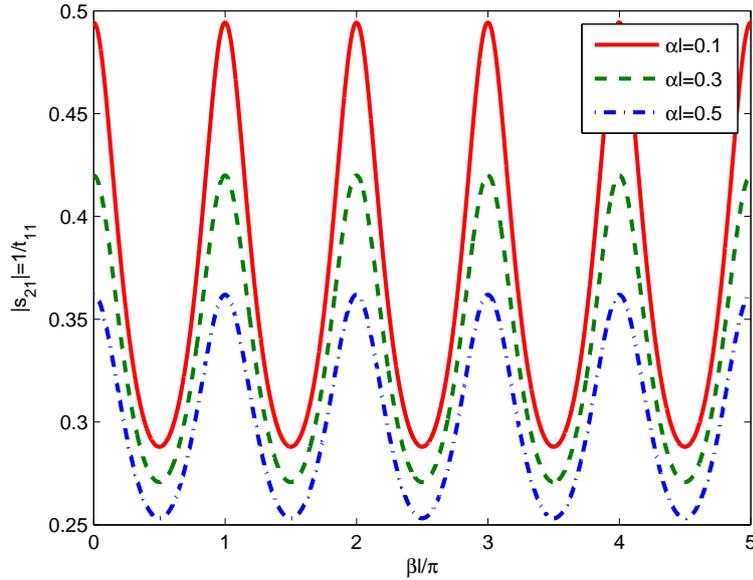
Figure 3.4: Lasing mode supported by the laser obtained from S/T matrix calculations. Only those modes that are an integral multiple of $\beta l/\pi$ are supported. The field is attenuated as the loss increases.

Thus, for the modes to be sharper within the cavity (narrower), as desirable, the losses in the laser cavity must be kept to a minimum, which is an intuitive and logical result . Eq. (3.38) to (3.40) are important because they demonstrate that an external perturbation such as OF can change the photon lifetime and thus alter the linewidth of the laser, and ultimately its quality factor. This will be commented in detail along Sec. 3.4, in particular Eq. (3.63). The same effect of narrowing the modes can be attained by increasing the reflection coefficient of the laser facet, but this brings on a subsequent reduction of the emitted power (Chapter 2, Eq. (2.30)).

Eq. (3.30) - (3.36) are the standard gain equations calculated using the formalism of S and T matrices. This shows that the scattering theory holds true for the solitary laser. Next, the model is extended to use S and T matrices to calculate the lasing conditions in the presence of a "lossy" external cavity formed due to the presence of a target placed at a distance L from the laser, that is, for lasers under optical feedback.

3.4 SCATTERING THEORY APPLIED TO LASER UNDER OF

In this Section, the S matrix (relating the forward and backward field at an interface) is used to find the equivalent reflection and transmission coefficient of the laser facet in the presence of an external cavity formed by a target placed at distance L [1] from laser. Referring to Fig. 3.6,

---

[1]Here the superscript ext is omitted for ease.
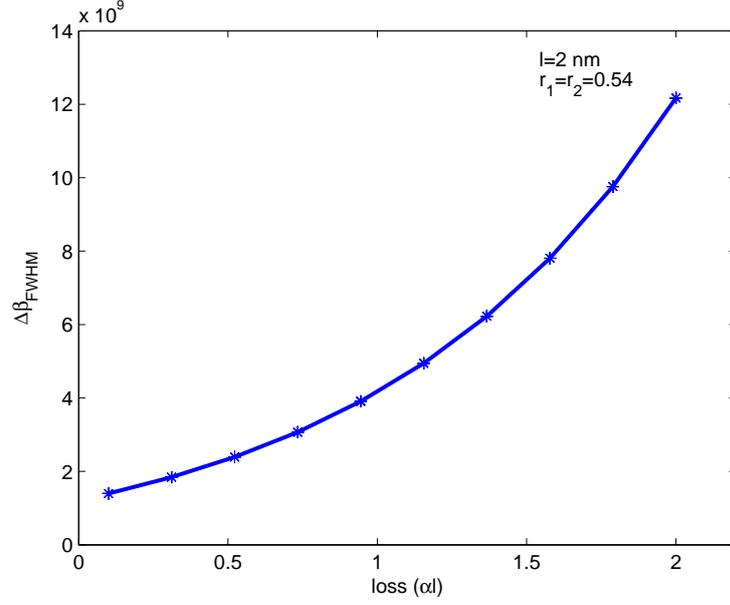
Figure 3.5: The FWHM of the lasing mode increases with the increase of losses in the cavity (obtained from Eq. (3.37))
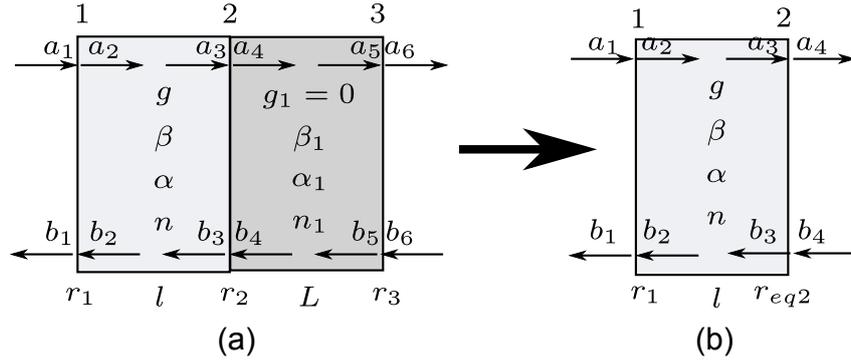
Figure 3.6: Scattering theory applied to the analysis of OF. (a) Schematic diagram of the fields due to external target placed at a distance L from the laser. (b) Concept of equivalent cavity.

at interface 2, using S matrix (Eq. (3.4)),

$$
\begin{bmatrix} b_3 \\ a_4 \end{bmatrix} = \begin{bmatrix} r_2 & t_2 \\ t_2 & -r_2 \end{bmatrix} \begin{bmatrix} a_3 \\ b_4 \end{bmatrix}.
\tag{3.41a}
$$

$$
b_3 = r_2 a_3 + t_2 b_4.
\tag{3.41b}
$$

$$
a_4 = t_2 a_3 - r_2 b_4.
\tag{3.41c}
$$

In the external cavity (between interface 2 and 3), using Eq. (3.11) has the shape,

$$
\begin{bmatrix} b_4 \\ a_5 \end{bmatrix} = \begin{bmatrix} 0 & e^{j\beta_1 L} e^{-\alpha_1 L} \\ e^{j\beta_1 L} e^{-\alpha_1 L} & 0 \end{bmatrix} \begin{bmatrix} a_4 \\ b_5 \end{bmatrix}.
\tag{3.42a}
$$

Table 3.1: List of relevant parameters involved in explaining laser dynamics in presence of OF. Interface 1 and 2 form the laser cavity and interfaces 2 and 3 form the external cavity.

Description	Symbol
length of the laser cavity	l
length of external cavity	L
reflection coefficient at interface 1,2 and 3	r_1, r_2 and r_3
confinement factor	Γ
laser gain per unit length	g
attenuation coefficient of material that form active region of laser	α
attenuation coefficient of material that form the external cavity	α_1
laser emission frequency	ω
phase constant of field in laser cavity	β
phase constant of field in the external cavity	β_1
refractive index of the material forming the first cavity	n_1
refractive index of the material forming the second cavity	n_2

$$b_4 = e^{j\beta_1 L} e^{-\alpha_1 L} b_5. \tag{3.42b}$$

$$a_5 = e^{j\beta_1 L} e^{-\alpha_1 L} a_4. \tag{3.42c}$$

At interface 3, using Eq. (3.4), it reduces to

$$\begin{bmatrix} b_5 \\ a_6 \end{bmatrix} = \begin{bmatrix} r_3 & t_3 \\ t_3 & -r_3 \end{bmatrix} \begin{bmatrix} a_5 \\ b_6 \end{bmatrix}. \tag{3.43a}$$

Using the new boundary conditions, $b_6 = 0$, as no beam enters the cavity system from behind the target

$$b_5 = r_3 a_5. \tag{3.43b}$$

$$a_6 = t_3 a_5. \tag{3.43c}$$

Using Eqs. (3.41b) and (3.42b), we get

$$b_3 = r_2 a_3 + t_2 b_5 e^{j\beta_1 L} e^{-\alpha_1 L}. \tag{3.44}$$

And using Eq. (3.43b)

$$b_3 = r_2 a_3 + t_2 r_3 a_5 e^{j\beta_1 L} e^{-\alpha_1 L}. \tag{3.45}$$

Which after using Eq. (3.42c) yields

$$b_3 = r_2 a_3 + t_2 r_3 a_4 e^{j2\beta_1 L} e^{-2\alpha_1 L}. \tag{3.46}$$

And finally using Eq. (3.41c), we get

$$b_3 = r_2 a_3 + t_2 r_3 (t_2 a_3 - r_2 b_4) e^{j2\beta_1 L} e^{-2\alpha_1 L}. \tag{3.47}$$

$$b_3 = r_2 a_3 + t_2^2 r_3 a_3 e^{j2\beta_1 L} e^{-2\alpha_1 L} - t_2 r_3 r_2 b_4 e^{j2\beta_1 L} e^{-2\alpha_1 L}. \tag{3.48}$$

Placing the value of $t_2 b_4$ from Eq. (3.41b) and $r_2{}^2 = 1 - t_2{}^2$ gets to the expression

$$b_3 = r_2 a_3 - r_3 r_2 b_3 e^{j2\beta_1 L} e^{-2\alpha_1 L} + r_3 a_3 e^{j2\beta_1 L} e^{-2\alpha_1 L}. \tag{3.49}$$

$$b_3 (1 + r_2{}_r 3 e^{j2\beta_1 L} e^{-2\alpha_1 L}) = a_3 (r_2 + r_3 e^{j2\beta_1 L} e^{-2\alpha_1 L}). \tag{3.50}$$

$$r_{eq2} = \frac{b_3}{a_3} = \frac{r_2 + r_3 e^{j2\beta_1 L} e^{-2\alpha_1 L}}{1 + r_2 r_3 e^{j2\beta_1 L} e^{-2\alpha_1 L}}. \tag{3.51}$$

$$= \frac{r_2 + r_3 e^{-2(\alpha_1 - j\beta_1)L}}{1 + r_2 r_3 e^{-2(\alpha_1 - j\beta_1)L}}. \tag{3.52}$$

$$= \frac{r_2 + r_3 e^{-2\gamma_1 L}}{1 + r_2 r_3 e^{-2\gamma_1 L}}., \tag{3.53}$$

where $\gamma_1 = \alpha_1 - j\beta_1$ is propagation constant of the field in the medium forming the external cavity and r_{eq} is the equivalent reflectivity at interface 2 resulting from the external target placed at distance L (Fig. 3.6). Although the equation for equivalent reflection coefficient derived in Eq. (3.53) looks different in the absence of attenuation coefficient, this is the same standard equation obtained by different authors such as Coldren et al. [1] and can be transformed in terms of coupling coefficient, κ (ch. 2, Eq. (2.60)) as proposed by Petermann [72]. Equating the attenuation coefficient in Eq. (3.53) to zero and re-writing it as follows

$$r_{eq2} = \frac{r_2 + r_3 e^{2\beta_1 L} + r_2^2 r_3 e^{j2\beta_1 L} - r_2^2 r_3 e^{j2\beta_1 L}}{1 + r_2 r_3 e^{22\beta_1 L}}. \tag{3.54}$$

It should be noted that the addition of the last two terms in the numerator of Eq. (3.54) cancels each other, so effectively it is the same as Eq. (3.53). Further, the first and third terms, and the second and fourth term are grouped, resulting in

$$r_{eq2} = \frac{r_2 (1 + r_2 r_3 e^{j2\beta_1 L}) + r_3 (1 - r_2^2) e^{j2\beta_1 L}}{1 + r_2 r_3 e^{j2\beta_1 L}}, \tag{3.55}$$

$$= r_2 + \frac{r_3 (1 - r_2^2) e^{j2\beta_1 L}}{1 + r_2 r_3 e^{j2\beta_1 L}}, \tag{3.56}$$

$$= r_2 + \frac{r_3 t_2^2 e^{j2\beta_1 L}}{1 + r_2 r_3 e^{j2\beta_1 L}}. \tag{3.57}$$

Equation (3.57) is the same obtained in [1, 30]. This proofs that Eq. (3.53) obtained above using scattering theory is a generalized form that which takes into account the attenuation, in

addition to the phase. Further, from ch. 2 (Eq. (2.60)), using $\kappa = (1 - r_2^2)r_3/r_2$, Eq. (3.56) is written as

$$r_{eq2} = r_2 + \frac{\kappa r_2 e^{j2\beta_1 L}}{1 + r_2 r_3 e^{j2\beta_1 L}} \tag{3.58}$$

Using Euler's formula $e^{j\theta} = cos(\theta) + jsin(\theta)$, and considering that the reflection coefficient is a real quantity (i.e. ignoring the imaginary part of Eq. (3.58)), Eq. (3.58) can be written as

$$r_{eq2} = r_2 + \frac{\kappa r_2 cos(2\beta_1 L)}{1 + r_2 r_3 cos(2\beta_1 L)}, \tag{3.59}$$

since $r_2 < 1$ and $r_3 < 1$, their product $r_2 r_3 << 1$ and the maximum value of $cos(\theta)$ is 1; so the condition $r_2 r_3 cos(2\beta_1 L) << 1$ holds true, and Eq. (3.59) reduces to

$$r_{eq2} = r_2 + \kappa r_2 cos(2\beta_1 L), \tag{3.60}$$

$$= r_2(1 + \kappa cos(2\beta_1 L)) \tag{3.61}$$

Equation (3.61) is exactly the same obtained in [30, 72]. Thus it is evident that the Eq. (3.53) is the equivalent reflection coefficient that takes different forms as derived by different authors [1, 72] under different conditions. From Eqs. (3.52) and (3.53), important conclusions are drawn. First, the described equivalent reflection coefficient (r_{eq}) is now dependent upon the attenuation coefficient α_1, the phase constant β_1, the reflection coefficient of the external target r_3, and the physical length L of the external cavity. Second, since the attenuation constant α_1 is a frequency dependent value, so will be the equivalent reflection coefficient, which will also vary with the frequency emission from the laser. Third, since, r_{eq} depends upon the phase constant β_1, which in turn depends upon the refractive index n_1 of the external cavity through $\beta_1 = 2\pi n_1/\lambda$, so if the refractive index n_1 changes, the effective reflectivity r_{eq} is also changed. Finally, r_{eq} is shown to be also dependent upon the physical cavity length L.

In particular, referring to Fig. 3.6 and considering the general case where air is the medium in the external cavity formed by the second laser facet and the target, simulation are carried out to determine the effect on the laser parameters of the different loss factors in external cavity, described by $\alpha_1 L$. From Fig. 3.7 (a), it is observed that increasing the value of $\alpha_1 L$, r_{eq} in general decreases. However, there exists a particular value of $\alpha_1 L$ (in this case it is 6×10^{-4}), for which a resonance is reached and r_{eq} is minimal. Beyond this value, r_{eq} increases again. It is also observed that for all the values of losses in the external cavity ($\alpha_1 L$), a minimal equivalent reflection coefficient is attained when the reflection coefficient of the external target is equal to that of the laser facet ($r_3 = r_2$). In addition, it was shown in Chapter 2 (Eq. (2.30)) that the optical field emitted by laser is dependent upon the reflection coefficient of the laser facet. In the absence of OF, in the conditions described in Chapter 2 (Fig. 2.7), the power emitted from the laser P_{02} is 0.54 mW. A simulation is carried under similar conditions to determine the effect of OF on and losses in the laser emission. Fig. 3.7 (b) shows the effect of OF on the power emitted
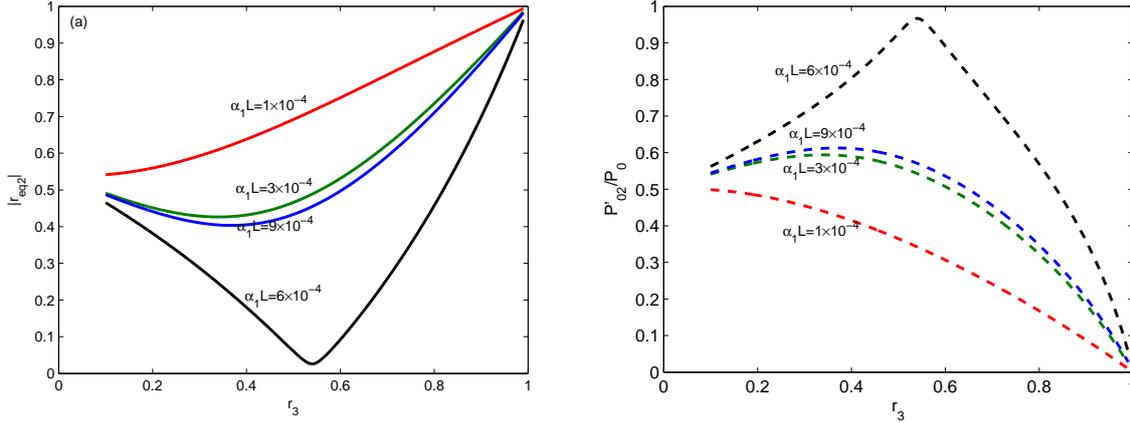
Figure 3.7: Effect of the external cavity on the laser parameters. (a) Effect of losses in the external cavity $\alpha_1 L$ on the equivalent reflectivity of laser ; (b) Optical power emitted under feedback normalized to total power without feedback . Simulation parameters $r_1 = r_2 = 0.54$, power output from laser in presence of optical feedback is obtained from Eq. (2.30), provided that r_{eq} (defined in Eq. (3.53)) is used. In the absence of OF, $P_{02}/P_0 = 0.5$ (see Ch. 2, Fig. 2.7)

by the laser, taking into account the losses in the external cavity ($\alpha_1 L$) at different values of external reflection coefficient (r_3). In short, the power emitted under OF (P'_{02}) is obtained by replacing r_2 in Eq. (2.30), with the r_{eq} value defined in Eq. (3.53). Unlike the results obtained in the case of r_{eq}, increasing the losses in the external cavity ($\alpha_1 L$) brings on the increase in the power emitted by laser under OF (P'_{02}), which increases until a resonance is reached (in this particular case, at $\alpha_1 L = 6 \times 10^{-4}$). Beyond that value, the emitted power starts to degrade. It is also observed that in all of the cases, the maximal optical power emitted from the laser under feedback takes place when the external reflection coefficient equals the laser facet reflection coefficient i.e. when $r_3 = r_2$. Thus, by engineering the experimental conditions, the amount of losses in the external cavity and the reflection coefficient of the target, the conditions for laser emission under feedback can be optimized using the theory being proposed.

Further, the strong dependence of r_{eq} and P'_{02} on the external parameters (L, n_1) is the basis of OF-based optical sensing. For instance, if the OPL between the laser and the external reflective target is modulated periodically by changing the physical length (L) (keeping the refractive index of the medium that forms the cavity constant) (Fig. 3.6), then the equivalent reflection coefficient r_{eq} (Eq. (3.53)) is also modulated periodically introducing the well-know modulation of emitted power P'_{02}.

Fig. 3.8 further explains this effect. The physical length of the external cavity L is modulated such that the peak modulation is $L_{ext0} = 3\lambda$, making the cavity length in the range $L_{ext}(t) \in L + L_{ext0}$. Such a modulation gets encoded in the optical power output of the laser, and is easily retrieved by processing such a power signal. In the absence of OF, as mentioned, the power emitted from the laser is $P_{02} = 0.54$ mW (Chapter 2, Fig. 2.7) and is a constant value (shown by the dashed line in Fig. 3.8). However, in presence of OF and when the described
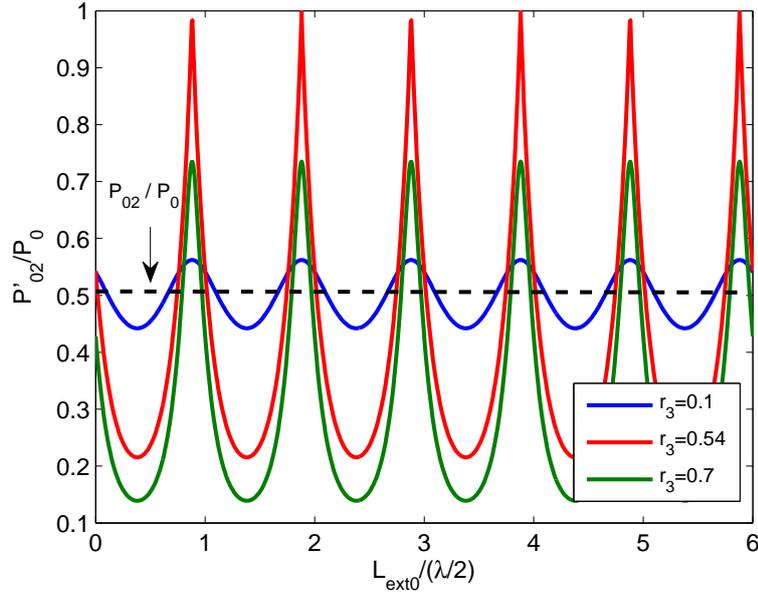
Figure 3.8: Basic mechanism for the OF-based sensor. Modulation of OPL causes the modulation of emission power P'_{02}, which would have been constant without modulation of OPL (P_{02}). With the increase in r_3, the laser emission power increases and a resonance is reached when $r_3 = r_2$. Simulation parameters:L_{ext0}=3λ; $r_1 = r_2 =$ 0.54; n_1=1; $\lambda = 692$ nm; $\alpha_1 = 0.005$/m.

modulation of OPL is introduced, it is no longer a constant and follows the modulation in OPL, being maxima or minima for each $\lambda/2$ change. The appearance of six fringes for an induced displacement of 3λ (Fig. 3.8) is similar to that obtained from the standard equation of OF for displacement measurement ($P_s = cos(4\pi L_{ext}(t)/\lambda)$). In addition to this information, the effect of r_3 in the OFS in terms of *pp* value and fringe width is also presented. It is observed that at low $r_3 = 0.1$, the OFS is still weak and has a low *pp* value with wider fringes[2] (fringe width normalized to $\lambda/2$ is in this case 0.28); at $r_3 = r_2 = 0.54$, a resonance is reached so the *pp* value of OFS increases drastically while the fringes are radically narrowed (normalized fringe width, in this case , is just 0.14) enabling easy and precise fringe detection through signal processing. Finally, by detuning r_3=0.7, the OFS starts to degrade and widens again (normalized fringe width becomes 0.16) as well.

The observation of the resonance related to OF is coherent with Fig.3.7 (b), where a resonance in emitted optical power occurs when $r_3 = r_2$. Besides, the increased sharpness, or narrowing of the fringes as r_3 increases can be explained by Eqs. (3.39) and (3.40). In the presence of OF, there are photons re-injected into the laser cavity that modify Eq.(3.39) and

---

[2]Maria et. al in [175] showed that the fringes in OFS have Gaussian distribution, so the fringe width is calculated as the width at which its magnitude become $1/e$ of peak value

Eq.(3.40) as

$$\frac{1}{\tau_p'} = \frac{1}{\tau_p^{ext}} + \frac{1}{\tau_p^{int}} - \frac{1}{\tau_p^{of}}, \tag{3.62}$$

$$Q' = \frac{\omega}{\Delta\omega_{FWHM}} = \frac{1}{\tau_p'}, \tag{3.63}$$

where the first two terms in Eq. (3.62) represent photon emission from the laser, and an additional term $-1/\tau_p^{of}$ has been added to represent the effect of the injection of photons in the laser cavity due to OF. Increasing r_3 causes more and more photons to be re-injected into the laser cavity, so the term -1/τ_p^{of} increases. This causes $1/\tau_p'$ to increase and ultimately the quality factor Q' to increase (Eq. (3.63)). This increment in the quality factor in turn poses a necessary condition on $\Delta\omega_{FWHM}$ so it needs to decrease (Eq. (3.38)), thus bringing on the sharpening of the fringes for increased r_3 values observed in Fig. 3.8. However, this holds true until the resonance condition at $r_3 = r_2$ is reached. Referring to Fig. 3.7 (a), beyond resonance ($r_3 > r_2$) the equivalent reflection coefficient of the laser facet decreases. This implies that less field is reflected from the laser facet (interface 1 in Fig. 3.6), and more field is transmitted through it, and at the same time more field is reflected from interface 3 in Fig. 3.6, making the laser acts as a single cavity (instead of two individual ones) with cavity length $l + L$. Hence, the effect of OF under these conditions is diminished, making the third term on the right side of Eq. (3.62) negligible and reducing it to the standard equation of the free-running laser Eq. (3.39), causing the broadening of fringes. An equivalent interpretation can be reached by considering the fact that increasing r_3, the coupling factor κ and the feedback strength C increase (Chapter 2, Eqs. (2.60) and (2.69)). Further C is in inverse relation to the spectral width of laser as $\Delta\nu_s = \delta\nu_0/(1 + C)^2$ [72]. From the above mentioned relationships, it can again be concluded that with increase in r_3, the fringes so produced have high fineness.

3.5 LASER WITH OPTICAL FEEDBACK FROM MULTIPLE CAVITIES

So far, in the previous sections scattering was used to analyze the detailed response of the laser to OF from a single external cavity. The effect of reflection coefficient of the external target on the laser emission was shown in Fig 3.8. Further, it was demonstrated that the resonance in laser emission is reached when the reflection coefficient of external target is close to that of laser facet. In this section, the same concept is extended to two external cavities with different cavity parameters, a situation relatively common when working with some transparent media, for instance in lab-on-chip applications. The different fields emanating from the two cavities are shown in Fig. 3.9(a). The setup is an extended version of the case of the external cavity just analyzed (Fig. 3.6). In the presence of a second external cavity (enclosed by interfaces 3 and 4), a set of additional new fields appear. The parameters that describe the second external
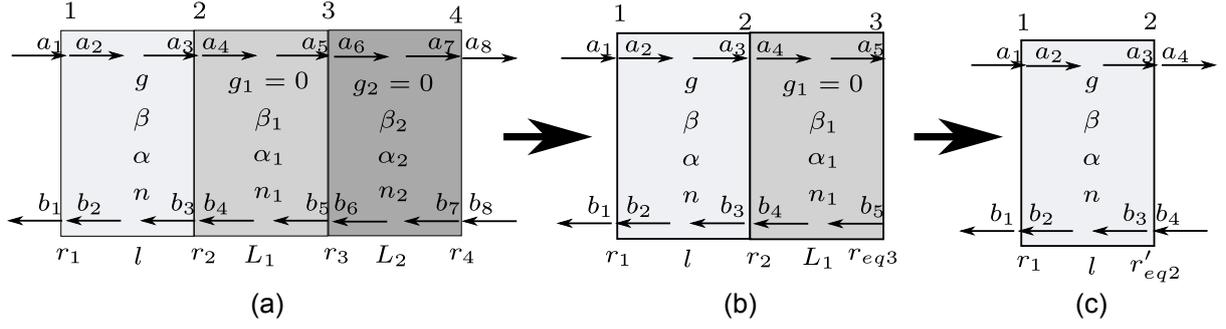
Figure 3.9: Scattering theory for multi cavity optical feedback. $N = 2$ number of external cavity is simplified to single cavity in $N = 2$ recursive steps. (a) Field propagation in forward and backward direction under optical feedback from two external cavities. (b) Intermediate step converting two external cavity to one external cavity. (c) Converting the two cavities in (b) to a single cavity.

cavity are desiged as $g_2, \beta_2, \alpha_2, n_2$, where all the parameters have the same physical meaning of those listed in Table 3.1. Since, the S matrix for interface 1 to 3 is exactly the same presented in Eqs. (3.41a), (3.42a) and (3.43a) for the previous case analyzed, and are repeated for ease of reading. So, the complete list of scattering matrices of the multiple cavity system is described as follows. The S matrix at interface 2, is given by

$$\begin{bmatrix} b_3 \\ a_4 \end{bmatrix} = \begin{bmatrix} r_2 & t_2 \\ t_2 & -r_2 \end{bmatrix} \begin{bmatrix} a_3 \\ b_4 \end{bmatrix} \tag{3.64}$$

In the first external cavity, that is, between interface 2 and 3, we get

$$\begin{bmatrix} b_4 \\ a_5 \end{bmatrix} = \begin{bmatrix} 0 & e^{j\beta_1 L_1} e^{-\alpha_1 L_1} \\ e^{j\beta_1 L_1} e^{-\alpha_1 L_1} & 0 \end{bmatrix} \begin{bmatrix} a_4 \\ b_5 \end{bmatrix} \tag{3.65}$$

At interface 3, the S matrix is given by

$$\begin{bmatrix} b_5 \\ a_6 \end{bmatrix} = \begin{bmatrix} r_3 & t_3 \\ t_3 & -r_3 \end{bmatrix} \begin{bmatrix} a_5 \\ b_6 \end{bmatrix}. \tag{3.66}$$

Furthermore, in the second external cavity, defined by interfaces 3 and 4, the S matrix is given by

$$\begin{bmatrix} b_6 \\ a_7 \end{bmatrix} = \begin{bmatrix} 0 & e^{j\beta_2 L_2} e^{-\alpha_2 L_2} \\ e^{j\beta_2 L_2} e^{-\alpha_2 L_2} & 0 \end{bmatrix} \begin{bmatrix} a_6 \\ b_7 \end{bmatrix}. \tag{3.67}$$

Finally, at interface 4

$$\begin{bmatrix} b_7 \\ a_8 \end{bmatrix} = \begin{bmatrix} r_4 & t_4 \\ t_4 & -r_4 \end{bmatrix} \begin{bmatrix} a_7 \\ b_8 \end{bmatrix}. \tag{3.68}$$

Using boundary condition, $b_8 = 0$

$$b_7 = r_4 a_7. \tag{3.69}$$

$$a_8 = t_4 a_7. \tag{3.70}$$

using the boundary condition $b_8 = 0$ (as no light enters the system from behind interface 4),and substituting b_7 from Eq. (3.69) in Eq. (3.67), enables to further solving Eqs. (3.67) and (3.66) to get,

$$r_{eq3} = \frac{b_5}{a_5} = \frac{r_3 + r_4 e^{j2\beta_2 L_2} e^{-2\alpha_2 L_2}}{1 + r_3 r_4 e^{j2\beta_2 L} e^{-2\alpha_2 L_2}}. \tag{3.71}$$

$$= \frac{r_3 + r_4 e^{-2(\alpha_2 - j\beta_2)L_2}}{1 + r_3 r_4 e^{-2(\alpha_2 - j\beta_2)L_2}}. \tag{3.72}$$

$$= \frac{r_3 + r_4 e^{-2\gamma_2 L_2}}{1 + r_3 r_4 e^{-2\gamma_2 L_2}}, \tag{3.73}$$

where $\gamma_2 = \alpha_2 - j\beta_2$ is propagation constant of the medium forming the second external cavity, r_4 is the reflection coefficient at interface 4. (after loss $\alpha_2 L_2$ has occurred) of the material in the second cavity, and r_{eq3} is the equivalent reflection coefficient at interface 3 resulting from the external target placed at distance L_1 (Fig. 3.9(b)). Now the problem of the two external cavities gets reduced to the case of the single external cavity previously explained using Eq. (3.53), provided that r_3 in Eq. (3.53) is replaced by r_3 (Eq. (3.73)). It is evident that the procedure proposed enables a setup with N external cavities which can be similarly converted into a single S matrix in N iterative steps. This observation is similar to the one in [172] when explaining scattering effects in DFB lasers. Hence the overall equivalent reflection coefficient for the two external cavities is given by

$$r'_{eq2} = \frac{r_2 + r_{eq3} e^{-2\gamma_1 L_1}}{1 + r_2 r_{eq3} e^{-2\gamma_1 L_1}}. \tag{3.74}$$

The use of the scattering matrix has thus enabled to reduce the laser cavity and the two external cavities with different optical properties to a single characteristic equation for the laser operation, which when solved describes the response of the laser under the considered conditions. One potential application of scattering theory could be to determine the optimal intermediate cavity length to get the maximal output power from the laser under OF in setups with multiple cavities. As an example, considering Fig. 3.9 (a), assume the first external cavity (between interface 2 and 3) is filled with air, and the second external cavity (between interface 3 and 4.) is filled with water or some solution under test.Under these conditions, the optimal intermediate cavity length which attains the maximum optical power emitted from the laser is desirable, which corresponds to the minimal equivalent reflection coefficient. Simulations are carried out in MATLAB to see the effect of the external cavities on the performance of the laser, and presented in Fig. 3.10. Keeping the second cavity parameters constant at $\alpha_2 L_2 = 5 \times 10^{-3}$, $n_2 = 1.33$ and $r_4 = 0.54$, an optimal value of total losses $\alpha_1 L_1 = 5 \times 10^{-4}$ is obtained in the intermediate cavity for which the equivalent reflection coefficient is minimal and the power emitted from the laser is maximized. Detuning the loss from this value causes significant degradation in optical output power, as observed in Fig. 3.10.

Scattering theory may also be applied to characterize optical feedback systems in presence of multiple cavities. For most of the use cases (e.g. lab-on-chip sensing applications), the first

77
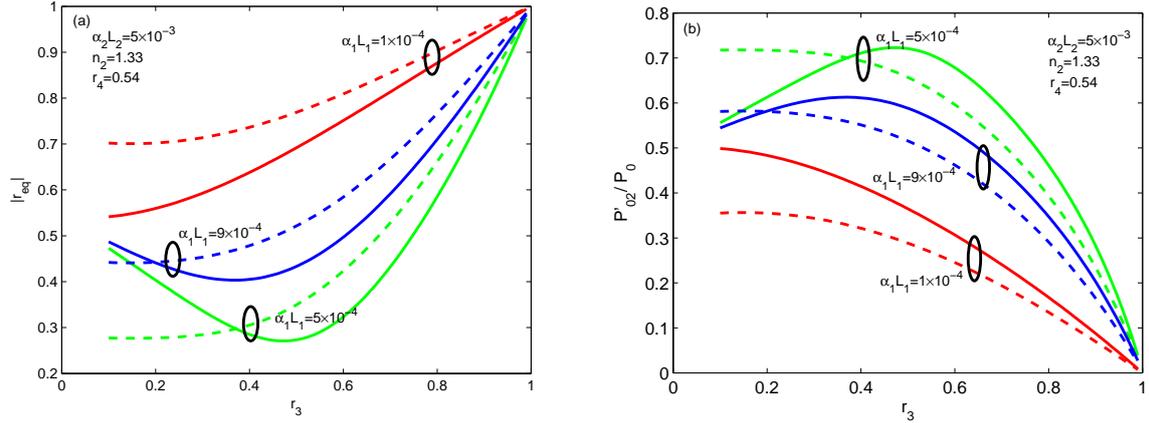
Figure 3.10: Comparison between the equivalent reflection coefficient calculated using scattering theory (a) and power emitted from laser P'_{02} (b) in the cases of single (solid) and double (dashed) external cavities.
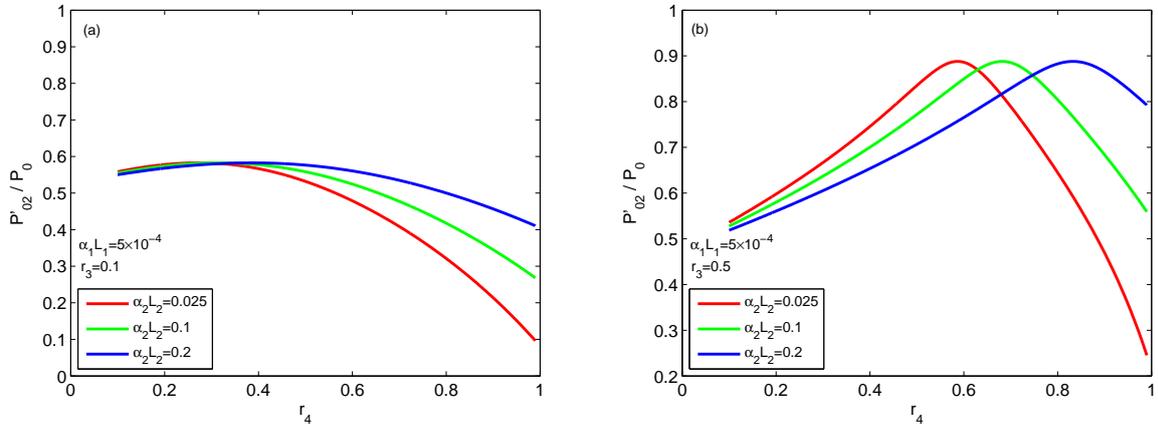
Figure 3.11: Effect of second external cavity on power emission from laser according to scattering theory (a) Away from resonance conditions; (b) Close to resonance conditions.

(intermediate) cavity is air and the second cavity is some semi-transparent media that is under test. It is thus desirable to fix the parameters of the first cavity and determine the system performance in terms of the parameters of the second external cavity. Using this approach, two different conditions are studied: the response of the laser away from resonance ($r_3 \ll r_2$) and its response near resonance ($r_3 \cong r_2$). The former case is depicted in Fig. 3.11 (a). The total loss in the intermediate cavity is kept fixed $\alpha_1 L_1 = 5 \times 10^{-4}$, and r_3 is set to 0.1, which in this case is the Fresnel reflection coefficient at the air ($n_1 = 1$) - water ($n_2 = 1.33$) interface. Then, the losses in the second external cavity $\alpha_2 L_2$ are varied in order to study its effects on the emitted power. Since for most of the cases, α_2 is a known value, basically varying loss is limited to varying the length of the second external cavity. It is observed that with an increase in r_4, the power output from the laser under OF normalized to the power of the free-running laser decreases drastically and the rate of decrease increases with the decrease in the total losses
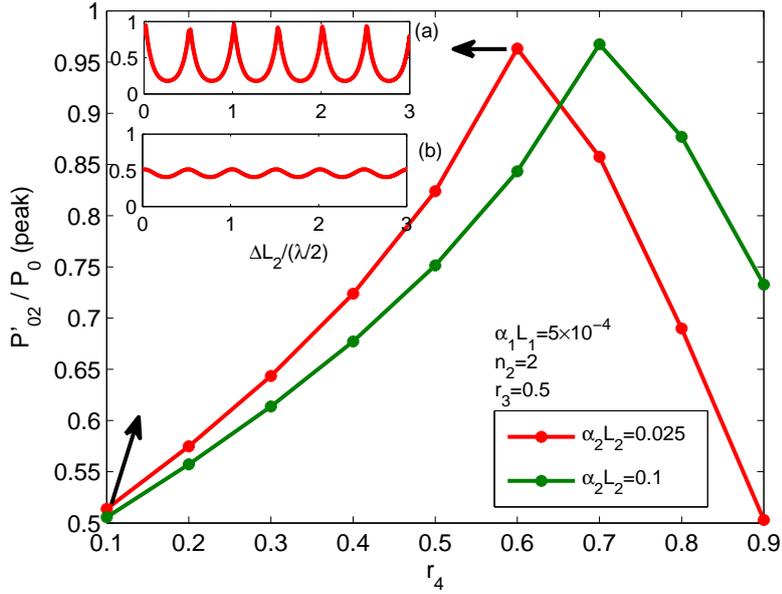
Figure 3.12: OFS as a function of losses in external cavities and external reflection coefficient.

in the second external cavity (which, known α_2, is understood as a reduction in length of the second external cavity).

For the later case, corresponding to the behaviour of the laser close to resonance, all the parameters are set as in the former case just described, provided that $r_2 \approx r_3 = 0.5$ (Fig. 3.11(b)). It is observed that the response of the laser can be divided in three regions. For the region $r_4 < r_3$, with an increase in r_4 the optical power output from laser increases, and its slope also increases with the decrease in total losses ($\alpha_2 L_2$) in the second external cavity. This means that, in this region, the shorter external cavity (with less losses) yields more power from the laser under feedback as compared to the free running laser at constant r_4 (unlike the previous case, where the optical power decreased with r_4). This is well illustrated by an example. Keeping $\alpha_2 L_2 = 0.025$ (red curve), increasing r_4 from 0.2 to 0.4, the power in OFS (compared to the solitary laser emission) increase from 0.6 to 0.7 as compared to 0.5 to 0.6 for the case when $\alpha_2 L_2 = 0.1$ (green curve). In the region $r_4 \approx r_3$ (more specifically $r_4 \approx r_3 \approx r_2$), the power output is maximal, although for different losses ($\alpha_2 L_2$) in the external cavity, resonance is reached at different r_4 values. This is an important conclusion as far as it states that the laser, under feedback from multiple cavities, presents a resonance condition dependent upon the losses in the second external cavity and its reflection coefficient. This result could be used to find the optimal second external cavity length for the most effective coupling of the light into the laser when under multiple cavity experiments, yielding an improved power output. This is particularly interesting in the case of highly diffusive samples under test where the power degrades with depth. Finally, beyond resonance $r_4 > r_3$, the power drastically falls down.

To complete the analysis of the double cavity case, it is desirable to study the fringe visibility

of the OFS under different conditions. To do so, the parameters of both cavities are kept the same to those in Fig. 3.11 and the OFS corresponding to a target motion of 3λ is obtained. The amplitude of OFS is recorded for each target reflection coefficient r_4. Fig. 3.12 shows the plot of amplitude of OFS as a function of r_4 at different external cavity loss conditions. For the case $\alpha_2 L_2 = 0.025$, when $r_4 = 0.1$, the OFS has a very low peak to peak value, resulting in fringes with reduced visibility and easily covered by noise in detection. Inset (b) in Fig. 3.12 shows the entire OF waveform under this conditions. However, increasing r_4 to 0.6 (in close vicinity to resonance), makes the amplitude of the OFS to increase drastically. Inset (a) in Fig. 3.12 shows the complete waveform obtained in these conditions and it improvement when compared to inset (b). It is clear that tuning of the parameters associated with individual cavities can very significantly improve the OFS and fringe visibility can be maximized, and the OFS can be detected in presence of disturbances like speckle or different types of noise.

Further, the theory developed in this Chapter may be used to explain the complexity of attaining a stable configuration when using OF sensors, as each modification in the length, reflectivity, or losses in any cavity introduces severe effects in the performance of the laser and the visibility of the fringes.

3.6 CONCLUSION

The scattering theory, described using S and T matrices, has been used as an effective tool to describe and characterize the effect of different external parameters in the performance of a solitary laser, of a laser with an external cavity under optical feedback, and of a laser with an external cavity with a vibrating target. The formalism enabled to include the effect of losses in every external media involved in the laser power output. It was shown that the expressions obtained can be used to describe the coupling of the optical field back into the laser cavity, and how the experimental setup provides some degrees of freedom which enable to optimize it in order to arrange an OFS with maximized visibility, given the parameters of the laser are known. Beyond the very relevant result of quantifying the optimal arrangement for a single cavity OFI setup, a further strength of the method lies in the fact that N cascaded multiple cavities can be explained extending the method in a recursive manner in N steps, calculating a final equivalent reflection coefficient. Further, such a multiple cavity model takes into account all the related external cavity parameters involved, including reflection coefficient, length, and losses all at once, but including a explicit description of the effects of each individual cavity. In the case of OF with two cavities, the losses in each individual cavity were analyzed in detail, a case which usually is neglected elsewhere. It was quantified how losses or length in each external cavity affect the parameters of the other, and the overall response of the laser emission. Thus, a tuning is necessary between all the parameters to optimize the response, and scattering theory has proven to be an effective tool to model the overall response. However,

analysis require accurate values of the external and internal cavity parameters to get reliable results, and the tuning gets more complex with the increase in the number of cavities. A further final conclusion is the behavioural complexity of single and multiple cavity systems under OF, which tremendously complicates the repeatability of the experimental conditions, a fact which is well known when working with OFI systems in the lab for accurate amplitude measurements.

4. Wavelet-Based Signal Processing of the Optical Feedback Signal

4.1 INTRODUCTION

The OFS is the result of the beat of the time delayed optical field (normally in the order of 10^{-7} to 10^{-2} relative to the emitted field) with the field of the standing wave existing inside of the laser cavity. As seen in different formulations in previous Chapters, the backscattered field interferes with the existent standing wave and changes the carrier density in the cavity, giving rise to a change in refractive index and to changes in the gain of the material in the active region of the laser. This results in a variation of the frequency of the free-running laser, as the gain shifts towards another dominant mode and phase of emission. This effect was explained in detail in Chapter 2. The additional phase and/or frequency modulation of the back-reflected optical field, introduced for instance, by a vibrating target, causes the conversion of the phase/frequency modulation into an intensity modulation of the laser emission, related to the interference of both fields, hence the name optical feeback interferometry (OFI). The intensity modulation is detected by the photodiode in the rear of the laser package which, when processed, delivers precise information about the external parameter causing the modulation (typically, the vibration of the target).

So far, OFS are processed in the time or the frequency domain to extract the vibrational parameters related to displacement and distance in the time domain, and to velocity in the frequency domain, but usually both of them are not processed simultaneously. In a classical paper, Donati et al. demonstrated measurement of displacement using theOFS without direction ambiguity with resolution of half the emission wavelength [50]. This method was based on FC, as each fringe corresponds to a $\lambda/2$ displacement of target motion. Since then, FC has been the basis for most of the methods. Even though, FC is a very simple methodology for determining target displacement, but it is limited and even not always feasible because of the presence of noise. Since the accuracy of the FC method depends upon accurate and precise localization of fringes, it is very important to detect fringes precisely, and even the loss of a single fringe automatically decreases the accuracy by $\lambda/2$. Typically, two independent types of noise corrupt the acquired OFS: Additive White Gaussian Noise (AWGN) and impulsive noise, which severely complicate the implementation of the FC method and its implementation. AWGN can in principle be removed by simple low pass filtering [67], but an additional conventional median filter is required to filter impulsive noise [67, 68]. There is, however, an unavoidable trade-off

between OFS filtering and the accuracy of fringe detection. On one hand, filtering is required to remove AWGN, but in case of over filtering, it makes the signal so smooth that even the fringes themselves may be smoothed, with the consequence of a loss in accuracy of the retrieved displacement. Furthermore, because of the impulse-like nature of impulsive noise in a very short time period, the spectrum of impulsive noise extends across to whole frequency spectrum so dedicated signal processing is normally required [163].

In addition to noise, another factor severely affecting fringe detection is speckle (as mentioned in 2.5.2.2). Speckle (a random interference of scattered fields in diffusive targets) causes severe, unwanted intensity modulation in the signal, which turns into unwanted power/voltage fluctuations in the OFS, in special if large target displacements are involved. Such undesirable phenomena complicate the work of fringe detection algorithms and result in relevant measurement errors due to missing (or extra) fringes. Speckle is specially relevant as far as OFI works typically using coherent sources focused onto diffusive targets, the ideal condition to induce speckle. In order to keep track of speckle, several approaches have been proposed. Zabit et al. in [69] proposed the use of a sliding window to determine the envelope of the OFS and to properly locate the fringes for target vibration reconstruction. There, finding the envelope of the signal was performed twice - for positive and negative envelope separately. Another approaches to manage speckle have involved actively tracking a bright speckle spot along time [167]. Atashkhooei et al. [10] proposed two methods denoted "adaptive technique" and "sensor diversity technique" to deal with speckle effects to correct erroneous measurements. The main disadvantage of the proposed techniques is the setup selected requires the use of two independent OFI setups, which need be precisely synchronized. Often the case, the velocity of vibration of the target is usually measured in frequency domain by finding the Doppler shift in the signal. Kliese and Rakic [176] demonstrated mathematically and experimentally the broadening of the Doppler spectrum due to speckle. Hence, even frequency domain analysis requires of some speckle compensation algorithms in order to improve the accuracy of the measurements performed.

To overcome the resolution limits and errors in accuracy which are inherent to the FC method, the PUM has been proposed for more precise determination of displacement [12, 14]. The use of the phase of the signal for extraction of displacement takes advantage of the fact that the phase of the OFS is substantially less susceptible to speckle and AWGN than the amplitude of the signal. Bernal et al. in 2013 [14] introduced IPUM, which optimized the PUM method to improve its performance. Authors in [177] proposed Hilbert transformation to analytically calculate the phase of OFS by representing it in the complex plane.

However, speckle and noise become relevant undesirable phenomena which complicate or limit the performance of fringe detection algorithms, resulting in measurement errors due to missing or imprecisely located fringes. In this Chapter, the use of the CWT is discussed to process the OFS signal in the time and frequency domain *simultaneously* for the first time to

our knowledge, with a single transformation addressing noise (both AWGN and impulsive noise), and allowing to extract parameters such as velocity and amplitude of vibration of the target, while delivering information for the management of speckle in the signal at the same time. The time domain component of the CWT is used to determine the target instantaneous displacement, and the time instance when direction reversal happens, while the frequency domain component, obtained using a single transformation, is used to determine the frequency and velocity of the vibration of the target. Such temporal information enables to detect relevant events of target motion in time out of the behaviour of the OFS whenever the target displacement is not harmonic. Unlike conventional Fourier analysis of the OFS, here the spectral characteristics of OFS are picked up directly from the time-frequency plane derived from the application of the CWT. The analysis of such time-frequency plane is, additionally, used to find the envelope of the amplitude of the OFS, and thus to keep track of speckle effects in the signal. Furthermore, the use of a complex wavelet [1] (the Morlet wavelet in this case) as an analyzing wavelet to process OFS results in wavelet coefficients represented in the complex plane, where the use of their imaginary and real components may be used to perform the PUM in order to determine the displacement of the target under test in the frequency domain. This method appears to have less error and better resolution than if obtained in the time domain using FC.

This Chapter has been organized as follows. Starting with Sec. 4.2, the basic mathematical definitions and principles behind the use of the complex Morlet wavelet for analysing the OFS are presented. Then, in Sec. 4.3 the methodology adopted to process the experimental OFS obtained from the periodic vibration of the target is discussed, followed by the experimental results obtained using the method proposed. It is shown that the CWT is used to remove AWGN and impulsive noise in OFS, and to extract most of the relevant vibrational parameters including target velocity, frequency of vibration, or target displacement without ambiguity, in a single shot. Such a performance may be appreciated even in presence of weak feedback, while at the same time it becomes possible to detect the envelope of the amplitude of the OFS to manage speckle, taking advantage of the complex amplitude coefficients of the CWT. Finally, in Sec. 4.3.4, taking advantage of the complex plane coefficients resulting from applying the CWT, a PUM method based on the CWT to process the OFS is described and compared with the classical FC method. Extending the algorithm, the CWT is used to analyse the OFS resulting from transient vibrations in the target (in particular, those induced by sinc-shaped pulses) and to characterize them in Sec. 4.4. A summary of the main contributions of this Chapter in Sec. 4.5 concludes the Chapter.

---

[1] a signal $x(t)$ is said to be complex if it contains real and imaginary part both and can be represented in form $x(t) = X + iY$

4.2 THE WAVELET TRANSFORM

The CWT is a mathematical operation that enable transforming the time domain signal into the time-frequency plane and investigate the time and frequency details of signals whose frequency content varies over time [178]. Wavelets are mathematically and conceptually defined as localized waveforms, which, instead of oscillating continuously and infinitely in time, oscillate only for a given duration in time and then rapidly decay to zero. The underlying property of wavelets, thus, is they are functions localized *both* in the time and frequency domains. This makes them different to other types of common basis, in particular to the well-known $e^{j\omega t}$ used in the Fourier transform. Since the OFS is dynamic in nature, the wavelet transform is a very well suited tool for its analysis, in special when non-periodic changes in the external cavity are involved, as it allows the retrieval of the most relevant parameters related to the vibration of a target, including *when* they happen.

The mathematical definition of the wavelet transform of a continuous signal $x(t)$ (the CWT of $x(t)$)is written as

$$W(a,b) = \frac{1}{\sqrt{a}} \int_{-\infty}^{+\infty} x(t)\psi(\frac{t-b}{a})dt, \tag{4.1}$$

where $W(a,b)$ is the coefficient of the transform, a represents the dilation wavelet parameter, also called the *scale* of the transform, and b represents the translation wavelet parameter, also known as shift. The coefficient $W(a,b)$ is normalized by $1/\sqrt{a}$ to ensure that all the wavelets of the basis have the same energy at every scale [71]. The scale parameter a is inversely proportional to the frequency component of the analysed signal, while b is related to the time instance at which a frequency component is generated. The physical interpretation of Eq. (4.1) is that $W(a,b)$ is obtained by correlating the scaled and shifted version of a mother wavelet $\psi(t)$ with the signal under analysis $x(t)$. As a decreases, $\psi(T-b)/a$ is shrunk in time, so increasing the resolution in time comes at the expense of decreasing the resolution in frequency, and viceversa.

There exist a number of wavelet families and choosing the right one among them depends upon the application considered and the nature of the information to be extracted. For the methods and applications shown in this Thesis, the complex Morlet wavelet is used as the analysing mother wavelet, since it has shown very good results in the analysis of sinusoidal-like signals, a linear phase response, it exhibits symmetry, and has a dyadic nature (the frequency/scale of wavelet is changed in factors of 2) [71, 179]. Furthermore, it is shown that the use of complex wavelet coefficients allow the detection of fringes in an OFS as well as the envelope of its amplitude. The former is obtained by taking advantage of the correlation nature of wavelet based processing and the later taking advantage of the real and imaginary parts of the coefficients. The Morlet CWT is defined in the time domain as

$$\psi(t) = e^{i\omega_0 t}e^{\frac{-t^2}{2}}, \tag{4.2}$$
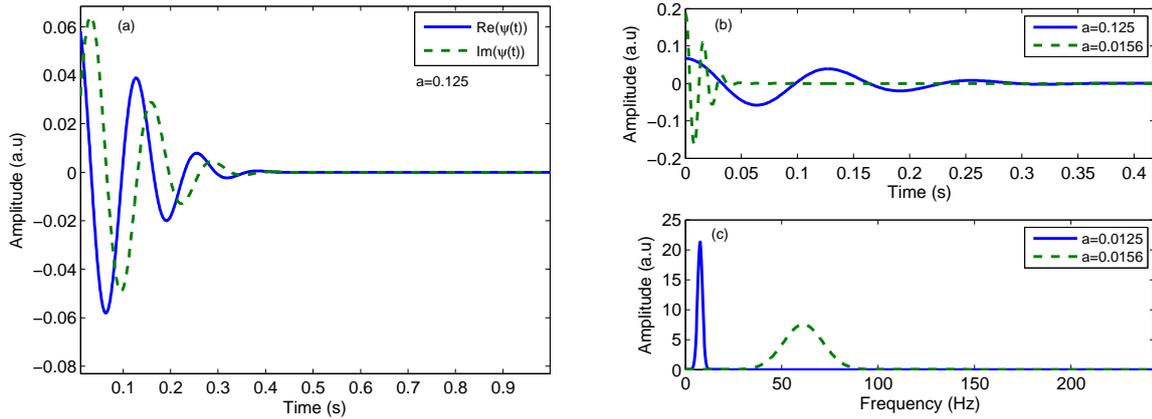
Figure 4.1: Concept of wavelet transformation using the Morlet wavelet. (a) Real and imaginary parts of the Morlet Wavelet ($\omega_0 = 6$ in Eq. (4.2)); (b) Effect of scaling in the time domain; (c) Effect of scaling in the frequency domain.

where the second term represents a rapidly decaying signal that constrains the sine and cosine of frequency ω_0 represented in the first term, to a limited time instance. Fig. 4.1 (a) shows the real and imaginary parts of the Morlet wavelet for a scale $a = 0.125$ and $\omega_0 = 6$ rad/s. (the choice of this value comes from the admissibility condition of wavelet, explained in following paragraphs). Fig. 4.1 (b) and 4.1 (c) show the effect of scaling the wavelet waveform in the time domain and in the frequency domain, respectively. By reducing the scale by a factor of 8, the wavelet in the time domain shrinks, while, from the time-frequency duality, its frequency is shifted to the higher part of the spectrum, thus having a higher bandwidth. Since the wavelet for a small scale (dashed line) changes rapidly and has a wider spectrum, it is suitable to extract information which varies rapidly with time but which does not change much with frequency. Inversely, at larger scale (solid line), the wavelet in the time domain is extended and its corresponding spectrum is much narrower. These properties are useful to extract information which varies rapidly with frequency, but not with time. Hence, depending upon the situation of either requiring high temporal or spectral resolution, the scale may be adjusted to better retrieve the desired information. This flexibility makes the wavelet transform advantageous when compared to classical Fourier transform, which use only sine and cosine as base functions.

In the frequency domain, the CWT is denoted as

$$\Psi(\omega) = \int_{-\infty}^{\infty} \psi(t) e^{-j\omega t} dt \tag{4.3}$$

$$= \sqrt{(2\pi)} e^{\frac{-(\omega - \omega_0)^2}{2}}. \tag{4.4}$$

The wavelet transformation converts 1D (time) signals to a 2D (time and frequency) plane. To retrieve back the 1D time-dependent signal, there should be no loss in information during the transformation. Thus, the condition of identity (equivalent to energy conservation, also known

86
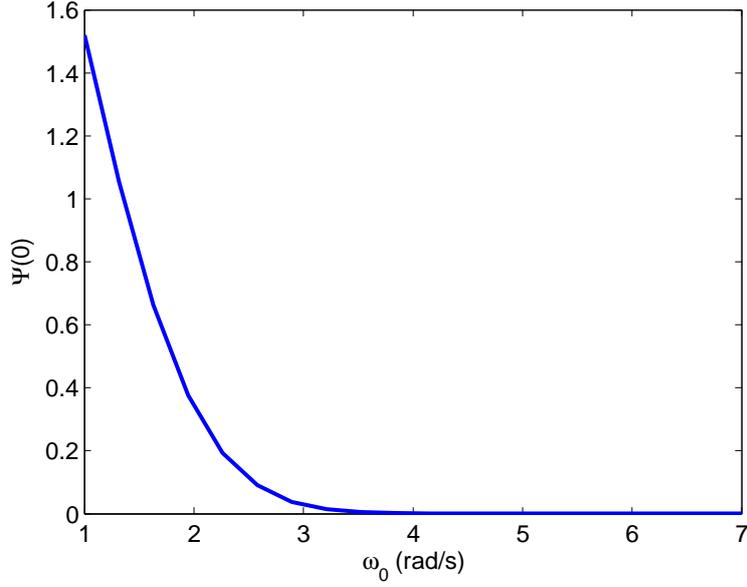
Figure 4.2: Admissibility condition for the Morlet wavelet.

as Parseval's equality) should be satisfied. This means the total energy in the 1D time domain should equal the total energy in the 2D (time-frequency) plane. It has been shown that in order to satisfy this condition [180],

$$\int_0^{+\infty} \frac{\mid \Psi(\omega) \mid^2}{\mid \omega \mid} d\omega < +\infty. \tag{4.5}$$

Eq. (4.5) is called the admissibility condition of a wavelet, which implies that the Fourier transform of the wavelet should be zero at zero frequency, i.e. a wavelet function is required not to have any DC component. Accoding to the admissibility condition,

$$\mid \Psi(\omega) \mid = 0 \quad at \quad \omega = 0 \tag{4.6}$$

This is the basis of the wavelet transformation, which suggests $\psi(t)$ to be a band-pass function which decays rapidly to zero as the frequency shifts towards zero (frequency localization). Equivalently, in the time domain, Eq. (4.6) can also be interpreted as a requirement on the wavelet to oscillate temporally, similar to a wave which needs to have zero mean value. Using the admissibility condition together with Eqs. (4.6) and (4.4) we get

$$\Psi(0) = \sqrt{2\pi} e^{\frac{-\omega_0^2}{2}}. \tag{4.7}$$

The value of $\Psi(0)$ at different values of ω_0 for the Morlet wavelet described in Eq. (4.7) is shown in Fig. 4.2. Hence, the value at which the admissibility condition $\omega_0(0) = 0$ is fulfilled is $\omega_0 \geqslant 5$. Along the remaining of the signal processing in this Chapter, ω_0 has been chosen to be 6, as it is the minimum value required to accomplish the admissibility condition.
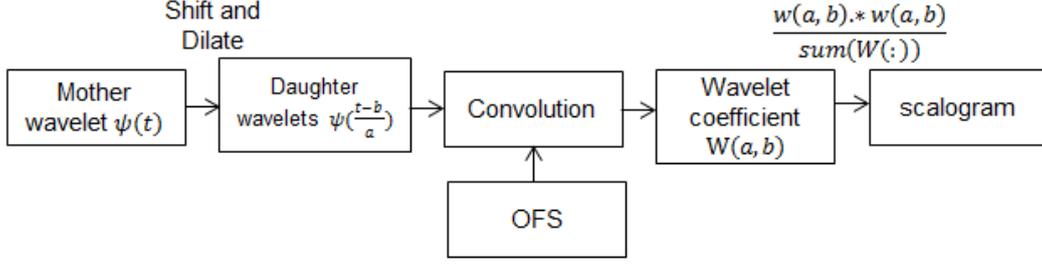
Figure 4.3: Flow of the signal processing procedure of OFS using wavelets.

Figure 4.4: Time-frequency plane evolved from wavelet transformation.

The use of the wavelet transform for processing the OFS presents a number of advantages over traditional derivative-based peak detection methods. For instance, it allows noise removal and detection of OF relevant parameters in the same processing step. Once the basics of the CWT have been explained in Sec. 4.2, the flow of the algorithm used to process the OFS is shown in Fig. 4.3. Such flow is described in the following steps.

1. A mother wavelet shapep ψ is chosen considering the type of signal to be anlyzed. As commented, Morlet is well suited to the OFS.

2. While time is kept constant (e.g. $a = 0$), the scale is varied as $a=a_j$ with $j = 0, 1, 2...J\text{-}1$. The total number of scale values (J) is given by Eq. (4.8). This process generates a series of daughter wavelets by a dilation process of the mother wavelet. Then the OFS under analysis $x(t)$ is convolved with each of the daughter wavelets resulting in wavelet coefficients at all scales at the particular time instance described by $b = 0$. This yields the first column of coefficients in the matrix depicted in Fig. 4.4 ($W(a = \{a_j\}, b = 0)$).

3. Next, time is incremented by a given amount (let us call it dt) so $b=b+dt$ (shift), and again the scale is varied from $a=a_j$, $j = 0, 1, 2...J\text{-}1$ (dilate), so now the mother wavelet is both shifted and dilated. Similarly to Step 2, the OF signal $x(t)$ is now convolved with each of the shifted and dilated daughter wavelets, resulting in another series of wavelet

coefficients at all scales and at a particular time instance, which constitutes the second column in Fig. 4.4 ($W(a=\{a_j\},b = dt)$).

4. Step 3 is performed for all the time instances remaining ((N-1)dt), obtaining in the end a matrix of wavelet coefficients ($W(a = \{a_j\},b=\{b_k\})$), where columns give information about the OFS at all scales (frequency components) at a particular instance of time, while rows give information about how each particular frequency components has evolved with time.

Taking advantage of the dyadic nature of wavelet based signal processing, the entire processing of a typical OFS takes only a few seconds. However, obviously the duration of the signal processing stage depends upon the computing resources available.

4.3 ANALYSIS OF A PERIODIC VIBRATION

In this section, a novel algorithm based on the CWT detailed in Sec. 4.2 is implemented to process to OFS resulting from the periodic vibration of a target, to show the abilities of the CWT to denoise, track down speckle, and extract the vibration parameters, namely velocity, displacement and frequency in a single processing step. In addition to the traditional FC method to detect the fringes and compute displacement, taking advantage of the complex nature of the Morlet wavelet, PUM is also implemented resulting in a reduced error in displacement retrieval.

4.3.1 EXPERIMENTAL SETUP

The setup in Fig. 4.5 (a) is used as experimental arrangement in the following Sections. A multiple quantum well InGaAsP Hitachi HL6501 laser with a 0.65 μm band was used. The emission wavelength measured using an Instrument System's SPECTRO 320(D) R5 was $\lambda = 692.5$ nm. The signal emitted by the laser was focused using a 352240-B Thorlabs aspheric lens with a fixed focal length of 8 mm and a numerical aperture of 0.5 mm. The lens was placed at a distance of 3.5 mm from the laser. A piezoelectric stage LISA P753.3CD with a maximum travel length of 38 μm (3.8 μm/V) was used as a target. The stage includes an embedded capacitive sensor with a resolution of 0.2 nm [4] which is used as a reference to compare with the obtained results. The target was placed at a distance of 12 cm from the laser, in the configuration presented in Fig. 4.5 (a). During the experiments, the target was vibrated by applying both a triangular and a sinusoidal signal with amplitude ($V_v(pp)$) = 2 V and a frequency $f_t = 10$ Hz for both of them. The OFS was retrieved using a Tektronix DPO2024B oscilloscope (Fig. 4.5 (b)). After the CWT based signal processing, the measured displacement was compared with the measurements of the capacitive sensor embedded in the piezoelectric stage [4]. The experimental parameters are summarized in Table 4.1. Equivalent conditions and parameters were applied for obtaining a sinusoidal motion of the target.
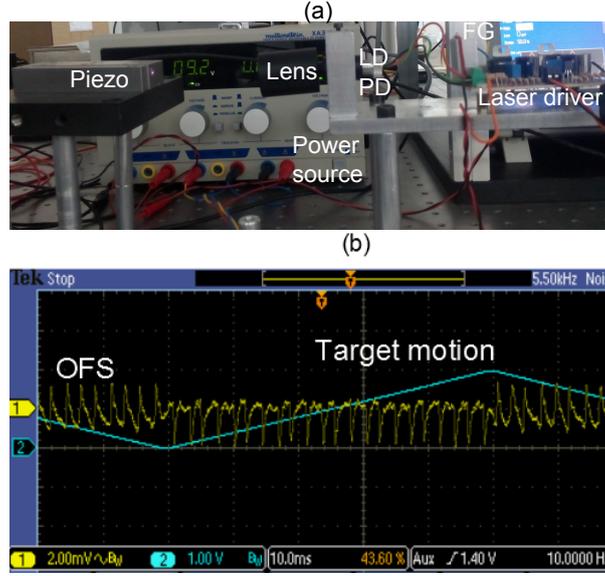
Figure 4.5: Experimental arrangement for OF based vibrometry. (a) Experimental setup. FG - Function generator. (b) Experimental OFS resulting from a triangular target displacement retrieved in the oscilloscope.

Table 4.1: Experimental parameters of the vibrometry setup used.

Parameters	Value
Distance to external target from the laser (L_{ext})	12 cm
Voltage applied to Piezo (V_v (pp))	2 V
Target vibration amplitude (A_t (pp))	7.6 μm
Target vibration frequency (f_t)	10 Hz
Operating point of laser (I_{op})	45 mA
Emission wavelength of laser (λ)	692.5 nm
Sampling time (dt)	8 μs
Sampling frequency (f_s)	125 kHz

4.3.2 METHODOLOGY

A flowchart diagram of the implemented processing method is depicted in Fig. 4.6. CWT, using Morlet as the analyzing wavelet, is first applied to the acquired OFS. Due to the dyadic nature of the Morlet [179], it is computationally efficient to choose a as powers of 2 given by

$$a_j = a_0 2^{jdj}, \quad j = 0, 1, 2...J - 1 \tag{4.8}$$

where a_0 is the smallest resolvable scale, which is set to the inverse of the Nyquist frequency, and dj is an increment in scale related to the expansion of the mother wavelet. To balance the resolution and computing time, it was chosen to be 1/8. The total scale J can be found out by setting the frequency range ($f_R = f_{max}$ - f_{min}) to be analysed, which determines the number

90
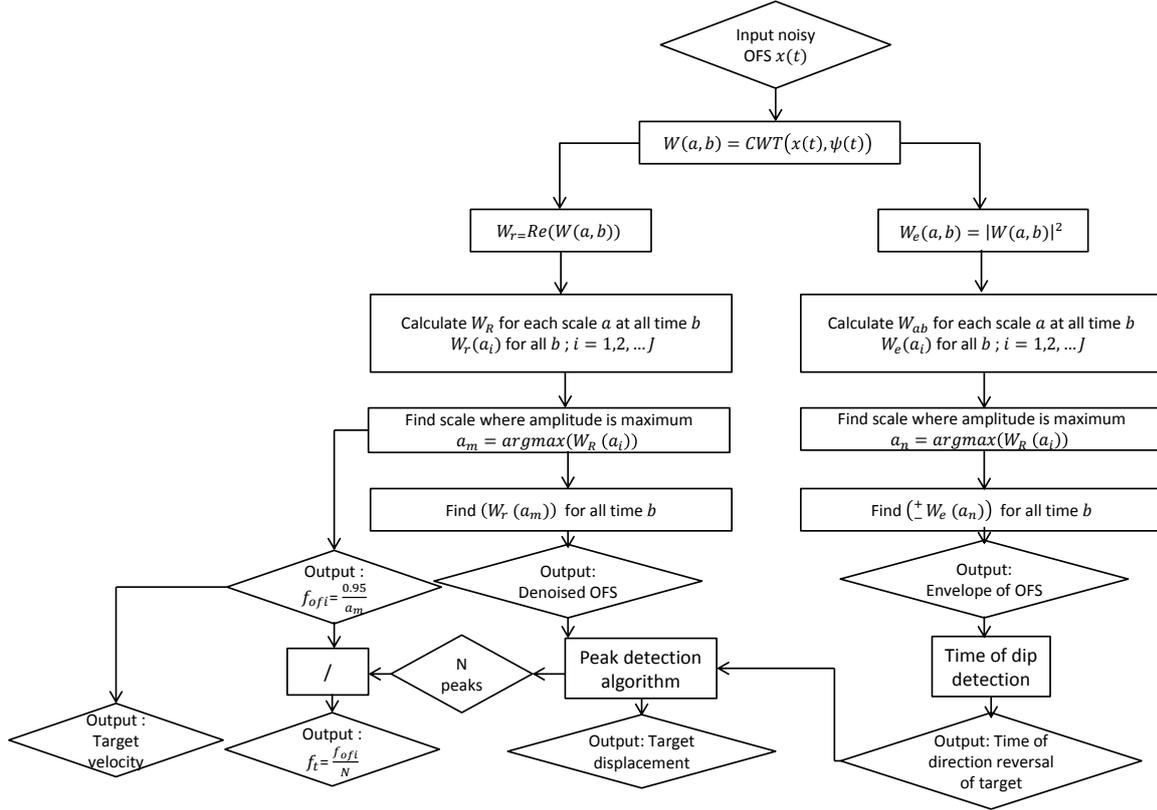
Figure 4.6: Flowchart diagram for parameter extraction of the parameters vibrating target using wavelets.

of resulting octaves (N_0)

$$J = \frac{N_o}{dj} = \frac{1}{dj}\log_2\left(\frac{f_{max}}{f_{min}}\right), \tag{4.9}$$

where f_{max} and f_{min} are the maximum and minimum analysed frequencies. An appropriate range of octaves and scales depends on the spectral content of the analysed signal, the highest requested CWT frequency and dj. Here, the maximum CWT frequency is selected to be equal to Nyquist frequency and frequency of analyzing mother wavelet to be $f_0 = \omega_0\ /(2\pi)$ where ω_0 is set to 6, as discussed in Sec. 4.2. The frequency f_a corresponding to a scale a is related to the central frequency f_0 of the wavelet by

$$f_a = \frac{f_0}{a} = \frac{0.95}{a}. \tag{4.10}$$

A summary of the wavelet parameters used for OFS analysis is presented in Table 4.2. After computing the CWT of the OFS (presented in Fig. 4.7 (a)) resulting from the triangular motion of the target under test (Fig. 4.7 (b)), the real part of $W(a,b)$ (further on noted as $W_r(a,b)$) is plotted in order to visualize the spatial and temporal components of the OFS (Fig. 4.8 (b)). The Doppler shift introduced in the signal by the target motion is then easily estimated using the maximum value of a, noted as a_{ofi}, shown in the scalogram presented in Fig. 4.9. This

91

Table 4.2: Wavelet parameters for analysing OFS.

Parameters	Value
Choice of wavelet	Morlet
Center frequency (ω_0)	6 rad/s
Minimum resolvable scale (a_0)	1.6×10^{-5}
Maximum frequency in CWT (f_{max})	62500 Hz
Scale increment (dj)	1/8
Total number of scale (J)	128

Doppler shift is related to the velocity of the target from Eq. (4.11). Thus, $W_r(a_{ofi}, b)$ is plotted for all time b, resulting in practice in a denoised OFS for the dominant scale. This waveform (Fig. 4.10) is used as the basis for the computation of target displacement. Similarly, from the squared complex amplitude of $W(a_{ofi}, b)$ i.e. $\pm W_e(a_{ofi}, b)$, the OFS envelope is obtained (Fig. 4.10 (solid black line)). The signal envelope becomes relevant as it allows the determination of the time instance at which the target changes its direction, showing singular time-dependent events which may be characterized using the information in the CWT. In addition, the envelope also helps track the speckle as well. Each fringe on $W_r(a_{ofi}, b)$ (represented by a solid blue line in Fig. 4.10) corresponds to a target displacement of $\lambda/2$. The presence of a dip in the signal envelope is interpreted as a change in the direction of the target, thus allowing to count all the fringes between two dips as displacements in the same direction. Hence, by counting the total number of fringes it is possible to estimate the target displacement and its trajectory. Finally, the vibration frequency is calculated by dividing the obtained Doppler frequency by the total number of fringes in one period of the acquired OFS as shown in Eq. (4.11).

4.3.3 RESULTS

In this subsection the methodology proposed above regarding the application of the CWT to an experimental OFS is explained in detail. Such an application is used as an example to show the potential of CWT in processing the OFS. The methodology used for extracting the different parameters from the OFS is discussed in detail, with an individual paragraph for each parameter.

TARGET VELOCITY

Once the OFS (Fig. 4.7 (a)) resulting from the target vibration (Fig. 4.7 (b)) is acquired, a CWT is applied as signal processing strategy. The wavelet coefficients $W_r(a,b)$ and the corresponding scalogram in frequency and time domains are then obtained by using $W_r^*W_r/\sum W(a)$ and shown in Fig. 4.8 (b) (the OFS is also shown in 4.8 (a) for clarity and to visualize the different frequency components generated at different instance of target motion). As mentioned
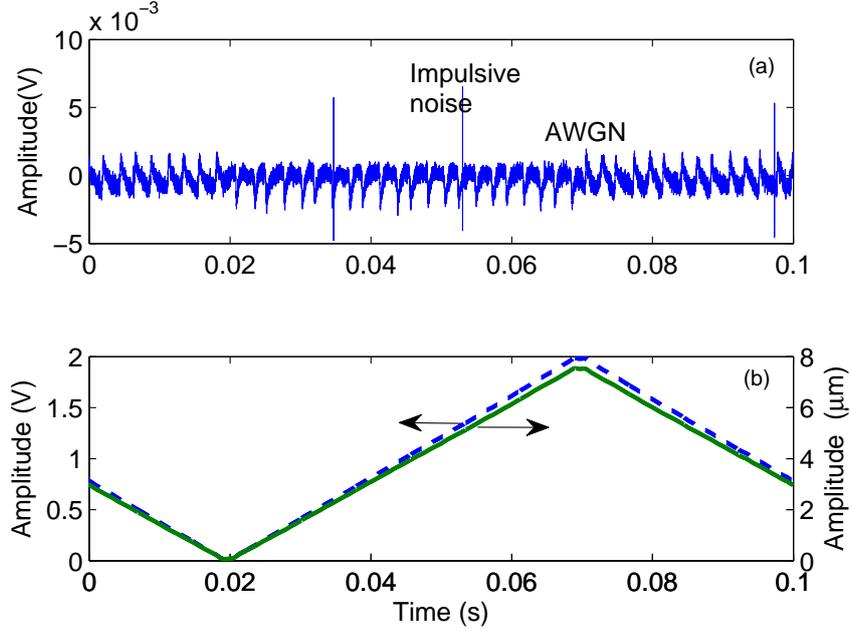
Figure 4.7: OFS and vibration reconstruction resulting from a triangular-shaped periodic vibration of the target. (a) Acquired OFS resulting from target vibration. (b) Voltage applied to the piezoelectric target (dotted line) and measured target motion (solid line) with the embedded capacitive sensor [4] used as reference.

above, the scalogram shows the fraction of energy contained by each given frequency component at a particular time instance in the OFS. It is also evident from the described approach that the energy components of the noisy OFS signal are localized at a particular scale, which is used to retrieve the information about the dominant frequency that it contains. Fig. 4.9 shows $W_r(a,b)$ as a function of scale. The maximum value of W_r is found at $a = a_{ofi} = 0.002125$. Using Eq. (4.10), the dominant frequency in the OFS is $f_{ofi} = 447.1$ Hz. This value can be used to obtain the velocity of the vibrating target using the Doppler shift property which relates target velocity and frequency using

$$f_D = \frac{2v_t}{\lambda}, \tag{4.11}$$

where f_D is the Doppler shift, v_t is the target velocity and λ is the emission wavelength. Substituting f_D with f_{ofi} in Eq. (4.11) and using λ from Table 4.1, the target velocity obtained results in $v_t = 0.15$ mm/s. This is in good agreement with the target velocity calculated from Fig. 4.7, as the target moves linearly 7.6 μm in 0.05 s, resulting in a velocity of 0.15 mm/s. Further, the saclogram also contains the information related to the moment of time reversal of the target motion, determined by the sharp decrease in the magnitude of the wavelet coefficients. In addition, this contrast in amplitude in the wavelet coefficient, as evident from the scalogram, is used in the following sections to find the envelope of OFS with speckle tracking purposes.

SIGNAL DENOISING

A typical experimental OFS contains both white and impulsive noise, as can be seen also in the
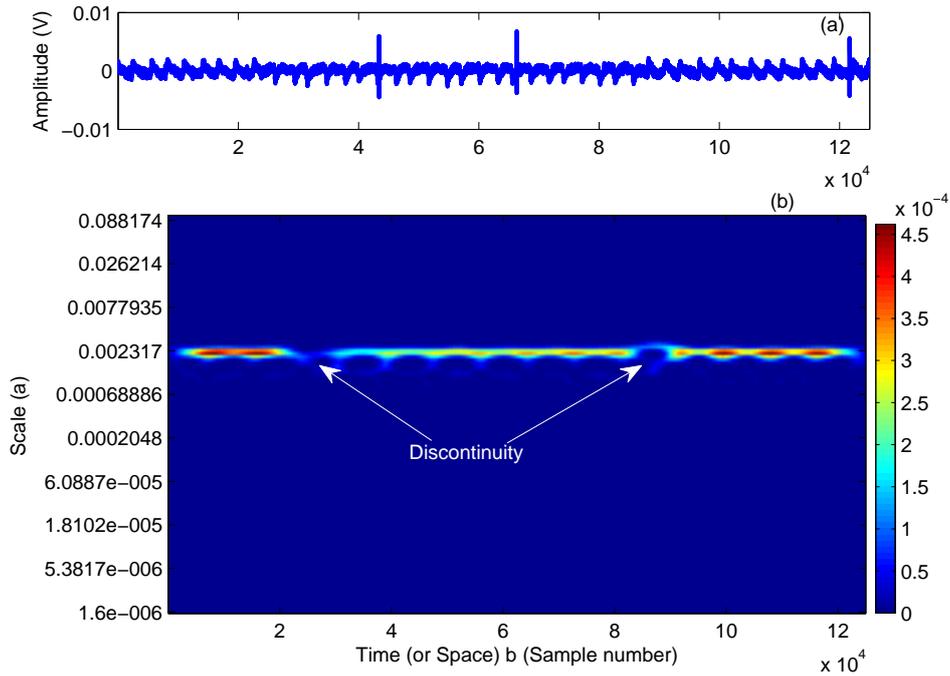
Figure 4.8: CWT of the OFS described in the text after CWT. (a) Acquired OFS obtained from a triangular displacement. (b) Scalogram of W_e. The presence of a clear dominant frequency and the detection of discontinuities at given moments in time due to velocity reversal is observed.

example proposed. White noise is usually removed using low-pass filtering, while for impulsive noise a median filter is used [67] [68]. The use of the CWT enables to remove the effect of noise in the signal in a more efficient way, since it avoids the need of using two different filters and the associated signal processing steps. This is used to reduce the computational cost and the time duration of the signal processing stage. As seen, the CWT is in essence a correlation between a scaled and shifted mother wavelet and the OFS. Since noise itself is uncorrelated to the OFS, the resulting wavelet coefficients corresponding to noise are lower in magnitude than those corresponding to the signal. In order to retrieve the denoised OFS, $W_r(a_{ofi},b)$ is plotted and shown in Fig. 4.10 (solid blue). As it can be seen, not only white and impulsive noise have been removed in a single step, but also signal processing and peak detection have been notably simplified. The effectiveness of wavelets being able to filter both types of noise at once is also demonstrated in Sec. 4.3.4.

ENVELOPE DETECTION

Speckle is an unwanted intensity modulation of the laser caused because of the finite size of the laser spot when irregularities greater than $\lambda/2$ are present in the surface of the target, as discussed before. Such irregularities can cause the laser beam to add field amplitude constructively or destructively when dispersed, resulting in a significant increase or decrease of the amplitude

94
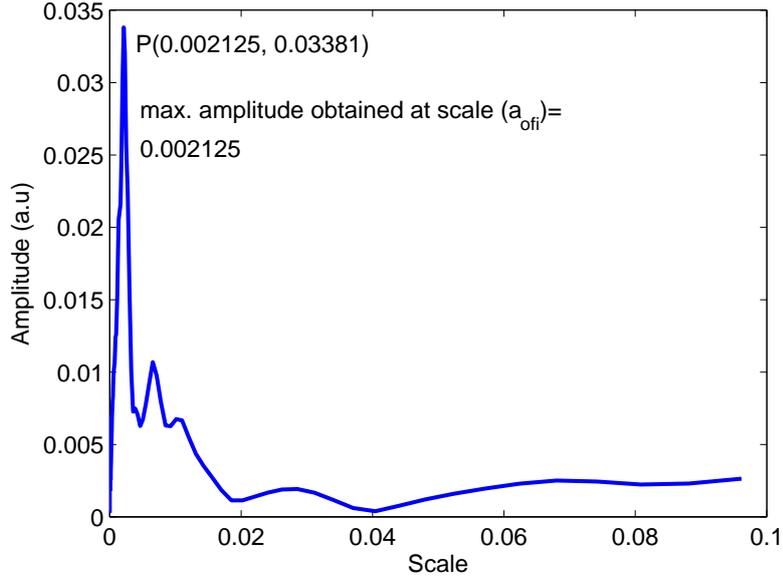
Figure 4.9: Amplitude changes in the dominant scale in the OFS signal. Real part of the complex wavelet coefficient plotted against scale value ($W_r(a_{ofi},b)$). At $a = a_{ofi} = 0.002125$, W_r a maximum showing the dominant frequency component is seen $f_{ofi} = 447.1$ Hz.

of the OFS which is detected. Given destructive interference due to speckle becomes dominant, the signal processing stage to detect the fringes becomes extremely difficult to implement accurately, as there are serious chances that some fringes go undetected, which turns into errors
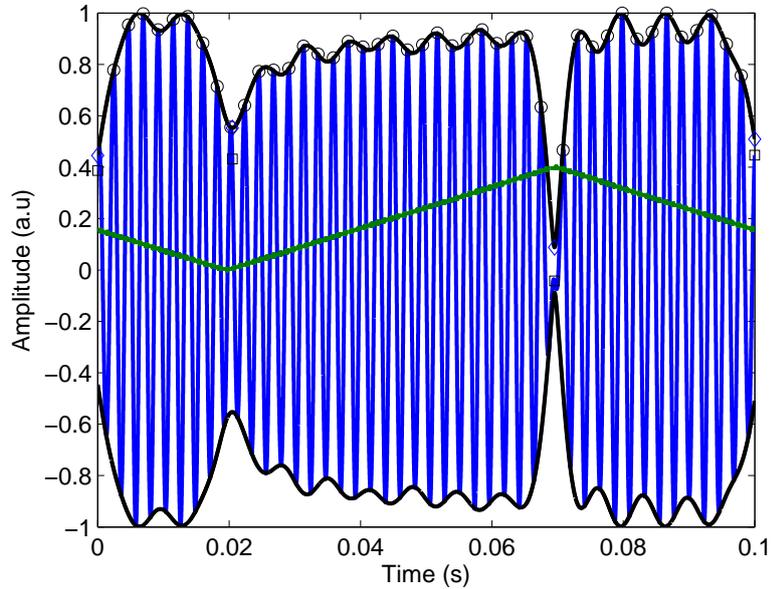
Figure 4.10: Signal processing of OFS. Envelope detection W_e (dark black); Denoised OFS (blue). Detected fringes (circle); Time instance of direction change (square); Scaled target motion (green) (original target motion (pp) is 7.6 μm and shown in Fig. 4.7 (b)).

95
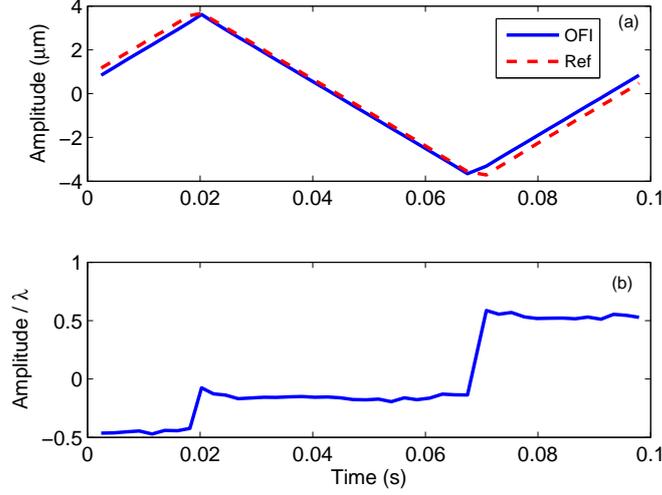
Figure 4.11: Target displacement retrieved using CWT: (a) Target displacement obtained from OFI compared with reference embedded capacitive sensor [4]. (b) Differences between OFI-based and embedded capacitive sensor measurements.

in target displacement reconstruction. Speckle is consubstantial to OFI due to its experimental conditions, with a coherent beam shone onto a rough target. Details on different features of speckle affecting the OFS can be found in [167]. To correctly detect and localize fringes, by keeping track of speckle-induced fluctuations in signal amplitude the envelope of the OFS is calculated using the square of the CWT magnitude ($W_e=|W(a,b)|^2$).

This envelope detection of OFS helps to follow its fading due to speckle enabling to apply some alternative compensation techniques [10], but it also enables to determine the time instance when the target motion reverses its direction. Because of the wavelet correlation properties, when a target changes its displacement direction the magnitude of the signal correlation decreases, resulting in lower wavelet coefficients which produce large fluctuations presented in black solid in Fig. 4.10. Envelope detection can then be used to determine the instant of time when there is a change in the direction of the target. Whenever the target motion[2] (green) in Fig. 4.10 reaches its maximum or minimum position, a rapid decrease of the magnitude of the envelope is detected. By calculating the time instance of this minimum, it is possible to identify the time at which the target changed its direction. In Fig. 4.10, the direction change is noted by the squares on the de-noised OFS. The circles, in the same figure, represent the time instance of the detected OF fringes.

TARGET DISPLACEMENT: FC METHOD

After denoising the OFS and detecting the time instance when target direction reverses, the next step is to calculate the displacement of the moving target. In this case, the peaks correspond

---

[2]the scaled version is used for clarity. The original target motion is shown in Fig. 4.7 (b)

to the displacement of $\lambda/2$ [50] for each direction, and they are easily counted following the traditional FC method of OFI, allowing the reconstruction of the displacement of the target with time. Since the OFS is almost symmetric, a simple fringe detection algorithm is implemented.

In the experiment, the fringes were detected properly (Fig. 4.10) and the target displacement was retrieved and compared against the signal in the embedded reference capacitive sensor of the piezoelectric stage (Fig. 4.11 (a)). This resulted in an absolute error value close to 0.6λ at the transitions, and around 0.1λ elsewhere (Fig. 4.11 (b)). It should be noted that using the FC method in a triangular-shaped signal introduces significant uncertainty and errors in the moment when the reversal of the movement happens (in addition, see Fig. 4.21 for appreciating the abrupt phase change in OFS at the transition).
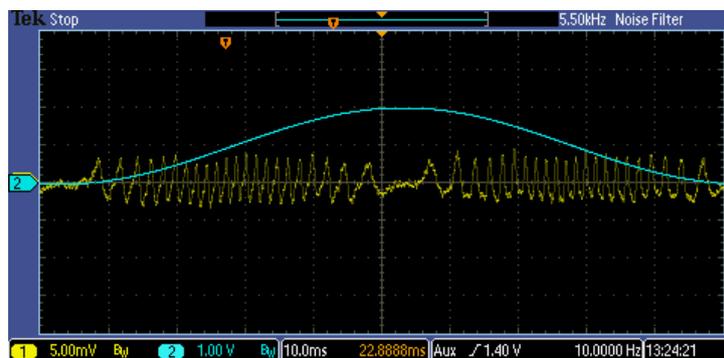
Figure 4.12: Experimental OFS resulting from sinusoidal target motion.
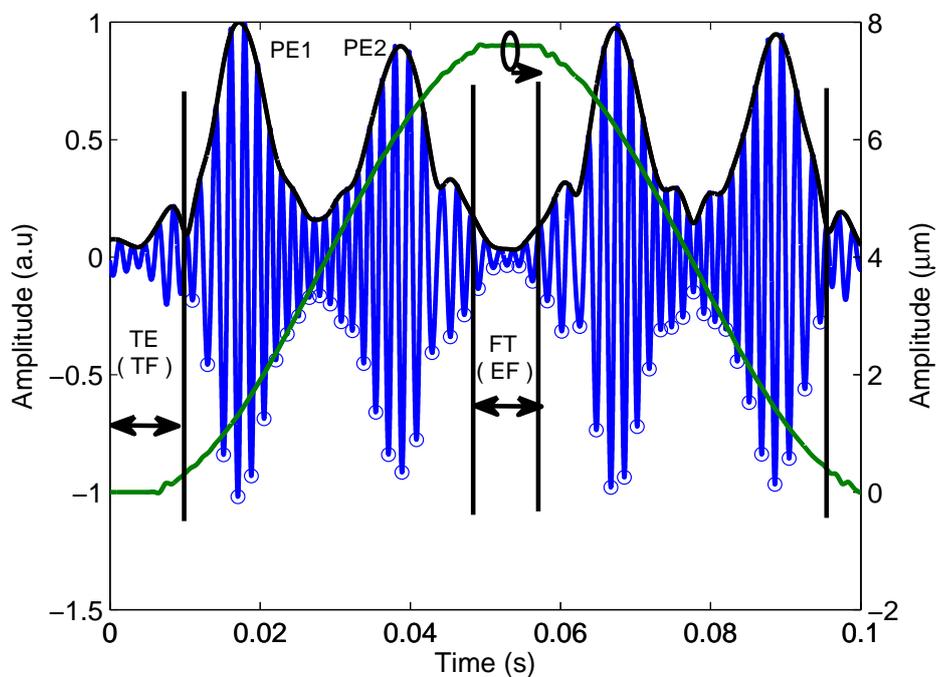
Figure 4.13: Different regions of the de-noised OFS and its envelope for a sinusoidal displacement of the target.

To validate the feasibility of the approach, an equivalent analysis was performed using a sinusoidal displacement of the target for comparison. Using the parameters presented in Table 4.1 the OFS shown in Fig. 4.12 was obtained. In the case of the triangular motion the change in direction occurs abruptly, causing a narrow dip in the envelope of the signal as shown in Fig. 4.10. However, in the case of a sinusoidal motion along the sine flat top region no sharp movement change happens, so the transition time is not localized and there exists a finite time interval along which the transition in direction of movement occurs. As a consequence, the particular instant in time when the reversal of direction happens is not so easy to determine. Such differences in temporal behaviour between sinusoidal and triangular motions are detected by the wavelet transform. The denoised OFS and its corresponding envelope for a sinusoidal target motion are shown in Fig. 4.13. There are a number of relevant conclusions that can be extracted from the analysis of the envelope of the signal. First, the presence of a dip in the center corresponds to a discontinuity in the target motion.

In order to continue the discussion let us denote the region corresponding to the sinusoidal movement reversal as the "flat top region" (FT), and the fringes inside the FT region as "error fringes" (EF). Such EF are very low in amplitude and can be eliminated using a proper threshold filter. They are due to computational error. At the top, the target is stationary, so there should be no fringes. The fringes appearing are due to numerical errors i.e. the wavelet coefficient should be zero, but in practice, the wavelet coefficients only tend to zero, but not reach it absolutely. It is possible to detect two pulsed envelope zones ($PE1,PE2$), symmetric about FT (along the rise and fall slopes of the target motion), where OFI fringes are present. All the fringes in this region contribute to the calculation of target displacement. Also, the envelope contains a tail at the edge denoted as the tail envelope (TE) with its corresponding tail fringes (TF), which, as in the case of EF, are not considered for displacement reconstruction as they represent the end or the beginning of a new cycle. A "discontinuity" at the tail denotes the fact that the slope of the movement of the target has significantly increased to cause effective fringes. The displacement reconstruction and its comparison with the reference sensor of the piezoelectric stage for the proposed experiment are shown in Fig. 4.14. As observed, the resulting error is within 0.2λ with a mean error of just 0.1λ in the full signal, showing the problems in the reconstruction of the triangular signal were much due to the uncertainty in fringe calculation introduced due to the sharp displacement transition.

FREQUENCY OF VIBRATION OF THE TARGET

Once the target displacement has been retrieved, a Fourier transform of the displacement profile can be used to obtain the frequency of the target vibration f_t. However, this is an indirect method for calculating the aforementioned frequency. There are several situations (e.g. in condition monitoring of vibrating objects) in which frequency is more relevant than displacement. In such cases, it is possible to attain directly the frequency f_t of a vibrating object dividing the
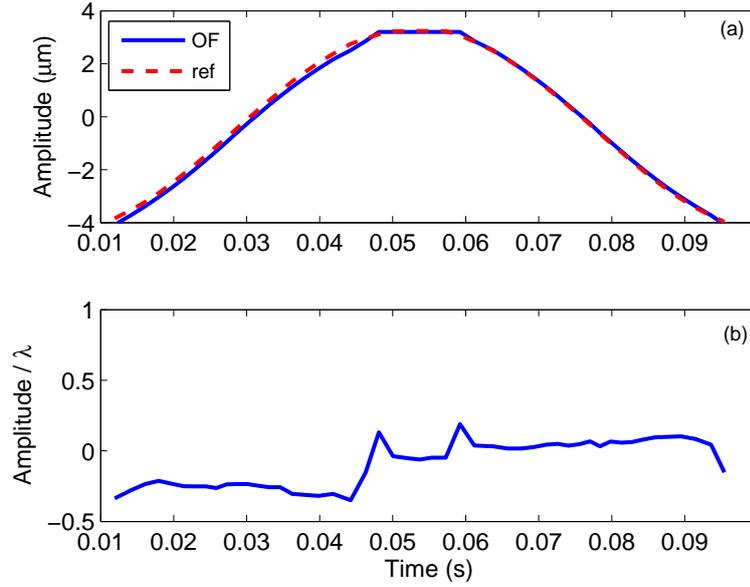
Figure 4.14: Displacement reconstruction for a sinusoidal movement of the target: (a) Retrieved target displacement using OFI compared with the embedded reference capacitive sensor [4]. (b) Resultant error within 0.2λ (average error of 0.1λ) obtained from the difference in the OFI and reference sensor in (a).

f_{ofi} by the number of fringes in one period of target motion N_f expressed as

$$f_t = \frac{f_{ofi}}{N_f}. \tag{4.12}$$

Using the previously calculated values for the triangular motion $f_{ofi} = 447.1$ Hz and $N_f = 43$, the target vibration frequency is estimated to be $f_t = 10.4$ Hz which is equal to the original target vibration frequency mentioned in Table 4.1. A similar analysis was performed using the Fourier transform method obtaining $f_t = 10.0$ Hz. Thus, the wavelet based approach is consistent with Fourier analysis and with experimental data.

4.3.4 TARGET DISPLACEMENT: WAVELET-BASED PUM

Two general-purpose methods are usually considered to retrieve the target displacement from OFS: the FC method already discussed, and the phase unwrapping method (PUM) [12]. In the FC method discussed in Sec. 4.3.3 it was shown how the real part of the complex coefficients calculated using the CWT were used to detect the fringes and to retrieve the displacement of the target. The information contained in the imaginary part of the coefficients, however, remained unused. In this Section, we make use of the complete information of the wavelet transformation by taking into account the imaginary part of the wavelet coefficients together with the real part, in order to obtain the phase angle of the OFS. The use of the complex plane (real and imaginary coefficients) resulting from the wavelet analysis of OFS with the complex Morlet wavelet as analyzing wavelet for target displacement using PUM is demonstrated, and its

99

Table 4.3: Experimental parameters for wavelet-based PUM displacement reconstruction.

Parameters	Value
Distance of external target to the laser (L_{ext})	12 cm
Voltage applied to Piezo used as target ($V_v(pp)$)	3 V
Amplitude of vibration of the target (peak) (A_t (pp))	11.4 μm
Frequency of vibration of the target (f_t)	10 Hz
Operating point of the laser (I_{op})	45 mA
Emission wavelength of the laser (λ)	692.5 nm

performance compared with the results of the FC method. A very relevant advantage of PUM is the larger number of sample points (determined by the acquisition device) to reconstruct the target displacement as compared to number of sampling points, limited by the emission wavelength, in the former case.

In order to further explore the capabilities of the CWT for removing AWGN and impulse noise to determine the target vibration profile, it is now desired to acquire a very noisy signal, which contains both types of noise, and to process the OFS using PUM to extract the key parameters of the displacement of the target. A setup equivalent to that in Fig. 4.5 (a) in Sec. 4.3.1 is used for the experiment. The piezo is vibrated using a triangular signal with amplitude (V_v (pp)) of 3 V and frequency 10 Hz from a general purpose signal generator. This results in a target motion with peak to peak amplitude of 11.4 μm. The CWT processing combined with PUM will be applied and compared to the measurements of the reference capacitive sensor embedded in the piezoelectric stage, as in the previous analysis [4]. Experimental parameters are summarized in Table 4.3. The acquired OFS due to target motion is shown in Fig. 4.15 (a), while Fig. 4.15 (b) shows the reference signal in voltage applied to the piezo, which results in a displacement of amplitude 11.4 μm and frequency 10 Hz. The information on target motion is contained in the OFS, but is embedded within an envelope of AWGN and impulsive noise. Instead of the conventional approach using an averaging filter to remove AWGN and a median filter to remove impulsive noise [67, 68], the CWT method alone deals properly with both of them simultaneously and extracts the relevant parameters of target motion.

As a first step, the CWT is performed upon the noisy OFS shown in Fig. 4.16 (a) in order to get the complex coefficients $W(a,b)$ (Fig. 4.16 (a) is same as Fig. 4.15 (a). It is repeated here for ease of visualizing the scalogram and correlate it with the target motion). Fig. 4.16 (b) shows the complete scalogram with all the scaled and shifted wavelet coefficients obtained. The figure shows a clear dominant scale (a_{ofi}) which contains the frequency information of the OFS. Fig. 4.17 shows the changes in the dominant scale $a_{ofi} = 0.0014$, which corresponds to a frequency of 578.5 Hz from Eq. (4.10). The real part of the complex wavelet coefficient at scale $a=a_{ofi}$ and at all time instances $W_r(a_{ofi},b)$ is plotted in Fig. 4.18 (a) to get the 1-D denoised
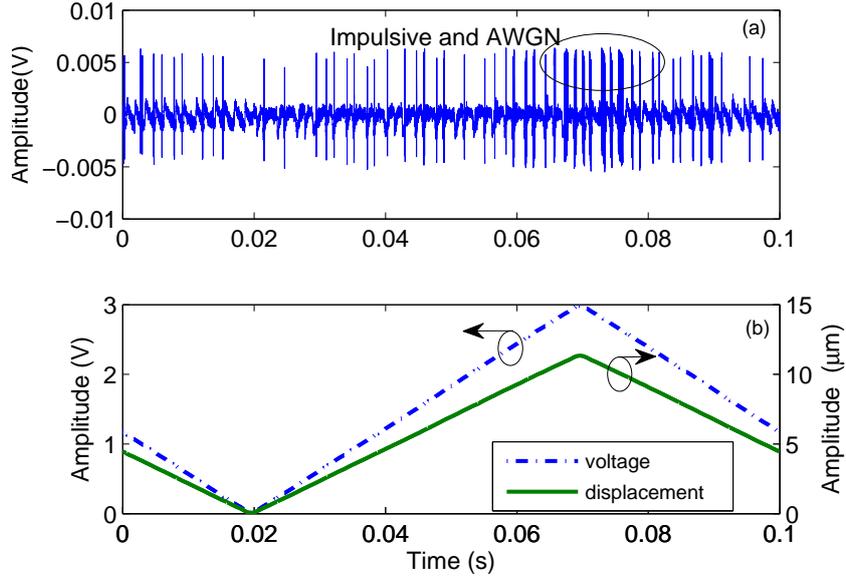
Figure 4.15: Experimental results for the measurement of the vibration of the target: (a) OFS showing relevant levels of both impulsive and AWGN noise. (b) Reference amplitude and frequency of vibration as a result of the voltage applied to the target. Amplitude is measured using the embedded capacitive sensor [4].

OFS, which contains the temporal and spatial information of the target motion.

It is evident that the strength of using the CWT lies in the fact that in a single shot it can denoise the experimental OFS, preserve the information content and convert a noisy OFS (Fig. 4.15 (a)) into a clean Fig. 4.18 (a) which enables an easy and precise fringe counting procedure. The denoised OFS is symmetrical around y-axis, so using a simple threshold fringe counting method, the number of fringes from Fig. 4.18 (a) can be easily counted (Fig. 4.18 (b)), so the determination of the motion of the target is set (Fig. 4.19 (a)). The error signal from the difference between the measurements of the OF sensor and the reference is shown in Fig. 4.19 (b). It is observed that most of the time error signal lie in between $\pm \lambda/2$, except at the transition point where the error signal exceeds $\lambda/2$.

FC method has thus been shown to be limited to a coarse resolution of $\lambda/2$. However, the complex nature of the wavelet coefficient can be used to unwrap the phase and to compute the target displacement with an enhanced resolution well below that value. The phase of the complex wavelet coefficient is given by

$$\phi(b) = tan^{-1}[\frac{W_i(a_{ofi}, b)}{W_r(a_{ofi}, b)}], \tag{4.13}$$

where $W_r(a_{ofi},b)$ and $W_i(a_{ofi},b)$ are the real and imaginary parts of the complex wavelet coefficient obtained at the dominant scale a_{ofi}. Further, the phase of the OFS is related to the target displacement as a function of time b $(A_t(b))$ by

$$\phi(b) = \frac{4\pi A_t(b)}{\lambda}. \tag{4.14}$$

101
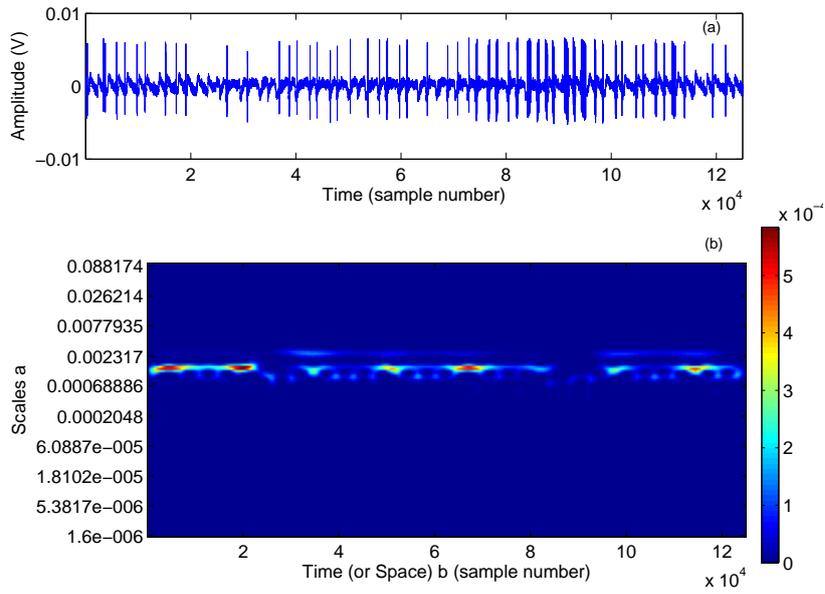
Figure 4.16: Time frequency plane resulting from Wavelet analysis. (a) Acquired OFS with impulsive and white noise. (b) Scalogram of absolute value squared of complex coefficients.
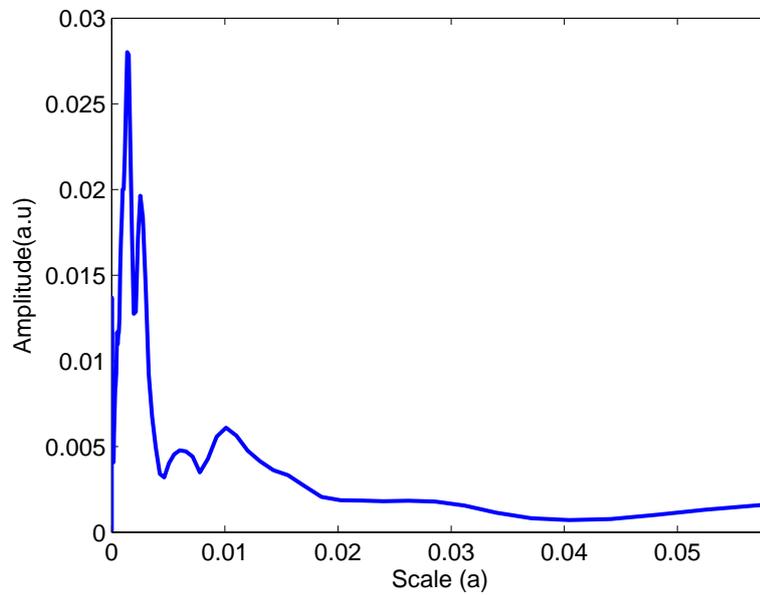
Figure 4.17: Dominant scale in the scalogram in Fig. 4.16, corresponding to $a_{ofi} = 0.0014$, and a frequency of 678.5 Hz.
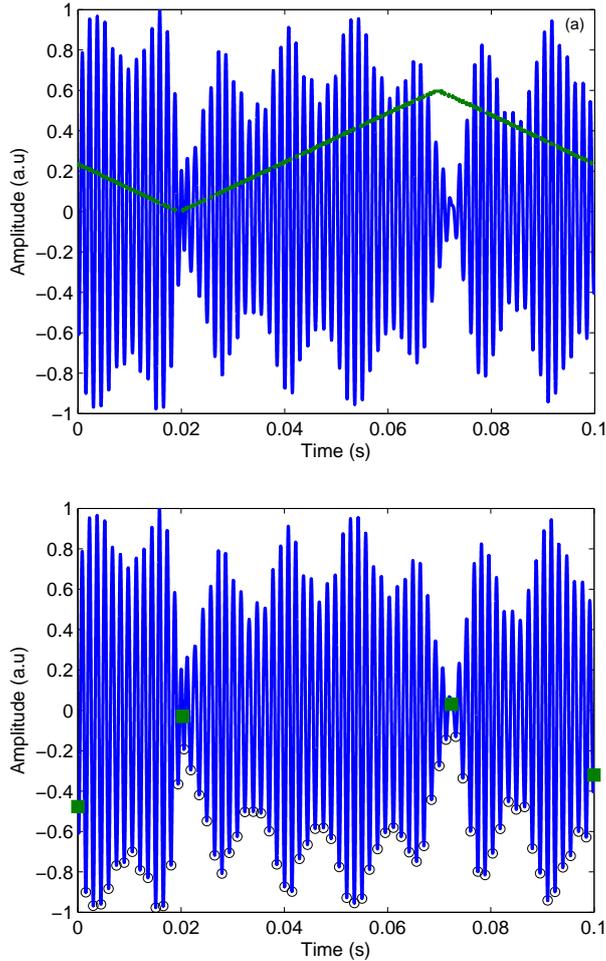
Figure 4.18: Intermediate stages for retrieving target displacement. (a) Denoised OFS ($W_r(a_{ofi},b)$). (b) Fringes detected (as circles). Time instance of a transition is determined by a sudden "dip" (as filled squares).

Fig. 4.20 (a) shows the wrapped phase, the unwrapped phase (Fig. 4.20 (b) (dashed line)), and the equivalent unwrapped displacement of target motion (Fig. 4.20 (b) (solid line)). The reconstructed target motion obtained is shown in Fig. 4.20 (c) compared with the reference signal from the embedded capacitive sensor [4]. The error signal shown in 4.20 (d) is the difference between the reference and the measurements based on OFI sensors. It is limited to a $\pm 0.2\lambda$ maximum value, which only appears at the edges or at the time instance when the target makes a reversal in the direction of the movement.

Such error magnitude, however, is not attributable to poor signal processing, but to the nature of the target motion itself. In the moment when the target reverses its direction, it induces brand new spectral content in the signal (as presented in Fig. 4.16 (b)). This causes the abrupt change in phase shown in Fig. 4.21. such a sensitivity of the phase of the signal to abrupt changes when the target changes its direction of movemen has advantages and disadvantages. Advantages lie in the fact that, due to the abrupt change in target motion, the phase of OFS

103
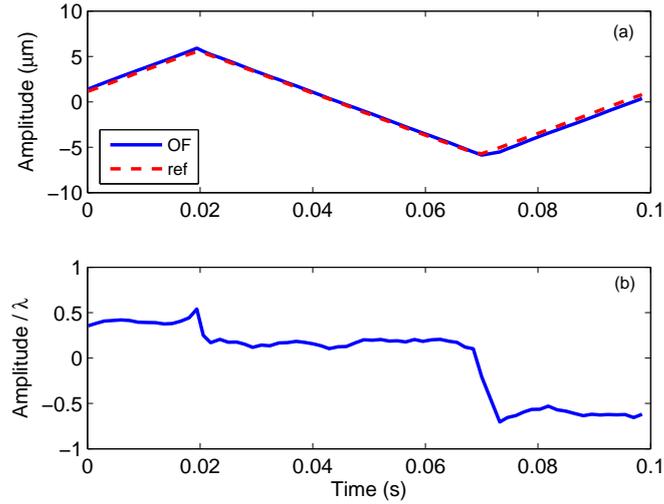
Figure 4.19: Displacement reconstructed using FC. (a) Retrieved displacement from OFS compared with the reference signal [4]. (b) Error signal in displacement reconstruction between OFI sensor using FC and reference signal.

changes abruptly so information about target reversal or change in direction may be extracted precisely. Disadvantages are that, since the phase of OFS is used to extract target displacement, any undesired change in phase (Fig. 4.21) introduces error in the signal reconstruction, as shown in Fig. 4.20(d).

Thus, it has been shown how wavelets enable processing the OFS both in the time and frequency domains simultaneously. While the time domain analysis enables to determine the target displacement using FC method with an error of $\pm \lambda/2$, processing it using the complete complex wavelet coefficients enables us to find the displacement with better accuracy of $\pm \lambda/5$. The detailed comparison of wavelet based analysis of OFS in the time and frequency using the FC and PUM methods is shown in Fig. 4.22.

4.4 ANALYSIS OF TRANSIENT VIBRATIONS

Transient vibrations[3] are used extensively in applications related to condition monitoring (e.g. fault detection), to biosensing and to medical signals (e.g. electroencephalograms or electrocardiograms) [181–183]. In the analysis of systems involving transient vibrations, most of the times it is required to idealize the cause of the vibration as a step or pulse function. Such causes may typically be either displacement, velocity, acceleration or force. So far OF has been used in the literature to analyse periodic vibrations using different signal processing schemes, including the fringe counting process described in Sec. 4.3.3, Fourier [184], Hilbert transformations [62], or phase unwrapping [14] to extract the vibrational parameters of the target.

---

[3]Temporarily sustained vibrations of a system, forced, free, or a combination of both. Mathematically, any signal whose statistics vary with time is considered a transient signal.
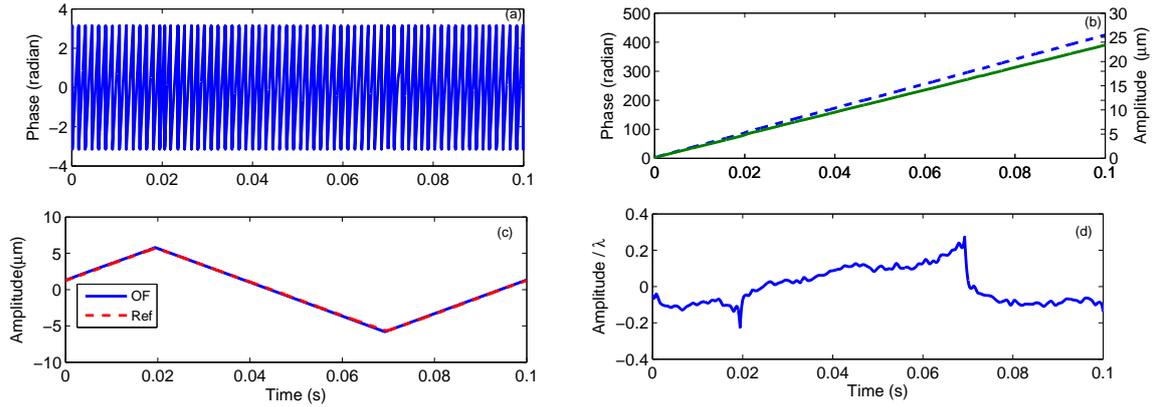
Figure 4.20: Wavelet-based implementation of PUM: (a) Wrapped phase; (b) Unwrapped phase (dashed line) and equivalent displacement (solid line); (c) Displacement reconstructed using PUM compared with reference [4]; (d) Error signal in displacement reconstruction between OFI and the reference signal.
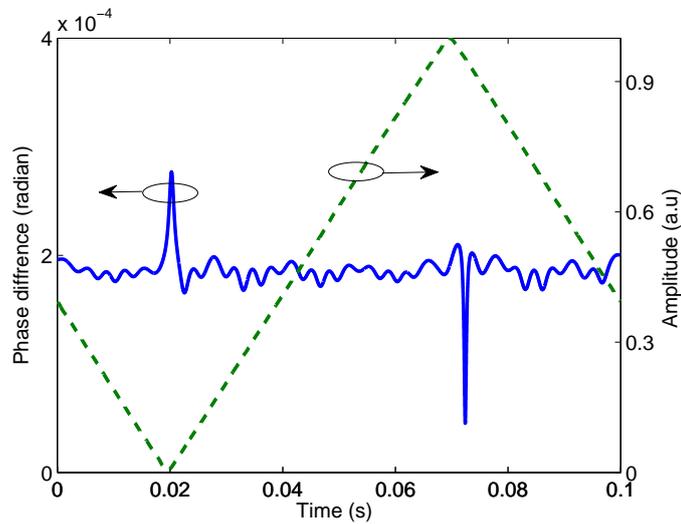
Figure 4.21: Phase fluctuation of OFS during the reversal in direction of the target.
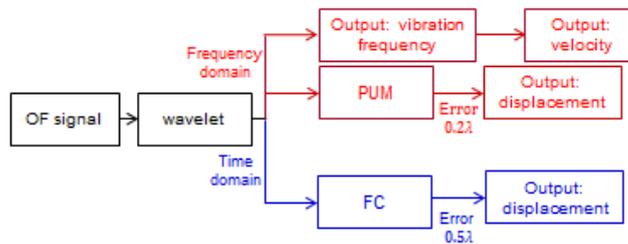
Figure 4.22: Summary of results.

Fringe counting is in general not suitable to process the transient signal as the threshold of detection would have to be changed or optimized depending on the displacement of the target. Fourier based signal processing is a very elegant approach, but it requires the knowledge
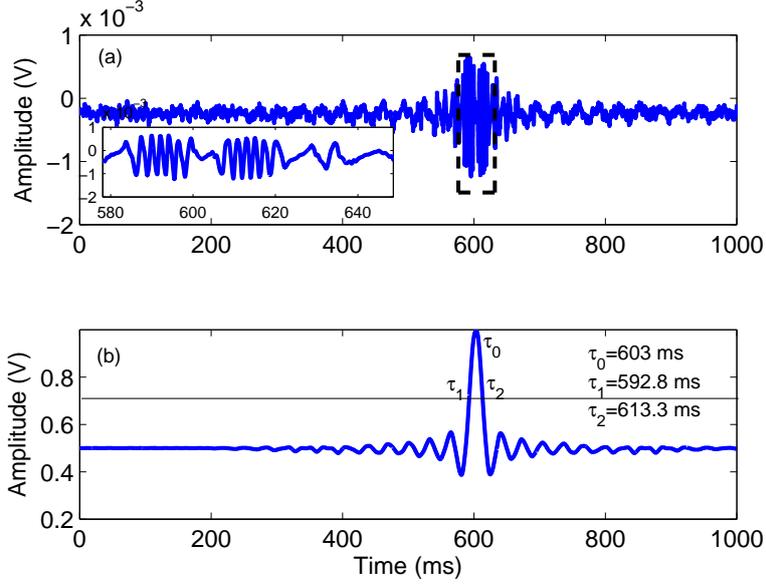
Figure 4.23: Experimental OFS obtained from a transient vibration: (a) OFS resulting from the transient motion of the piezo; the inset shows the OFS under a magnified time scale close to the moment when the transient reaches its peak; (b) Transient signal applied to the piezo used as target.

or estimation of the complete behaviour of the signal over time, so it becomes very limited to analyze transient signals, or even signals with unknown future behaviour. Though Hilbert transform on the signal converts it to the analytic complex plant, it is not always easy and straight forward to calculate the Hilbert transform. For more advanced functions techniques from complex analysis is need in order to handle the integral such as contour integrals in the complex plane and the residue theorem. Further, in the case of phase unwrapping approach, the OFS has to be processed time and frequency domain separately thus adding complexity as well. To overcome the drawbacks, the study presented here includes the analysis of a transient vibration using OF hence broadening its scope.

Due to its localization in time and frequency properties, wavelet is ideally suited to the analysis of transient signals [185, 186]. After applying the CWT, the frequency domain reflects the behaviour of a temporally localized version of the signal, ideal to study transient signals. The experimental setup for measuring transient vibrations using OFI is the same already discussed in Fig. 4.5 (a). A transient signal in the shape of a sinc pulse is applied to the piezo (Fig. 4.23 (b)). A 3 dB pulse duration (the time duration for which the voltage of pulse becomes $1/\sqrt{2}$ of its maximum value) was set to be $\tau_{3dB}=\tau_1-\tau_2 = 613.3\text{-}592.8=20.5$ ms, where τ_1 and τ_2 are the first and second 3 dB points. The peak value of the pulse occurs at $\tau_0=603$ ms, where it reaches a maximum value $V_0=1$ V. This induced a transient vibration in the piezo of amplitude $A_m = 3.8$ μm $= 5\lambda/2$. The vibration is then captured into the OFS as shown in Fig. 4.23 (a). It is observed for most of the time the signal applied to the piezo is constant, producing no vibration of the target and subsequently no fringes. At the time instance $t=\tau_0=603$ ms, the

106
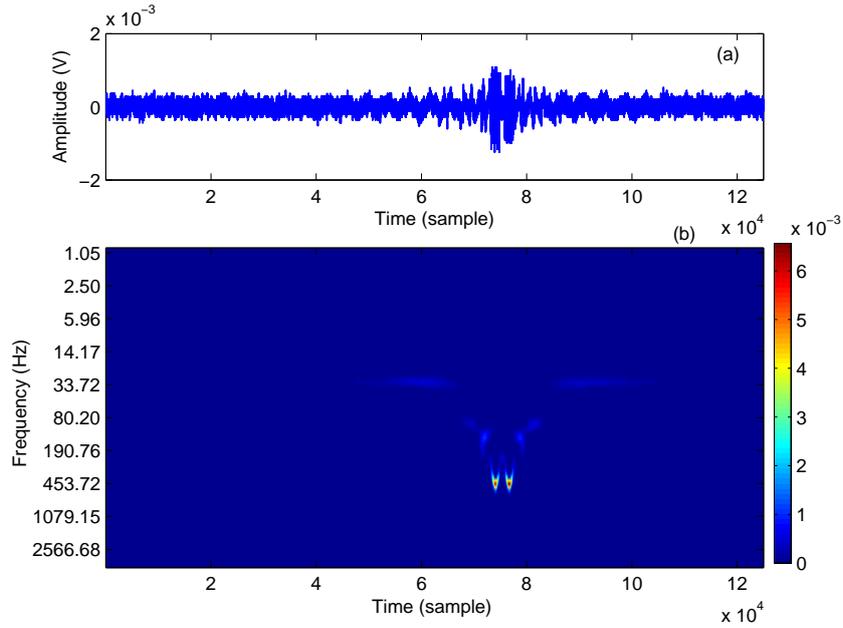
Figure 4.24: Time-Frequency representation of the OFS: (a) OFS; (b) Scalogram obtained using CWT. It should be noted that here the ordinate is the frequency, obtained by using the relation described in Eq. (4.10), unlike the scale in previous figures. The direct representation in terms of frequency gives the added advantage to obtain the pulse width with ease.

voltage switches to V_0=1 V following a sinc temporal profile, and the OFS fringes are produced and captured (Fig. 4.23 (a)). The number of fringes obtained N_f=5 is consistent with the amplitude of vibration [50] and may be seen in the inset in Fig. 4.23 (a).

The wavelet and algorithms described in Sec. 4.2 and 4.3.2 to process the OFS are used here on the OFS of transient signal as well. Using the CWT, the spectral and temporal information related to vibration as (a) duration and (b) instantaneous velocity profile of the transient vibration are obtained. Fig. 4.24 (b) shows the scalogram obtained for the transient OFS (Fig. 4.24 (b)) resulting from CWT. For most of the time of the experiment, the wavelet coefficients are close to zero (representing a negligible spectral component), but during the duration of the sinc perturbation their value change significantly, showing the appearance of new spectral components resulting from the Doppler shift related to the pulse duration. From Fig. 4.24 (b), we see how the Doppler frequency is f_D=453.72 Hz.

To measure the 3 dB pulse duration of the transient vibration, the wavelet coefficients at $f = f_D = 453.72$ Hz for all time i.e $W(f_D)$ is extracted from the scalogram. For simplicity, only the wavelet coefficients in the vicinity of the pulse are shown in Fig. 4.25. It is observed that the value of $W(f_D)$ is significant only during the pulse duration and zero elsewhere. The plot of $W(f_D)$ has two maxima at τ'_1 and τ'_2 with a sharp dip at τ'_0 represented by point A, C and B respectively in Fig. 4.25. The 3 dB width (τ'_{3dB}) and center of pulse (τ'_0) are calculated from

107
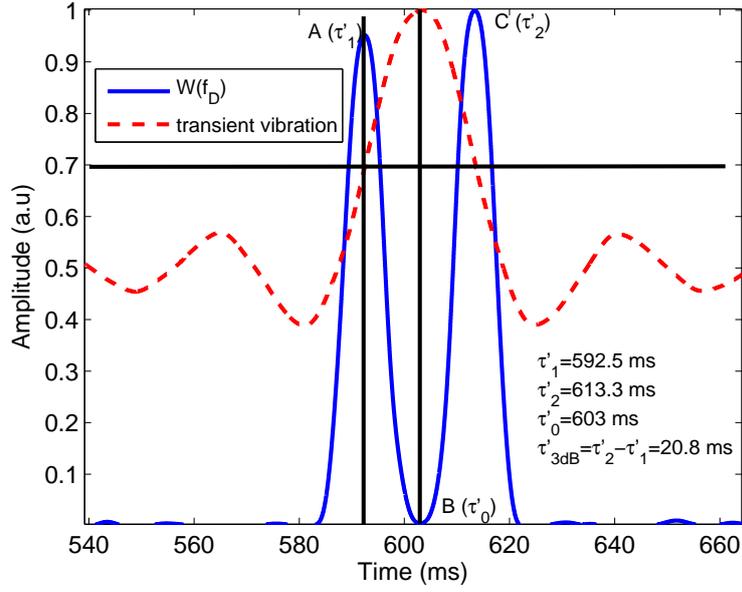
Figure 4.25: Experimental results. Characterizing the pulse - determining 3 dB width and center time of pulse.
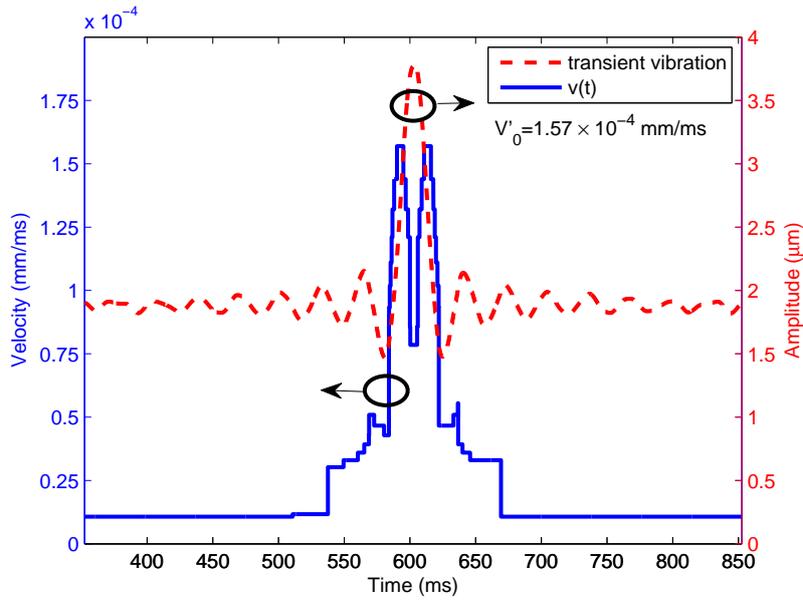
Figure 4.26: Experimental results. Velocity profile of transient vibration determined using wavelets.

Fig. 4.25 as

$$\tau'_{3dB} = \tau'_2 - \tau'_1 = 613.3 - 592.5 = 20.8 \quad ms \tag{4.15}$$

$$\tau'_0 = 603 \quad ms. \tag{4.16}$$

To determine the velocity profile v_t, we proceed as described next. First of all the maximum wavelet coefficient present at each instance of time is obtained from scalogram (Fig. 4.24).

108

Table 4.4: Comparison between the reference and extracted pulse parameters.

Parameters	Original value	Calculated value	Error
Center pulse time	$\tau_0 = 603$ ms	$\tau_0' = 603$ ms	0.0
First 3 dB time	$\tau_1 = 592.8$ ms	$\tau_1' = 592.5$ ms	0.05%
Second 3 dB time	$\tau_2 = 613.3$ ms	$\tau_2' = 613.3$ ms	0.0
3 dB pulse duration	$\tau_{3dB} = \tau_2 - \tau_1 = 20.5$ ms	$\tau_{3dB}' = \tau_2' - \tau_1' = 20.8$ ms	1.4%
peak velocity	$V_{t0} = 1.65 \times 10^{-4}$ mm/ms	$V_{t0}' = 1.57 \times 10^{-4}$ mm/ms	4.8%

Then the corresponding frequency is found, which gives the value of the Doppler frequency as a function of time $f_D(t)$. Once the instantaneous frequency is known, the velocity of target is obtained as $v_t = f_D(t)\lambda/2$ and shown in Fig. 4.26. It is observed that the calculated peak velocity of the target is $V_{t0}' = 1.57 \times 10^{-4}$ mm/ms as compared to original value of $V_{t0} = 1.68 \times 10^{-4}$ mm/ms (from Fig. 4.26, the target makes a displacement of 3.8 μm in 23 ms). In addition, a sharp dip in the velocity profile is observed showing how the target has reached its maximum value and now vibrates in opposite direction. Table C.7 shows the comparison between the original pulse parameters and the corresponding ones determined by the wavelet based signal processing. It is shown how all parameters are recovered within small error margins, being the determination of peak velocity the one which has a larger error value (although limited to below 5%).

4.5 CONCLUSION

In this chapter it was demonstrated that analysis of the OFS based on CWT, in particular using the complex Morlet wavelet, is proven to be a well suited, simple and efficient technique for signal de-noising, retrieving the parameters characteristic of the vibration, managing speckle and performing analysis of transients in a single processing step, because it processes the OFS in the time and frequency domain simultaneously. Wavelet-based signal processing was shown to extract the different vibration parameters from a conventional experimental OFS very efficiently. Furthermore, the use of the Morlet wavelet to recover the envelope of OFS proved to be an advantage in those cases where speckle induced signal fading. The method is computationally very efficient as compared to other techniques described in the literature. Two methods - FC and PUM - were demonstrated for displacement reconstruction using wavelets. While the former results present a time domain error of $\lambda/2$ in a triangular signal reconstruction, later they were reduced by processing them in the frequency domain with an error of just $\lambda/5$. It was also demonstrated that wavelet analysis permits to precisely pick and detect the occurrence of fringes, hence, allowing to minimize error in target displacement retrieval. Finally, it was used to

characterize a transient vibration and to extract several of its displacement-related parameters, such as the duration of the transient vibration, the precise evolution of the displacement over time, and the instantaneous velocity of the target.

5. Injection Modulation Induced Stability in Laser in Presence of Strong Feedback

5.1 INTRODUCTION

As shown in detail in Chapter 2, OF with modulation of the current feeding the laser is a particularly interesting type of perturbation, as the source of the perturbation is externally controlled in a very easy manner. It has shown instabilities such as quasi periodicity, period doubling or tripling, and even chaotic output depending upon the modulation frequency (f_m) and amplitude (A_m) of the current modulation [32–34]. Within the current Chapter, it is demonstrated that adjustments in injection modulation can be used to induce laser stability even for high C values. The modulation of the injection current of the laser causes not only IM, but also a modulation of the refractive index and the optical path of the active region of the laser, which results in FM [187]. However, IM and FM modulations present different features and cause different effects. While IM follows directly the light-current (L-I) curve (which is exponential in nature) of the laser, FM shows a linear dependence with the modulation current, which enables a separate influence of IM and FM on the laser performance tailored to the application.

FM results in a frequency spectrum of emission which consists in a central modulation frequency (f_m) accompanied by a series of side-bands separated by the same value. The amplitude of the side-band pairs is given by a Bessel function of the first kind $J_1(M)$, whose argument M is the frequency modulation index, defined as the ratio of maximum induced frequency deviation (Δf) to the modulation frequency (f_m) i.e. $M = \Delta f / f_\mathrm{m}$. Since $\Delta f = \Omega_f A_m$, the amplitude of the side-band depends upon the amplitude and frequency of the current modulation, and upon the frequency coefficient of the laser Ω_f [188].

This chapter is devoted to study the dynamics of the laser when subject to OF *and* IM, in particular, to the ability of such intensity modulation to prevent the feedback induced instabilities described in former chapters. The dynamics of the laser under optical feedback in presence of injection modulation is studied extensively. It is shown that the frequency deviation of the field emanating from the laser due to injection modulation alters the dynamic state and boundary conditions of the laser in such a way that even lasers under strong feedback conditions may attain stability and perform under a single mode state. The model developed to describe

the behaviour of the laser is based on the Lang-Kobayashi rate equations [30]. Experimental evidence of the theoretical predictions concerning the laser dynamics, making use of injection modulation to stabilize an laser in presence of strong feedback levels is presented. Next, an experimental set-up based on CWFM-OF is presented to measure the frequency coefficient of the laser Ω_f, which is a key parameter for inducing stability. Finally, it is demonstrated that the frequency deviation in the emission of the laser caused by injection modulation induces a phase change in the laser which opposes to that of the phase change induced by OF. It is shoen that an optimal modulation current exists with the ability to compensate the effects of optical feedback and maintain the laser in its single-mode stationary state. In summary, this chapter presents an experimental method to prevent from feedback-induced instabilities in the laser making use of injection modulation.

In detail, this chapter is organized as follows. In Sec. 5.2, the response of laser under the two main types of OF (C-OF and CWFM-OF) is briefly reviewed, covering only the aspects most relevant to this section and not presented in Chapter 2. In Sec. 5.3 it is shown that C may be interpreted as a frequency deviation parameter. The effect of having quite different boundary conditions for OF and CWFM-OF brings on that the value of C determines different number of solutions from the excess phase equation in both cases. Next, the effect introduced by the interaction of the frequency deviation due to C, and the one due to the modulation current A_m at different L_{ext} is discussed. It is shown that they both act in opposite directions so given the proper conditions are set, they may make the laser to be monomodal even in presence of high C values. Further, the frequency modulation coefficient of the laser (Ω_f), one of the key factors in the determination of laser stability in presence of high feedback strength, is measured experimentally in Sec. 5.4.1. Using this experimental value of Ω_f, the modal behaviour of the laser as a function of C, A_m and L_{ext} is analyzed, and the optimal working conditions based on those parameters which retain the laser in a single mode state are presented. Finally, in Sec. 5.4.2, an experiment is performed to show that frequency deviation caused by the introduction of laser injection modulation pulls back the laser from its potentially undesired (for metrology applications) multimodal state to a quasi stationary state even under high C values. A discussion and conclusion of the main contributions presented in Section 5.5 ends the Chapter.

5.2 THEORY

Different approaches have been used to explain the dynamics of SCL in presence of OF, such as the delay difference equation [26–28] or the compound cavity model [29]. In this chapter, the theoretical description based on the Lang-Kobayashi (L-K) formulation [30], already presented in Chapter 2 is used. From the L-K rate equation, a refined investigation of how the stationary state of the laser under feedback undergoes changes, loses its stability, and with growing feedback

strength gives rise to a more complex behavior is studied, showing it is possible to push back the laser to a stable monomode state by introducing injection current modulation. In its free-running state, with a constant pump current required to cause population inversion, the set of equations governing the dynamics of carrier density and photon density inside the laser cavity are given by the coupled equations (5.1) and (5.2) [93] (equivalent to Eq. (2.11) in Chapter 2)

$$\frac{dN}{dt} = \frac{\eta_i I}{qV} - \frac{N}{\tau} - v_g g N_p, \tag{5.1}$$

$$\frac{dN_p}{dt} = \Gamma v_g g N_p + \Gamma \beta_{sp} R_{sp} - \frac{N_p}{\tau_p}, \tag{5.2}$$

where the symbols have the usual meaning used in previous chapters, detailed in Eqs. (2.10) and (2.11), respectively. However, in presence of OF, the laser dynamics are no longer described by Eqs. (5.1) and (5.2), and the more complex (L-K) equations [30] are required to describe the C-OF case. Considering the external target has been placed at a distance L_{ext} from the laser, the time-delayed difference equation caused by optical feedback is given by Eqs. (5.3) and (5.4) [30]

$$\frac{dE(t)}{dt} = \frac{1}{2}(1 - j\alpha)\Gamma v_g a(N - N_{tr})E(t) + \gamma_{fb}E(t - \tau_{ext})e^{j\omega_0 \tau_{ext}}, \tag{5.3}$$

$$\frac{dN(t)}{dt} = \frac{\eta_i I}{qV} - \frac{N(t)}{\tau} - [\frac{1}{\tau_p} + \Gamma v_g a(N - N_{tr})]E(t)^2, \tag{5.4}$$

where the symbols have usual meaning, explained in Eqs. (2.72) and (2.73). The first term on the right side of Eq. (5.4) represents the rate of carriers injected, and the second and third terms represent the rate of loss of carrier concentration due to spontaneous and stimulated emission, respectively. It may be shown that the coherent beating between the emanating field inside the laser cavity and the field reflected from an external target causes a multistable state depending on the strength and the phase of the reflected optical field. Furthermore, the periodic vibration of the external target causes the change in OPL (transformed into a change in the round trip delay), and ultimately causes the optical power to present periodic variations as well (Chapter 2, Eq. (2.74)). Similarly, for the case of CWFM-OF, the equations (5.3) and (5.4) can be modified by adding a term describing the presence of current modulation, instead of the constant bias of the former case.

The phase equation of the laser under OF *and* CWFM-OF is given by Eq. (5.5) and (5.6), respectively [52, 93]

$$\phi_v(t) = 2\pi(f - f_0)\tau_{ext}(t) + C\sin(2\pi(f - f_0)\tau_{ext}(t) + 2\pi f_0 \tau_{ext}(t) + tan^{-1}\alpha), \tag{5.5}$$

$$\phi_m(t) = 2\pi(f - f_0)\tau_{ext} + C\sin(2\pi(f - (f_0 - \Omega_f i(t)))\tau_{ext} + 2\pi f_0 \tau_{ext} + tan^{-1}\alpha), \tag{5.6}$$

where f, f_0, τ_{ext}, α, and $i_m(t)$ are the emission frequency of laser under feedback, the emission frequency of the free running laser, the external round trip delay, the linewidth enhancement factor, and the modulation current, respectively. C-OF as defined by Eq. (5.5) is a non-linear

equation and its state is thus dependent upon the feedback parameter C and the feedback phase $(\phi_0 = 2\pi f_0 \tau_{ext})$ [87]. As discussed in Chapter 2, for $C < 1$, there is only one solution to Eq. (5.5) and only one mode exists in the cavity. However, for $C > 1$, multiple solutions to Eq. (5.5) may appear and the laser behaves as a multimodal system. However, in the case of CWFM-OF, governed by Eq. (5.6), the addition of the effect of the modulation current introduces a novel factor, easy to control and monitor externally, which changes the boundary conditions and so the modal behaviour of the laser.

5.3   PUSH-PULL EFFECT IN THE SEMICONDUCTOR LASER

The excess phase in presence of optical feedback in C-OF and CWFM-OF is a non-linear transcendental equation which cannot be solved analytically. In the case of C-OF (Eq. (5.5)), the phase of the laser is dependent upon the C and τ_{ext} (L_{ext}), but in the case of CWFM-OF (Eq. (5.6)), the phase of the laser that determines the number of solutions (i.e. modes in the cavity) is dependent upon C and τ_{ext} (L_{ext}), but also upon Ω_f and $i_m(t)$. In the following section, numerical and experimental methods to solve both excess phase equations (5.5) and (5.6) are analyzed. Relevant conclusions are drawn from such analysis, in particular the existence of a push-pull effect for the phase in Eqs. (5.5) and (5.6) when considering feedback and intensity modulation.

As a first step to illustrate such effect, it is desirable to show that the feedback parameter C acts as a frequency deviation parameter for the emitted frequency under feedback. Heil et. al in [189] demonstrated theoretically and experimentally that the frequency deviation of the field emitted by the laser under C-OF is proportional to its C value. Here it is analyzed the case of CWFM-OF in an equivalent manner. That is, the time-delayed reflected optical field from the remote target and the field inside the laser cavity produce an equivalent beat frequency with the magnitude of the frequency deviation, proportional to C. Eq. (5.6) (corresponding to CWFM-OF) is solved numerically to find the frequency emission (f) in presence of OF by equating the phase term to zero i.e. $\phi_m(t) = 0$ at different C values. The results are plotted in Fig. 5.1 (a). It is observed that with an increase in C, the frequency of emission under feedback increases proportionally. The CWFM-OF signal is obtained as $P_m = cos(2\pi ft)$[1] The frequency spectrum of the CWFM-OF signal, obtained by Fourier transform at different feedback levels is illustrated in Fig. 5.1 (b). This plot also confirms the argument that new frequency components are generated, and power in those components increases with an increase in C. It is also evident that at a low value of C, the frequency deviation follows a sinusoidal pattern, while at higher values ($C = 5$), hystheresis with sudden mode jumps are observed, as expected (Fig. 5.1 (a)).

---

[1]It should be recalled that the cosine term holds true for low feedback strength, while for higher feedback strengths a more complex triangular function is desirable. Taking advantage of fact that the triangular function is the sum of harmonics of cosine (sine) function, cosine is used here in a general sense for simplicity.
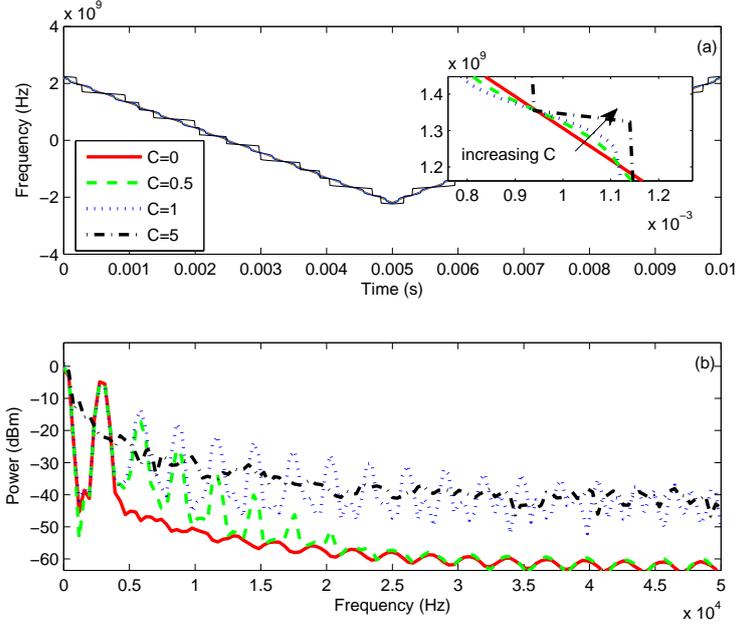
Figure 5.1: Graphical solution of Eq. (5.6). C, as in C-OF, acts as a frequency deviation parameter for CWFM-OF as well: (a) Frequency deviation increases with increase in C. (b) Spectrum of CWFM-OF signal at different C values.

The number of modes in the laser cavity is dependent on the solutions of the transcendental equation Eq. (5.5) (Eq. (5.6)) for C-OF (CWFM-OF). It has been shown that, in the general case, as long as $C < 1$, there is only one solution to Eq. (5.5) [30]. However, in the case of CWFM-OF, the additional frequency shift introduced by the modulation current in the field emanating from the laser needs be considered. From [30], it is evident that a number of frequencies appear due to the beating of the time delayed field coming back from the target with that emanating from the laser cavity. Only those frequencies that lie within the gain spectrum of laser, or the modes with minimum linewidth, dominate [72]. The evolution of the induced phase for both cases as a function of time and frequency is presented in Figs. (5.2) and (5.3) respectively, under the same axes and scales. Feedback strength was fixed at $C = 0.9$ for illustrative purposes only. The detailed effect of C on the laser dynamics, and in particuar the effect of diferent C values in the laser performance is explained in sections to follow. Fig. 5.2 (a) shows the phase profile of the C-OF signal evolved over time in the frequency range $\Delta f = $ [-0.7,0.7] GHz. For example, the phase profile over all times at a particular $\Delta f = 0.7$ GHz is shown in Fig. 5.2 (b). It is observed that the phase changes to 2π for each $\lambda/2$ displacement of target motion (the displacement due to vibration of the taret being 4λ (pp)). Similarly, the phase profile of CWFM-OF over the same frequency interval mentioned above is shown in Fig. 5.3 (a), and the phase profile at $\Delta f = 0.7$ GHz is shown in 5.3 (b). The differences in phase in both cases is clearly observable. The phase change in this case is attributed to the frequency modulation coefficient (Ω_f) and the amplitude of injection modulation (A_m). Since Ω_f is a key

115
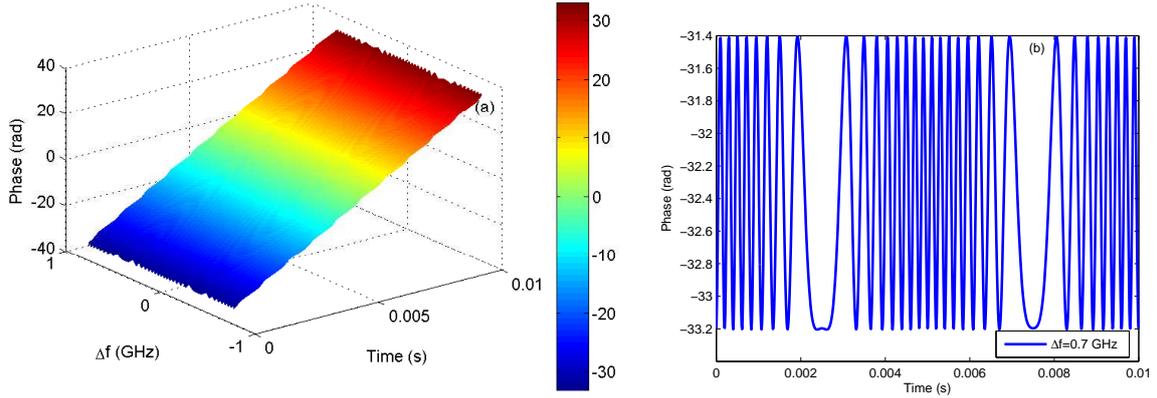
Figure 5.2: Phase profile of the C-OF signal at ($C = 0.9$). (a) Phase changes in C-OF as a function of time and frequency; (b) Phase profile at $\Delta f = f - f_0 = 0.7$ GHz.

factor that can help to compensate the effect of C in frequency, it is desirable to measure it experimentally, which is done in next section 5.4.1.

Next, the practical implications of the differences in the phase terms under C-OF and CWFM-OF are analyzed, in particular their effect into the number of modes (N_m) allowed in the laser cavity. The number of modes, which provide a solution to equation Eq. (5.6), as described in Chapter 2, is numerically obtained by equating the phase term $\phi_m(t)$ to zero. Let L_{ext}, $L_{ext}(pp)$ and Ω_f be set to typical values 0.45 m, 0.14 A and 0.005 nm/mA, respectively. The choice of L_{ext} is chosen to be compatible with the working conditions in laboratory, $A_m(pp)$ is chosen to be compatible with the laser specifications [190] used in the experiments and Ω_f is measured experimentally in Sec. 5.4.2.
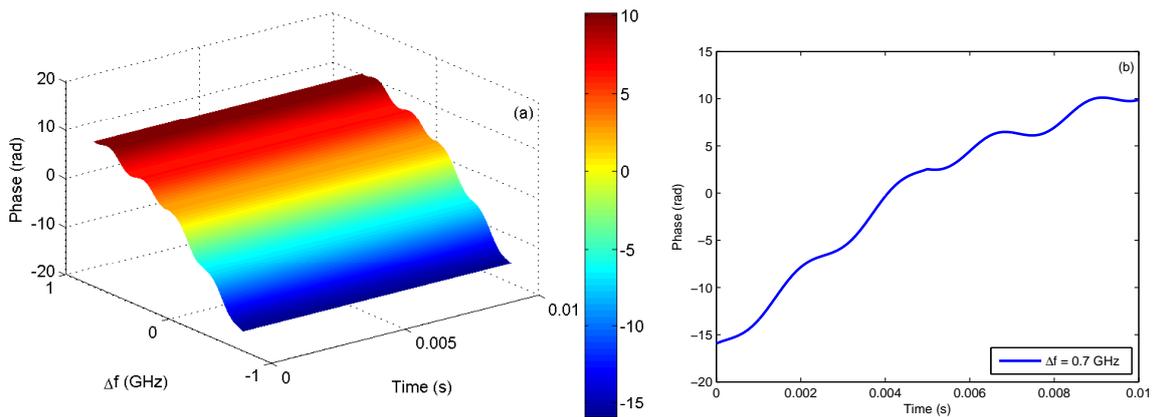
Figure 5.3: Phase profile of CWFM-OF signal ($C = 0.9$). (a) Phase changes in CWFM-OF as a function of time and frequency. (b) Phase profile at $\Delta f = f - f_0 = 0.7$ GHz.

116
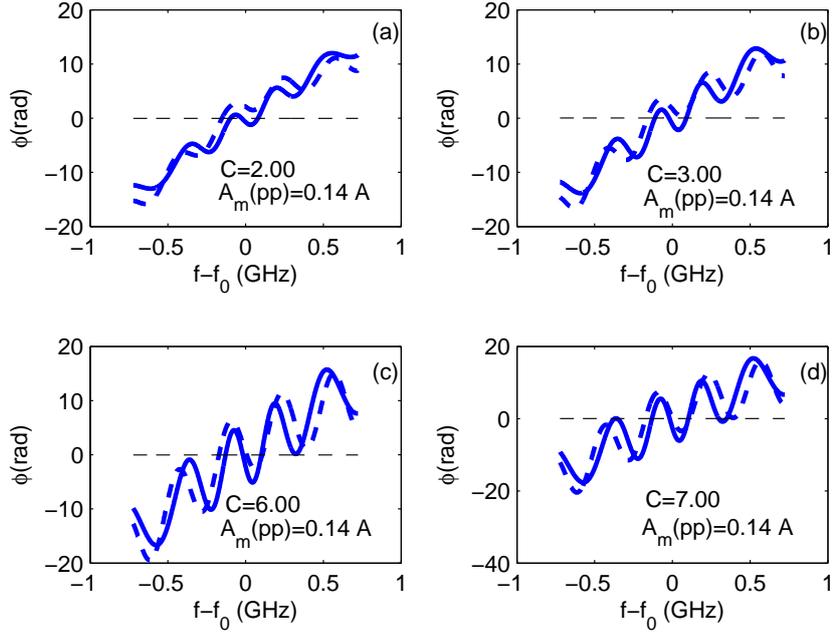
Figure 5.4: Graphical solution of Eqs. (5.5) and (5.6). Variation of the number of modes for C-OF (solid) and CWFM-OF (dash) at $L_{ext} = 0.45$ m, $A_m(pp) = 0.14$ A for different C values. Results show CWFM-OF is less susceptible to increase in C than C-OF.

Under these conditions, C is varied in a range from 2 to 7 (moderate to strong feedback) to see the profile of the phase $\phi_m(t)$ against the change in frequency of the emission, and the number of modes, seen as the number of crossings across zero of $\phi_m(t)$. Each plot contains equivalent conditions for C-OF and CWFM-OF in order to compare the behaviour of the phase term (Fig. 5.4). Under these conditions, and as depicted by classical theory, the number of modes for C-OF is greater than one ($N_m > 1$) when $C > 1$, resulting in multi-modal behaviour, and potentially hystheresis and mode hopping. However, the CWFM-OF behavior is seen to present a wide range of C values for which a single mode is still attained, even for C values as large as 3 (Fig. 5.4 (a) and 5.4 (b)).

Further increasing C causes multiple modes in the cavity for CWFM-OF as well, as seen in Fig. 5.4 (c) and Fig. 5.4 (d). However, increasing the amplitude of the injection current, $A_m(pp)$ from 0.14 A to 0.30 A at $C = 6$ (Fig. 5.4 (d)), the laser is pulled out of its multi-modal state back to a single mode one, as shown in Fig. 5.5. This attribute is associated to the negative value of Ω_f of the laser i.e. to the fact that an increase in the amplitude of modulation decreases the emission frequency and affects the phase term in opposite sense to that of C (which increases the frequency deviation as C increases, as shown in section 5.3). Hence, CWFM-OF acts as a "push-pull" system where there exists at least one theoretical value of A_m for each value of C which is able to compensate the effect of the complementary term so the laser is maintained in a single mode state. As a further example, Fig. 5.6 (a) shows a CWFM-OF case where at $C = 2$
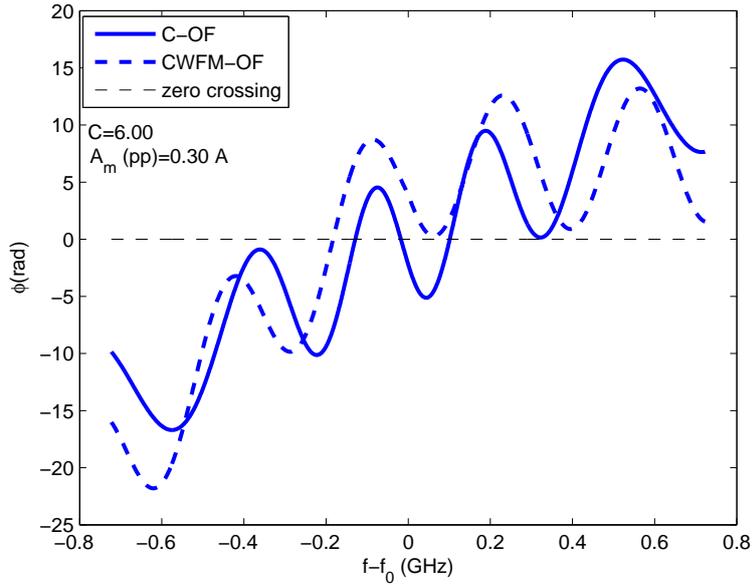
Figure 5.5: Modal behaviour of laser under OF. Laser exhibit multiple mode at $C = 6$ for C-OF. By addition of injection modulation, laser is pulled back to single mode state by choosing the optimal modulation amplitude $A_m(pp) = 0.3$ A.

and $A_m(pp) = 0.14$ A, the laser is kept in the single mode state. By decreasing the $A_m(pp)$ value to 0.03 A brings the laser back into a multi-modal state. Alternately, in Fig. 5.6 (b), with a feedback strength of $C = 5$, deviating $A_m(pp)$ from 0.14 A to 0.2 A pulls the laser from a multi mode to a single mode state. It is to be noted that the same value of $A_m(pp) = 0.14$ A causes the laser to attain single mode or multi mode state depending upon C. To clarify the conditions where this happened, simulations were carried out in MATLAB to carefully study the effect of L_{ext}, C and A_m on the number of modes N_m, and a detailed overview is presented in Fig. 5.7.

Several applications of lasers under OF (with our interest, sensors and metrology, among them) benefit from having the laser in a single mode state. One of the main applications of this push-pull behaviour is thus to retain the laser in a single mode state under high feedback strength, using a parameter of the laser which may be controlled externally. As a consequence, a detailed analysis of the $A_m(pp)$ values required to retain the laser in single mode state under large feedback strength was performed. Fig. 5.8 shows the relationship between them for the cases of different L_{ext} values ranging from 0.4 to 0.8 m. Points show the value for which a given C value is compensated by a given $A_m(pp)$ value. Based on the results in Fig. 5.8, no fixed relationship is obtained between them and each individual case is different. However for $L_{ext} = 0.45$, 0.5 and 0.55 m, the relation tends to be linear. At $C = 4$ and $L_{ext} = 0.45$ m, for instance, $A_m = 0.064$ A is required to retain the laser in a single mode state. The optimal value of A_m required to pull back the laser into single mode state depends upon the combination of
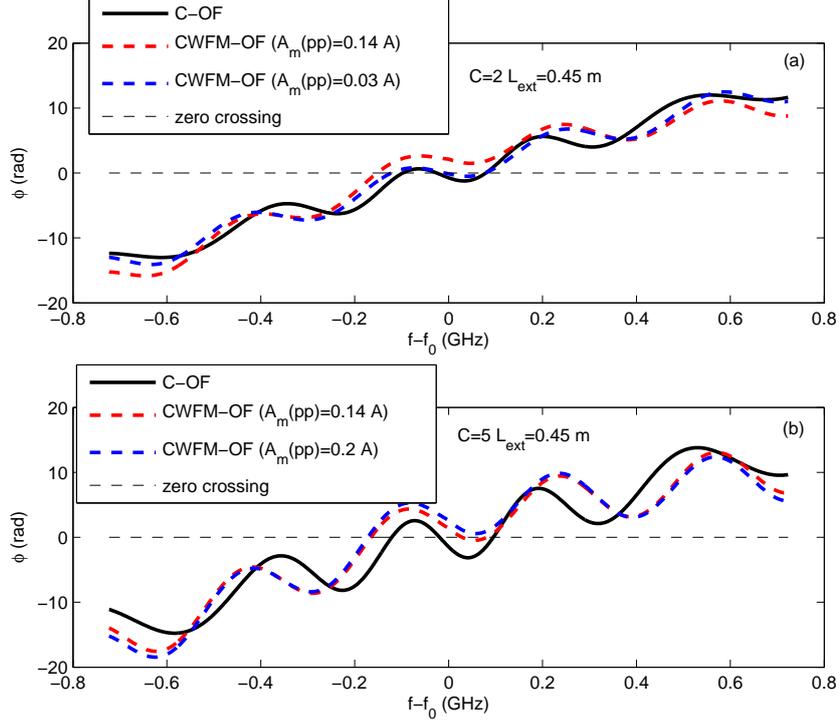
Figure 5.6: Relationship between A_m and C. The amplitude of current modulation required to bring the laser back to single mode behaviour depends upon feedback strength.

L_{ext} and C. However, in practice, there is a limit on the value of $A_m(pp)$ determined by the specifications of the laser considered which limits the maximum feedback strength which may be pulled back.

In addition to the role of the $A_m(pp)$ in the determination of the number of modes for the CWFM-OF signal, the role of frequency is discussed next. The effect of the number of modes on $f_m = 100$ Hz and $f_m = 1$ kHz at different C is shown in Fig. 5.9. It is observed that the modulation frequency does not observably affect the modal behaviour of the system. This is a consequence of Eq. (5.6). Since τ_{ext} (in the third term on right side, $(f - (f_0 - \Omega_f i_m(t)))\tau_{ext})$ is constant in this case, the only perturbation factor is the modulation current $i_m(t) = I_m tri(2\pi f_m t)$. f_m gives the perturbation rate and the magnitude of maximum frequency deviation is given by $\Omega_f I_m$, which is independent from f_m. In case τ_{ext} was a function of time, the dynamics of the system are detiled in Chapter 6.
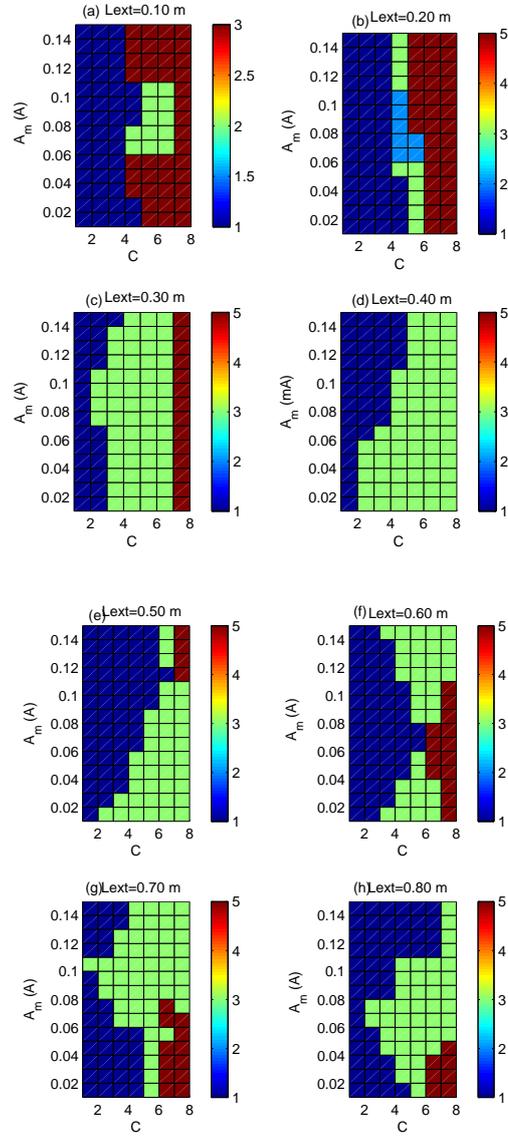
Figure 5.7: Number of modes in the CWFM-OF case as a function of feedback strength (C), amplitude of modulating current (A_m) and external cavity length (L_{ext}).
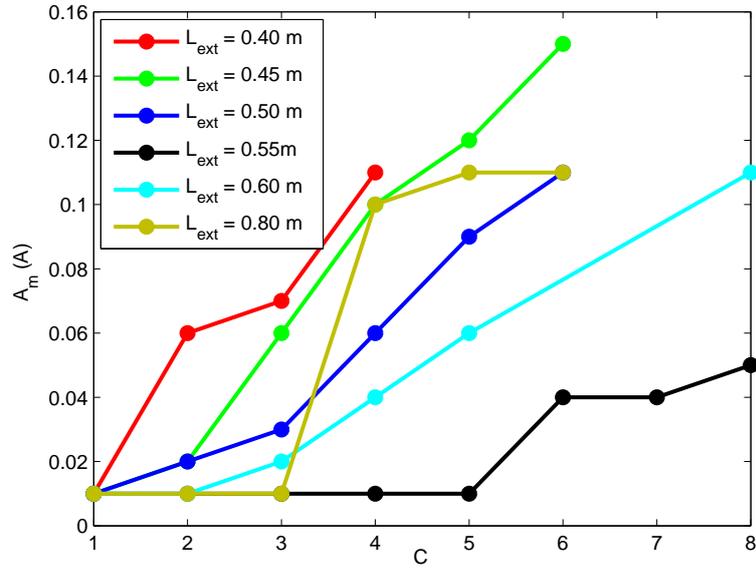
Figure 5.8: Relationship between C and A_m to pull laser back into single mode state.
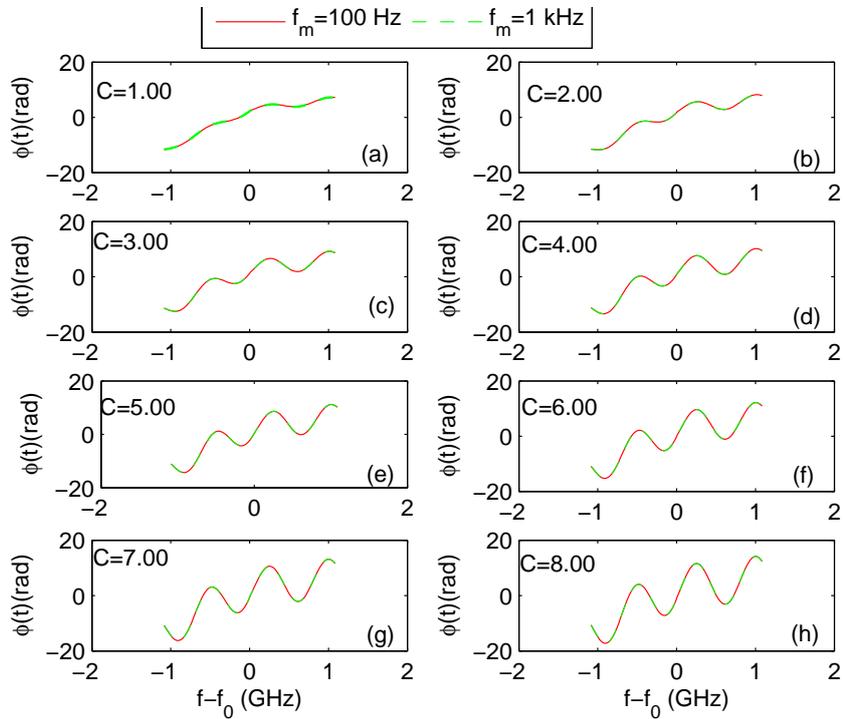
Figure 5.9: Effect of modulation frequency on N_m at different C. $A_m(pp) = 0.15$ A, $L_{ext} = 0.2$ m.

5.4 EXPERIMENTS: SINGLE MODE STABILITY INDUCED BY INJECTION MODULATION

Two different experimental tasks have been developed related to the contents of this Chapter. On one side, to implement properly the results regarding modal stability a precise measurement of the frequency coefficient of the laser Ω_f is required, as it has a key role regarding the number of modes in the laser emission under CWFM-OF. Such experimental measurements of Ω_f are covered in Sec. 5.4.1. Next, in Sec. 5.4.2, experimental results showing that the laser may be used under single mode conditions even under large feedback strength using the amplitude of the modulating current are presented.

5.4.1 EXPERIMENTAL MEASUREMENT OF Ω_f

In equations (5.5) and (5.6), the role of Ω_f in the determination of the number of modes emitted by the laser under OF was presented. This makes it a key parameter in laser performance under modulation conditions, so it is desirable to present a method which enables to measure it precisely. The experimental setup used for the measurement of the frequency coefficient of the laser is given in Fig. 5.10, being obviously a conventional CWFM-OF setup. As shown in Fig. 5.10, a HL8337MG AlGaAs laser was used in the experiment. The emission wavelength was measured using an Instrument System's SPECTRO 320(D) R5 unit, resulting in $\lambda = 826.5$ nm. The optical beam emitted from the laser was focused using a Thorlabs lens 352240 (not shown in the block diagram) with focal length of 8 mm and numerical aperture of 0.5, on a moving target. The target was a piezoelectric linear stage PI-LISA (P-753.3CD) which includes an embedded capacitive sensor with a resolution of 0.2 nm [4]. It was placed at $L_{ext} = 0.1$ m from the laser. Initially, the current to the laser was modulated by a triangular signal from the signal generator to introduce the frequency sweeping effect in the laser emission desired. The number of fringes (N_f) which form in a CWFM-OF set-up is related to the distance of the laser to the target (L_{ext}) and to the frequency modulation coefficient of the laser (Ω_f) and is
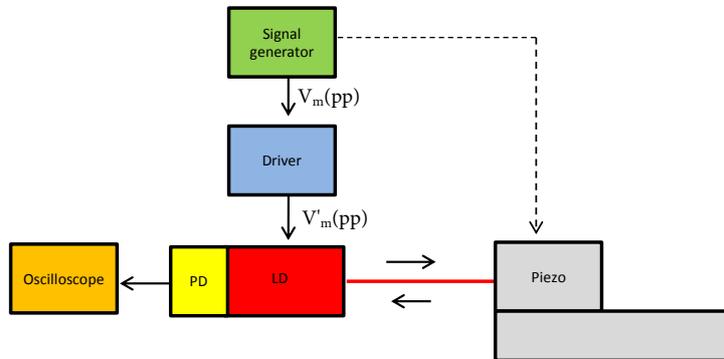
Figure 5.10: Experimental setup to measure the frequency coefficient of the laser (Ω_f) using CWFM-OF

Table 5.1: Experimental parameters

Parameter	Value
Distance to external target from the laser (L_{ext})	0.1 m
Modulation frequency (f_m)	$1 - 7$ kHz
Modulation voltage $(V_m(pp))$	700 mV (1 V)
Emission wavelength of the laser (λ)	826.5 nm
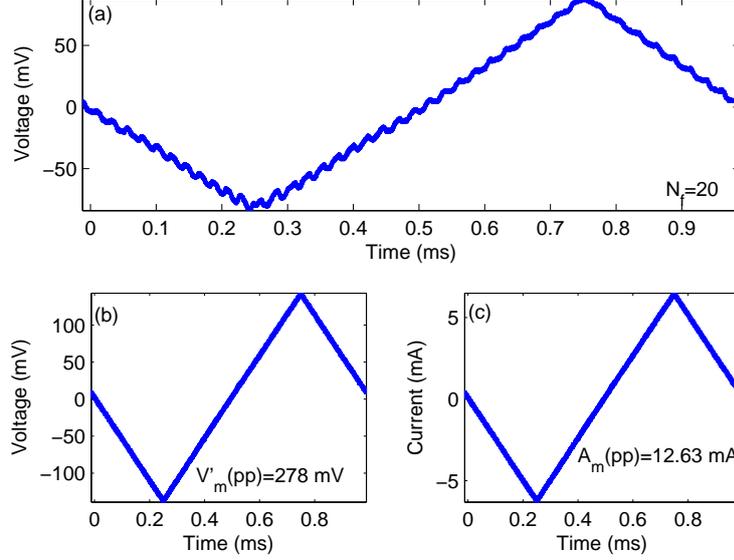
Figure 5.11: Experimental results for measuring the frequency coefficient (Ω_f) of the laser under test. (a) CWFM-OF signal obtained from PD having $N_f = 20$ fringes (b) Change in voltage across the laser $(v'_m(t))$; (c) Change in injection current $(i_m(t))$.

expressed as [52]

$$L_{ext} = \frac{\lambda^2 N_f}{2\Delta\lambda} = \frac{\lambda^2 N_f}{2A_m(pp)\Omega_\lambda} = \frac{N_f c}{2\Delta f} = \frac{N_f c}{2A_m(pp)\Omega_f}, \tag{5.7}$$

where symbols have the usual meaning used in former sections. $\Delta\lambda$ is the peak to peak change in wavelength.

An experimental arrangement with the parameters described in Table 5.1 was arranged. Keeping the target fixed at a distance of $L_{ext} = 0.1$ m, a modulation voltage $v_m(t)$ with peak to peak value $V_m(pp) = 700$ mV. A range of modulation frequencies $f_m = [1 - 7]$ kHz was applied to the laser using the signal generator. The frequency coefficient was then computed for each modulation frequency. To ensure repeatability, the same experiment was performed under equivalent conditions with $V_m(pp) = 1$ V. For illustrative purposes, a particular measurement case when $f_m = 1$ kHz, and $V_m(pp) = 700$ mV is shown in Fig. 5.11. The CWFM-OF signal is seen to have $N_f = 20$ fringes (Fig. 5.11 (a)). The peak to peak voltage change across the
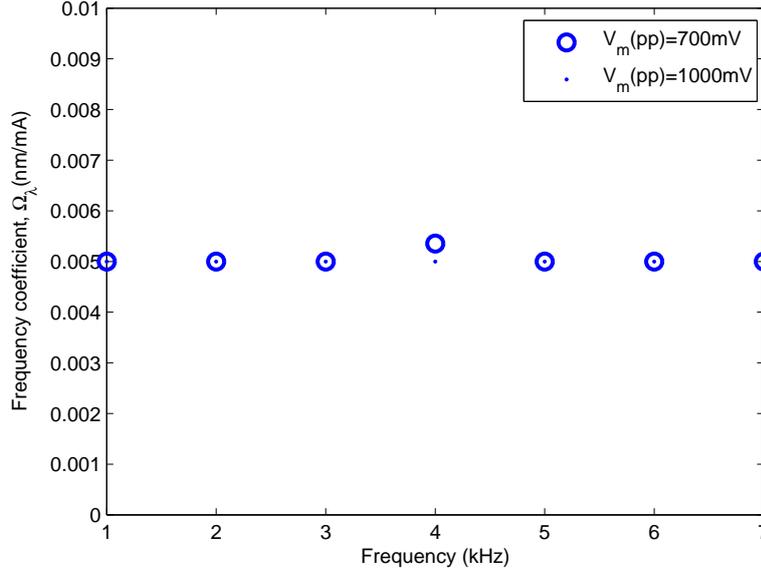
Figure 5.12: Experimental results. Measured frequency coefficient Ω_λ of the laser under test at different modulation frequencies $f_m = 1 - 7$ kHz and amplitudes $V_m(pp) = 700$ mV and 1 V. The frequency coefficient of laser is constant in the range considered with a value of 0.005 nm/mA.

diode was $V'_m(pp) = 278$ mV (Fig. 5.11 (b)), and the peak to peak change in the current was measured to be $A_m(pp) = 12.63$ mA (Fig. 5.11 (c)). Substituting the values of $N_f = 20$, $c = 3 \times 10^8$ m/s, $A_m(pp) = 12.63$ mA and $L_{ext} = 0.1$ m, in Eq. (5.7), the only unknown term, Ω_λ, is determined. The result yields $\Omega_\lambda = 0.005$ nm/mA. With a wavelength of 826.5 nm this also may be expressed as $\Omega_f = -2.2$ GHz/mA (with the negative sign showing that the emission frequency decreases with increased injection current). The obtained value is consistent with the value of -3.0 GHz/mA in AlGaAs lasers cited by [191]. Ω_λ has been calculated for a number of experimental cases, and the results are shown in Fig. 5.12. It is evident that, within the range considered, Ω_f can be considered a constant equal to 0.005 nm/mA.

In order to further investigate the effects of external parameters on Ω_λ, an alternative approach is taken into account. Taking advantage of the fact that the N_f in the first approach can be changed (Eq.(5.7)) by varying the values of L_{ext} and $A_m pp$, the modulation voltage and frequency from the signal generator is fixed to be $V_m(pp) = 700$ mV and $f_m = 5$ kHz respectively. This gives a modulation voltage at the laser $V'_m(pp) = 210$ mV corresponding to a modulation current to the laser $A_m(pp) = 9.54$ mA. Next, the distance of the external target from the laser L_{ext} is varied from 14 to 7 cm. The variation of N_f with the change in L_{ext} at constant $A_m(pp)$ is shown in Fig. 5.13 (a). The experimental data shows a linear relationship between them with an slope of 0.8 cm/fringe. Equating the slope of Eq. (5.7), $\lambda^2/(2A_m(pp)\Omega_\lambda) = 0.8$ and placing the value of $A_m(pp) = 9.54$ mA, $\lambda = 826.5 \times 10^{-7}$ cm, Ω_λ is found again to be 0.005 nm/mA. The same result may be reached by varying the $A_m(pp)$ and noting the N_f (Eq. (5.7)), provided that the distance of external target is kept constant, $L_{ext} = 7$ cm. Fig. 5.13 (b)
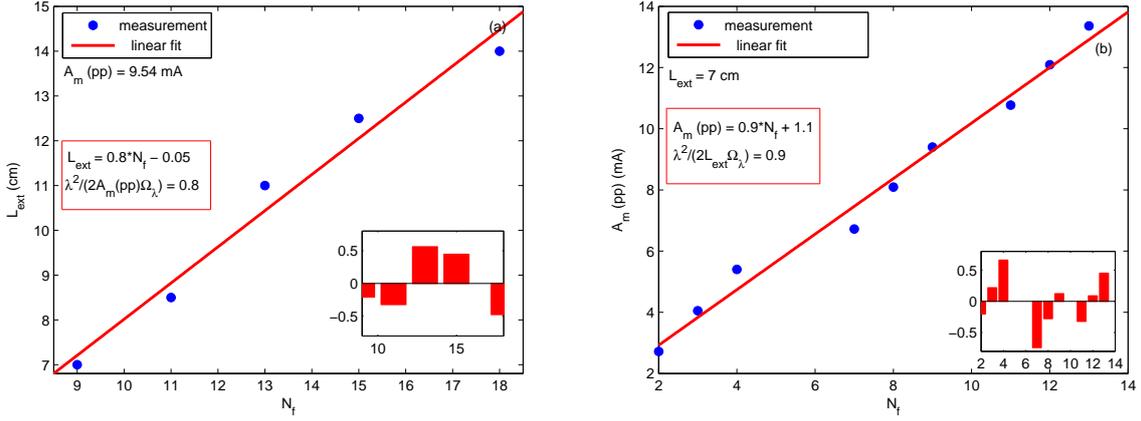
Figure 5.13: Alternate methods of finding Ω_λ (from Eq. (5.7)): (a) Varying L_{ext} to vary N_f while keeping $A_m(pp)$ constant. The Ω_λ value computed from the slope of the linar fit is 0.005 nm/mA. Deviations in the fit shown in inset; (b) Varying $A_m(pp)$ to vary N_f while keeping L_{ext} constant. The Ω_λ value computed from the slope of the linear fit is again 0.005 nm/mA.

shows the linear relation between them and having slope 0.9 mA/fringe. Similar to the previous method, equating the slope $\lambda^2/(2L_{ext}\Omega_\lambda) = 0.9$, the only unknown quantity Ω_λ is found to be 0.005 nm/mA as well. Hence, different approaches confirm that the frequency modulation coefficient of laser under consideration is 0.005 nm/mA.

5.4.2 EXPERIMENT: SINGLE MODE STABILITY INDUCED BY INJECTION MODULATION

Having measured the frequency coefficient (Ω_f) of the laser and studied the relationship of the number of modes with the amplitude of injection modulation in Sec. 5.4.1, next it will be shown experimentally how injection modulation can pull the laser into a quasi stable state even in presence of strong feedback, or when the feedback is strong enough to cause the laser to hop between two or multiple states. The block diagram of the experimental setup is equivalent to that in Fig. 5.10, but in this case the target (piezo) was placed at a distance of 8 cm from the laser. The system is then perturbed by setting the piezo to vibration by applying a triangular voltage of $V_v(pp) = 0.326$ V which results in a displacement (pp) of 1.24 μm ($3\lambda/2$). Under these experimental conditions, the C-OF signal is acquired using a LabVIEW code and presented in Fig. 5.14 (a). In the case of C-OF, each fringe corresponds to a displacement of $\lambda/2$, so the OFS has three fringes in each period, as expected [50]. From the fringes the in C-OF signal waveform, it is concluded that C should be close to one, and that the laser is close to the transition between moderate and weak feedback [50]. To push the laser towards a stronger feedback regime, the position of the lens is tuned to focus the optical power into a smaller spot on the target, so that C increases. The C-OF signal is then acquired (Fig. 5.14 (b)). In general, the fringe loss condition is accepted as characterizing the strong feedback regime of the
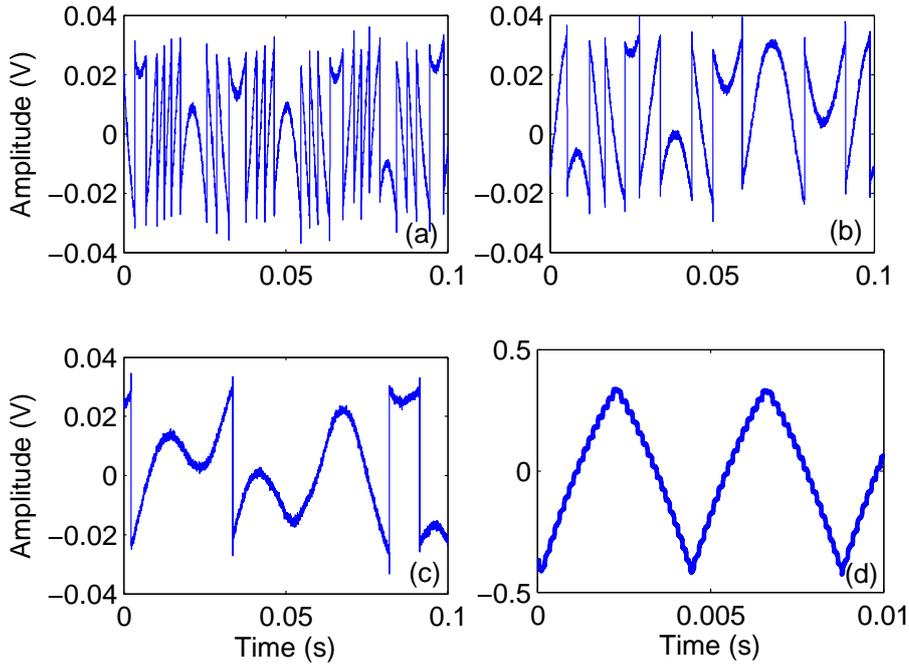
Figure 5.14: Experimental results. (a) C-OF experiment described in the text; (b) The laser is forced into a strong feedback regime by modifying the distance between the laser and the focusing lens, so fringe loss appears; (c) Further increasing C brings on the fringes to disappear; (d) While in the conditions of (c), the introduction of injection modulation causes the laser to attain a quasi stationary state under strong feedback.

laser [192]. It is observed that increasing C has caused fringe loss in the OFS and thus the laser is operating under strong feedback conditions [192]. The lens is then further adjusted to cause a more severe fringe loss condition, and subsequently to increase C. The waveform is shown in Fig. 5.14 (c), showing no visible fringes. It is worth mentioning that no quantitative approach has been made to measure the value of C. Approaches to measure the value of C may be found in [150, 193]. While keeping the experimental set up of Fig. 5.14 (c) unaltered, a triangular modulation voltage $V_m(pp) = 700$ mV resulting in a current modulation of $A_m(pp) = 12.63$ mA was applied to the laser. The waveform for this case is shown in Fig. 5.14 (d), and its magnified view repeated in Fig. 5.15 for clarity. It is observed that the laser formerly under strong feedback is now back under the weak feedback regime, due to the presence of the right number of sinusoidal fringes over the ramp [52,126] typical of a laser under single mode performance, and under weak feedback. The value of C that forced the laser to instability or multi modal state in the case of C-OF is thus pulled back to quasi stationary state under the same C conditions with the introduction of injection modulation. Hence the effect of C in both types of OF is different, with CWFM-OF being less susceptible to it. For further clarity, the ramp in Fig. 5.14 (d) is filtered to get a clear view of the number and shape of fringes, as they are related to the C value. The fringes obtained are presented in Fig. 5.16 (a), with an inset which gives the magnified view of the shape of fringes. The number of fringes obtained $N_f = 14$ is clearly
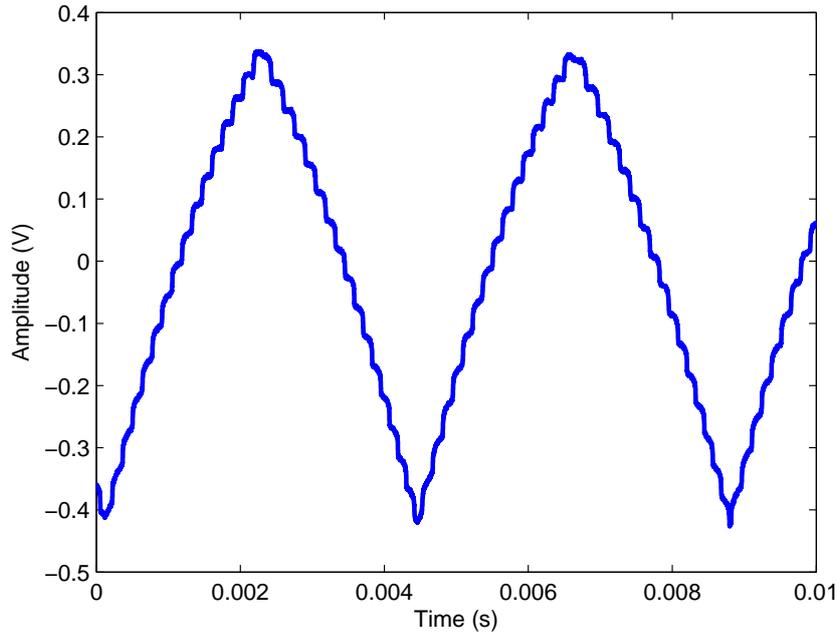
Figure 5.15: Magnified view of Fig. 5.14 (d) for clarity.

visible in one ramp, corresponding to the known $L_{ext} = 7.5$ cm (calculated from Eq. (5.7) and compared to original distance of 8 cm). This itself is evident that the laser is (quasi) stable and the presence of sinusoidal fringes proofs that it is under weak feedback. To further confirm the results, a simulation is performed in MATLAB with the parameters of the experiment under weak feedback $C = 1$, and the results are presented in Fig. 5.16 (b). The experimental CWFM-OF signal at Fig 5.16 (a) and that obtained from simulations at Fig. 5.16 (b) resemble each other both qualitatively and quantitatively, as both of them have same number of fringes, N_f = 14 and a similar fringe shape. Further, simulations to obtain the CWFM-OF signal at high feedback strength $C = [3, 4]$ are shown in Fig. 5.16 (c) and (d), respectively. The distortion in signal under high feedback strength is clearly appreciable (as compared to Fig. 5.16 (a) and (b)). Hence, we conclude the experimentally obtained CWFM-OF signal obtained in Fig. 5.16 (a) was obtained under weak feedback and that amplitude modulation, as explained by the theory, is able to modify the laser behaviour under strong feedback conditions.

Thus, modulation induced stability can have direct significance in attaining stability in the emission of the laser diode under strong optical feedback and / or quasi-periodicity, a desirable phenomenon for practical applications of OFI sensors for metrology, but also in chaotic communications [32]. Further, the narrowing of linewidth of the semiconductor laser is dependent upon the feedback strength. The laser linewidth under feedback ($\delta\nu_f$) relative to the standalone laser ($\delta\nu$) is inversely proportional to C as expressed in $\delta\nu_f = \delta\nu/(1 \pm C)^2$, depending upon the feedback phase [194]. Thus, provided that the laser is stable at high feedback strength, it
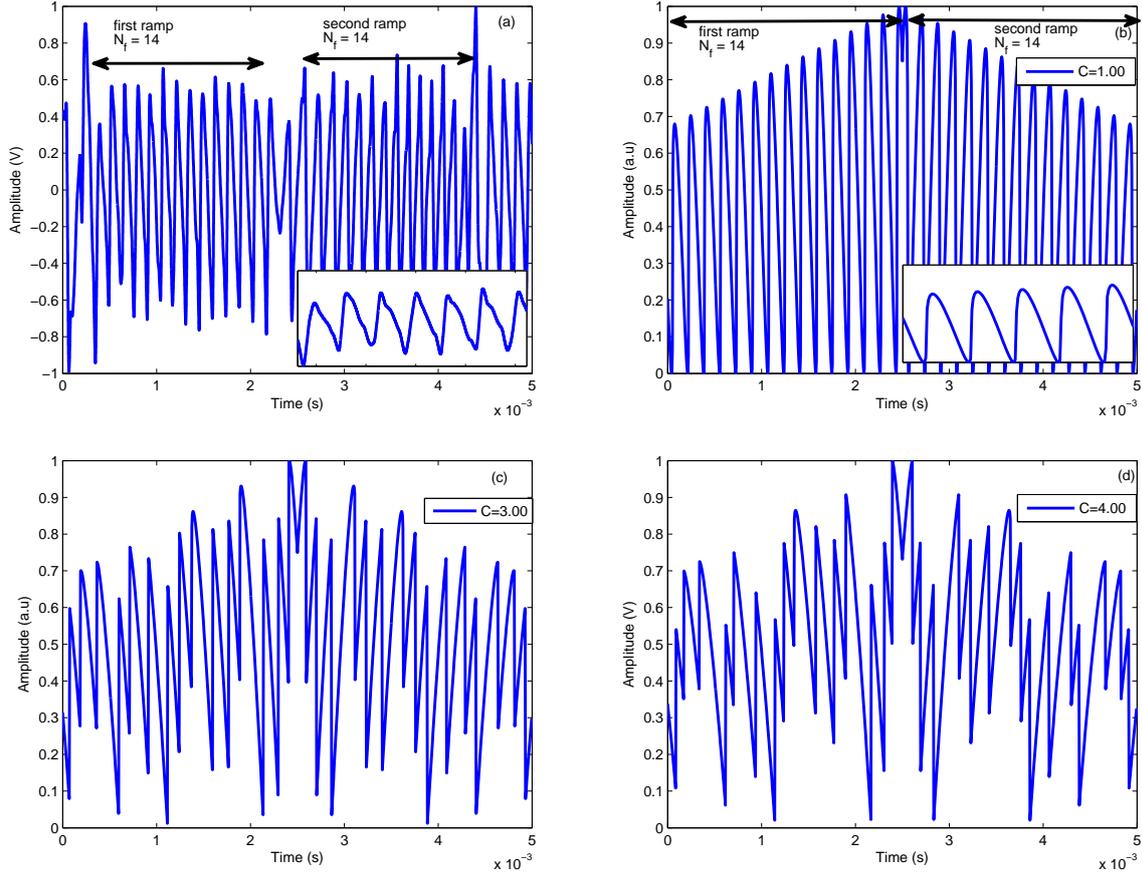
Figure 5.16: Comparison of experimental CWFM-OF signal with that obtained from simulation at different feedback levels. (a) Experimental CWFM-OF signal obtained after removing the ramp in Fig. 5.14 (d) (the inset gives the magnified view of fringes); (b) Simulated CWFM-OF signal at $C = 1$ (inset gives the magnified view of fringes); (c) Simulated CWFM-OF signal at $C = 3$; (d) Simulated CWFM-OF signal at $C = 4$. Experimental and simulation conditions are the same with parameters $L_{ext} = 8$ cm, $\lambda = 826.5$ nm; $\Omega_\lambda = 0.005$ nm/mA (obtained experimentally in Sec. 5.4.1), $A_m(pp) = 12.63$ mA (measured experimentally in Sec. 5.4.2).

can then be used to reduce the linewidth as well, which may find applications in the field of spectroscopy.

5.5 DISCUSSION AND CONCLUSION

The dynamics of the laser subject to optical feedback in case of C-OF and CWFM-OF leading to frequency modulation were studied and compared. It was shown that the feedback strength C may be interpreted as a frequency deviation parameter. In case of large C values, it is well known and accepted that a number of new frequencies evolve, the power in each of the frequency components is also increased and the laser attains a multi modal state. The introduction of injection modulation, on the other side, causes also the frequency modulation of the emission

to change, but in this case it changes in opposite direction to the change induced by C-OF. Such inverse effect in frequency deviation induced because of OF and IM permits to search an equilibrium condition that compensates each other's effects, and induces mode stability in the laser even under strong feedback conditions. Since the frequency modulation of the laser induced by intensity modulation plays a significant role in the understanding of the laser's modal behaviour in CWFM-OF, the frequency coefficient of laser (Ω_λ) was measured experimentally for the laser unit being used, and it was confirmed to be 0.005 nm/mA, equivalent to -2.2 GHz/mA, centred at 826.5 nm, using three different approaches. The response of the laser in terms of number of modes in presence of different levels of feedback, external distance and injection modulation amplitude was studied and the optimal conditions to retain the laser in mono modal state were demonstrated. Finally, it was experimentally shown that the introduction of injection modulation or electron pumping pulls the laser to stability even in presence of strong feedback.

6. CWFM Differential Optical Feedback

6.1 INTRODUCTION

Within this chapter, a novel method of measurement which uses laser non-linear dynamics under OF for sensing sub-wavelength displacements is demonstrated. This is considered one of the main contributions of this Thesis. The proposed methodology combines the two types of optical feedback discussed insofar, C-OF and CWFM-OF, to measure vibration amplitudes smaller than $\lambda/2$ with resolutions of a few nanometers and a bandwidth depending upon the distance to the external target, the amplitude, and the frequency of the current modulation applied to the laser. The basic theoretical details involved in the measurements and not described already, together with a detailed mathematical model for the proposed measurement principle are described in the following Sections. Experimental results, using a dedicated setup which was specifically designed and built for this purpose are presented. A conventional OFI sensor working as a vibrometer measureing a target vibration of amplitude $\lambda/5$ (137.5 nm), and results for a mean peak to peak error of 2.4 nm are demonstrated just by pointing the laser onto the target and applying appropriate signal processing.

As seen in previous Chapters, C-OF methods are limited to the measurement of displacements with total amplitudes larger than $\lambda/2$, with a resolution varying upon the type of experiment and, specially, upon the type of signal processing strategy applied. As discussed, the original fringe counting method enables a $\lambda/2$ resolution [50], while during the last two decades the increase of accuracy of the measurements has been a driver of the research in the field [168, 195, 196]. The capability to measure vibration displacements smaller than $\lambda/2$ has also been demonstrated recently [63] using mechanical modulation and a double laser set-up. In that approach, the bandwidth of the sensor was dependent upon the product of the frequency and amplitude of the linear mechanical stage used to produce a reference OFS which was later on compared to the measurement signal. The use of a mechanical modulator with a linear response increased the sensor's cost and size while limiting the measurement bandwidth.

To overcome those problems, a novel approach that takes advantage of the amplitude-frequency coupling in the laser (that is, the existence of a finite non-zero linewidth enhancement factor α) is developed in order to replace the mechanical modulation depicted in [63] by an electronic modulation. The developed method introduces two main advantages over [63]. First, the set-up is simplified since the use of a second laser and of external mechanical elements to
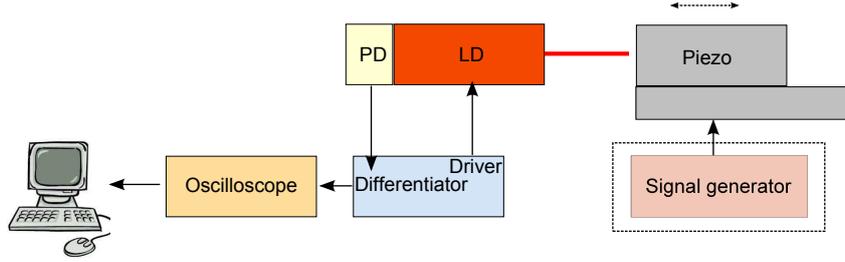
Figure 6.1: Schematics of the experimental setup.

provide the modulation is no longer necessary. This reduces the cost and size of the sensor while making it comparable in cost to C-OF applications, but keeping the desired improved performance. The use of only one laser also reduces the possibility of bias in the measurement introduced by the difference of the physical properties between each laser or its circuitry. Second, the bandwidth and resolution of the proposed method is dependent only upon the laser and its electro-optical parameters, in contrast to the mechanical scheme described before. This, in turn, allows to reach larger bandwidths since the method is no longer limited by mechanical constraints.

In the following sections the working principle of the proposed optical sensor based on CWFM-DOF, including the methodology to calculate the target vibration waveform and amplitude, plus the frequency bandwidth of the sensor is explained in detail. Both periodic and transient vibrations will be measured. A final discussion section analyzing the effects of the modulation current onto the spectral behavior of the laser will be presented, anticipating some of the potential limits of the setup and trends of future work to be developed.

6.2 SYSTEM DESCRIPTION AND THEORY

The proposed concept of the experiment is shown in Fig. 6.1. First, a periodic current modulation is applied to the laser while the target is kept stationary. When the current feeding the laser is modulated, not only the intensity of the emitted signal is changed, but also its emission wavelength, because of the coupling between amplitude and frequency modulation characterized by α. To attain the linear wavelength changes recommended for measurement purposes, a triangular wave is used as a modulation signal. Under these conditions, the laser can be thought as a multi-wavelength source whose wavelength (and intensity) changes with time proportionally to the injected current. The field emitted by the laser then hits the stationary target and is partially back reflected into the laser cavity, where it interferes with the standing wave already present, producing interference fringes in the emitted power with a phase difference of 2π between them. Of course, this is the working principle of CWFM-OF [107].

The OFS obtained consists of a series of small ripples, caused by the beating of the time delayed reflected field with the emitted field inside the cavity, superimposed onto the power

131

signal ramp induced by the modulated intensity, as shown in Fig. 6.2 (a). The signal is then subjected to processing, starting by a differentiator which separates the ripples caused by interference from the linear power ramp induced by modulation. It is shown that the number of fringes which appear on the ramp depends upon the round trip time delay, that is, upon the distance between laser and target, and upon the wavelength changes (*pp*) caused by the modulation current [196]. This is termed as the *reference case* and the interference fringes produced as *reference fringes.*

Let's see what happens when, under the same arrangement, the target is not static anymore but presents a displacement to be measured. Since each $\lambda/2$ target displacement produces an interference fringe in the signal [30,50], if the target vibration amplitude is smaller than $\lambda/2$ no additional fringes are produced as a result of the target motion. Even though the total number of fringes remains constant, the target motion changes the frequency seen by the laser due to the change in OPD, in the equivalent to a Doppler shift in the frequency domain.

Thus, when compared to the former reference case, the new set of fringes is shifted in time proportionally to the OPD change introduced. From this point onward, this case is referred to as *vibration case*, and its interference fringes as *vibration fringes.* It is shown that by comparing the reference and vibration cases, the complete information of the displacement of the target can be extracted, hence the name given as continuous wave frequency modulation *differential* optical feedback (CWFM-DOF). In order to build the mathematical model of the measurement, all parameters related to the *reference case* are denoted by the subscript r, and the ones related to the *vibration case* by the subscript v. The excess phase and emitted power (with $x = [r, v]$) equations that govern both cases are defined by [52]

$$\phi_r(t) = 2\pi(f_r - (f_0 + i_m(t)\Omega_f))\tau_{ext} + C sin(2\pi f_r \tau_{ext} + tan^{-1}\alpha), \tag{6.1}$$

$$P_r(t) \approx cos(2\pi f_r(t)t), \tag{6.2}$$

$$\phi_v(t) = 2\pi(f_v - (f_0 + i_m(t)\Omega_f))\tau_{ext}(t) + C sin(2\pi f_v \tau_{ext}(t) + tan^{-1}\alpha), \tag{6.3}$$

$$P_v(t) \approx cos(2\pi f_v(t)t), \tag{6.4}$$

where L_{ext} is the stationary distance from the laser to the target, and $L_{ext}(t) = L_{ext}+a(t)$, with $a(t) = A_t cos(2\pi f_t t)$ describes a sinusoidal target motion with peak amplitude A_t and frequency f_t. $\tau_{ext} = 2L_{ext}/c$ is the external round trip delay for the reference case, while $\tau_{ext}(t) = 2L_{ext}(t)/c$ is the external round trip delay for the vibration case; f_r and f_v are the emission frequencies of the laser under feedback for the reference and vibration cases, respectively; f_0 is the standalone laser frequency at its operating point; $i_m(t)$ is the triangular AC modulation current driving the laser; Ω_f is the frequency coefficient of laser; C is the feedback strength; and P is the emission power of the laser under feedback.

Simulations of performance based on Eqs. (6.1) - (6.4) have been carried out using the parameters listed in Table 6.1. The goal of the simulation is to prove the appearance of power shifts in time between the interference fringes of the reference and vibration cases. Non-linear

132

Table 6.1: Parameters used in the simulation described in the text

Parameters	Value
Distance of external target from laser (L_{ext}) (forward path)	0.3 m
Peak to peak modulating current ($A_m(pp)$)	1.5 mA
Modulation frequency (f_{m})	100 Hz
Target vibration amplitude ($A_t(pp)$)	$\frac{\lambda}{10}$
Target vibration frequency (f_t)	200 Hz
Frequency modulation coefficient (Ω_f) [52]	-3 GHz/mA
Feedback strength (C)	0.9
Emission wavelength of the laser (λ_0)	692 nm
Linewidth enhancement factor (α)	3
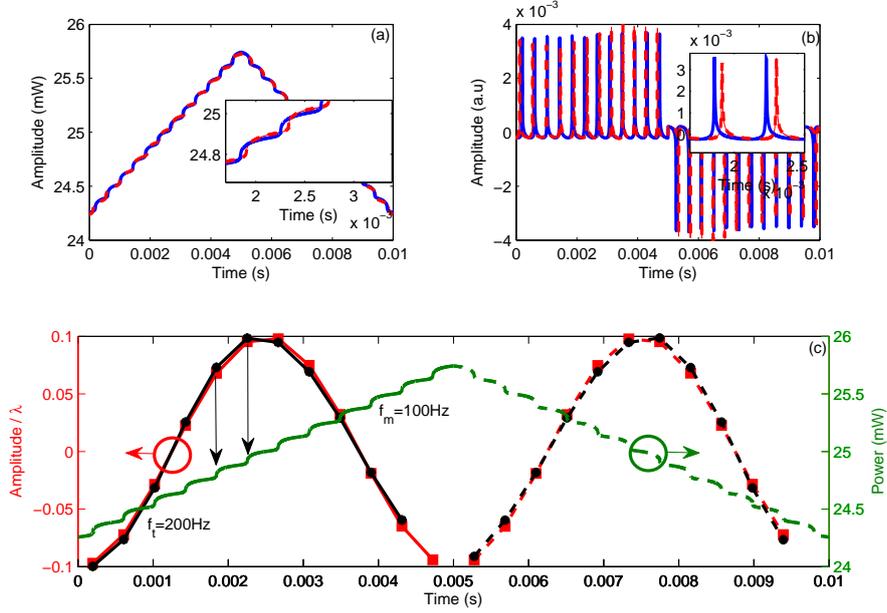
Figure 6.2: Results of the simulation: (a) Emitted power variations in reference (blue solid) and vibration (red dash) cases (inset gives a magnified view); (b) Shift in fringes in both cases after fintering the ramp; (c) Target waveform reconstructed (black star) compared with reference displacement (red square), overlapped on the simulated power output of the laser. Vertical arrows indicate the position of sampling points due to existing fringes. Because of the symmetry of the modulation signal, processing any one ramp gives full information about target vibration, making the other ramp redundant.

equations Eq. (6.1) and (6.3) are solved numerically, equating them to zero, to find f_r and f_v respectively. The corresponding power fluctuations are calculated using Eqs. (6.2) and (6.4). The results of the simulation are presented in Fig. 6.2(a) and 6.2(b), which show a significant shift of the emission power related to target motion which we can be used for measurement purposes. In the next paragraphs we will analyze the features of the proposed measurement

scheme regarding the most usual measured parameters.

6.2.1 DISPLACEMENT OF THE TARGET

The displacement of the target out of the time shift which appears between the vibration and reference fringes is our first calculation. It is to be noted that in the case of C-OF, the phase difference between each consecutive fringe is equivalent to a 2π phase change, which in OFS is related to $\lambda/2$ if a displacement is present. Thus, the fraction of time shift in the vibration fringes relative to the reference fringes multiplied by $\lambda/2$ is the equivalent target displacement. Let $\mathbf{t_r^n}$, $\mathbf{t_v^n}$, $\mathbf{t_{rv}^n}$, $\mathbf{t_{rr}^{n-1}}$ be vectors containing the time of occurrence of the reference and vibration fringes, the time difference between consecutive reference and vibration fringes, and the time difference between consecutive reference fringes obtained in half period of current modulation. The superscript is the number of elements in the considered vector and t_k is the moment of occurrence of the kth fringe. Thus, the reconstructed target displacement $\mathbf{A_{t,rec}}$ can be computed simply using

$$\mathbf{A_{t,rec}} = \frac{\mathbf{t_{rv}^{n-1}}}{\mathbf{t_{rr}^{n-1}}} \times \lambda/2 \tag{6.5}$$

Using Eq. (6.5), the target waveform is reconstructed as shown in Fig. 6.2(c). It is worth noting that since the target vibration is twice the modulation frequency, the entire target waveform has been arranged to lie within one ramp (half period) of the modulation signal. Vertical arrows illustrate that each fringe corresponds to a measurement point. To extract the information on the displacement of the target it is then enough to process one of the ramps in the modulation signal.

6.2.2 FREQUENCY BANDWIDTH

Let $f_m = 1/T_m$ be the modulation frequency of the current feeding the laser. In a time $T_m/2$ (considering only one ramp of the modulation signal, this discussion is extended in Sec. 6.3), there are N_f fringes giving $N_f - 1$ sample points. Thus, the sampling rate for target reconstruction is given by $f_{s,rec} = (2N_f f_m - 1)$. From Nyquist theorem, the maximum frequency that can be reconstructed is half the sampling rate and using $2N_f f_m >> 1$, it can be estimated that $f_{t,rec} \simeq N_f f_m$. As a consequence, it is evident that the maximum frequency of target vibration that can be reconstructed using the proposed sensor is dependent upon the product of the frequency of the modulation of the laser and the number of fringes, which is defined by the absolute distance between laser and target. Hence, keeping the number of fringes N_f constant, the frequency of vibration of the target that can be detected is directly proportional to the modulation frequency i.e. $f_{t,rec} \propto f_m$. Since a laser can be modulated at larger frequencies (MHz) keeping significant frequency deviation [188] when compared to mechanical vibration of laser (KHz) this method gives significantly wider bandwidth than its mechanical counterpart [63].

6.2.3 OPTIMIZATION OF RANGE AND BANDWIDTH

An increase in the frequency bandwidth is one of the expected benefits of the electronic current modulation in CWFM-OF, so it is worth exploring its dependencies in order to optimize it. In the case of CWFM-OF the phase after a round trip is given by $\phi = 4\pi L_{ext}/\lambda$. The change in phase with respect to the change in wavelength induced by the modulation is

$$\Delta\phi = -\frac{4\pi L_{ext}}{\lambda^2}\Delta\lambda. \tag{6.6}$$

The phase change between two consecutive fringes is 2π. If there are N_f fringes, the phase change from the first to the last fringe is given by $2N_f\pi$. Putting this value in Eq. (6.6), the formula for external distance is

$$D = \frac{\lambda^2}{2\Delta\lambda}N_f \tag{6.7}$$

Eq. (6.7) shows that keeping the target distance L_{ext} and the peak to peak amplitude of the modulation current constant[1], the number of fringes N_f is constant. Further, from Sec. 6.2.2 it is evident that the bandwidth of the proposed sensor (the maximum target frequency that can be measured) is directly dependent upon the number of fringes and the modulation frequency of the current. The later parameter is laser dependent, and is defined by the specifications of the laser model used in the experiment. However, the former parameter can be tuned depending upon the circumstances, in particular adjusting the distance from the laser to the target. Hence, the larger the number of fringes, the better the bandwidth of the sensor. Increasing the frequency of modulation also enhances the bandwidth directly. From Eq. 6.7, N_f can be computed as

$$N_f = \frac{2\Delta\lambda L_{ext}}{\lambda^2} = \frac{2(2A_m\Omega_f)L_{ext}}{\lambda^2} = \frac{4A_m\Omega_f L_{ext}}{\lambda^2} \tag{6.8}$$

From Eq.(6.8), it is seen that N_f can be increased by increasing the amplitude of the current modulation (A_m). This parameter depends upon the particular laser unit considered, as the amplitude of current cannot be increased beyond the laser specifications. This value is determined by the linear region of the current-wavelength curve of laser. It was shown in Eq. (6.7) that the distance measured using CWFM-OF is a function of N_f, given by $L_{ext} = \lambda^2 N_f/2\Delta\lambda$, where the resolution ($r$) of such measurement is given by $\lambda^2/2\Delta\lambda = \lambda^2/2A_m(pp)\Omega_\lambda$. Hence, the resolution of the system in the measurement of the absolute distance to the target is dependent upon the wavelength sweep, and ultimately upon the modulation current ($A_m(pp)$). Fig. 6.3 shows experimental results illustratig this effect. It is seen in Fig. 6.3 (a) how doubling $A_m(pp)$ from 6.72 mA to 13.36 mA, N_f doubles from 6 to 12 fringes, and the resolution of the system, determined by the fringe spacing, doubles from 1.2 cm to 0.6 cm.

Secondly, N_f can be increased by choosing a laser with a large frequency coefficient (Ω_f), although this is also determined by the specifications of the laser manufacturer. For instance,

---

[1] Keeping the modulation amplitude constant, the change in the emitted wavelengths is also constant, from $\Delta\lambda = \Omega_\lambda A_m(pp)$
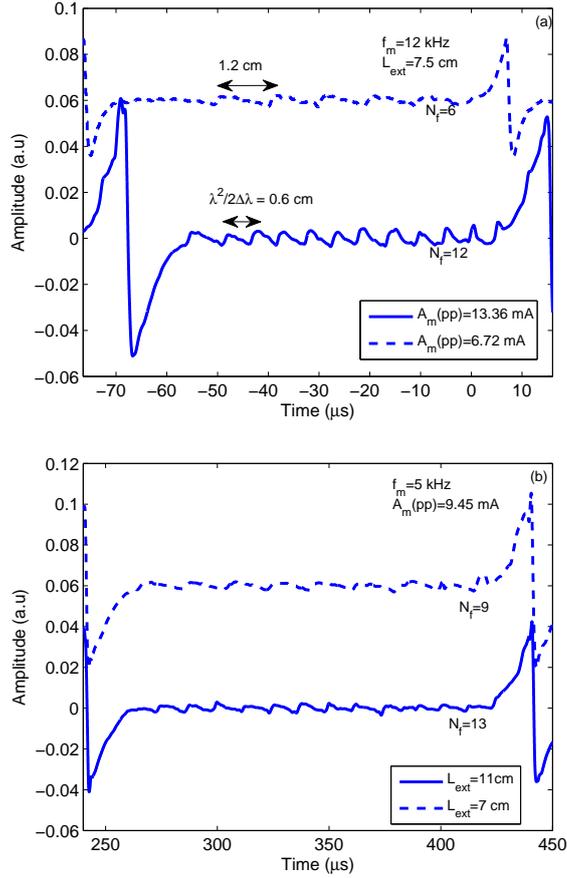
Figure 6.3: Experimental results demonstrating the effect of (a) $A_m(pp)$; and (b) L_{ext} on N_f.

with the laser used in Ch. 5 (Oclaro's HL8337MG), its value was found to be 0.005 nm/mA; however, for the laser (Hitachi's HL6501) used in Sec. 6.3 and beyond the value is 0.1 nm/mA (measured from the slope in Fig. 6.5). It is noted that an experimental value of Ω_f was measured in Ch. 5 of this Thesis.

Finally, N_f can also be increased by increasing the distance L_{ext} between the laser and the external target, as shown in Fig. 6.3 (b). This is typically quite simple in practice, as when keeping the modulation current constant, simply increasing the distance from the laser to the target increases the number of fringes. As a summary, we see that the frequency bandwidth of the sensor proposed is determined by the parameters of the laser, the peak to peak amplitude of the modulation current, and the distance of the target to the laser, which gives a number of free parameters to optimize the frequency response of the sensor to the considered application.

6.2.4   MINIMUM DETECTABLE AMPLITUDE

From Eq.(6.5), the target reconstruction depends upon the shift of fringes between the vibration and reference conditions. The minimum detectable amplitude of vibration of the target is reached when the shift of fringes is the minimum detectable shift in time, which is determined

by the sampling time $t_s = 1/f_s$. Thus the minimum detectable amplitude of target vibration is given by

$$A_{t,rec}^{min} = \frac{t_s}{t_{rr}} \times \frac{\lambda}{2}. \tag{6.9}$$

For example, considering some typical values like $t_s = 8 \times 10^{-8}$ s ($f_s = 12.5$ MHz), $t_{rr} = 0.4167$ s, and $\lambda = 692$ nm, the minimum detectable amplitude of vibration of the target $A_{t,rec}^{min}$ is 6.64×10^{-5} nm, which is the maximum resolution which can be attained by the proposed sensor. It should be noted that the measurement is a difference in time occurrences of the fringes, so the limit in resolution is dependent upon the sampling frequency of the oscilloscope or acquisition card. The higher the sampling frequency (the lower the sampling time), the better is the minimum measurable amplitude. However, a further effect to be discussed is related to the detection of fringes shifted by a known sample time, which becomes limited by different types of noise and by the duration of the peak in amplitude being measured.

6.2.5 TRADE OFF BETWEEN MINIMUM DETECTABLE AMPLITUDE AND BANDWIDTH

From Eq. (6.9), the minimum detectable amplitude of target motion, $A_{t,rec}^{min}$ is inversely proportional to the time difference between consecutive reference fringes, t_{rr}. Hence the larger the time difference, the smaller the minimum detectable amplitude and hence the better the sensor performance in terms of amplitude detectivity. However, such an approach has a trade-off on the frequency of vibration that can be detected by the proposed sensor, that is, in the bandwidth of the sensor $f_{t,rec}^{max}$.

In Sec. 6.2.2 it was shown that the maximum frequency that can be detected by a CWFM-DOF sensor is directly proportional to the detectable number of fringes. This implies that there must be a large number of fringes in a given modulation period in order to provide a larger bandwidth of the sensor, that is, a larger $f_{t,rec}^{max}$. This in turn requires that the reference fringes must be spaced as closely as possible, so the time difference between them is short enough to make t_{rr} small, which in turn reduces the minimum detectable amplitude for the vibration of the target $A_{t,min}$. Writing it in short

$$A_{t,rec}^{min} \quad \alpha \quad \frac{1}{t_{rr}} \quad \alpha \quad N_f. \tag{6.10}$$

$$f_{t,rec}^{max} \quad \alpha \quad N_f \quad \alpha \quad \frac{1}{t_{rr}}. \tag{6.11}$$

As an example, in the case discussed in (Fig. 6.2), let us consider an increase in the number of fringes by a factor of M=4, for instance by increasing the laser-target distance. Then $f_{t,rec}^{max}$ and $A_{t,rec}^{min}$ would change from its previous values of 1200 Hz and 6.63×10^{-5} nm to new values of 4800 Hz (better) and 26.5×10^{-5} nm (worse), respectively. For most of the practical cases the gain in bandwidth of the sensor is overridden by the need of a minimum detectable amplitude (extremely small in normal conditions, in the 10^{-14}m range), so in general it is always desirable
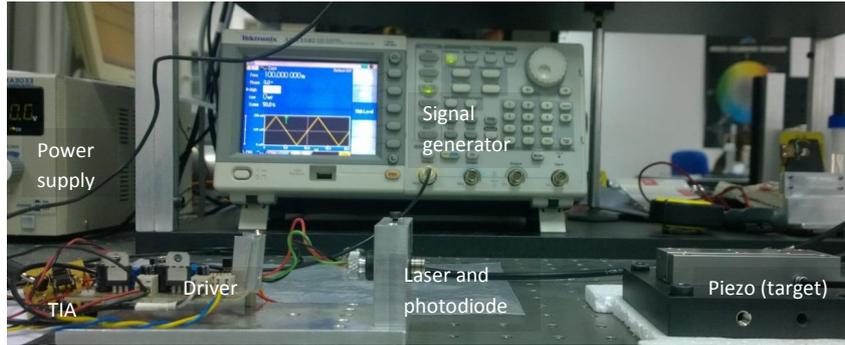
Figure 6.4: Experimental setup (TIA: Trans-Impedance Amplifier).

to have a larger number of fringes. The number of fringes, however, is a variable which may be freely modified in a majority of lab cases to adjust the performance of the sensor.

However, the constraint of having a large number of fringes in one ramp of the modulation signal to detect a larger bandwidth has another undesirable trade-off. Firstly, the increase in the number of fringes brings on an increase in the bandwidth of the OFS, so a detector with wide bandwidth is required to detect it. Secondly, in order to process the signal, a wide band filter, differentiator or amplifier is required to retrieve the fine details involved and hence to extract the vibration related parameters accurately. The design of such filter for a given experiment needs to take into account the bandwidth of the sensor. Finally, due to the coherent and differential nature of the CWFM-DOF sensor, the phase of the above mentioned detection and filtering stages needs to be set, so constant phase or phase linearity is maintained, making the design more complicated and difficult to attain in practice. Such complications are invtigated in more detail in Appendices C and D of this Thesis.

6.3   MEASURING PERIODIC VIBRATION

The experimental setup (based on the scheme presented in Fig. 6.1) to test the proposed methodology is shown in Fig. 6.4. Experimentally, a Hitachi HL6501 laser was used to test the method. The emission wavelength was measured with an Instrument System's SPECTRO 320(D) R5 unit. The laser was then directly modulated in intensity to obtain the desired frequency sweeping. Since under this operating conditions the laser may show mode hopping, a detailed analysis of its spectral characteristics as a function of the injection current was performed to locate the optimal operating point (Fig. 6.5). The operating point of the laser was selected as 48 mA, corresponding to an emission wavelength of 692.5 nm. The choice of this operating point intended to bring the laser close to its threshold, where the efficiency of OFI is optimal as suggested in [89]. The laser was kept powered on and under stable working conditions when acquiring the reference and vibration measurements. To produce the frequency sweep, the current to the laser was modulated using a triangular waveform with a peak to peak
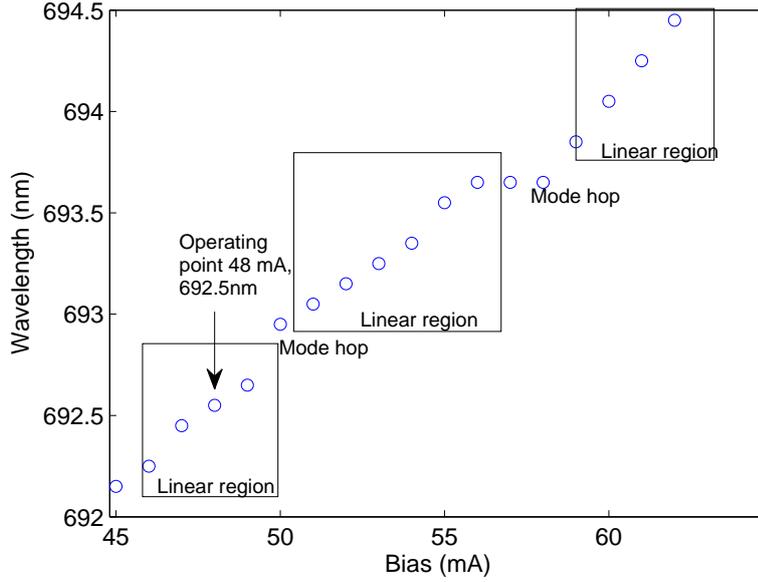
Figure 6.5: Variation of the emission wavelength with bias current. Ω_λ (calculated from the slope of the plot) is 0.1 nm/mA.

amplitude of 250 mV, which caused a change in modulation current A_m (pp) of 0.2 mA and a frequency sweep of $f_m = 100$ Hz. The laser was focused on the target using a Thorlabs lens 352240 with focal length of 8 mm and numerical aperture of 0.5 placed at a distance of 3.5 mm from the laser. A piezoelectric linear stage PI-LISA (P-753.3CD) placed at a distance of 12 cm from the laser was used as target, which includes an embedded capacitive sensor with a resolution of 0.2 nm [4], which, as in former arrangements, is used as a reference for the comparison of the obtained results. Previous to each measurement, the laser is set to work in the weak feedback regime and is allowed to attain a stable state. To dissipate the heat produced by the laser under operation, it is mounted on a heat sink made using an aluminium platform.

In a first step, a measurement of the reference condition is acquired (Fig. 6.6(a)) and denoised (Fig. 6.6(c)) using a *sym*6 wavelet transform. Although other families of wavelets could be used, *sym*6 wavelet contributed a significant enough improvement in noise reduction, and was used for simplicity against the more complex coding of the Morlet wavelet used in Chapter 4. This also follows directly from the choice made by authors in [197]. The time of occurrence of the reference fringes is then recorded. Next, the target is set into vibration by applying an AC sinusoidal signal with amplitude 55 mV and frequency 200 Hz to the piezoelectric stage using a signal generator, resulting in a 137.5 nm displacement measured by the embedded capacitive sensor [4]. Notice the frequency has been selected so the entire target vibration waveform lies within one ramp of the modulation signal. The choice of a target vibration frequency of 200 Hz is a result of different simulations and theoretical tests taking into account the limits in frequency performance of the piezo. Due to the type of target motion introduced,
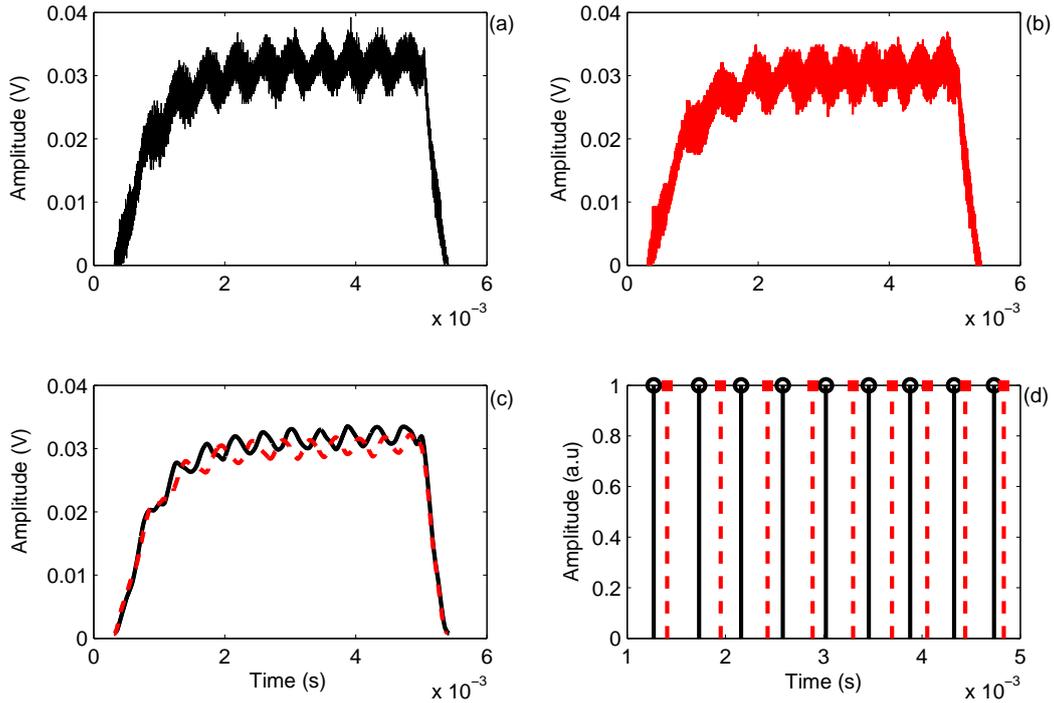
Figure 6.6: Experimental results. (a) OFS, reference case, after differentiation for separating the fringes from the ramp in the acquired signal; (b) OFS, vibration case, also after differentiation; (c) Denoised and differentiated OFS for reference (solid line) and vibration (dashed line) cases overlapped; (d) Shift in the time occurrence of the fringes in the vibration cases relative to the reference case, used as data for the calculation of displacement.

the optical path difference between the laser and the target changes periodically, resulting in a shift of the fringes when compared to the reference case. As in the reference case, the signal is acquired (Fig. 6.6(b)), denoised (Fig. 6.6(c)) and the time of occurrence of the vibration fringes is recorded. The fringe shift is easily appreciated in Fig. 6.6(d).

Once the time of occurrence of each fringe is computed for the reference and vibration cases, the target displacement is calculated using Eq. (6.5). Fig. 6.7 (a) shows the experimental target displacement retrieved, corresponding to the detected fringes resulting from a single oscillation of the target presented in Fig. 6.6, compared with the data obtained from the embedded capacitive sensor [4]. It should be noted that only one ramp is processed to get the full period of the target waveform (as the target vibration frequency was set to double the modulation frequency in the defintion of the experimental conditions), as seen in Fig. 6.7 (b). The experiment was performed nine times under equivalent conditions with similar results. The mean error in the measured amplitude (*pp*) in all measurements was 2.4 nm (shown in Fig. 6.8).

To gather more information on the repeatability and accuracy of the proposed methodology, an statistical analysis based on the classical t-test analysis was performed. A t-test analysis is a hypothesis testing method used when the sample size is small. Its shape resembles the normal

140
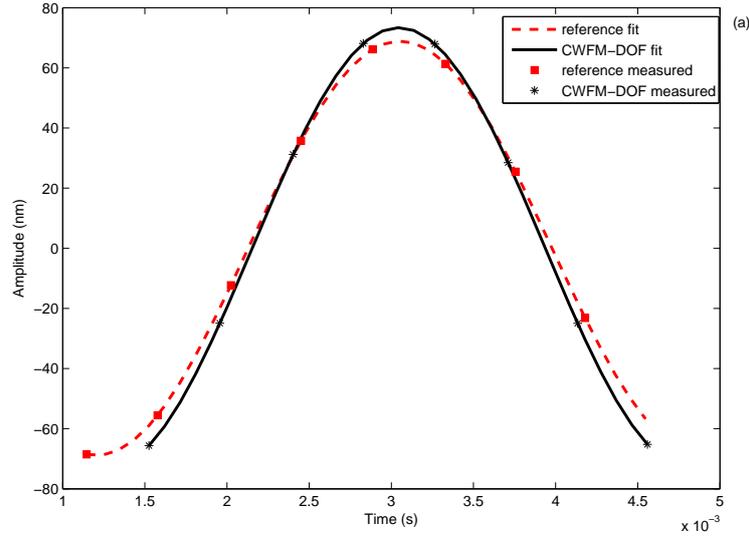
Figure 6.7: Experimental results (third measurement in a series of nine) in Fig. 6.8, with absolute residual error (*pp*) 1.5 nm). (a) CWFM-DOF sensor target displacement against embedded capacitive sensor [4]; (b) Direct oscilloscope view of the section of displacement under the fringes. (yellow) Vibration OFS (after differentiator), (pink curve) target motion. It clearly demonstrates that an entire cycle of target motion lies with in one period of modulation current. The markers (a and b in pink) measures the section of target motion from first fringe to its peak.

distribution for a larger number of samples [198]. A t-test of the null hypothesis shows the data in vector x (in this case the sample obtained from CWFM-DOF) and y (the samples obtained from the reference embedded capacitive sensor) have equal mean values, against the alternative that means were not equal [198, 199]. Using the $N_s = 9$ samples measured with a number of degrees of freedom $df = 2N_s - 2 = 16$ and a significance level[2] $\alpha_s = 0.05$, the probability of obtaining sample data given the null hypothesis was true is $p = 0.92$. The step-by step procedure of calculating a t-test analysis may be found in [198, 199]. Since $p > \alpha_s$, it is concluded that the

---

[2]The significance level is the probability of rejecting the null hypothesis (in this case, the mean of samples obtained from CWFM-DOF and that of the reference capacitive sensor is equal). In practice it is standardized as 5% (0.05). The physical meaning, in this particular case, is that a significance level of 0.05 indicates a 5% risk of concluding that a difference exists between them when there is no actual difference.
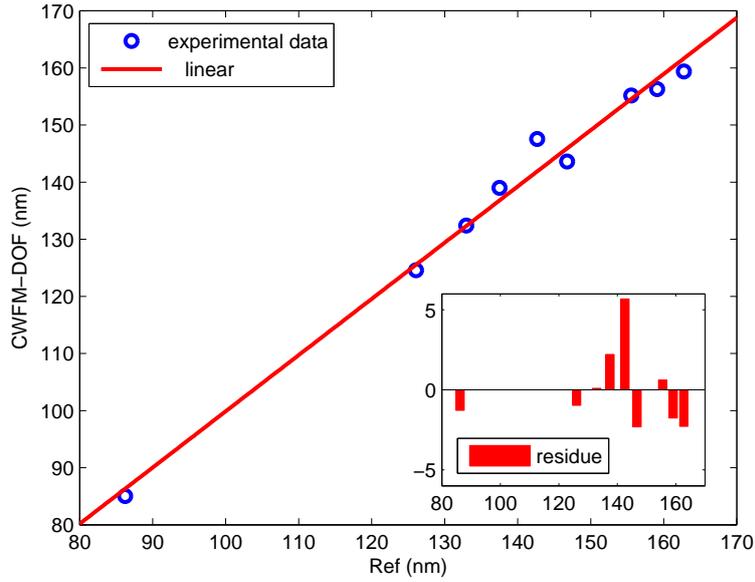
Figure 6.8: Experimental results. Comparison of the CWFM-DOF with the reference embedded capacitive sensor (inset gives the residue of the linear fit with reference sensor, in all cases are within the 5 nm range).

data samples from the proposed sensor and the reference (Fig. 6.8) have the same mean value with a 95% confidence level. For illustration purposes, the third experimental measurement, which had an error (*pp*) of 1.5 nm is shown in Fig. 6.7. Fig 6.8 shows the deviation of the linear fit expected from the comparison of the experimental measurement and the reference experimental displacement, which is in all cases smaller than 5 nm (shown in inset).

6.4 MEASURING DIFFERENTIAL DISPLACEMENT

The concept introduced above for measuring displacements smaller than half the emission wavelength can be extended to the measurement of differential displacements, as well. It is only needed to consider a modified reference case where the target initially vibrates with an amplitude lower than half the emission wavelength i.e. $A_{tr} < \lambda/2$, in difference with the previous reference case where the target is stationary. Under these conditions, since $A_{tr} < \lambda/2$, no additional fringes will be produced in the OFS signal, although the phase shift in the beam does occur. Now if a vibration case is set so the target is allowed to vibrate with amplitude A_{tv}, provided that $A_{tv} < \lambda/2$ and the sum of amplitudes accomplishes $A_{tr} + A_{tv} < \lambda/2$, an associated additional phase shift is produced compared to the reference case, which contains information about the target vibration although no extra fringes are present. Figure 6.9 shows the effect of target amplitude vibration on the phase of the CWFM-DOF signal compared with the conventional CWFM-OF signal (solid). It is observed that the variation in the amplitude of vibration of the target induces a proportional phase change. Thus, a one-to-one relationship

between the target vibration amplitude and the phase profile of the OFS is observed.

It is worth mentioning that both the displacement calculation in Sec. 6.3 based on CWFM-DOF and the *differential* displacement calculated in this section can be explained from the curves in Fig. 6.9. For instance, if we pick the $A_t = 0$ curve (red solid) as the reference case and any of the other curves where $A_t \neq 0$ (e.g. say $A_t = 0.01\lambda$) (cyan dash) for the vibration case, then this exactly gives the displacement calculation explained in Sec. 6.3. However, if any two curves such that $A_t \neq 0$ are chosen, say e.g $A_t = 0.01\lambda$ (cyan dash) for the reference case and $A_t = 0.05\lambda$ (blue dash) for the vibration case, then the manipulation of these curves yields the *differential* displacement calculation, which is the discussion carried out in this section. It is clear that the same principle which was used for measuring displacement in Sec. 6.3 can be extended to differential displacement as well. Based on this observation, a simulation with the parameters listed in Table 6.2 was performed as a proof of concept to measure differential displacements of the target. the frequency of vibration was again set to double the modulation frequency. It should be noted that, due to the arrangement, similarly to Sec. 6.2 (Fig. 6.2), only the first ramp of the OFS is processed to get the entire waveform describing the vibration of the target, and is presented in Fig. 6.10.
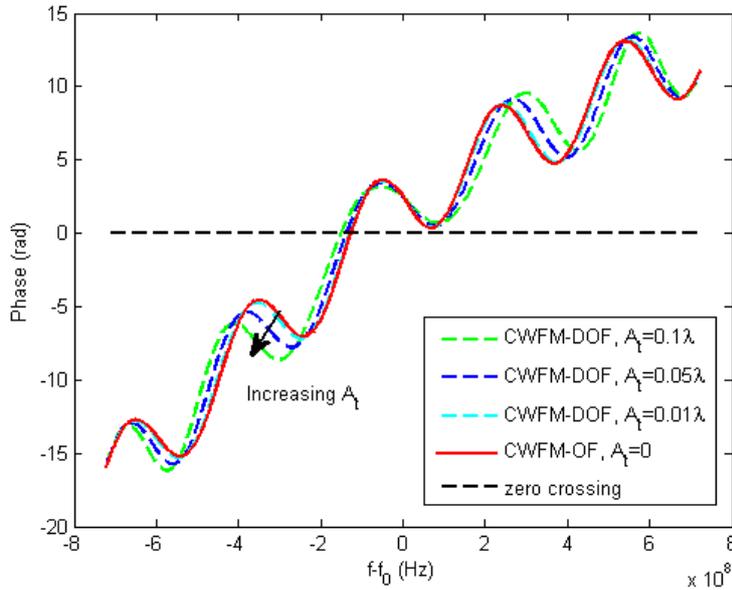
Figure 6.9: Phase change in the case of CWFM-DOF for different amplitudes of displacement of the target ($A_{tt} = 0.1\lambda, 0.05\lambda$ and 0.01λ) compared with coonventional CWFM-OF signal ($A_t = 0$). There exists a one-to-one relationship between the amplitude of vibration of the target and the phase of the OFS.

Table 6.2: Simulation parameters

Parameters	Value
Emission wavelength of the laser (λ)	692.5 nm
Distance of external target from the laser (L_{ext}) (forward path)	0.4 m
Peak to peak modulating current ($A_m(pp)$)	1 mA
Modulation frequency (f_m)	200 Hz
Amplitude of vibration of the target (reference case) (A_{tr} (pp))	0.3λ
Amplitude of vibration of the target (vibration case) (A_{tv} (pp))	0.2λ
Frequency of vibration of the target (f_t)	200 Hz
Differential displacement, $d(t)$ (frequency)	$A_{tr} - A_{tv} = 0.1\lambda$ (100 Hz)
Frequency modulation coefficient (Ω_f) [52]	-3 GHz/mA
Feedback strength (C)	0.9
Linewidth enhancement factor (α)	3
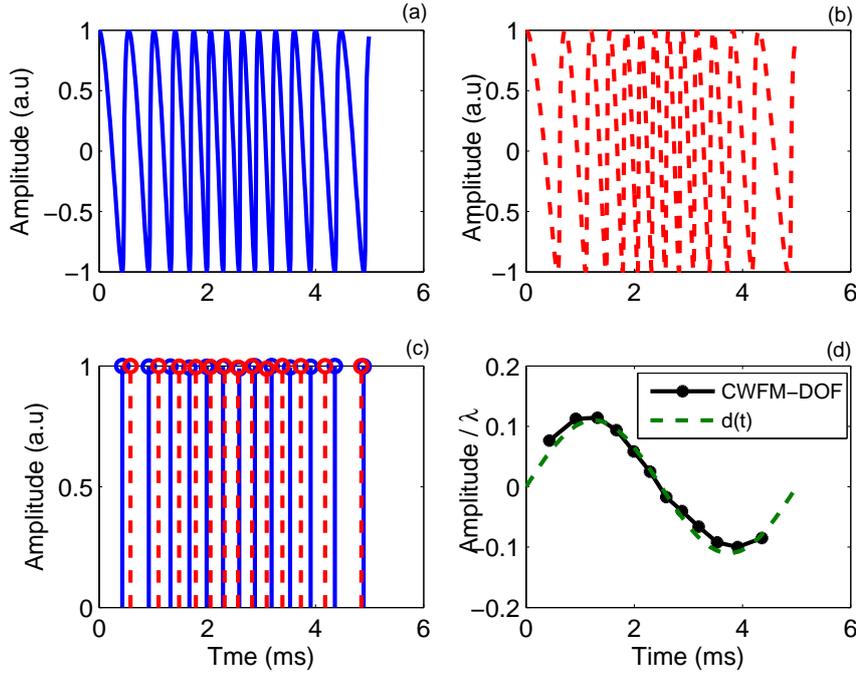
Figure 6.10: Results from simulation for differential displacement measurements using CWFM-DOF. (a) CWFM-DOF signal resulting from "modified" reference case (the target initially vibrates with amplitude $A_{tr} = 0.3\lambda$); (b) CWFM-DOF signal resulting from vibration case (the target amplitude is decreased to $A_{tv} = 0.2\lambda$); (c) Shift in the fringes obtained by comparing (a) and (b); (d) Differential displacement calculated using Eq. (6.5) computed differential displacement $d(t)$ [4].

Figure 6.11 shows the experimental results obtained using the experimental setup already presented in Fig. 6.4. In close similarity to Sec. 6.2, the laser is first modulated with a ramp-like triangular signal with modulation frequency $f_\mathrm{m} = 100$ Hz. Then, for the reference case,
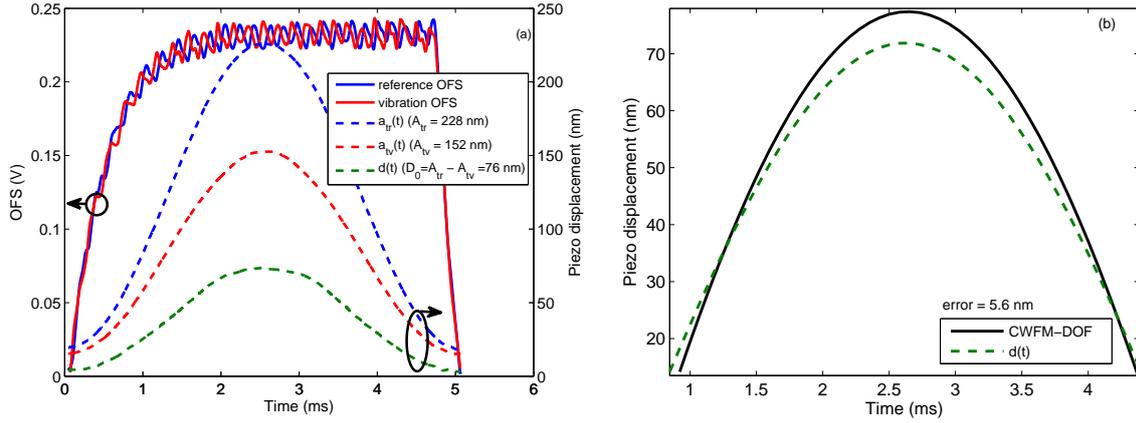
Figure 6.11: Experimental results for a differential displacement measurement using CWFM-DOF. (a) Reference and vibration fringes resulting from the reference and vibration case described, after modulation carrier removal. Dashed plots show the reference and vibration cases induced, and the expected differential displacement $d(t)$; (b) Experimental differential displacement measured and compared with reference.

the piezo (used as target) is vibrated with a sinusoidal signal with peak to peak voltage of 60 mV and frequency 200 Hz such that the entire waveform of target vibration is under one ramp. Using the conversion factor of the piezo elctric transducer [4], this voltage causes a sinusoidal displacement of the piezo $a(t)_r = A_{tr}sin(2\pi f_t t)$ with peak to peak amplitude $A_{tr} = 228$ nm (0.33λ) and frequency of vibration $f_t = 200$ Hz. The vibration of the target (dashed lines) and the fringes for the reference case (solid line) are shown in Fig. 6.11 (a) in blue. Keeping the setup unperturbed, the vibration case is set so the voltage applied to the piezo is decreased to 40 mV, causing the motion of the piezo to be $a(t)_v = A_{tv}sin(2\pi f_t t)$, with a peak to peak amplitude $A_{tv} = 152$ nm (0.22λ). The target vibration (dashed line) and fringes (solid line) for the vibration case are shown in Fig. 6.11 (b), in red. The shift in the fringes in both cases is significant and may be easily detected. Under these conditions, the differential displacement of the piezo is $d(t) = a(t)_r - a(t)_v = D_0 sin(2\pi f_t t)$, where $D_0 = A_{tr} - A_{tv} = 76$ nm (0.11λ). The differential displacement is shown in Fig. 6.11(a) as a green dashed line. From the measured shift in time of the fringes, the differential displacement of the target is calculated using Eq. (6.5) and compared with that of the embedded capacitive sensor used as reference [4]. The peak to peak error obtained reduces to 5.6 nm (Fig. 6.11 (b)).

Thus, the system can be extremely useful in the measurements of tiny displacements of the target, even with moving targets, so small perturbations of periodic movements may be easily detected, e.g. in the control of precision periodic displacements. The main drawback of this technique is the use of a dedicated differentiator (a low pass filter) upon the acquired OFS (in the reference and vibration cases) in order to detect the fringes. One critical parameter in the design of the differentiator for processing OFS is its bandwidth, which should be in principle larger than that of the acquired OFS, which in turn is dependent upon the frequency of vibration (f_t),

the modulation index (m) and the number of fringes N_f which appear in the application. The bandwidth of the differentiator needs then be tuned every time depending upon the particular features of the OFS to be acquired. This has a direct practical implication in the use of variable resistors or tunable capacitors, or to vary the different components in the electronic card used in acquisition. The detailed relationship between m and N_f to the bandwidth of the differentiator required to retrieve back the OFS with minimal error is explained in Appendix C. It is shown there that the optimal bandwidth of the differentiator is related to the ripple in the response of the filter allowed in the passband frequencies. The lower the passband ripple, the larger will be the effective bandwidth of the filter/amplifier, hence the lower will be the error in retrieving back the OFS. This dependence is a serious drawback, as a small passband ripple in a wide band differentiator is difficult to attain in practice. In addition, the requirement to have a constant phase effect of the filter used to process the reference and vibration fringes adds complexity to the hardware design. The conclusions drawn from the detailed analysis of these filters are shown as a graphical summary in Fig. 6.12. However, it is worth explaining different parameters again and how they contribute to the different trade-offs. One of the most desirable parameters is the N_f, as it contributes to better resolution in the retrieved displacement (Eq. (6.5)) and increases the bandwidth of the system (Sec. 6.2.2). This, as usual, involves a trade-off as it has undesirable effects such as the increase in the bandwidth of the OFS, which requires of filters/amplifiers of high bandwidth and gain to avoid losses in the detection of fine details in the OFS (Sec. C.3). In practice, the N_f can be increased by increasing the amplitude of current modulation (A_m) and/or the external distance (L_{ext}) from the laser to the target (Eq. (6.8)). However, they cannot be increased on demand. The former factor becomes limited by the laser specification, and in addition an increase in A_m may cause phenomenon such as multimodal behaviour of laser, mode hopping and linewidth broadening (**??**). These parameters in turn may make the use of the laser undesirable for OFI purposes. The later factor, and increase in L_{ext} may cause the feedback level to become lower, potentially reducing the efficiency of OFI and reducing the fringe visibility, making the detection of the fringes more difficult to detect and process. Another relevant parameter is the modulation index of the OFS (m). An increase in m has as direct effect an increase in fringe visibility that makes fringe detection easier. In addition, as explained in appendix C, it makes the OFS to have high power, making filters/amplifiers with low roll off applicable to filter and amplify the signal, a very desirable feature. However, it also has the adverse effect of an increase in bandwidth of the OFS (Appendix C.2), which brings on a requirement of high gain and bandwidth in filters/amplifiers in order to process the OFS and extract displacement related information.

Taking into account all these trade-offs and its associated drawbacks, which are introduced in the experimental OFS due to the use of a differentiator, a novel algorithm based on a zero phase filter (Appendix D) has been developed in order to detect the fringes offline, eliminating the need of a differentiator (Fig. 6.13). This algorithm will be applied to the measurement of
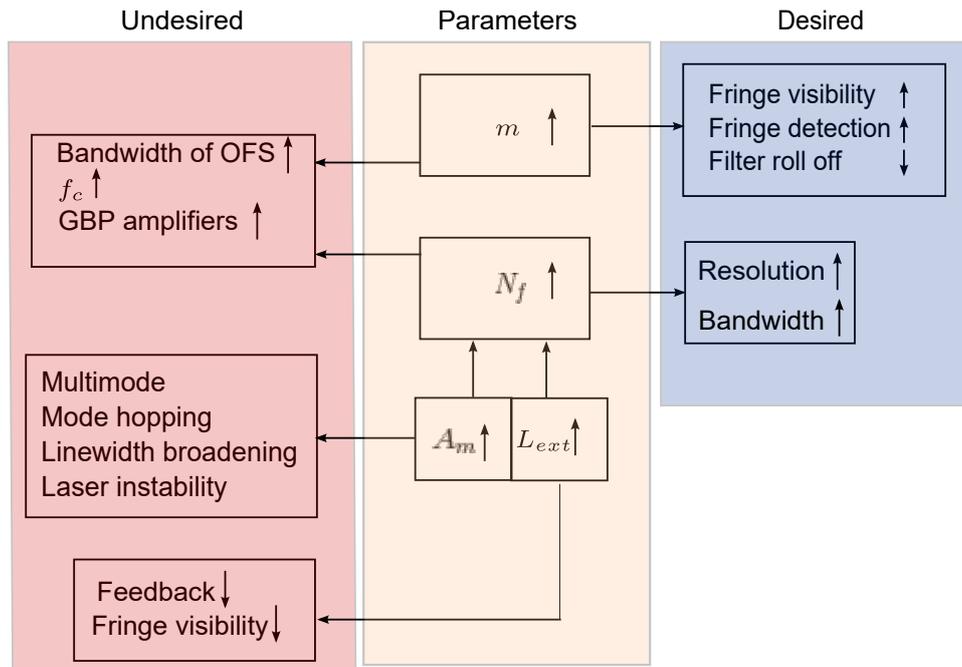
Figure 6.12: Summary of the effect of different experimental parameters on CWFM-DOF sensor performance. GBP is the product of the gain and the bandwidth product of filter/amplifier.

nanometric transient motions (a Gaussian pulse) explained in the following section.

6.5 MEASURING A TRANSIENT VIBRATION

In order to further prove the capabilities of the proposed methodology, it was applied to detect arbitrary waveform shapes. The schematics of the experimental setup are shown in Fig. 6.13. It is very similar to Fig. 6.1, except that the output of the PD is directly captured and used for processing, eliminating the dedicated active filter. The block-diagram of the signal processing steps involved is presented Fig. 6.14. Piezo is allowed to vibrate in the form of Gaussian pulse of width 4 ms and amplitude 63.8 nm (Fig. 6.15 (a)). The inset shows its spectrum obtained from the signal of the reference capacitive sensor. It should be noted that unlike the periodic sinusoidal signal, the spectrum of a Gaussian pulse is also Gaussian so the dominant frequency is around 200 Hz. As a first step of signal processing (Fig. 6.14), the zero phase FIR filter is applied to the reference and vibration OFS to obtain the smoothed signal without changes in the phase, which forms the reference for separating the fringes (shown in Fig. 6.15 (b)). For clarity, only the FIR filtered reference signal is shown. Then the reference and vibration OFS are subtracted from the filtered signal to obtain the fringes (Fig. 6.5(c)). Finally, from the shift of fringes in both the cases, and using Eq. (6.5), the displacement is retrieved showing an error (*pp*) of 4.05 nm measured under conditions comparable to that of Fig. 6.7 (Fig. 6.15 (d)). The relatively high error obtained in the Gaussian waveform reconstruction is due to the limited number of sample points available to track the rapid changes in the slope of the displacement, which give rise to rapid phase changes, as compared to the experiments in former Sections.
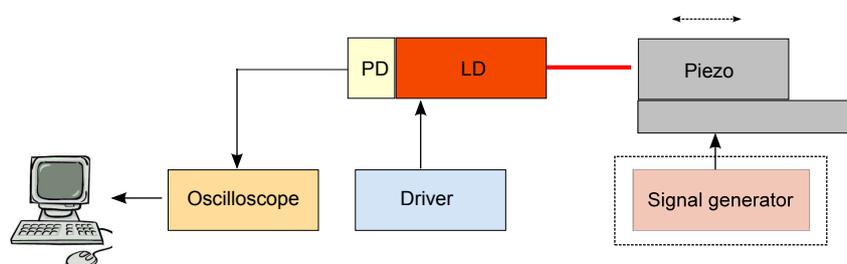
Figure 6.13: Experimental setup. Note the differentiator described in Fig. 6.1 has been eliminated following the comments in the end of Sec. 6.4
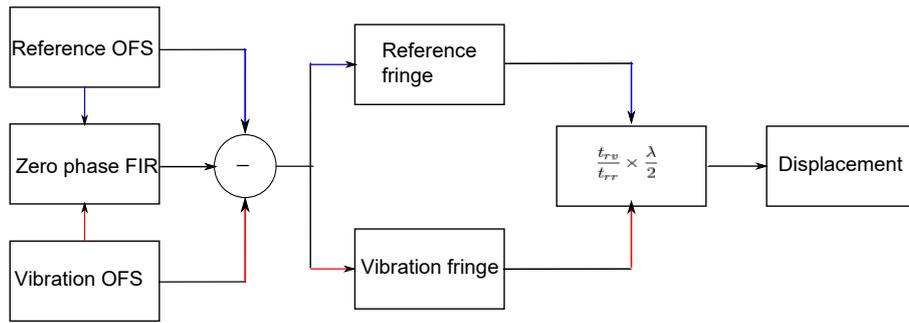
Figure 6.14: Signal processing using a zero phase FIR filter.
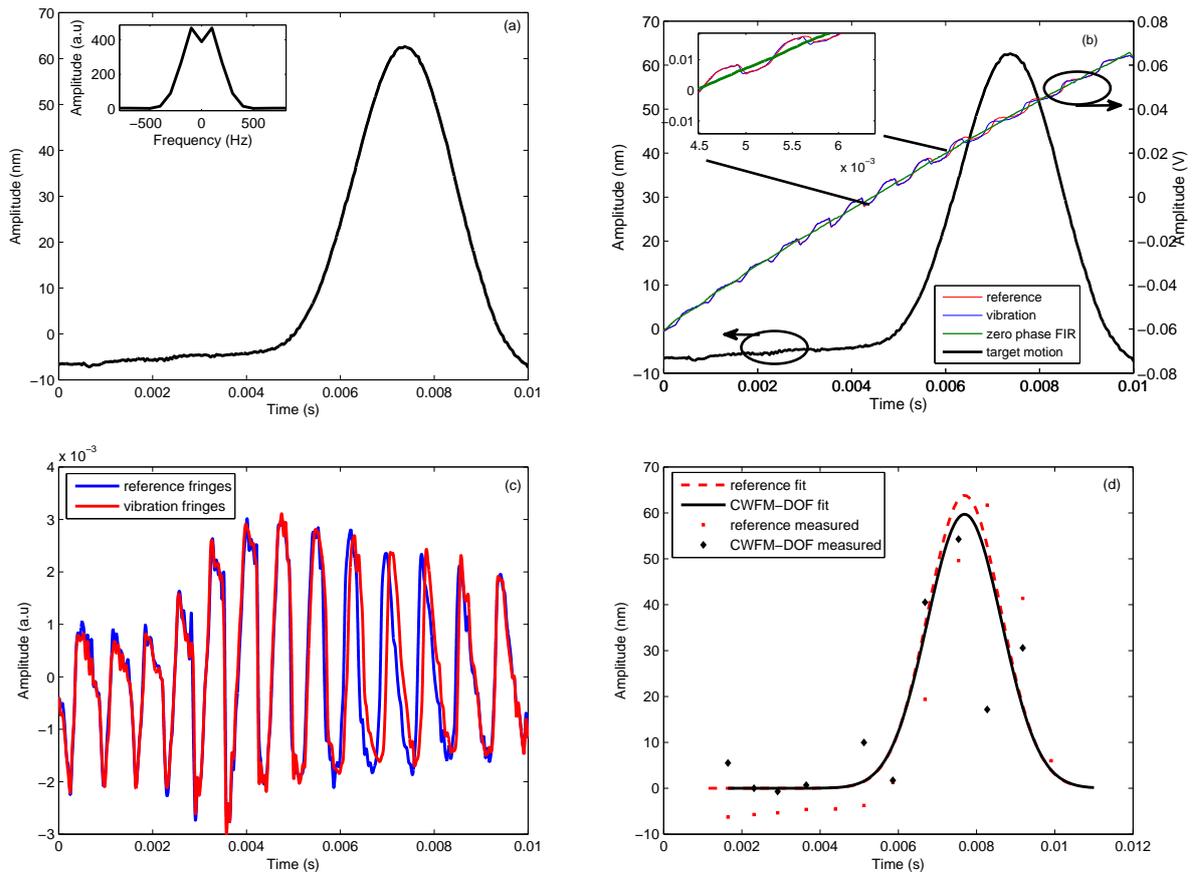
Figure 6.15: Experimental results. (a) Gaussian displacement of width 4 ms and amplitude 63.8 nm. The inset gives the spectrum of the Gaussian pulse showing a dominant frequency at 200 Hz (from the signal obtained with the reference capacitive sensor); (b) The reference and vibration OFS are shown together with the reference filtered signal (for clarity only the reference case is shown). Inset shows the magnified view; (c) Shift in reference and vibration fringes; (d) CWFM-DOF retrieved displacement compared with the reference capacitive sensor.

6.6 DISCUSSION:SPECTRAL EFFECTS DUE TO CWFMOF

A practical application of CWFM-DOF is proposed for measurement of displacement amplitudes in range 76-165 nm frequencies of $f_t = 200$ Hz (up to 27 kHz in Ch. 7) with an extremely

Figure 6.16: Experimental set-up to characterize laser under CWFM-OF. OSC: oscilloscope, PS: power supply, FG: function generator, SM: spectrometer, C: computer, T: stationary target, BS: beam splitter, L: lens, LD: laser diode, PD: photo-diode, DR: driver and modulator.

simple and cheap laser sensing strategy. Because of the limited number of fringes that translate to measurement points, error is introduced in the measured waveform. The accuracy of the CWFM-DOF method can be significantly increased by increasing the number of fringes, which in turn depends upon the amplitude of the modulation current, as commented in Sec. 6.2. To explore this approach, the detailed experimental analysis of the effects of the modulation current on the spectral properties of the laser, including linewidth, emission mode and fringe visibility, was studied. Fig. 6.16 shows the experimental setup. The laser used here is the HL8337MG model (used in Ch. 4 and to be used in Ch. 7). The laser is modulated using its driver from the signal generator. The IM laser emission is splitted into two paths (forward and orthogonal) using a conventional beam splitter. In the forward path, a stationary target is placed at distance of 10 cm from laser to produce CWFM-OF. The time domain CWFM-OF signal is monitored by an oscilloscope in the direct path. In the orthogonal path, the spectral features are simultaneously observed using an spectrometer. The output of the spectrometer is connected to the computer to visualize the spectral properties of the laser under CWFM-OF, while the oscilloscope simultaneously registers the time domain CWFM-OF signal. In order to differentiate the spectral properties of the laser in its free-running state and under CWFM-OF, it is desirable to measure the spectral properties of the standalone laser as well. To do so, the bias current to laser is not modulated, but set to $I_{op} = 48$ mA, and the forward path is set unperturbed (the stationary target in Fig. 6.16 is removed).

The experimental spectral properties of the standalone laser are shown in Fig. 6.17. It is observed that the laser is completely monomode and shows a neat Gaussian profile, with a center wavelength at $\lambda = 826.5$ nm, and a 3 dB linewidth (one sided)[3] which equals $\delta\lambda = 0.2$ nm. Next, the spectral properties under CWFM-OF, in particular the linewidth and the emission

---

[3]Since the linewidth of the laser is Gaussian in nature, the 3 dB width is calculated as the value of wavelength at which the value of intensity becomes 1/e of the peak value
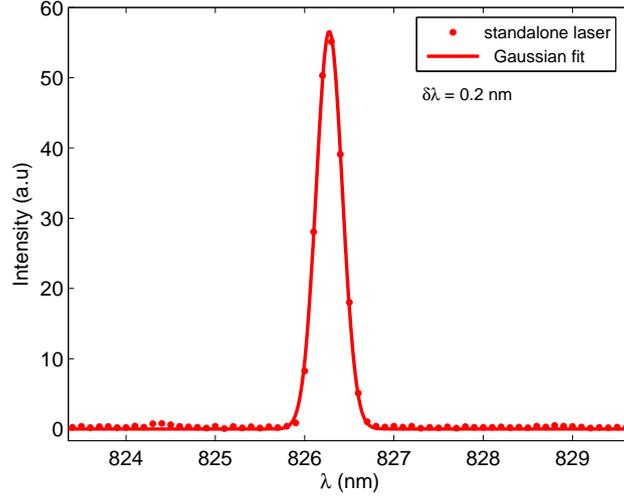
Figure 6.17: Laser emission mode in the standalone HL8337MG laser.
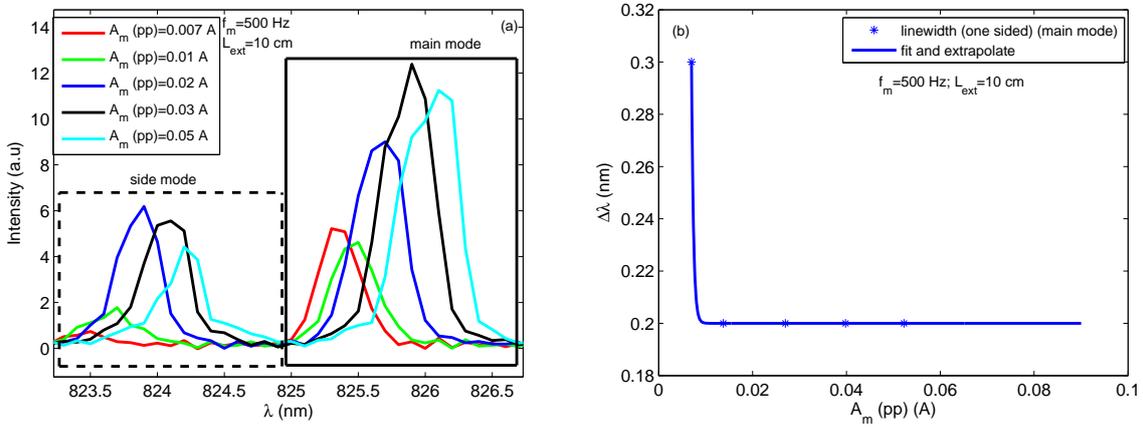
Figure 6.18: Effect of CWFM-OF on laser emission. (a) Additional modes appear as the modulation current increases; (b) Measured line width of main modes at different $A_m(pp)$.

modes of the laser are explored. As shown in Ch. 2, they critically determine the coherence of the laser and in turn the efficiency of the OFI phenomena in general. Fig. 6.18 (a) shows the effect of the amplitude of the modulation current (A_m (pp)) on the spectral properties of the laser, while keeping the modulation frequency constant at an arbitrary frequency of $f_m = 500$ Hz, and the distance to the target constant at $L_{ext} = 10$ cm. It is observed that an increase in $A_m(pp)$, brings on the appearance of undesired side modes in the laser emission, in addition to the main mode. Thus, the originally monomode free running laser has now additional side modes under CWFM-OF. However, such side modes are approximately one third of the main mode. In addition to the relative intensity of each mode (main and side ones), the linewidth of the emission is also a crucial factor which affects the efficiency and fringe visibility of the CWFM-OF signals. So, the 3 dB linewidth of the main mode for each $A_m(pp)$ is computed and shown in Fig. 6.18 (b). It is observed that the linewidth almost remains constant and equals
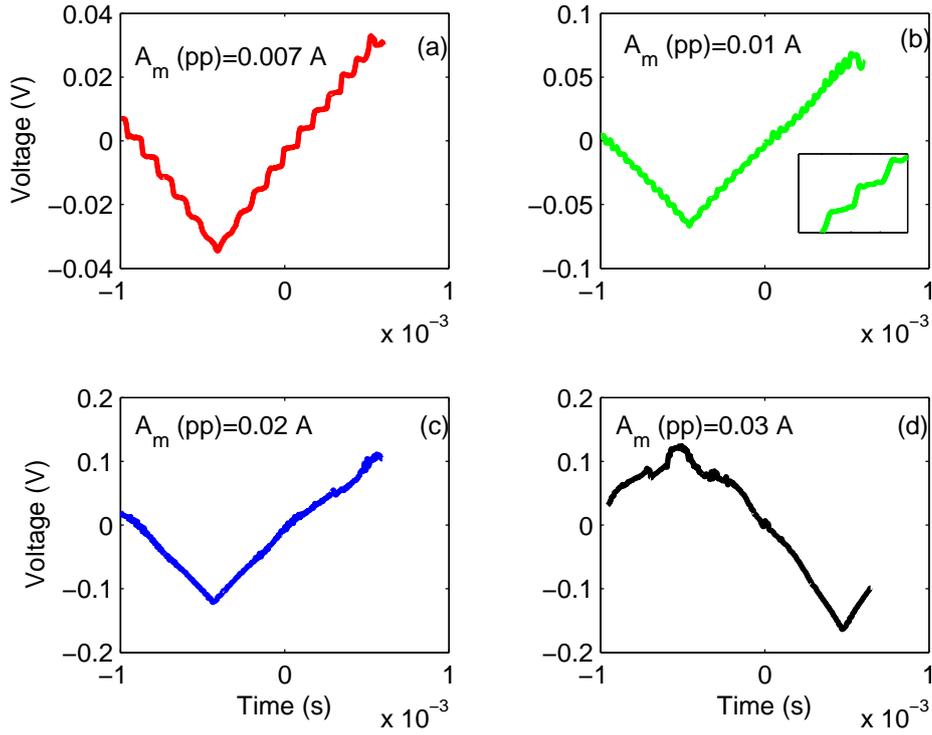
Figure 6.19: Effect of modulation current ($A_m(pp)$) on fringe visibility: (a) Fringes are visible; (b) fringe visibility degrades (inset gives the magnified view); (c)-(d) the fringes disappears. This could be due to the interaction of main and side modes explained in detail in Fig. 6.20.

that of the standalone laser. This is an important conclusion as it illustrates that the modulation current does not cause the laser to be "incoherent" under the experimental conditions defined above.

Note, however, what is happening simultaneously in the time domain regarding the fringes in Fig. 6.19: at a given $A_m(pp)$ value and beyond the fringes completely disappear. The interaction between the side and main modes, in our opinion, might have caused the severe fringe losses shown for the same experiment. It should be noted that the separation of the target from laser also might play its role, so the spectral properties of the laser might be totally different for different distances, although clearly an increase in amplitude of the modulation current brought on the degradation of the visibility of the fringes until them disappeared. Some more ideas can be drawn out of the shape of the envelope for the main and side modes as a function of $A_m(pp)$. Referring back to Fig. 6.18, the peak intensity of the main and side mode at different $A_m(pp)$ are shown in Fig. 6.20. The main conclusions drawn are (a) the spectral profile for both main and side modes are shifted Gaussian distributions. There exists a particular value of $A_m(pp)$ for which main modes reach a maximum intensity, and then it falls thereafter. The same can be said from side modes. In this particular case, maximum values are shifted in wavelength being
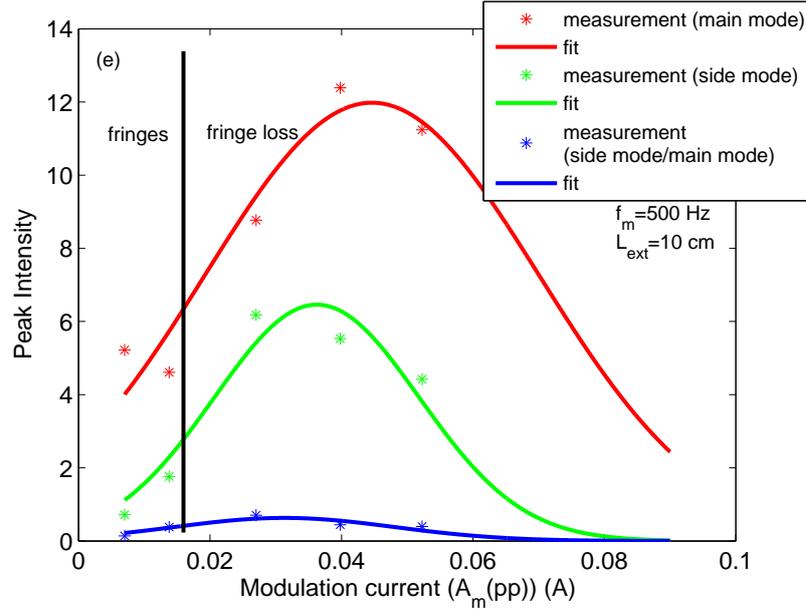
Figure 6.20: Comparison of the spectral properties of the laser under CWFM-OF at different $A_m(pp)$. The peak intensity of main and side mode have skewed Gaussian distributions as a function of the modulation current. The fringe visibility is lost when the ratio of intensity of the side and main modes becomes greater than 0.44.

44 mA for the main mode and 36 mA for the side mode; (b) A relationship between the $A_m(pp)$ value and the fringe visibility exists, and a relationship to the fraction of intensity in the side mode relative to the main mode was studied and established for the considered laser. Referring to Fig. 6.18 (a), at $A_m(pp)$=0.02 mA, the fringes are completely lost (Fig. 6.19) (c) and these condition corresponds to a ratio of intensities of side and main modes of 0.44 (visualized by the vertical line in Fig. 6.20). Thus, until the ratio is smaller than 0.44, the fringes are still visible and CWFM-OF can be used as an optical sensor. Beyond this value the fringes are lost and its functionality as a sensor becomes limited. Nonetheless, it is worth mentioning there are several parameters e.g. distance, frequency, or feedback strength to name a few that might alter the total behaviour of the spectral properties of the laser. To overcome such an spectral behaviour, the choice of DFB lasers could be an alternative owing to better spectral purity and stability, and should be analysed in detail. Further work related to the characterization of this spectral behaviour for different experimental parameters is currently being undertaken.

6.7 CONCLUSION

We have proposed and experimentally demonstrated a methodology to make use of the combination of direct laser injection current modulation to induce continuous wave frequency modulation (CWFM), and of nonlinear dynamic effects in a laser subject to optical feedback, to build a sensor able to measure nanometric amplitude displacements. The key contribution of this work is the use of a single laser diode to detect sub-wavelength target vibrations with nanometric ac-

curacies, using the modulation of the injection current and expanding the bandwidth of former differential SMI (DSMI) sensors [63] to at least the MHz frequency range in detection, depending upon the modulation frequency of laser, The mean peak to peak error of the proposed sensor out of nine different measurements of a single oscillation was shown to be 2.4 nm when applied to a periodic sinusoidal motion. Next, the scope of the technique was increased using the theoretical predictions related to the excess phase equation derived from the solution of the LK equation. Such predictions enabled to measure sub-wavelength differential displacements, that is, removing the restriction on the target to be stationary, and enabling accurate monitoring of sub-wavelength periodic displacements.

In addition, since the phase linearity of the differentiator is a small fraction of its total bandwidth and this induces errors in the reconstruction of the displacement of the target, a novel signal processing technique based on a zero phase FIR filter is implemented to process the OF fringes, thus eliminating the need of a differentiator to separate the fringes from the ramp. Based on this, a transient Gaussian pulse of width 4 ms and amplitude 63.8 nm is measured with an error of 4.05 nm pp. As a summary, a novel laser vibrometry sensor based on CWFM-DOF has been introduced with its maximum detectable target vibration limited to $\lambda/2$, and a bandwidth of the sensor proportional to the number of fringes in the OFS and the frequency of the laser current modulation.

Finally, we presented a discussion on the spectral consequences of the increase in $A_m(pp)$, which showed a significant increase in side modes which resulted, under given conditions and for the considered FP laser, in the complete lossof the fringes. Further work related to this spectral behavior under different parameters is currently under development.

7. Application of CWFM-DOF to the characterization of acoustic vibrations

7.1 INTRODUCTION

Acoustic wave sensing is currently a well established technology in non-destructive testing, with a number of applications where it has become the current standard. Although it is a very well established technology, its applications become limited due to the contact nature of their sensors, and the need of a well-suited propagating media for the acoustic perturbation. Besides, the need for sensitive methods for the detection and visualization of acoustic surface perturbations has grown with the increasing interest in fields such as ultrasonic or SAW detection [129], laser ultrasonics [200], acoustic trapped energy resonators [127] and acoustic holography [127, 128], among others.

In particular, with regard to surface or acoustic sensor devices, the vibration of the membrane reveals important information, as power flow and attenuation in the overall system. This is an information which is very relevant to design and manufacture acoustic transducers. In trapped energy resonators, for instance, the surface perturbations reflect the pattern of acoustic localization of the energy, which is essential for its utilization. Advanced testing methods for the dynamics of the membrane are required to develop reliable sensors, which could be used as systems for the measurement of the dynamic displacement and/or the vibration of the membranes of MEMS, ultrasound or acoustic transducers. In order to fully understand the behaviour of many of these devices used to generate and detect acoustic or ultrasound waves it is necessary to be able to measure the behaviour of their dynamic displacement [131,132]. Acoustic holography provides a complementary approach, with the wave emanating from the transducer and inciding upon the surface of the target. The incident acoustic pressure wave causes an instantaneous surface displacement, transferring the acoustic pattern to the interrogating optical beam, which when processed reveals the acoustic hologram [127].

As discussed in Ch. 6, optical methods permit to study the acoustic waves at any point in/on the specimen without either absorbing part of the energy or interfering with them in any way, as they are in another energy range and are inherently noncontact. However, the experimental setup required for optical acoustic wave detection are in most of the cases complex, bulky, and require the use of several optical and electrical components, making them difficult to apply in

industrial conditions. Even with this limitations, the use of lasers or optical methods to detect acoustic waves has been an emerging area of research. Authors in [7], for instance, have devised a simple setup using OF to measure acoustic fields in 2D without the complex setups of previous methods.

Further within this chapter, the CWFM-DOF method described in Ch. 6 is applied for the first time, to the best of our knowledge, to detect "pulsed" perturbations of nanometric amplitude generated by acoustic beams. More specifically, CWFM-DOF is used to measure the amplitude of vibration of the membrane of a transducer acoustically perturbed at a frequency of $f_t = 26$ kHz, and the instantaneous surface displacement of a remote target (an Aluminium plate 0.1 mm thick) under acoustic pressure. This Chapter is organized as follows. In Sec. 7.2, the AW generated by a general-purpose acoustic transducer is characterized in terms of pulse repetition time (T_t), pulse width (τ_t) and emission frequency (f_t), using the echo mode of the transducer. In Sec. 7.3, after some criteria are checked in order to ensure the amplitude of vibration of the membrane is smaller than half the emission wavelength, the CWFM-DOF method is implemented to characterize the membrane displacement. In Sec. 7.4, the instantaneous surface displacement of a distant remote target due to the acoustic radiation pressure is measured using CWFM-DOF. This concept of transferring the acoustic radiation pressure into surface deformation, and then to the optical beam forms the basis of the acoustic holographic principle and of holographic reconstruction [127, 128], although here it is exploited using a different approach. Finally, Sec. 7.5 ends this Chapter with a review of the conclusions and discussions attained.

7.2 CHARACTERIZING THE WAVE GENERATED BY AN ACOUS-TIC TRANSDUCER

In this section, the features of the wave generated by the acoustic transducer to be used as source in forthcoming sections is characterized in terms of frequency of emission (f_t), pulse repetition time (T_t) and pulse width (τ_t) using the echo mode of the transducer. When in echo mode, the transducer acts both as a transmitter and a receiver, where it can listen to its own transmitted signal using an oscilloscope.

The setup used is outlined in Fig. 7.1 (a). An Airmar's ATK50TDH Airducer [201] driven by the developer's module for evaluation of this family of transducers [202] is used as source of AW. The jumper settings on the board are adjusted such that the emission frequency lies within the range $25 - 34$ kHz, the pulse repetition rate is 3 Hz and the pulse period lies within $0.12 - 24$ ms. The output from the transducer is connected to the oscilloscope in order to characterize experimentally the AW pulse emitted in detail. The frequency of the AW generated is measured to be $f_t = 26$ kHz, within the expected range, and is shown in Fig. 7.1 (b), including a magnified inset around the main frequency. In addition to the main dominant frequency (26 kHz), and
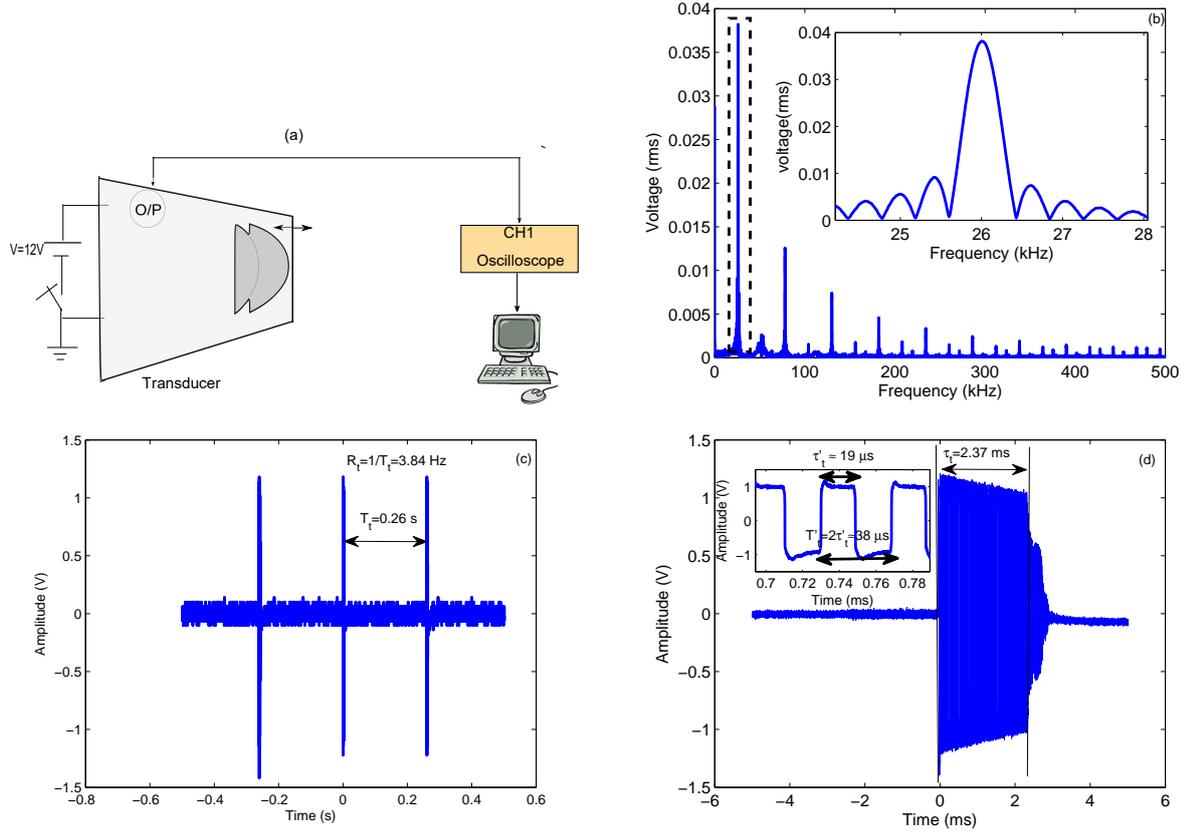
Figure 7.1: Characterization of the transducer under test in echo mode: (a) Schematics of the setup; (b) Frequency spectrum of the AW emitted by the transducer; (c) Pulse repetition rate of the AW; (d) Pulse period of the AW. Inset gives the magnified view of the AW pulse in (c).It consists of secondary AW pulses of width $\tau_t' \approx 19$ μs, and period $T_t' = 2\tau_t' \approx 38$ μs. Each secondary AW period consists of both a positive and a negative secondary AW pulse.

because of the pulsed nature of the AW generated, significant additional harmonics in the power spectrum are present as well. However, their amplitudes are three orders of magnitude smaller, so they can be ignored. The pulse repetition time of the AW is measured to be $T_t = 0.26$ s, which gives a pulse repetition rate ($R_t = 1/T_t$) of 3.84 Hz, shown in Fig. 7.1 (c). Finally, the AW pulse width is measured to be 2.37 ms, which is shown in Fig. 7.1 (d). Inset in (d) shows a very informative magnified view of the AW pulse in (c). It shows that the main pulse described up to now consists of a number of secondary AW pulses of width $\tau_t' \approx 19$ μs, with period $T_t' = 2\tau_t' \approx 38$ μs. Each secondary AW period consists of positive and negative secondary AW pulses. Thus, it is observed that all the measured parameters of the AW pulse emitted by the transducer lie within the range mentioned in the specification [202], and its precise values have been determined.

7.3 MEASURING THE DISPLACEMENT OF THE MEMBRANE OF THE TRANSDUCER USING CWFM-DOF

Fig. 7.1 (d) has shown that the secondary AW period was $T_t' = 2\tau_t' \approx 38$ μs, with each of its two pulses showing a width of $\tau_t' \approx 19$ μs. Our next step is to measure the amplitude of the vibration of the membrane of the transducer perturbed by the acoustic wave generated by itself.

As described in Chapter 6, in order to implement the CWFM-DOF setup it is necessary to superimpose the vibration waveform to be measured (in this case, the secondary AW pulses that cause the vibration of the membrane of the transducer) on the ramp of modulation current. Hence, the choice of the frequency of modulation f_m needs be fixed according to this criteria, although the procedure to choose f_m is limited by different factors (e.g. the number of fringes, see Ch. 6). To set f_m, let's suppose we want to measure the vibration of the membrane of the transducer due to only one of the secondary pulses of the AW. Hence, we need a ramp of the modulation signal of period equal to the complete secondary AW period ($T_t' \approx 38$ μs), making $f_m = 26$ kHz. At this frequency of modulation, the OFI fringes were clearly visible (Fig. 7.2). As CWFM-DOF needs the amplitude to be measured to be below half the emission wavelength, a first qualitative estimation of the magnitude of the amplitude of vibration is needed, based on the criteria of "absence of additional fringes". Fig. 7.3 shows the schematics of the experimental
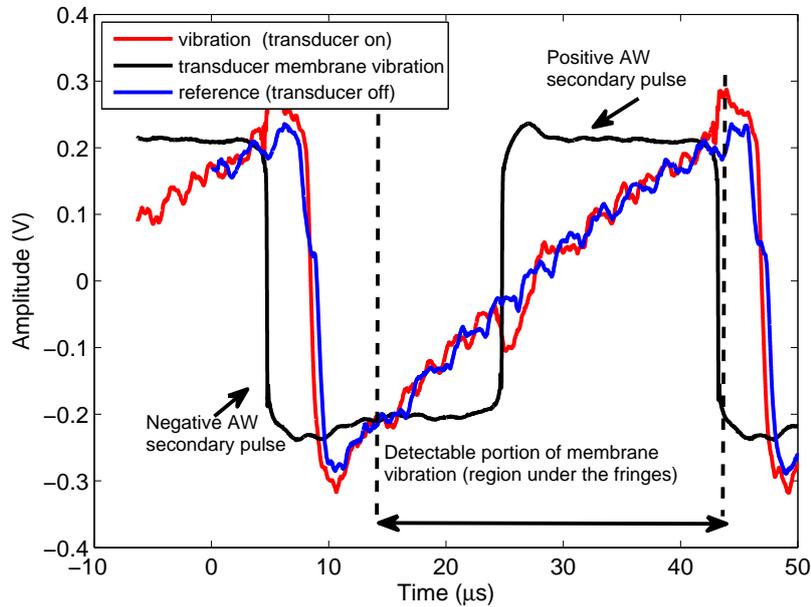
Figure 7.2: A full period (including a positive and a negative pulse) of the secondary AW waveform superimposed on the intensity modulation ramp. The ripples on the ramp are due to OF effect. The positive and negative secondary AW pulse are half the duration of the ramp and enclose equal number of fringes (five). Although the entire period of secondary AW waveform lies on one ramp, only the portion that lies between the fringes is detectable (the portion shown between the dashed boundaries).
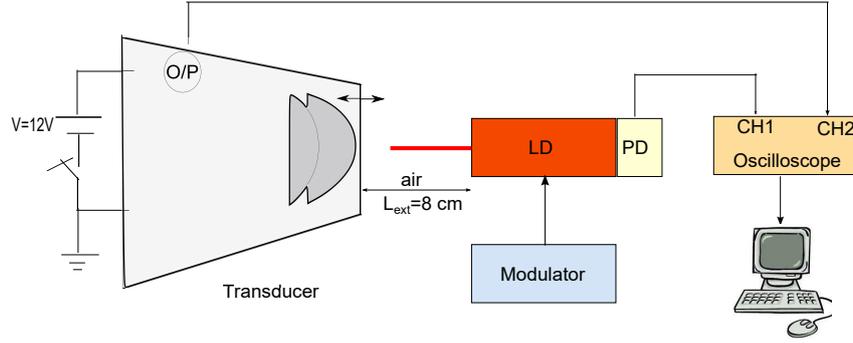
Figure 7.3: Schematics of the experimental setup to measure the amplitude of vibration of the membrane of the transducer.

Table 7.1: Experimental parameters.

Parameters	Value
Acoustic wave frequency (f_t)	26 kHz
Modulation frequency (f_m)	26 kHz
Modulation amplitude (ramp) (A_m (pp))	9.54 mA
Number of fringes/ramp (N_f)	11
Separation between laser and transducer (L_{ext})	8 cm
Laser emission wavelength (λ)	826.5 nm

setup used to determine the amplitude of the vibration of the membrane of the transducer.

An OpNext's AlGaAs laser diode HL8337MG with a MWQ structure is placed axially at a distance of $L_{ext} = 8$ cm from the transducer. A custom-built intensity modulator is used to modulate the injection current of the laser. A Thorlabs lens 352240 with focal length 8 mm and numerical aperture 0.5 (not shown in the figure) was placed at a distance of 8 mm from the laser to focus its beam onto the membrane of the transducer. First, the transducer is turned off, and a ramp modulation voltage of amplitude $V_m = 700$ mV and frequency $f_m = 26$ kHz, (as explained above) from the signal generator is applied to the driver, resulting in a current modulation of $A_m = 9.54$ mA (pp). The experimental parameters are listed in Table 7.1.

It is worth a small digression regarding the techniques implemented during the data acquisition, as they affect the results obtained, in specially regarding a discussion of the triggering strategy of both signals. Ideally, a double triggering is required, so the OFS and the secondary AW pulses are triggered separately and synchronously, so that one exact period of secondary AW pulses lies within one ramp of the OFS. The oscilloscope is configured such that the output of PD (thus, the OFS) is connected to channel 1 in the oscilloscope, and the output of the transducer (the secondary AW pulse) is connected to channel 2 (Fig. 7.3).

However, the oscilloscope available in the lab (a Tektronix's DPO2024) had only one trig-
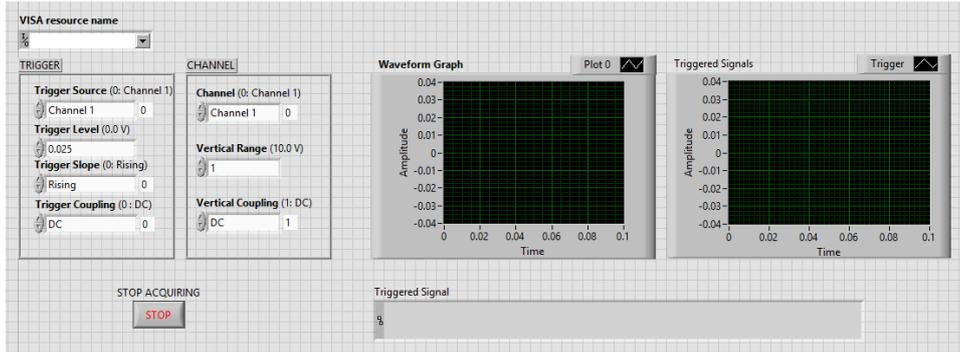
Figure 7.4: LabVIEW interface for acquiring the triggered OFS.

gering port, which was used to edge trigger the secondary AW pulses. So, the external edge triggering function available in LabVIEW was selected to trigger the OFS which was being acquired in Channel 1 in the oscilloscope. This is depicted in Fig. 7.4. Although such a technique enabled to acquire the required OFS, the synchronization of both signals was lost. Since the positive and negative secondary AW pulses need be imposed over a single modulation ramp, during the transitions in the AW pulses (coincident with the end of each period), the edge threshold could not be maintained and edge triggering did not work properly. As a second approach, pulse-width triggering was adopted in order to trigger the secondary AW pulses, while LabVIEW triggering was reserved for the OFS. Pulse-width triggering appeared as a reasonable alternative, as it applies to pulses that are smaller or larger than a certain specified width and in addition it can work both on positive or negative pulses [203, 204]. The triggering width was set to be equal to the width of the secondary AW pulses ($\tau_t' = 19$ μs). However, with this configuration, the effect of only one of the secondary AW pulses (say the positive) was acquired, leaving the effect of the second (negative) secondary AW pulse outside the triggering width, and thus unaccounted. It is stressed that this is a not a problem if oscilloscopes with two triggering ports, or external devices or electronics which can synchronize the two signals using some combinational logic circuits are available, which unfortunately was not our situation. Finally, we decided to first set the time scale of the oscilloscopes adjusted such that two secondary AW pulses (one period) is visible on the screen. Data acquisition for the reference case is then straightforward, as the transducer is off. In this situation, only the acquisition of the OFS is needed and this is done using the LabVIEW interface presented in Fig. 7.4. To capture the vibration fringes, the transducer is turned on, and the manual stop button on the oscilloscope is used so when two of them lie within the same ramp (triggered by LabVIEW) is again acquired by LabVIEW, the vibration OFS is acquired as well. One such acquisition is shown in Fig. 7.2.

Having set the data acquisition technique, the OFS for reference and vibration used for signal processing and extraction of the related vibration of the membrane case is acquired and shown in Fig. 7.5. Modulation ramps for both the reference and vibration cases are removed,
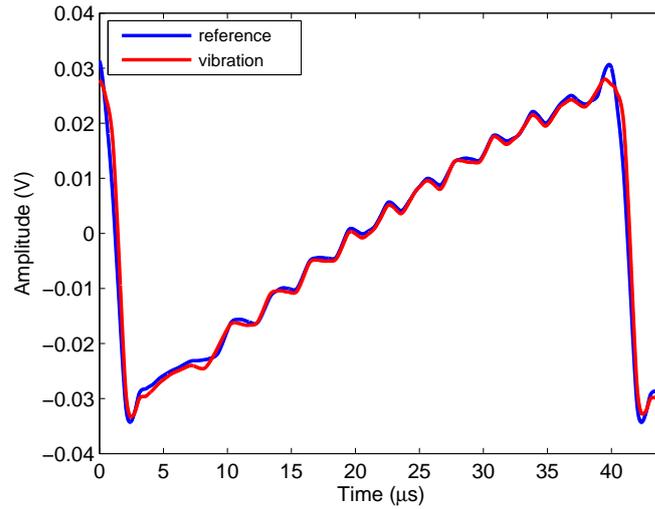
Figure 7.5: CWFM-OF signal obtained for the reference and vibration cases. The transducer in Fig. 7.3 is turned off (on) for reference (vibration) case.
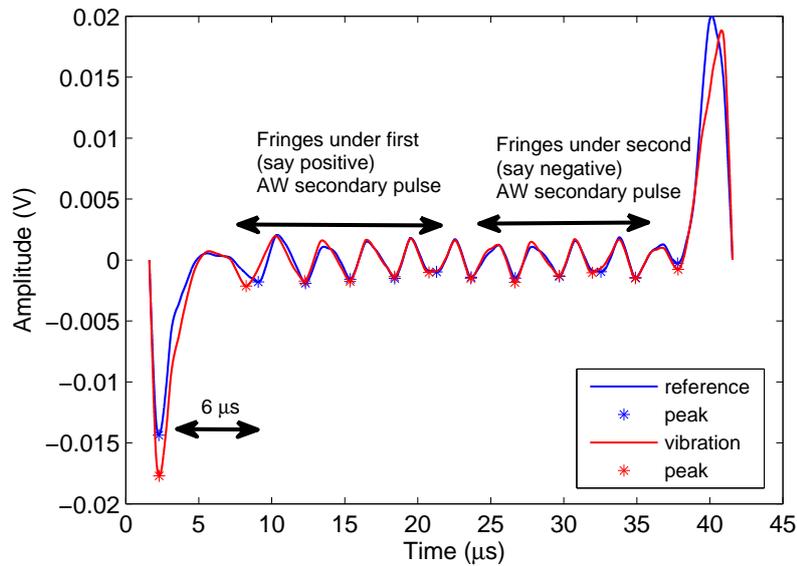
Figure 7.6: Shift in vibration fringes relative to reference fringes due to the membrane perturbed by the AW. First ramp from Fig. 7.5 is selected and peaks detected. The fringes at the edges are be not taken into account as they contribute to errors in measurement, so five effective fringes for each of the pulses are detected.

and the corresponding fringes have been detected using a zero phase FIR filter (Appendix D and Fig.6.14), and shown in Fig. 7.6. From the shift observed in the fringes, the amplitude of vibration of the membrane of the transducer is calculated using Eq. 6.5.

Finally, we need to account for the ambiguity of the direction of movement from the detected fringes. The fringes in the positive and negative secondary AW pulses are processed separately. Since the global effect of the positive and negative secondary AW pulse on the membrane of
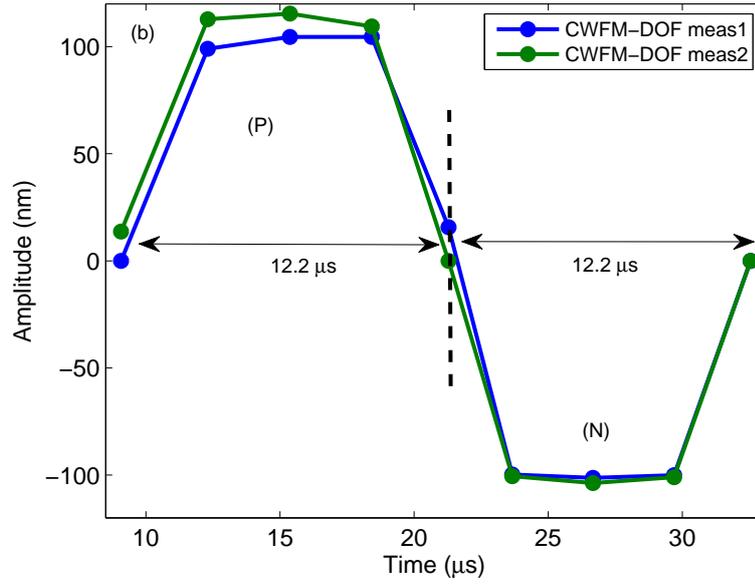
Figure 7.7: Vibration of the membrane of the transducer reconstructed using CWFM-DOF in two independent measurements. P (N) corresponds to the vibration of the membrane due to the positive (negative) secondary AW pulse. The displacement (pp) is 104.5 nm and 101.9 nm, and the pulse width is 12.2 μs wide in both cases, which should have added a fixed 6 μs value in both cases due to lost fringes. See text for details.

the transducer is known, we use our previous knowledge of the shape of the pulse to invert the displacement of the negative pulses. The reconstructed vibration of the membrane of the transducer using CWFM-DOF is shown for two independent measurements in Fig. 7.7 (a). Its amplitude (pp) is measured to be $A_t = 104.5$ nm, and $A_t = 101.87$ nm for the first and second measurements, respectively, and its respective durations $\tau_{tm1} = \tau_{tm2} = 12.2$ μs, which, when the extra 6 μs not accounted for due to the first (last) unprocessed fringe of the positive (negative) pulse are added fit very well with the amplitude of the pulse measured using the echo mode of the transducer ($\tau'_t = 19$ μs)).

It is confirmed, thus, that the pattern, the amplitude and the pulse width of the vibration of the membrane has been quantitatively measured in two independent measurements with a repeatability of 2 nm in amplitude and equivalent pulse widths, although the measurement of pulse width gets permanently biased in time by a constant value of 6 μs due to lost fringes at the edges of the modulation ramp.

7.4 DISPLACEMENT IN A METALLIC TARGET INDUCED BY THE ACOUSTIC PRESSURE WAVE

Once the amplitude of the vibration of the membrane induced by the AW is measured, the same concept is applied to detect the amplitude of the mechanical vibration induced in a separate
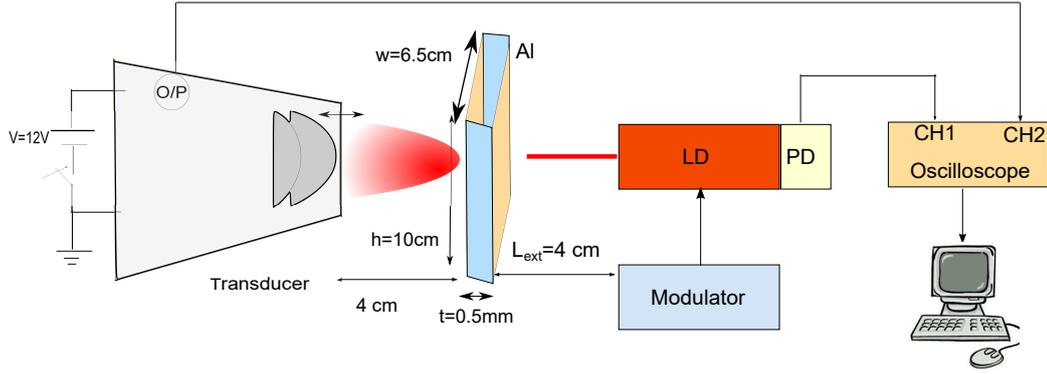
Figure 7.8: Experimental setup to detect the nanometric displacement in an Al plate using CWFM-DOF.

metallic (Al) plate. The schematics of the experimental setup are now shown in Fig. 7.8, which are similar to the one presented in Fig. 7.3, provided that an Al plate of dimensions width (w), height (h) and thickness (t) $650 \times 1000 \times 0.5$ mm respectively is placed between the laser and the transducer. The distance of the Al plate to the laser is set to $L_{ext} = 4$ cm, while its distance to the membrane of the transducer is also set to 4 cm. For the measurement procedure, in the reference case, the OFS is acquired using the same LabVIEW configuration described in Sec. 7.3. For the vibration case, because of the commented technical difficulties, the moment of time in which the transducer was turned on could not be transmitted to the LabVIEW interface. So an alternate automated iterative procedure for time triggering is used. The transducer is turned on and using the timer in the LabVIEW block diagram (shown in Fig. 7.9 by an arrow), the vibration-related OFS is continuously acquired along a 500 ms interval. This time is chosen so there is sufficient time for LabVIEW to acquire without flooding the buffer. About ten acquisitions are typically made. Finally, the reference and vibration fringes are processed to obtain the displacement waveform. Qualitative information about the displacement due to acoustic pressure wave (APW) is estimated depending upon the reconstructed displacement waveform. If it is symmetric, the pressure waveforms lies exactly on the ramp (desirable), while if it is asymmetric or skewed, the pressure waveform is shifted relative to the OFS (not desirable). After observing the reconstructed waveform, adjustments are made to the acquisition timing so again reference and vibration OFS are acquired and processed, until a symmetric displacement waveform is reconstructed. This confirms the triggering of the measurement has been set properly.

Similar to Sec. 7.3, first the transducer is turned off and a set of reference fringes are obtained (Fig. 7.10 (a)). Then, the transducer is turned on to get the vibration fringes. The bulk APW from the transducer propagates across the medium (air in this case) towards the Al plate, exerts a force on it, and causes it to displace from its equilibrium position. This nanometric displacement shifts the vibration from the reference fringes in a quantity which depends upon the amplitude of vibration(Fig. 7.10 (a)). Once again, by comparing the relative position of both sets of fringes in time, the amplitude of the displacement in the Al plate induced
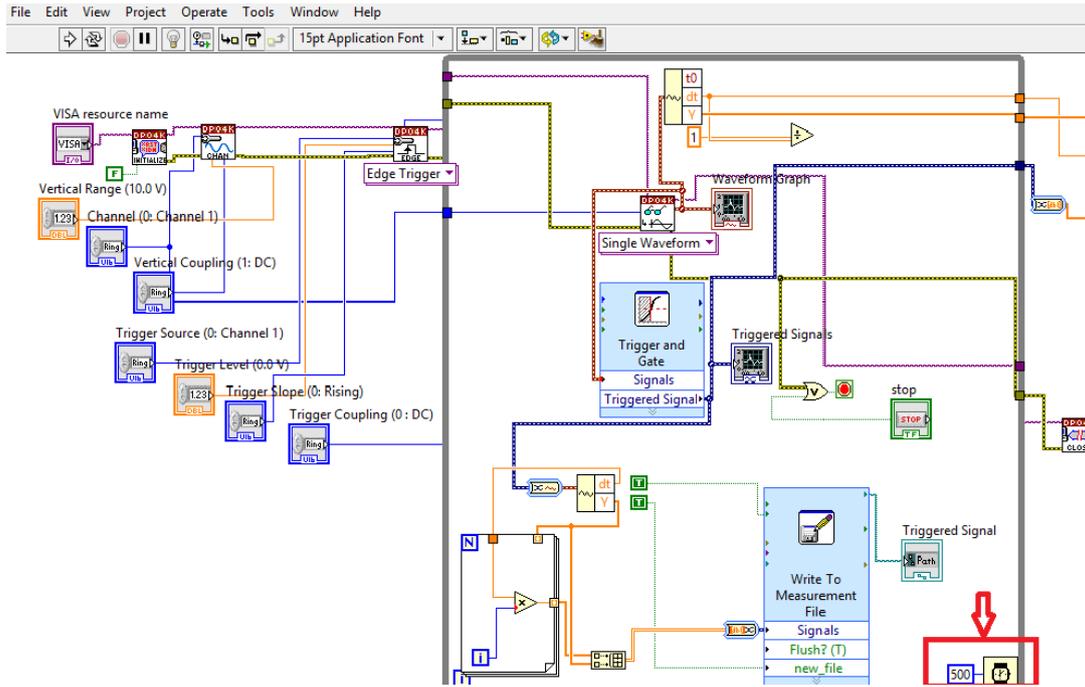
Figure 7.9: LabVIEW blockdiagram for data acquisition.

by the APW is determined (Fig. 7.10 (b)). The waveform is distorted as expected, although it follows the same pattern as the AW in the membrane [205].

As in the former case, a second measurement is also performed to estimate the repeatability of the experiment, and compared with the first one. Both measurements show that the displacement of the Al plate in the region sensed by the laser follows the pulsed-like pattern of the APW (Fig. 7.10 (b)), being approximately 14 μs wide in time, in good accordance with previous measurements. The amplitude of vibration of the Al plate perturbed by the APW is calculated to be 75 nm (pp) in the case of the positive secondary AW pulse and 80 nm (*pp*) for the negative secondary AW pulse. Results in amplitude are equivalent in both measurements, although the shape of the waveform present some deviations, as seen in Fig 7.10 (b). The reduction of amplitude compared to that of the measured vibration of the membrane of the transducer in Sec. 7.3, (Fig. 7.7) is assumed to be due to the attenuation in acoustic power in travelling from the transducer to the Al target, together with the mechanical absorbance of acoustic energy in the Al plate.

It should be noted that the reconstructed vibration in the Al plate is broadened when compared to the one from the transducer. Such a broadening in the reconstructed waveform could be because of the interaction of the AW with the Al layer. However, an insufficient number of sample points (just five fringes per pulse) are available to reconstruct the waveform vibration in detail, and the relaxation time of the Al plate could also have caused the described distortion. In addition, the increase in the amplitude of the vibration in the second pulse (78 nm) relative to the first (68 nm) in the reconstructed vibration, could be due to some bias introduced by the
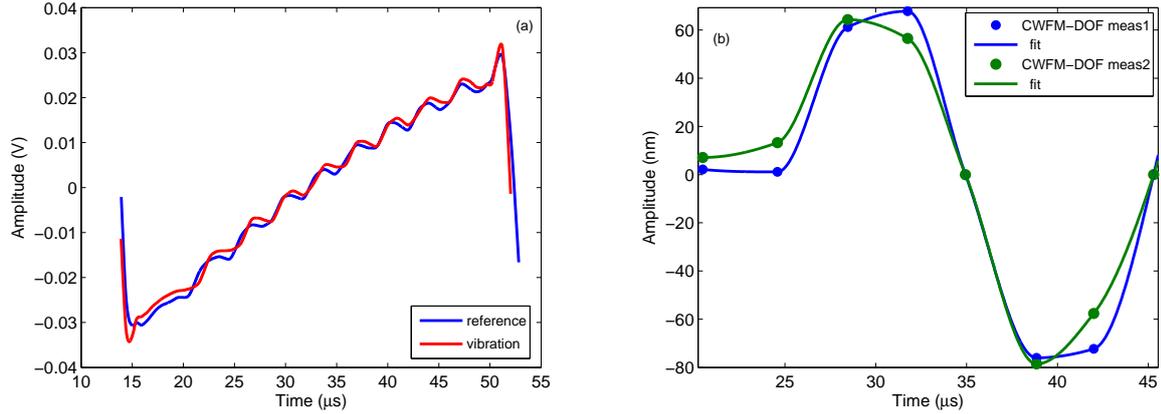
Figure 7.10: Detection of the displacement induced by the AW in the Al plate using CWFM-DOF: (a) Reference and vibration fringes; (b) Measured displacement in two independent cases calculated using CWFM-DOF.

positive secondary AW pulse on the negative.

7.5 CONCLUSION AND DISCUSSION

A practical application of CWFM-DOF has been proposed for the characterization of electro-mechanical devices and remote objects under a pulsed AW excitation of extremely small size at acoustic frequencies. It was demonstrated that the measurement of displacement amplitudes in the order of 100 nm at frequencies of $f_t = 26$ kHz was feasible using CWFM-DOF, an extremely simple and cheap laser sensing strategy where only a laser points to the target to be measured, controlled by simple electronics.

The concept of transferring the acoustic radiation pressure to the surface deformation and then to the optical beam is the basis of acoustic holography [127,128], hence CWFM-DOF may be one well suited alternative for sensing in acoustic holography setups. In this context, we demonstrated measurements of the induced vibration of the APW in a remote Al plate with amplitudes in the 75 nm range.

However, although results obtained are coherent and show the feasibility of the technique in this type of measurements, the simplicity of the setup and the limitations of the electronics available resulted in several inconveniences. First of all, an improved triggering strategy enabling a better control of the triggering of the AW, the modulation ramp and the OFS would greatly enhance the results of the experiment. Further, the limited number of fringes available, which translated to a limited number of measurement points, did not enable a satisfactory enough reconstruction of the measured waveform. The accuracy of the method can be significantly increased by increasing the number of fringes, which in turn depends upon the amplitude of the modulation current, as commented in Ch. 6. To explore this approach, further work in different types of lasers regarding the analysis of the effect of the modulation current on the

spectral properties of the laser at higher frequencies is being undertaken.

8. Conclusion

The aim of this research work has been to study the dynamics of the laser under OF such that controlled OF into its own cavity transforms the laser into a compact photonic sensor. In particular, the inclusion of an injection modulation has added a relevant variant to the classical OF sensor which makes the sensing more versatile. The combination of modulation and optical feedback turns the laser into a compact, economic, interferometric sensor useful for several real world sensing purposes, and in particular capable to measure sub-wavelength displacements by just pointing the laser onto the remote target under test and some signal processing. Further, the electronic modulation overcomes some of the limitations of former experimental setup, based on mechanical modulation.

The main contribution of this Thesis is the development of a variant of OFI based on the modulation of the laser current and its effects, which, based on a differential signal processing strategy is useful in measurements of displacement in periodic and non periodic signals well below half the emission wavelength. This has profound implications and increases the scope of OFI towards several relevant applications including LUS, PAT, or acoustic holography, to name a few. The study presented in this Thesis has intended to cover the full explanation of such a laser sensor, including the theoretical analysis of the dynamics of laser feedback with a laser under injection modulation based on the theoretical formulations available in the literature, the performance of simulations to analyze its performance in different conditions, and the design, execution and interpretation of a number of novel experiments which have been properly validated. Within this final chapter the major findings from the research activities presented in each Chapter will be summarized, and it will conclude with some relevant questions raised by the study, and suggestions for future research.

Along the different Sections a number of techniques have been examined to explain the effect of OF on the modulated laser and its use as a sensor. In Chapter 2, a detailed review of the theory which describes the semiconductor laser was reviewed, to make clear the origin of the full terminology used in this Thesis, and to introduce from the beginning the main parameters which become relevant in the description of the laser under a injection modulation. Next, the main approaches used to describe the laser under feedback in the literature were revised, including both the equivalent cavity and the Lang-Kobayashi model. At this point, a thorough review of the different reported applications of optical feedback was performed. We finalised this Chapter with a Section reviewing the different improvements applied to signal processing in order to improve and extend the performance of the OFI sensor, stating the basis from which we will described further Chapters of this work.

Particular attention has been paid along Chapter 3 to describe in detail the dynamics of the laser in response to OF based on scattering theory. To our knowledge, it is the first time that a complete model including the attenuation of the propagating optical field in each individual cavity, and its effects on the visibility of the fringes visibility produced by OFI is presented. It was demonstrated and quantified how the losses in each propagation media affect the visibility of the fringes, and hence the efficiency of OFI, and which are the main parameters involved and its role. One of the main strengths of scattering theory lies in the fact that the computation of all the effects involved as a transfer function of the system in presence of OF results in a simple matrix manipulation. This property has enabled to extend the same concept recursively to build a transfer function in a multiple cavity system. It was possible to incorporate in the model the effect of losses and phase relationships occurring in each individual cavity, quantifying its overall effect in the fringe visibility. Further, the model developed enables to predict the optimal depth of the cavity as a function of the reflection coefficient that corresponds to the maximal fringe visibility in a multiple cavity case. Hence, the model described the boundary conditions for the optimal OFS , and provides ways to improve fringe visibility by adjustments in the external cavities. This multiple cavity model including scattering is also developed, to our knowledge, for the first time, and paves the way for the extension of the use of OFI sensors into applications where multiple cavities exist, such as lab-on-chip or biomedical sensors.

Another relevant contribution of this work towards an improved OFI sensor was done along Chapter 4 , in the field of signal processing. Among the different signal processing techniques available in the literature to process the OFS and extract the vibration parameters of the remote target with the highest possible accuracy, most of them involve processing in the time domain (e.g. FC) to extract displacement or in the frequency domain (e.g. Fourier, PUM , IPUM) to extract the velocity and frequency of the vibration, but not both domains simultaneously. In this Thesis a novel technique based on wavelet analysis was proposed and experimentally demonstrated utilizing Morlet wavelets, localized *both* in the time and frequency domain. The advantage in the use of wavelets was shown to be three-fold. First, it results in a transformation of the OFS to a time-frequency plane, in opposition to Fourier and comparable techniques, which transfer the signal to the frequency domain while the time domain information is lost. This ensures its processing in a single shot in time and/or frequency, depending upon the application of the sensor and the parameters to be measured. Second, the use of Morlet as an analyzing wavelet transform translates the OFS to a complex plane, which has some added advantages, such as the use of PUM - like methods. Third, the wavelet transform is equally efficient in the management of different types of noise simultaneously (in particular, AWGN and impulsive noise), speckle management, and detection of the envelope of the signal and of the moment of occurrence of a discontinuity, all in a single shot. This avoids the need of low pass and median filtering at different moments, or the use of additional extensive setups and/or signal processing stages to track speckle. The proposed algorithm was first tested upon periodic signals (both

sinusoidal and triangular) to extract vibration-related parameters from the OFS. In particular, for the different experimental cases it was shown that wavelet analysis was able to combat AWGN and impulse noise equally well in a single step, while processing the OFS in the time domain, detecting fringes properly and limiting the error in reconstruction to within $\pm\lambda/2$, which is comparable to standard FC methods available by various authors in the literature. Next, making use of the information in the time-frequency plane and of the complex amplitude values of the wavelet coefficients, the reconstruction of the target displacement was improved and limited to a mean error of $\pm\lambda/10$. In addition, the vibration frequency of the target and its velocity were retrieved, with results equivalent to that obtained by Fourier analysis, in a single processing step. Finally, the same wavelet-based algorithm was tested to characterize a transient pulse, in particular a sinc function. The proposed algorithm enabled an exact retrieval of the center pulse time, the pulse width (with error 1.4 %), the moment in time which presented direction reversal, the instantaneous velocity profile, and the peak velocity (with an error 4.8 %) all in a single processing step.

Further, in addition to C-OF, another variant CWFM-OF was studied in detail and presented an interesting novelty which also extended the performance of OFI sensors. Chapter 5 analyzed a phenomena not described before, to our knowledge, which enables to maintain single mode behaviour in laser even in presence of strong feedback conditions. The phenomena is mathematically modelled out of the basis settled in Chapter 2, and experimental evidences of its theoretical predictions are presented. It is noticed that both optical feedback and intensity modulation cause the frequency of the emission of the laser to change, with the interesting feature that both act in opposite directions, so mutual compensation under certain optimal conditions may be attained. The laser dynamics subjected to OF and IM were modelled based on the LK rate equations. The formalism included the effect of different external parameters, such as distance, feedback strength, modulation current, and frequency of the IM on the number of modes emitted by the laser. Further, using CWFM-OF, an experiment was designed and implemented to measure the frequency modulation coefficient of the laser. Two different approaches were analyzed from the fact that in the case of CWFM-OF, the number of fringes can be altered either by changing the distance to the target or the amplitude of the modulation current ($L_{ext} = \lambda^2 N_f / 2\Delta\lambda$). Experimental results based on both approaches involving of thirteen measurements, confirmed that the frequency modulation coefficient of the laser was 0.005 nm/mA, which is consistent with several authors in the literature.

Chapter 6 was devoted to present a variant of optical feedback based on the interaction of C-OF and CWFM-OF, which we named CWFM-DOF. It is proposed in this Thesis to measure vibration waveforms with amplitude smaller than half the emission wavelength, and discussed how its resolution and bandwidth are dependent upon the distance of external target, the amplitude and frequency of the current modulation, and, in general the number of fringes, while its setup is essentially the same as that of C-OF. The proposed technique, thus, further

expands the use of OFI for a wider range of vibration measurements. Complete theoretical and mathematical descriptions were presented for the proposed technique, and the predictions of the mathematical model were confirmed by experiments. The proposed methodology was tested upon measurements of amplitude of both periodic and transient vibrations within the 65-160 nm range (*pp*). The errors were limited to 6 nm, backed by statistics and hypothesis testing (t-test) methods. Using the same set-up, a differential displacement of 76 nm was also measured with also within the 6 nm value.

Finally, along Chapter 7 the proposed CWFM-DOF sensor was applied to a real world application, in the shape of the measurement of acoustic vibrations. CWFM-DOF is a method limited to an amplitude of vibration smaller than half the emission wavelength, so the feasibility to measure the pulsed transducer membrane was first tested using CWFM-DOF. Then, a complete CWFM-DOF experimental setup for the measurement of the vibration of the membrane of an acoustic transducer was performed, measuring an acoustic frequency of 26 kHz, pulse width 18.5 μs and displacement of 100 nm, in good agreement with the values obtained from the transducer in echo mode. Further, the same setup was applied to the measurement of the instantaneous surface displacement of a remote metallic target due to the acoustic radiation pressure emanating from the transducer, which resulted in a 80 nm amplitude displacement. This concept of transferring the acoustic radiation pressure to surface deformation and then to optical beam is the basis of the acoustic holography principle and of holographic construction, making the proposed CWFM-DOF technique a well-suited candidate for its implementation.

Up to here, the list of development so far this Thesis has been presented. However, some pending tasks are remnant. Although the CWFM-DOF sensor has a wide bandwidth, dependent upon the modulation frequency of the laser, (see Section 6.2.2), we were limited to detect the target vibration at a frequency of just 26 kHz. Beyond this frequency fringe loss occured, either by some mode hopping effect or by some low pass filtering effect which limited the fringe visibility and its further detection at larger frequencies. There is, apparently, no fundamental limit to the use of a larger frequency, which, if raised to the MHZ range, would have significant applications. Thus, a further study of the phenomenon undergoing that loss of visibility of the fringes needs to be performed and sets the basis for a new PhD. With regard to this observation, the spectral properties of the laser and its response to C-OF, CWFM-DOF was studied.

A. Relaxation Resonance Frequency of Laser

To derive the Eqs. (2.36), (2.38) and (2.37), Eqs. (2.31) to (2.35) need be rewritten for ease of manipulation.

$$\frac{dN}{dt} = \frac{\eta_i I}{qV} - \frac{N}{\tau} - v_g a(N - N_{tr})N_p. \tag{A.1}$$

$$\frac{dN_p}{dt} = \Gamma v_g a(N - N_{tr})N_p - \frac{N_p}{\tau_p}. \tag{A.2}$$

$$I = I_0 + A_m e^{j\omega_m t}. \tag{A.3}$$

$$N = N_0 + N_m e^{j\omega_m t}. \tag{A.4}$$

$$N_p = N_{p0} + N_{pm} e^{j\omega_m t}. \tag{A.5}$$

Writing the value of I, N and N_p in Eqs. (A.1), we get

$$\frac{dN_0}{dt} + \frac{N_m e^{j\omega_m t}}{dt} = \frac{\eta_i I_0}{qV} + \frac{\eta_i A_m}{qV} e^{j\omega_m t} - \frac{N_0}{\tau} - \frac{N_m}{\tau} e^{j\omega_m t}$$
$$- v_g a(N_0 + N_m e^{j\omega_m t} - N_{tr})(N_{p0} + N_{pm} e^{j\omega_m t}) \tag{A.6}$$

$$= \frac{\eta_i I_0}{qV} + \frac{\eta_i}{qV} A_m e^{j\omega_m t} - \frac{N_0}{\tau} - \frac{N_m}{\tau} e^{j\omega_m t} \tag{A.7}$$
$$- (v_g a(N_0 - N_{tr}) - v_g a N_m e^{j\omega_m t})(N_{p0} + N_{pm} e^{j\omega_m t})$$

$$= \frac{\eta_i I_0}{qV} + \frac{\eta_i}{qV} A_m e^{j\omega_m t} - \frac{N_0}{\tau} - \frac{N_m}{\tau} e^{j\omega_m t} - v_g a(N_0 - N_{tr})N_{p0} \tag{A.8}$$
$$- v_g a(N_0 - N_{tr})N_{pm} e^{j\omega_m t} - v_g a N_m N_{p0} e^{j\omega_m t} - v_g a N_m N_{pm} e^{j2\omega_m t}$$

Equating the constant terms of both sides to zero as they do not change with time, and using $a(N_0 - N_{tr}) = g_{th} = 1/\Gamma v_g \tau_p$ (Eqs. (2.9) and (2.16)), and neglecting higher harmonics, we get

$$\frac{dN_m}{dt} e^{j\omega_m t} = \frac{\eta_i A_m}{qV} e^{j\omega_m t} - \frac{N_m}{\tau} e^{j\omega_m t} - \frac{N_{pm}}{\Gamma \tau_p} e^{j\omega_m t} - v_g a N_m N_{p0} e^{j\omega_m t}. \tag{A.9}$$

Eq. (A.9) gives the rate of change of carrier concentration with IM. Further, using the time frequency duality, $d/dt \to j\omega$ and cancelling $e^{j\omega_m t}$ both sides, its effect in the frequency domain is computed as

$$j\omega_m N_m = \frac{\eta_i A_m}{qV} - \frac{N_m}{\tau} - \frac{N_{pm}}{\Gamma \tau_p} - v_g a N_m N_{p0}. \tag{A.10}$$

Proceeding similarly, putting the value of I, N and N_p in Eq. (A.2), we get

$$j\omega_m N_{pm} = \Gamma v_g a N_m N_{p0}. \tag{A.11}$$

To find the equation of resonance frequency ω_R, Eqs. (A.10) and (A.11) are multiplied, the higher harmonics are ignored and the coefficient of $N_m N_{pm}$ are equated in both sides so

$$-\omega_R^2 N_m N_{pm} = -\frac{\Gamma v_g a N_m N_{p0} N_{pm}}{\Gamma \tau_p}. \tag{A.12}$$

On further simplification, the equation of resonance frequency of laser is given by

$$\omega_R^2 = \frac{v_g a N_{p0}}{\tau_p}. \tag{A.13}$$

and using $N_{p0} = P_0/h\nu v_g \alpha_m V_p$ from Eq. (2.25) and $\Gamma = V/V_p$ (defined in Eq. (2.8)), it gets to

$$\omega_R^2 = \frac{\Gamma v_g a}{\tau_p} \frac{P_0}{h f_0 v_g \alpha_m V_p}. \tag{A.14}$$

using $v_g \tau_p = 1/(\alpha_i + \alpha_m)$ (from Eq. (2.16)) and $\eta_d/\eta_i = \alpha_m/(\alpha_i + \alpha_m)$ (defined in Eq. (2.27)), the equation for resonance frequency in terms of the optical power output from the laser is given by

$$\omega_R = \left(\frac{\Gamma v_g a}{h f_0 V} \frac{\eta_i}{\eta_d}\right)^{\frac{1}{2}} \sqrt{P_0}. \tag{A.15}$$

Similarly, using $P_0 = \eta_d \frac{h f_0}{q}(I - I_{th})$ from 2.27, the resonance frequency of the laser is expressed in terms of bias current as

$$\omega_R = \left(\frac{\Gamma v_g a}{qV} \eta_i\right)^{\frac{1}{2}} \sqrt{(I - I_{th})}. \tag{A.16}$$

B. Transfer function of the laser

The transfer function of the laser is defined as the ratio of output power to the input current. Mathematically it is defined as $H(\omega_m) = P_{ac}(\omega_m)/A_m(\omega_m)$. The equation for transfer function of the laser is well derived from the resonance conditions as follows. From Eq. (A.11),

$$N_m = \frac{j\omega_m N_{pm}}{\Gamma v_g a N_{p0}}. \tag{B.1}$$

Now, placing the value of N_m from Eq. (B.1) in Eq. (A.10)

$$j\omega_m(\frac{j\omega_m N_{pm}}{\Gamma v_g a N_{p0}}) = \frac{\eta_i A_m}{qV} - j\omega_m\frac{N_{pm}}{\Gamma v_g a N_{p0}\tau} - \frac{N_{pm}}{\Gamma \tau_p} - v_g a N_m N_{p0}. \tag{B.2}$$

Using the value of N_m from Eq. (B.1) and $v_g a N_{p0} = \omega_R{}^2 \tau_p$ from Eq. (A.13), we get

$$-\frac{\omega_m^2 N_{pm}}{\Gamma \omega_R^2 \tau_p} + j\omega_m\frac{N_{pm}}{\Gamma \omega_R^2 \tau_p \tau} + \frac{N_{pm}}{\Gamma \tau_p} + j\omega_m\frac{N_{pm}\omega_R^2 \tau_p}{\Gamma \omega_R^2 \tau_p} = \frac{\eta_i A_m}{qV}. \tag{B.3}$$

$$N_{pm}\frac{1}{\Gamma \tau_p}[(1 - \frac{\omega_m^2}{\omega_R^2}) + j\frac{\omega_m}{\omega_R}(\frac{1}{\omega_R \tau} + \omega_R \tau_p)] = \frac{\eta_i A_m}{qV}. \tag{B.4}$$

and now using $N_{pm} = P_{ac}/hf_0 v_g \alpha_m V_p$ from Eq. (2.25),

$$\frac{P_{ac}}{hf_0 v_g \alpha_m V_p}\frac{1}{A_m}\frac{1}{\Gamma \tau_p}[(1 - \frac{\omega_m^2}{\omega_R^2}) + j\frac{\omega_m}{\omega_R}(\omega_R \tau + \omega_R \tau_p)] = \frac{\eta_i}{qV}. \tag{B.5}$$

$$\frac{P_{ac}}{A_m} = \eta_i\frac{hf_0}{qV}v_g \alpha_m V_p \Gamma \tau_p \frac{1}{[(1 - \frac{\omega_m^2}{\omega_R^2}) + j\frac{\omega_m}{\omega_R}(\frac{1}{\omega_R \tau} + \omega_R \tau_p)]}. \tag{B.6}$$

Finally, using $v_g \tau_p = 1/(\alpha_i + \alpha_m)$ (from Eq. (2.16)), $\Gamma = V/V_p$ (defined in Eq. (2.8)) and $\eta_d = \eta_i \alpha_m/(\alpha_i + \alpha_m)$ (defined in Eq. (2.27)), the transfer function of laser is obtained as

$$\frac{P_{ac}}{A_m} = \eta_d\frac{hf_0}{q}\frac{1}{[(1 - \frac{\omega_m^2}{\omega_R^2})\frac{1}{\Gamma \tau_p} + j\frac{\omega_m}{\omega_R}(\frac{1}{\omega_R \tau} + \omega_R \tau_p)]}. \tag{B.7}$$

C. Frequency domain analysis of OFS

C.1 FREQUENCY SPECTRUM OF THE INTENSITY MODULAT-ED SIGNAL

From Fourier analysis, the bandwidth of the triangular signal which modulates the laser is not limited to a particular fundamental modulation frequency, as it contains a significant number of odd frequencies and harmonics as well. The spectrum of the intensity of the IM laser output by a triangular waveform is shown in Fig. C.1. It is evident that even though the fundamental frequency (at 3 dB) is 24 kHz, the IM signal output of laser is wide band and extends up to approximately 0.2 MHz. This is expected because the triangle waveform not only contains a single fundamental frequency, but a number of harmonics as well, making the spectrum broader.

To properly design an active filter (or amplifier) for processing electronically the resulting OFS, it is necessary to carefully answer the following question: What is the minimal bandwidth of the filter (or amplifier) required to properly retrieve the triangular signal back? The optimal bandwidth (which is defined by its cut-off frequency f_c) is a function of filter type, order and
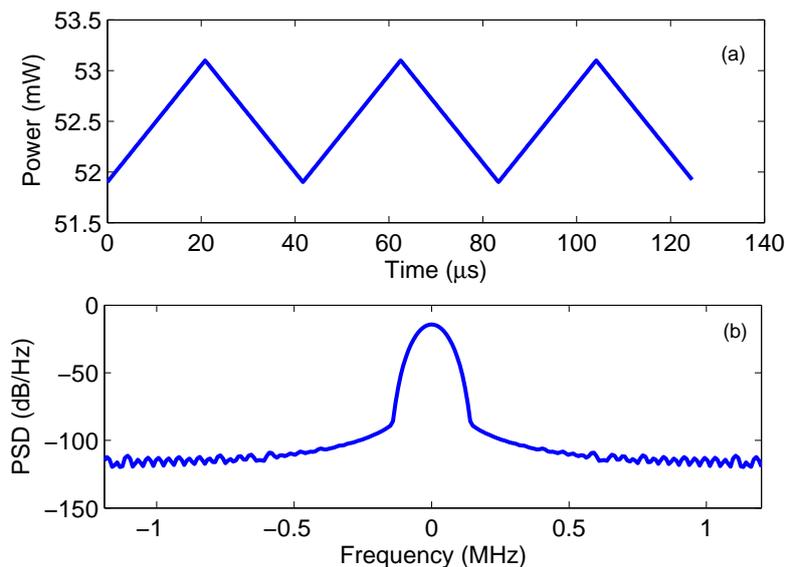
Figure C.1: (a) Power emitted by a laser modulated by an IM triangular waveform at 24 kHz; (b)Frequency spectrum of an IM signal. The 3 dB bandwidth is $\approx$ 24 kHz.
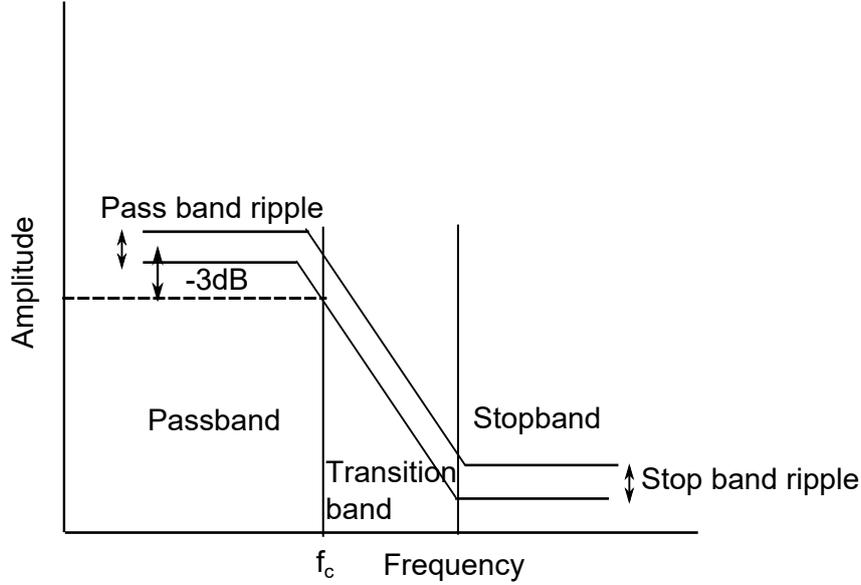
Figure C.2: Parameters of a conventional filter.

pass-band (or stop-band) ripple. Let us set the filter type to be Chebyshev (type I) and limit its order to the first, as higher order filters have a non-linear transfer function and show phase non-linearity [206], which is undesirable in our application. The choice of a Chebyshev filter is made here because it provides an optimal trade-off between the roll-off (defined as the steepness in the transition from passband to stopband) and the passband ripple (r_{pb}) and can be completely described in terms of only one parameter, r_{pb} [206]. In this sense, r_{pb} can be varied in order to get the optimal bandwidth to retrieve back the triangular waveform. Figure C.2 show the basic parameters of a filter. Passband is the range of frequencies that the filter allows to pass through it. The cut-off frequency (f_c) is the frequency at which the magnitude of the signal falls by 3 dB. Stopband refers to the band of frequencies that are highly attenuated by the filter. The transition band refers to the switching of the filter from passband to stopband. The pass-band and stop-band ripple refers to the fluctuations of the signal around their mean values in the corresponding bands. Among various parameters, as mentioned earlier, a Chebyshev filter (type I) can be defined in terms of r_{pb}), so the main concern in designing is the selection of the optimal r_{pb} value and how it affects f_c and the phase linearity of the filter.

Fig. C.3 shows the effects of the pass-band ripple in the frequency domain, comparing the filtered time domain signal to the original IM signal. In each subplot, different f_c values have been used, and at the same time each subplot is associated to a given value of ripple in the passband r_{pb}. It is seen that the lower the passband ripple, the lower the bandwidth (expressed through the cut-off frequency, f_c, normalized to the Nyquist frequency $f_s/2$, with f_s being the sampling frequency) required to properly retrieve the triangular waveform back. Looking at the issue from another point of view, Fig. C.4 shows the root mean square error (RMSE) of the IM signal retrieved back decreases with an increase in f_c, but at the cost of a decreased r_{pb}. This

175
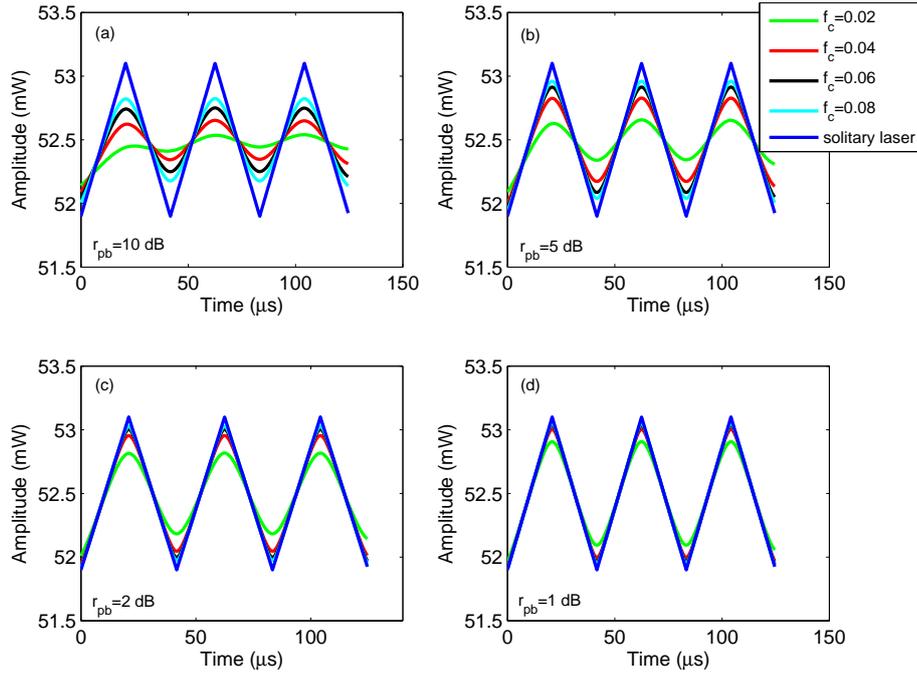
Figure C.3: Effect of pass band ripple in the cut-off frequency required to retrieve back the triangular waveform. The cut-off frequency f_c is normalized to the Nyquist frequency ($f_s/2 = 0.12$ MS/s). In (a)-(d) the filter parameter is set to different values of r_{pb} equal to 10, 5, 2, and 1 dB respectively. For each r_{pb} value f_c is varied as 0.02 (green), 0.04 (red), 0.06 (black) and 0.08 (cyan) to visualize the combined effect of r_{pb} and f_c on the waveform retrieval (blue).

trade-off is better understood with a numerical example. When $r_{pb} = 10$ dB, *increasing* the f_c from 0.04 to 0.06, the RMSE in waveform retrieval *decreases* from 0.26 mW to 0.18 mW. Said in another way, if the f_c is fixed to 0.04, to decrease the RMSE from 0.26 mW to 0.18 mW, r_{pb} must be changed from 10 dB to 5 dB.

Clearly, an increase in the pass-band ripple is undesirable, as it introduces non-linearity in the phase response of the filter and thus reduces its effective bandwidth when a linear phase response of the filter is desired. This is the case for the CWFM-DOF sensor proposed, as explained in detail in Appendix D.
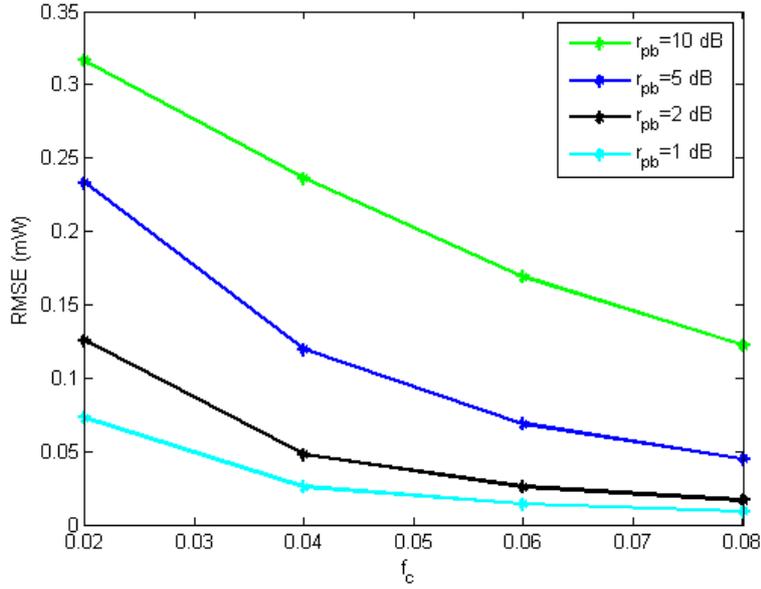
Figure C.4: Trade off between passband ripple and optimal bandwidth required to retrieve back a triangular waveform with minimal error. Cut-off frequency normalized to the Nyquist frequency ($f_s/2 = 0.12$ MS/s).

Figure C.5: Spectral properties of OFS in response to different values of m ($m = 0.002$ and $m = 0.02$) with $N_f = 17$ fringes; (a) Fringes introduced in the modulation signal due to optical feedback ($m = 0.002$); (b) Increased fringe visibility due to an increased m value ($m = 0.02$); (c) Power spectrum of the OFS under $m = 0.002$ and $m = 0.02$.
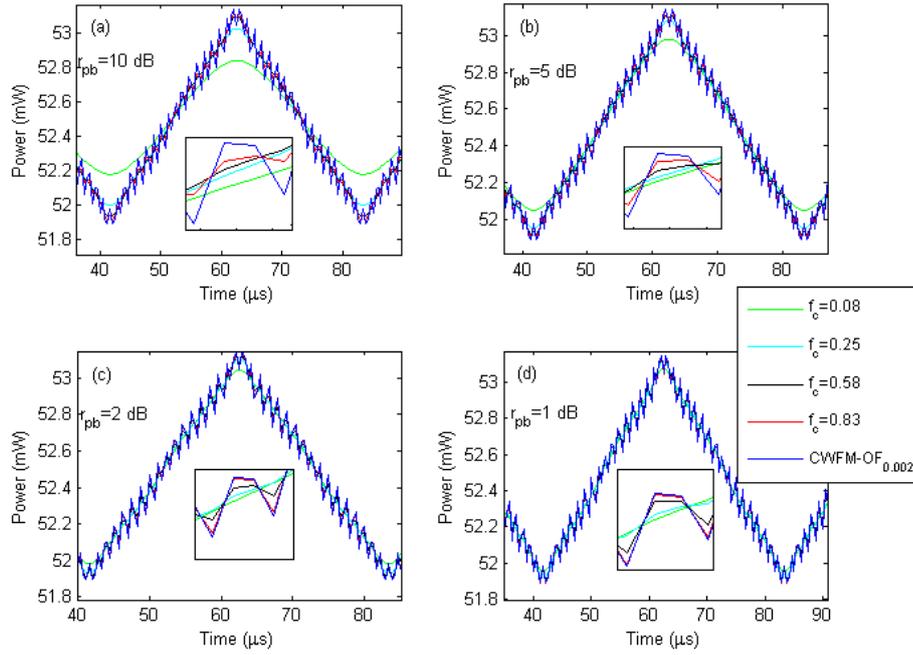
Figure C.6: Effect of pass band ripple on optimal bandwidth of filter to retrieve back the $\text{OFS}_{0.002}$. Inset gives the magnified view of fringes. Cut-off frequency is normalized to Nyquist frequency ($f_s/2 = 0.12$ MS/s).

C.2 EFFECT OF m ON FILTER BANDWIDTH

A comparable analysis is now performed on the CWFM-OFS[1] modulated at $f_\text{m} = 24$ kHz with two different modulation values defined by $m = 0.002$ and $m = 0.02$, and a constant number of $N_f = 17$ fringes in half period of the modulation signal. The time domain and frequency domain (power spectrum) responses of a triangular modulation waveform for the standalone laser and the OFS for the two modulation cases described are shown in Fig. C.5. From the comparison of the power spectral density (PSD) values in the three cases it becomes clear that both of them have frequency components which change from $0-0.2$ MHz. The 3 dB bandwidth in both cases is seen to be 36 kHz (Fig. C.5(c)). Furthermore, the OFS has spectral components at 0.8 MHz which are not appreciated for the standalone laser. This is due to the presence of 34 fringes in one cycle of the modulation current, which gives an effective frequency equal to 34 times the original modulation frequency, yielding a value of 0.8 MHz (24 kHz $\times$ 34 = 0.8 MHz). This effect of the beat power spectrum induced by the returned field is also seen as ripples when observed in the time domain (Fig. C.5(a),(b)). In addition, from the spectrum of OFS obtained at $m = 0.002$ and $m = 0.02$ (denoted as CWFM-OF$_{0.002}$ and CWFM-OF$_{0.02}$), it is observed that the nature of the PSD does not change qualitatively. The main lobe is

---

[1]Let us skip the CWFM part of the term in the upcoming text for better readability, so CWFM-OFS will shown in the rest of this Appendix simply as OFS.
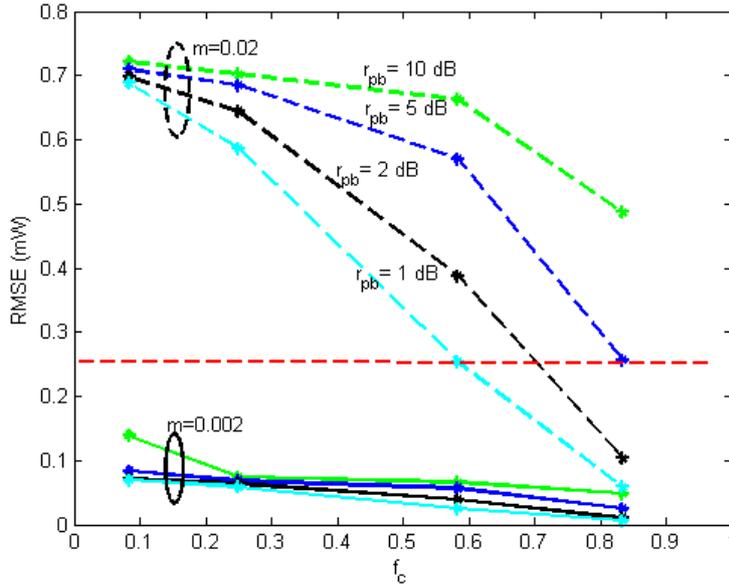
Figure C.7: Trade off between r_{pb} and optimal bandwidth (f_c) required to retrieve OFS. f_c is normalized to Nyquist frequency ($f_s/2 = 0.12$ MS/s).

seen to be identical, and both spectra with a feedback component have beat frequencies at 0.8 MHz. However, the quantitative nature of PSD does change. In the $m = 0.002$ case, the power in the side lobes is significantly lower than in the $m = 0.02$ case. This shows that changing the modulation index does not add new spectral components to the signal, but modifies the power distribution within the higher harmonics. Under this approach, our interest is to find the optimal bandwidth of the filter or amplifier required to retrieve back the OFS. The OFS output from a filter with different f_c and different r_{pb} values in the $m = 0.002$ case is shown in Fig. C.6. For the purpose of illustration, let us focus in the case when $r_{pb} = 10$ dB (Fig. C.6 (a) (inset)). For an increase in f_c from 0.08 to 0.83, the retrieved OFS becomes increasingly better as f_c increases, but still a significant amount of error exists. Similarly, for the case when $r_{pb} = 2$ dB (Fig. C.6 (c) (inset)), an increase in f_c from 0.08 to 0.83, improves the retrieved OFS, although now the errors are relatively small compared to the former case. We can conclude then, that larger f_c values and smaller r_{pb} values improve the RMSE value of the reconstruction, as one could expect theoretically.

A more detailed analysis of the RMSE values obtained when retrieving back the OFS after filtering as a function of different f_c for $m = 0.002$ and 0.02 is shown in Fig. C.7. From the comparison, two important conclusions are drawn. First, there exists a trade off between bandwidth (cut-off frequency) and the allowable ripple r_{pb} in the pass-band at a constant modulation index. At fixed m, keeping r_{pb} constant, f_c has to be increased to retrieve back the OFS with minimal error. For example, at $m = 0.2$ and $r_{pb} = 2$ dB, f_c has to be increased from 0.3 to 0.6 to reduce error from 0.6 mW to 0.25 mW. Alternately, to attain a desired error value, f_c and r_{pb}

have to be tuned precisely. For instance, to attain an RMSE of 0.25 mW at $m = 0.02$, the f_c has to be increased from 0.58 to 0.83 for the choice of r_{pb} of 1 and 5 dB respectively (indicated by the dashed horizontal line). Secondly, the RMSE of the reconstruction significantly increases with m. Taking similar conditions in the reconstruction $f_c = 0.1$, and $r_{pb} = 10$ dB, the RMSE for $m = 0.002$ is 0.14 mW as compared to 0.7 for $m = 0.2$. This may be explained, as with the increase in m the fringe visibility is increased (see Fig. C.5 (b)), while, on the other hand, the PSD increases as well (Fig. C.5 (c)). Both increments have as a direct implication that the f_c value of the filter has to be increased to accommodate additional spectral components, as well as the roll-off factor of the filter has to be lowered. Thus, an additional trade-off exists between the choice of m and the ease of signal processing. On one hand, a large m value is desirable so the fringes are easily detected and processed to measure the vibration of the target. However, on the other hand, the choice of large m values restricts the selection of the cut-off frequency f_c of the filter.

C.3   EFECT OF N_f ON FILTER BANDWIDTH

Let us close this Appendix including the discussion of the effect of the number of fringes N_f in the OFS in the design of the filter. For most of the applications, and when comparing with experimental laboratory conditions, typically an OFS with a modulation index close to $m = 0.002$ is obtained. Keeping $f_m = 24$ kHz as in previous sections, we intend to explore the variation in bandwidth of the OFS (and ultimately of the filter or amplifier) with number of fringes (N_f). Here the laser to target distance is quartered in order to ensure a quarter of the number of fringes obtained in the previous case, turning the fringe number into $N_f = 4$ in one ramp of the modulation signal. Fig. C.8 (c) shows the spectrum of the OFS resulting from different modulation index $m = 0.002$ and $m = 0.02$ (Fig. C.8 (a)(b)). The spectrum is quite similar to the one previously obtained in Fig. C.5 (c), provided that there are additional frequency components at integral multiples of 0.2 MHz (24 kHz $\times$ 8 = 0.2 MHz compared to 0.8 MHz in Fig. C.5 (c)), the power of which gradually decreases with frequency. It is also observed that the power in each frequency component increases with an increase in m. Also an increase in fringe visibility in the time domain (Fig. C.8 (b)) may be appreciated, following the conclusions of the previous Section. Fig. C.9 shows the retrieved OFS from filters showing different r_{pb} and f_c. For the purpose of illustration, let us consider the case when $r_{pb} = 10$ dB (Fig. C.9 (a) (inset)). With an increase in f_c from 0.08 to 0.83, the retrieved OFS improves (unlike in the previous case in Fig. C.6 (a), where the error was significant). Detailed analysis of the error introduced after filtering as a function of different f_c values for $m = 0.002$ and 0.02 is shown in Fig. C.10. It is evident that in this case as well, the RMSE decreases with the decrease in m. However, the comparison between RMSE resulting at constant $m = 0.02$ and different $N_f = 17$ and 4 is shown in Fig. C.11. It is concluded that with a lower number
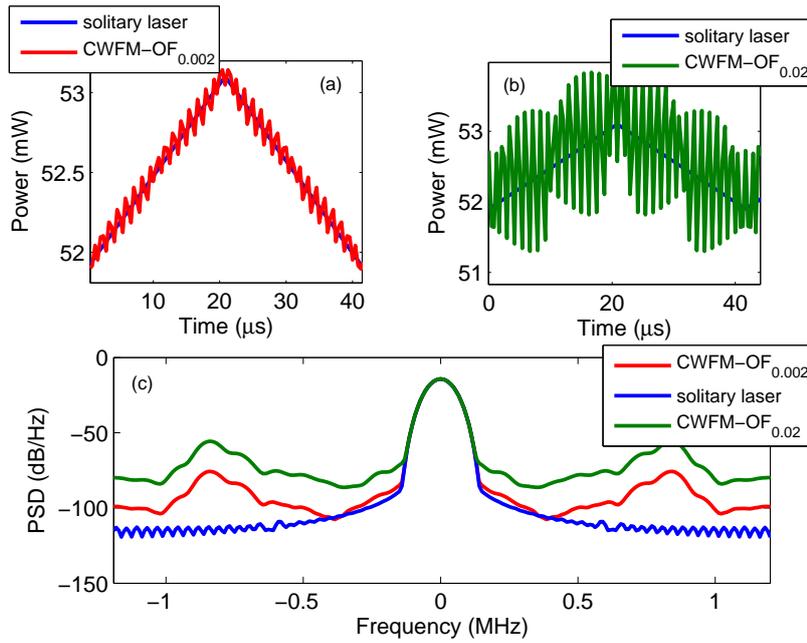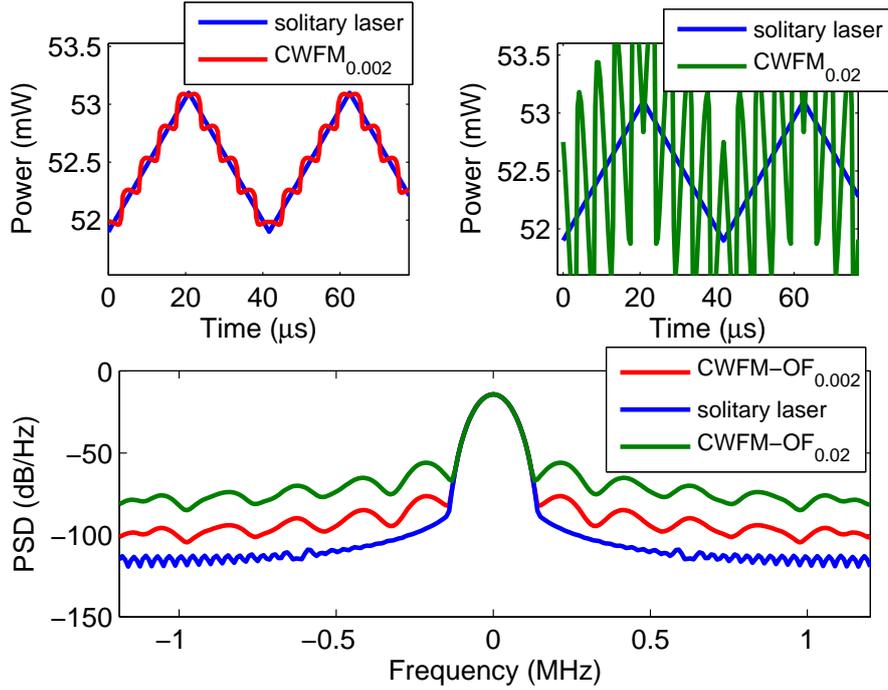
Figure C.8: Spectral properties of OFS in response to different $m = 0.002$ and $m = 0.02$ with $N_f = 4$ fringes; (a) Fringes introduced in the modulation signal because of optical feedback ($m = 0.002$); (b) Increased fringe visibility due to increased $m = 0.02$; (c) Power spectrum of the OFS under different $m = 0.002$ and $m = 0.02$.

of fringes, the same RMSE is attained at lower f_c if compared to the RMSE obtained with a larger number of fringes. For example, referring to Fig. C.11, to maintain RMSE 0.27 mW with $N_f = 17$ and $r_{pb} = 1$ dB, f_c is 0.58 as compared to 0.25 under similar conditions for $N_f = 4$ (explained by dash line). Said in another way, a OFS with a larger number of fringes requires a larger f_c and a smaller r_{pb} to attain the same RMSE when compared to a signal with a smaller number of fringes.
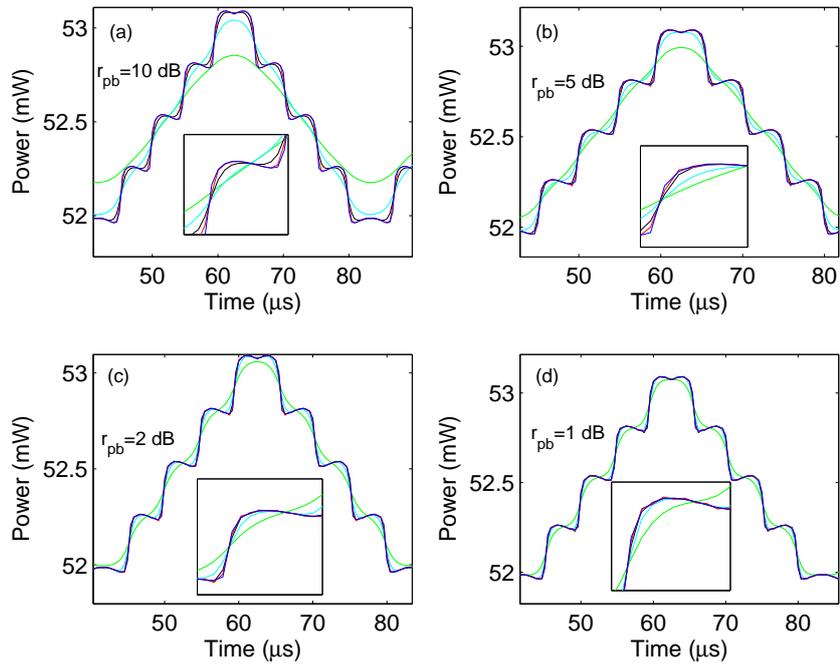
Figure C.9: Effect of pass band ripple on optimal bandwidth of filter to retrieve back the OFS. Inset gives the magnified view of fringes. Cut-off frequency is normalized to Nyquist frequency ($f_s/2 = 0.12$) MS/s. (a)-(d) the filter parameter set to different r_{pb} equal to 10, 5, 2, and 1 dB respectively. For each r_{pb} the f_c is varied as 0.08 (green), 0.25 (cyan), 0.58 (black) and 0.83 (red) to visualize the combined effect of r_{pb} and f_c on the OFS retrieval (blue).
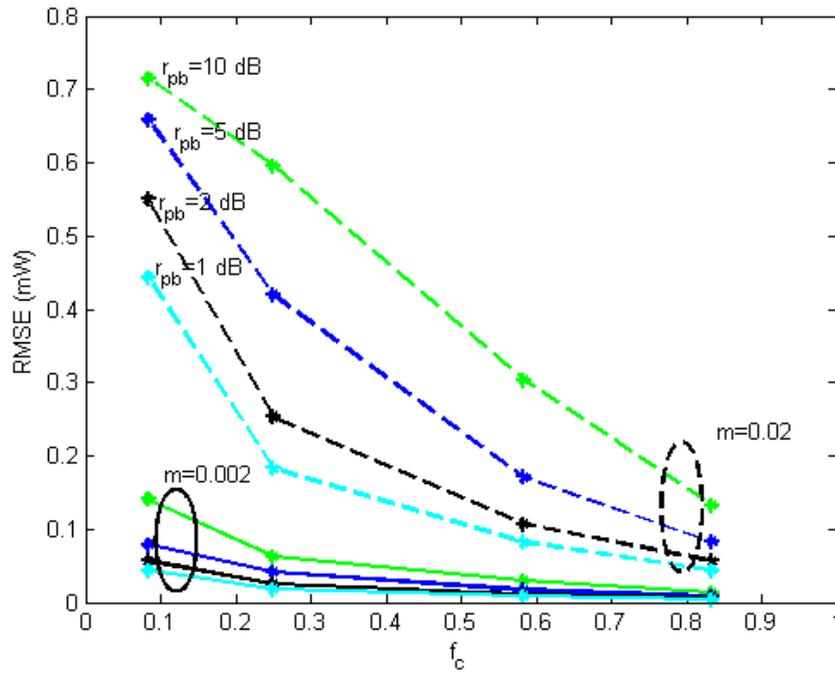
Figure C.10: Trade off between passband ripple r_{pb} and optimal bandwidth f_c required to retrieve the OFS. Cut-off frequency is normalized to the Nyquist frequency ($f_s/2 = 0.12$ MS/s).
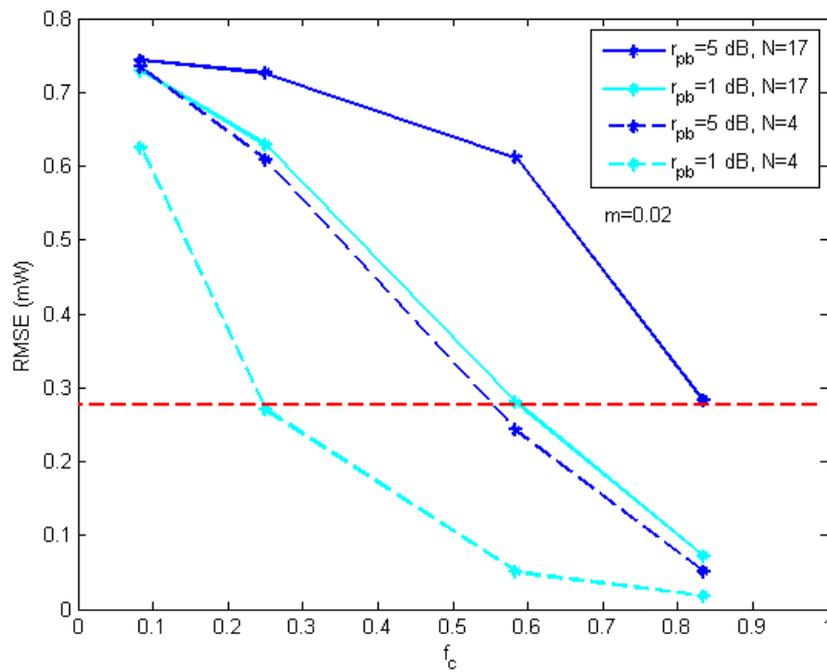
Figure C.11: Effect of the number of fringes in the parameters used for filter design.

D. ZERO PHASE FIR FILTER

In appendix C, it was shown that the bandwidth of the OFS, and ultimately that of differentiator is dependent upon f_c, m and N_f (with N_f depending upon the distance of the target to the laser (L_{ext}) and the amplitude of the modulation current (A_m)). Further in Fig. C.10 it was shown that there exists a trade off between the choice of cut off frequency f_c and the pass band ripple r_{pb}. Keeping f_c constant, a decrease in r_{pb} decreases the error in the retrieved OFS. However, only the magnitude response of the filter (differentiator) was taken into account, while the phase response was ignored. Since CWFM-DOF is a coherent process involving the phase of reference and vibration OFS to calculate the displacement of the vibrating target, it is desirable to retrieve its spectral component (phase) with high accuracy, not keeping limited to its amplitude. The design of the filter or amplifier including the differentiator stage for such application requires a constant or, ideally, a zero phase delay. Thus, a very relevant question regarding the processing of the reference and vibration OFS (and, hence, regarding the implementation of CWFM-DOF) becomes the determination of the effective bandwidth of the differentiator that has a constant phase response.

Fig. D.1 (a) shows the magnitude (solid) and phase (dash) response of a filter with different r_{pb} values for a typical Chebyshev (type I) first order filter. It is observed that with an increase in the allowed r_{pb} the phase linearity decreases. This means that with a lower passband ripple in the filter (the effective cut-off frequency (f_l), defined as the maximum frequency up to which the phase of the filter is constant) tends to be larger as compared to that with larger pass band ripples. Another very important parameter that quantifies the phase response of the filter is its phase delay (shown in Fig. D.1 (b)). It is observed that keeping r_{pb} constant while increasing f_c, the phase linearity increases and the delay introduced in the processing of measured samples decreases. For ease of understanding, this concept is again better illustrated by an example. Consider Fig. D.1 (b), at $r_{pb} = 1$ dB and $f_c = 0.08$. The effective frequency (f_l) of the filter is 0.002 (normalized to Nyquist rate) and the delay introduced by filter (τ_ϕ) is 1.93 samples (denoted by point A). A direct relationship of this fact with CWFM-DOF is that the phase of each individual frequency component ($< f_l$) in reference and vibration OFS would be shifted by a constant value of 1.93 samples.

Since the vibration detection strategy used in CWFM-DOF is differential in nature, this constant phase delay does not affect the measurement at all as it is simultaneously introduced in both the reference and vibration measurements. However, for the frequency components in the reference and vibration OFS ($> f_l$) it is phase shifted by a different amount so an error is introduced. Similarly, at $f_c = 0.25$, f_l is increased to 0.006 and, simultaneously, the τ_ϕ value
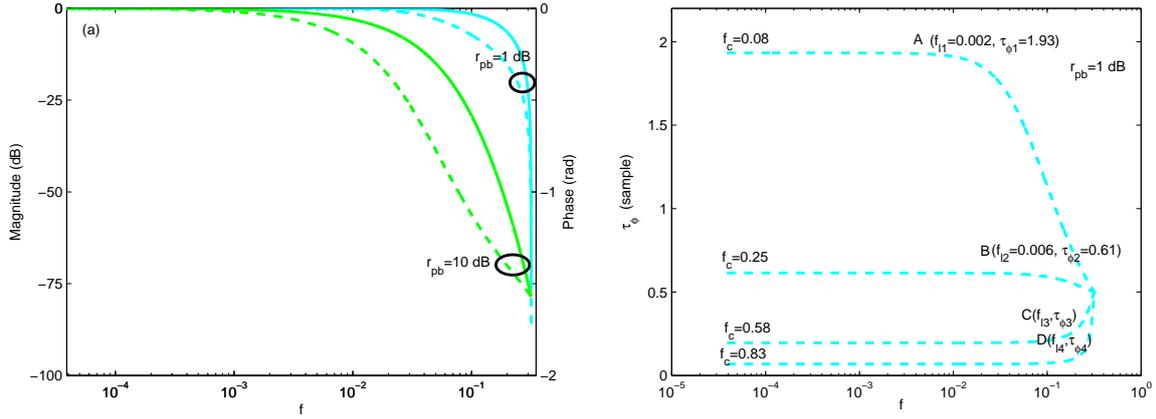
Figure D.1: Frequency response of a typical Chebyshev (type I) first order filter. (a) Magnitude (solid) and phase (dash) response at $r_{pb} = 10$ and 1 dB. (b) Phase linearity and phase delay as a function of r_{pb}.
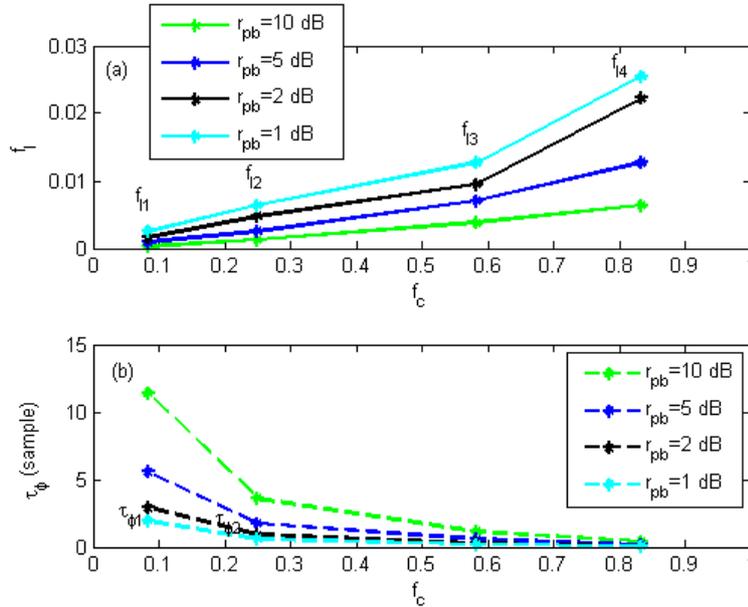
Figure D.2: Effect of cut-off frequency (f_c) and the passband ripple (r_{pb}) on (a) the effective frequency (f_l) that maintains constant phase delay on the OFS (b) sample delay introduced in OFS .

is decreased to 0.061 samples (shown by point B in Fig. D.1 (b)). A similar analysis can be made for filters with different f_c and r_{pb} values, and the comparison is shown in Fig. D.2. Two important conclusions are drawn of this Figure. First, keeping the pass band ripple constant, an increase in f_c increases the effective frequency f_l (D.2 (a)). At the same time, the delay in phase decreases (D.2 (b)). Secondly, at constant f_c, with a decrease in r_{pb}, the effective frequency increases while the phase delay decreases. However, it is worth mentioning that, even in the best case ($r_{pb} = 1$ dB), the ratio of f_l to f_c is less than a 5 % ($f_l = 0.028$, $f_c = 0.83$). This suggests that only a very small fraction of the available bandwidth can be used to process reference and vibration OFS accurately.
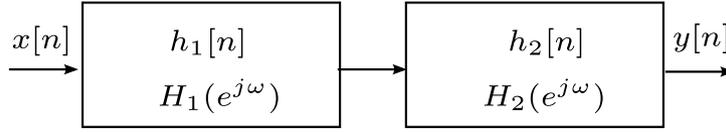
Figure D.3: Cascade filtering for zero phase delay.
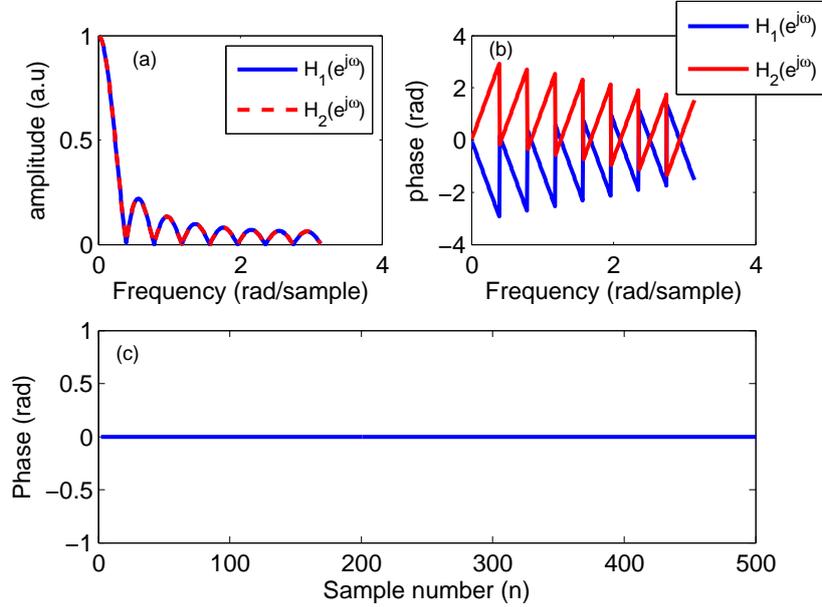
Figure D.4: Cascade filtering for zero phase delay: (a) Magnitude response of individual filter having transfer function $H_1(e^{j\omega})$ and $H_2(e^{j\omega})$, where $H_2(e^{j\omega}) = H_1^*(e^{j\omega})$ (Fig. D.3); (b) Phase response of individual cascaded filter of cascade system as shown in Fig. (D.3); (c) Overall phase response of cascade system in Fig. D.3.

The point of this detailed discussion is to show the use of the differentiator filter as an inefficient procedure which can be enhanced. To overcome this problem, it becomes desirable to process the reference and vibration OFS off-line, using a zero phase FIR filter in a computer [206]. This has a two-fold advantage. First, the cut-off frequency f_c of the filter becomes independent of the parameters analyzed in previous sections 6.2.2, C.2 and C.3 (f_t, m and N_f). Thus, a properly processed OFS does not need any more tuning the filter cut-off frequency each time depending on the experimental configuration. Second, due to the low efficiency of the filter obtained (less than 5 %) , it does not make sense to implement it in a dedicated manner. We recall here that a zero phase filter is basically a cascade of two independent filters with opposite transfer functions, as seen in Fig. D.4 [206].

Let $x[n]$ be the time domain signal passing through the two cascaded filters, with an impulse response $h_1[n]$ and $h_2[n]$, and a frequency response $H_1(e^{j\omega})$ and $H_2(e^{j\omega})$, respectively. Then the output of the cascaded filters in the time and frequency domains will be given by

$$y[n] = h_1[n] * h_2[n] * x[n] \tag{D.1}$$

$$Y(e^{jw}) = H_1(e^{jw})H_2(e^{jw})X(e^{jw}) \tag{D.2}$$

186

where the operation (*) is a classical convolution, which becomes a multiplication in the frequency domain. Now, if the second filter having a frequency response $H_2(e^{j\omega})$ is the complex conjugate of the first one, i.e. $H_2(e^{j\omega}) = H_1^*(e^{j\omega})$, then Eq. (D.2) becomes

$$Y(e^{jw}) = H_1(e^{jw})H_1^*(e^{jw})X(e^{jw}) \tag{D.3}$$

$$= |H(e^{jw})||H(e^{jw})|e^{(jwM/2)}e^{(-jwM/2)}X(e^{jw}) \tag{D.4}$$

$$= |H(e^{jw})|^2 X(e^{jw}) \tag{D.5}$$

From Eq. (D.5) it is observed that passing the signal again through a cascaded filter which has a frequency response of the second filter as the complex conjugate of the first filter causes the phasor to rotate in opposite directions resulting in the perfect cancellation of the phase shift introduced by the filter. This is illustrated in Fig. D.4, and is fully equivalent to the "Lead-Lag" compensation used in control systems, and to the "spectral reversing" technique to combat dispersion in optical fibre communications. When there is no phase shift introduced by a system, the subtraction of the output from the input is dictated solely by their magnitudes, which is the desired situation for CWFM-DOF.

E. List of Publications, Conferences, Talks and Posters

Manuscript in Prepration

1. **A. Jha**, F. Azcona, R. Atashkhooei, C. Yanez, S. Royo, "Injection Modulation Induced Stability of Laser Diode under High Feedback Strength," IEEE J. Quant. Electron. (In prep)

2. **A. Jha**, F. Azcona, C. Yanez, S. Royo, "Optical Feedback Based on Scattering Theory," (In prep)

3. **A. Jha**, F. Azcona, C. Yanez, S. Royo, "Characterizing Acoustic vibration using CWFM-DOF," (In prep)

Licensed Patents

4. Santiago Royo, Francisco j. Azcona Guerrero, **Ajit Jha**, "A method of measuring a change in an optical path using differential laser self-mixing interferometry and a differential laser Self-mixing interferometry measuring system," European Patent no. EP13005853.0 (licensed to Beamagine, Terrassa, Spain)

5. Santiago Royo, Francisco j. Azcona Guerrero, **Ajit Jha**, "Method, device and computer programs for measuring a fetal arterial pulse wave," European Patent no. 14003368.9 -1506 (licensed to BCB Informatics y Control, Madrid, Spain)

Peer-reviewed Journals

6. F. J. Azcona, **A. Jha**, C. Yanez, R. Atashkhooei, S. Royo, "Microcantilever displacement measurement using Differential Optical Feedback Interferometry," Sensors, Vol. 26, no. 9, pp. 997, 2016

7. J.Perchoux, A. Quotb, R. Atashkhooei, F. Azcona, E.E. Ramirez-Miquet, O. Bernal, **A. Jha**, A. Arriaga, C. Yanez, J. Caum, T. Bosch, S. Royo, "Current developments on optical feedback interferometry as an all-optical sensor for biomedical applications," Sensors, Vol. 16, pp. 694, 2016

8. **A. Jha**, F. J. Azcona and S. Royo, "Frequency-Modulated Optical Feedback Interferometry for Nanometric Scale Vibrometry,"IEEE Photon. Technol. Lett., vol. 28, no. 11, pp. 1217-1220, June, 2016

9. **Ajit Jha**, Francisco. Azcona,Carlos Yanez, Santiago Royo, "Extraction of Vibration Parameters from Optical Feedback Interferometry Signals using Wavelets," App. Optics, 54, 10106-13, 2015

10. A. Arasanz, F. J. Azcona, S. Royo, **A. Jha**, J. Pladellorens, "A new method for the acquisition of arterial pulse wave using self-mixing interferometry," Opt. Laser. Technol, Vol. 63 pp. 98-104, Nov 2014

11. F.J. Azcona, R. Atashkhooei, S. Royo, J. Mendez, **A. Jha**, "A Nanometric Displacement Measurement System Using Differential Optical Feedback Interferometry," IEEE Photon. Tech. Lett., vol. 25, No. 21, pp. 2074-7, Nov. 2013

Conference Proceedings

12. **Ajit Jha**, Francisco J. Azcona, Carlos Yanez, Santiago Royo, "Vibrometria de alta resolucion utilizando interferometria optica retroalimentada diferencial por modulacion electronica," Proc. IX Optoelectronics Spanish Meeting (OPTOEL), 13-15 July, Salamanca, Spain, 2015

13. **Ajit Jha**, Francisco. Azcona, Santiago Royo, "Ultracompact vibrometry measurement with nanometric accuracy using optical feedback," Proc. SPIE, Optical Measurement Systems for Industrial Inspection, 95251Y June 22, 2015

14. Francisco J. Azcona, **Ajit Jha**, Carlos Yanez, Santiago Royo, "Differential self-mixing interferometry for micro-cantilever motion sensing," Proc. SPIE 9529, Optical Methods for Inspection, Characterization, and Imaging of Biomaterials II, 95291B, June 22, 2015

15. **Ajit Jha**, Santiago Royo, Francisco Azcona, Carlos Yanez, "Extracting vibrational parameters from the time-frequency map of a self-mixing signal: An approach based on Wavelet analysis," IEEE Sensors Proceedings, pp. 1881-1884, Nov, 2014

16. Francisco Javier Azcona, Santiago Royo, **Ajit Jha**, "Towards Atomic Force Microscopy Measurements Using Differential Self-mixing Interferometry," IEEE Sensors Proceedings, pp. 766-770, Nov, 2014

17. F. J. Azcona, S. Royo, R. Atashkhooei, **A. Jha**, J. M. Astudillo, "A method to measure sub nanometric amplitude displacements based on optical feedback interferometry," Proc. SPIE, Modeling Aspects in Optical Metrology IV, 878908, May 13, 2013

Unpublished Conferences, Posters and Talks

18. "Skin Cancer Diagnosis and Prognosis Using Laser Imaging: Technical and Clinical Progress," Terrassa, Barcelona, Spain, 31 March - 1 April 2016.

19. "Light Sciences and Technologies (LiST) for a New World," June 15-19, Santander, Spain, 2015

20. **A. Jha**, "Optical feedback based sub-wavelength frequency and displacement detection: an application towards detecting photo-acoustic wave in tissue," **Talk** session presented at Biophotonics In Cancer Detection: Technologies And Sensing Porto, Portugal, 4 -5 May, 2015

21. **Ajit Jha**, "Nonlinear dynamics in laser cavity with optical feedback for subwavelength sensing," **Talk** session presented at Photonics Engineering, Nanophotonics and Biophotonics summer school, Paderborn, Germany, 13 April-16 April, 2015

22. **Ajit Jha**, "High frequency sub nanometric vibrometry : A novel approach based on frequency sweeping and optical feedback interferometry," **Poster** session presented at: Photonics Engineering, Nanophotonics and Biophotonics summer school, Porquerolles island, France, 31 March-3 April, 2014

23. Francisco J. Azcona, S.Royo, Jorge Mendez Astudillo, **Ajit Jha**, "Differential self-mixing interferometry: a low cost approach for a nm displacement sensor," Poster session presented at Jornada de la recerca i la innovacio tecnologica al Campus de la UPC a Terrassa, Terrassa, Barcelona, 2013

24. Santiago Royo, Miguel Ares, Reza Atashkhooei, Francisco J. Azcona, Vincent Suc, Jorge Mendez-Astudillo, **Ajit Jha** "Nuevas lineas de trabajo en metrologia optica en el CD6 de la UPC," Poster session presented at Jornada de la recerca i la innovacio tecnologica al Campus de la UPC a Terrassa, Terrassa, Barcelona, 2013

25. **Ajit Jha**, "Double Self Mixing Interferometry (SMI) using single laser to calculate target distance and displacement," **Poster** session presented at: Photonics Engineering, Nanophotonics and Biophotonics summer school Pforzheim, Germany, 8-10 April, 2013

Bibliography

[1] L. Coldren and S. Corzine, *Diode lasers and photonic integrated circuits.* New York: J. Wiley, 1995.

[2] B. G. Streetman and S. K. Banerjee, *Solid State Electronic Devices.* New Delhi: PHI Learning Private Limited, 2009.

[3] R. Tkach and A. Chraplyvy, "Regimes of feedback effects in 1.5μm Distributed Feedback Lasers," *J. Lightwave Technol.*, vol. 4, no. 11, pp. 1655–1661, 1986.

[4] *Physikinstrumente.com, P-753 LISA Linear Actuator & Stage, 2016*, Accessed: 30-03-2016.

[5] M.-C. Amann, T. Bosch, M. L. R. Myllyla, and M. Rioux, "Laser ranging: a critical review of usual techniques for distance measurement," *Opt. Eng.*, vol. 40, January 2001.

[6] G. Beheim and K. Fritsch, "Range finding using frequency-modulated laser diode," *Appl. Opt.*, vol. 25, pp. 1439–1442, May 1986.

[7] K. Bertling, J. Perchoux, T. Taimre, R. Malkin, D. Robert, A. D. Rakić, and T. Bosch, "Imaging of acoustic fields using optical feedback interferometry," *Opt. Express*, vol. 22, pp. 30346–30356, Dec 2014.

[8] M. Norgia, A. Pesatori, and L. Rovati, "Self-mixing laser doppler spectra of extracorporeal blood flow: A theoretical and experimental study," *IEEE Sensors J.*, vol. 12, pp. 552–557, March 2012.

[9] Y. Sun, Y. Yu, and J. Xi, "Wavelet transform based de-noising method for self mixing interferometry signals," *Proc. SPIE*, vol. 8351, pp. 83510G–83510G–7.

[10] R. Atashkhooei, S. Royo, and F. Azcona, "Dealing with speckle effects in self-mixing interferometry measurements," *IEEE Sensors J.*, vol. 13, pp. 1641–1647, May 2013.

[11] A. L. Arriaga, F. Bony, and T. Bosch, "Progress on self-mixing sensors for in-situ displacement measurement," in *International Workshop of Electronics, Control, Measurement, Signals and their application to Mechatronics (ECMSM)*, pp. 1–5, June 2013.

[12] U. Zabit, F. Bony, T. Bosch, and A. Rakic, "A self-mixing displacement sensor with fringe-loss compensation for harmonic vibrations," *IEEE Photon. Technol. Lett.*, vol. 22, pp. 410–412, March 2010.

[13] C. Bes, G. Plantier, and T. Bosch, "Displacement measurements using a self-mixing laser diode under moderate feedback," *IEEE Trans. Instrum. Meas.*, vol. 55, pp. 1101–1105, Aug 2006.

[14] O. Bernal, U. Zabit, and T. Bosch, "Study of laser feedback phase under self-mixing leading to improved phase unwrapping for vibration sensing," *IEEE Sensors J.*, vol. 13, pp. 4962–4971, Dec 2013.

[15] A. Einstein, "On the quantum theory of radiation," *Phys.Z*, vol. 18, pp. 121–128, 1917.

[16] J. P. Gordon, H. J. Zeiger, and C. H. Townes, "The maser-new type of microwave amplifier, frequency standard, and spectrometer," *Phys. Rev.*, vol. 99, pp. 1264–1274, Aug 1955.

[17] T. Maimam, "Optical and microwave - optical experiments in ruby," *Phys. Rev. Lett.*, vol. 4, pp. 564–567, July 1960.

[18] R. N. Hall, G. E. Fenner, J. D. Kingsley, T. J. Soltys, and R. O. Carlson, "Coherent light emission from gaas junctions," *Phys. Rev. Lett.*, vol. 9, pp. 366–368, Nov 1962.

[19] A. E. Siegman, *Lasers.* University Science Books, 1986.

[20] C. O. Weiss and R. Vilaseca, *Dynamics of lasers.* VCH Weinheim, 1991.

[21] Z. I. Alferov, A. D. Andreev, V. I. Korolkov, E. L. Portnoi, and D. N. Tretyako, "Injection properties of $n - Al_x Ga_{1-X} As - p - GaAs$ heterojunctions," *Sov. Phys. Semicond.*, vol. 2, p. 843, Nov 1969.

[22] J. J. Coleman, "The development of the semiconductor laser diode after the first demonstration in 1962," *Semicond. Sci. Technol.*, vol. 27, no. 9, p. 090207, 2012.

[23] F. P. Mezzapesa, L. L. Columbo, M. Dabbicco, M. Brambilla, and G. Scamarcio, "QCL-based nonlinear sensing of independent targets dynamics," *Opt. Express*, vol. 22, pp. 5867–5874, 2014.

[24] F. P. Mezzapesa, L. L. Columbo, M. Brambilla, M. Dabbicco, M. S. Vitiello, and G. Scamarcio, "Imaging of free carriers in semiconductors via optical feedback in terahertz quantum cascade lasers," *Applied Physics Letters*, vol. 104, no. 4, 2014.

[25] P. G. R. King and G. J. Steward, "Metrology with an optical maser," *New Sci.*, vol. 17, p. 180, 1963.

[26] T. Heil, I. Fischer, W. Elsaber, and A. Gavrielides, "Dynamics of semiconductor lasers subject to delayed optical feedback: The short cavity regime," *Phys. Rev. Lett.*, vol. 87, pp. 243901–1–4, Nov 2001.

[27] D. Pieroux, T. Erneux, B. Haegeman, K. Engelborghs, and D. Roose, "Bridges of periodic solutions and tori in semiconductor lasers subject to delay," *Phys. Rev. Lett.*, vol. 87, p. 193901, Oct 2001.

[28] D. Pieroux, T. Erneux, T. Luzyanina, and K. Engelborghs, "Interacting pairs of periodic solutions lead to tori in lasers subject to delayed feedback," *Phys. Rev. E*, vol. 63, p. 036211, Feb 2001.

[29] A.A.Tager and K. Petermann, "High-frequency oscillations and self-mode locking in short external-cavity laser diodes," *IEEE J. Quantum Electron.*, vol. 30, pp. 1553–1561, Jul 1994.

[30] R. Lang and K. Kobayashi, "External optical feedback effects on semiconductor injection laser properties," *IEEE J. Quantum Electron.*, vol. 16, pp. 347–355, March 1980.

[31] D. Lenstra, B. H. Verbeek, and A. J. Denboef, "Coherence collapse in single-mode semiconductor-lasers due to optical feedback," *IEEE J. Quantum Electron.*, vol. 21, no. 6, pp. 674–679, 1985.

[32] S. Bennet, C. M. Snowden, and S. Iezekiel, "Nonlinear dynamics in directly modulated multiple-quantum-well laser diodes," *IEEE J. Quantum Electron*, vol. 33, pp. 2076–2082, 1997.

[33] E. Hemery, L. Chusseau, and J. M. Lourtioz, "Dynamic behaviors of semiconductor lasers under strong sinusoidal current modulation: Modeling and experiments at 1.3 μm," *IEEE J. Quantum Electron.*, vol. 26, pp. 633–641, April 1990.

[34] C. Lee, T. Yoon, and S. Shin, "Period doubling and chaos in a directly modulated laser diode," *Appl. Phys. Lett.*, vol. 46, pp. 95–97, 1985.

[35] A. P. Willis and D. M. Kane, "Modulation induced coherence collapse in FM diode lasers," *Opt. Commun.*, vol. 107, pp. 65–70, 1994.

[36] A. Schremer, T. Fujita, C. F. Lin, and C. L. Tang, "Instability threshold resonances in directly modulated external-cavity semiconductor lasers," *Appl. Phys. Lett.*, vol. 52, pp. 263–265, 1988.

[37] T. Fujita, S. Ishizuka, K. Fujito, H. Serizawa, and J. Sato, "Intensity noise suppression and modulation characteristics of a laser diode coupled to an external cavity," *IEEE J. Quantum Electron.*, vol. QE-20, pp. 492–498, 1984.

[38] N. Onodera, A. J. Lowery, L. Zhai, Z. Ahmed, and R. S. Tucker, "Frequency multiplication in actively mode-locked semiconductor lasers," *Appl. Phys. Lett.*, vol. 62, pp. 1329–1331, 1992.

[39] N. Onodera, Z. Ahmed, R. S. Tucker, and A. J. Lowery, "Stability of harmonically driven mode-locked semiconductor lasers," *Appl. Phys. Lett.*, vol. 59, pp. 3527–3529, 1991.

[40] Z. Ahmed, L. Zhai, A. J. Lowrey, N. Onodera, and R. S. Tucker, "Locking bandwidth of actively mode-locked semiconductor lasers," *IEEE J. Quantum Electron.*, vol. 29, pp. 1714–1720, 1993.

[41] R. Nagar, N. T. D. Abraham, A. Faenkel, G. Eisenstein, E. P. Ippen, U. Koren, and G. Raybon, "Frequency-modulation mode locking of a semiconductor lasers," *Opt. Lett.*, vol. 16, pp. 1750–1752, 1991.

[42] R. Nagar, D. Abraham, and G. Eisenstein, "Pure phase-modulation mode locking in semiconductor lasers," *Opt. Lett.*, vol. 17, pp. 1119–1120, 1992.

[43] J. Bosl, R. Bauer, H. Rauch, U. Penning, G. Weimann, and W. Schlapp, "Mode-locking of algaas laser diode by intracavity AlGaAs phase modulator," *Electron. Lett.*, vol. 25, pp. 864–866, 1989.

[44] J. Sacher, D. Baums, P. Panknin, W. Elsasser, and E. O. Gobel, "Intensity instabilities of semiconductor lasers under current modulation, external light injection, and delayed feedback," *Phys. Rev. A*, vol. 45, pp. 1893–1905, 1992.

[45] D. W. Sukow and D. J. Gaunthier, "Entraining power-dropout events in an external cavity semiconductor laser using weak modulation of the injection current," *IEEE J. Quantum Electron.*, vol. 36, pp. 175–183, 2000.

[46] Y. Takiguchi, Y. Liu, and J. Ohtsubo, "Low-frequency fluctuation induced by injection-current modulation in semiconductor lasers with optical feedback," *Opt. Lett.*, vol. 23, pp. 1369âĂŞ–1371, 1998.

[47] W. Majeed, M. Magnuson, and S. Keilholz, "Spatiotemporal dynamics of low frequency fluctuations in bold fmri of the rat," *J. Magn. Reson. Imaging*, vol. 30, no. 2, pp. 384–393, 2009.

[48] A. Destrez, Z. Toffano, I. Joindot, and C. B. L. Hassine, "Measurement of spectral characteristics of semiconductor laser diodes-effect of injected current modulation and optical feedback," *IEEE Trans. Instrum. Meas.*, vol. 42, pp. 304–310, April 1993.

[49] Y. Yanguang, G. Giuliani, and S. Donati, "Measurement of the linewidth enhancement factor of semiconductor lasers based on the optical feedback self-mixing effect," *IEEE Photonics Technol. Lett.*, vol. 16, pp. 990–992, April 2004.

[50] S.Donati, G.Giuliani, and S.Merlo, "Laser diode feedback interferometer for measurement of displacements without ambiguity," *IEEE J. Quantum Electron.*, vol. 31, pp. 113–119, 1995.

[51] F. P. Mezzapesa, L. Columbo, M. Brambilla, M. Dabbicco, A. Ancona, T. Sibillano, F. D. Lucia, P. M. Lugarà, and G. Scamarcio, "Simultaneous measurement of multiple target displacements by self-mixing interferometry in a single laser diode," *Opt. Express*, vol. 19, pp. 16160–16173, Aug 2011.

[52] E. Gagnon and J.-F. Rivest, "Laser range imaging using the self-mixing effect in a laser diode," *IEEE Trans. Instrum. Meas.*, vol. 48, pp. 693–699, June 1999.

[53] A. Valavanis, P. Dean, Y. L. Lim, R. Alhathlool, M. Nikolic, R. Kliese, S. Khanna, D. Indjin, S. Wilson, A. Rakic, E. Linfield, and G. Davies, "Self-mixing interferometry with terahertz quantum cascade lasers," *IEEE Sensors J.*, vol. 13, pp. 37–43, Jan 2013.

[54] F. Azcona, S. Royo, and A. Jha, "Towards atomic force microscopy measurements using differential self-mixing interferometry," in *IEEE SENSORS*, pp. 766–770, Nov Valencia,2014.

[55] M. Suleiman, H. Seat, and T. Bosch, "Interrogation of fiber bragg grating dynamic strain sensors by self-mixing interferometry," *Sensors Journal, IEEE*, vol. 8, pp. 1317–1323, July 2008.

[56] R. Teysseyre, F. Bony, J. Perchoux, and T. Bosch, "Laser dynamics in sawtooth-like self-mixing signals," *Opt. Lett.*, vol. 37, pp. 3771–3773, Jan 2012.

[57] M. Wang and G. Lai, "Displacement measurement based on Fourier transform method with external laser cavity modulation," *Rev. Sci. Instrum.*, vol. 72, no. 8, pp. 3440–3445, 2001.

[58] W. Mao, S. Zhang, L. Cui, and Y. Tan, "Self-mixing interference effects with a folding feedback cavity in zeeman-birefringence dual frequency laser," *Opt. Express*, vol. 14, pp. 182–189, Jan 2006.

[59] Y. Tan and S. Zhang, "Self-mixing interference effects of microchip Nd:YAG laser with a wave plate in the external cavity," *Appl. Opt.*, vol. 46, pp. 6064–6068, Aug 2007.

[60] R. Addy, A.W.Palmer, K. Thomas, and V.Grattan, "Effects of external reflector alignment in sensing applications of optical feedback in laser diodes," *J. Lightw. Technol.*, vol. 14, pp. 2672–2676, Dec 1996.

[61] S. Ozdemir, I. Ohno, and S. Shinohara, "A comparative study for the assessment on blood flow measurement using self-mixing laser speckle interferometer," *IEEE Trans. Instrum. Meas.*, pp. 355–363, Feb 2008.

[62] A. L. Arriaga, F. Bony, and T. Bosch, "Speckle-insensitive fringe detection method based on hilbert transform for self-mixing interferometry," *Appl. Opt.*, vol. 53, pp. 6954–6962, Oct 2014.

[63] F. Azcona, R. Atashkhooei, S. Royo, J. M. Astudillo, and A. Jha, "A nanometric displacement measurement system using differential optical feedback interferometry," *IEEE Photonics Technol. Lett.*, vol. 25, pp. 2074–2077, Nov 2013.

[64] F.Azcona, R.Atashkhooei, S.Royo, J. Astudillo, and A.Jha, "A method to measure sub nanometric amplitude displacements based on optical feedback interferometry," in *Proc. SPIE*, pp. 878901–08, Nov Munich, 2013.

[65] A. Jha, F. Azcona, and S. Royo, "Ultracompact vibrometry measurement with nanometric accuracy using optical feedback," in *Proc. SPIE*, pp. 95251–60, July Munich, 2015.

[66] A. Jha, F. J. Azcona, and S. Royo, "Frequency-modulated optical feedback interferometry for nanometric scale vibrometry," *IEEE Photonics Technol. Lett.*, vol. 28, pp. 1217–1220, June 2016.

[67] Y.Kazuyoshi, K. Itoh, and T.Minami, "Nearest-neighbor median filter," *Appl. Opt.*, vol. 27, pp. 3445–3450, 1988.

[68] P. Windyga, "Fast impulsive noise removal," *IEEE Trans. Image Process.*, vol. 10, pp. 173–179, 2001.

[69] U. Zabit, O. D. Bernal, and T. Bosch, "Self-mixing laser sensor for large displacements: Signal recovery in the presence of speckle," *IEEE Sensors J.*, vol. 13, pp. 824–831, Feb 2013.

[70] K. Kurokawa, "Power waves and the scattering matrix," *IEEE Trans. Microwave Theory Tech.*, vol. 13, pp. 194–202, Mar 1965.

[71] M.Farge, "Wavelet transforms and their applications to turbulence," *Annu. Rev. Fluid Mech.*, vol. 24, pp. 395–457, 1992.

[72] K. Petermann, *Laser diode modulation and noise.* Dordrecht: Kluwer Academic Publishers, 1988.

[73] K. Petermann, "External optical feedback phenomena in semiconductor lasers," *IEEE J. Sel. Topics Quantum Electron.*, vol. 1, pp. 480âĂŞ–489, Jun 1995.

[74] W. T. Silfvast, *Laser Fundamentals.* USA: Cambridge University Press, 2004.

[75] Y. Z. Huang, "On the rate equations of semiconductor lasers for measuring spontaneous emission factor," *IEEE Photonics Technol. Lett.*, vol. 7, no. 9, 1995.

[76] J. Perchoux, A. Quotb, R. Atashkhooei, F. J. Azcona, E. E. Ramirez-Miquet, O. Bernal, A. Jha, A. Luna-Arriaga, C. Yanez, J. Caum, T. Bosch, and S. Royo, "Current developments on optical feedback interferometry as an all-optical sensor for biomedical applications," *Sensors*, vol. 16, p. 694, May 2016.

[77] J. W. Scott, B. J. Thibeault, C. J.Mahon, L. A. Coldren, and F. H. Peters, "High modulation efficiency of intracavity contacted vertical cavity lasers," *Applied Physics Letters*, vol. 65, no. 12, pp. 1483–1485, 1994.

[78] T. L. Koch and R. A. Linke, "Effect of nonlinear gain reduction on semiconductor laser wavelength chirping," *Appl. Phys. Lett.*, vol. 48, pp. 613–615, Mar. 1986.

[79] R. Schimpe, J. E. Bowers, and T. L. Koch, "Characterisation of frequency response of 1.5 μm InGaAsP DFB laser diode and InGaAs pin photodiode by heterodyne measurement technique," *Electron. Lett.*, vol. 22, pp. 453–454, April 1986.

[80] P. A. Roos, M. Stephens, and C. E. Wieman, "Laser vibrometer based on optical-feedback-induced frequency modulation of a single-mode laser diode," *Appl. Opt*, no. 35, pp. 6754–6761, 1996.

[81] R. F. Broom, E. Mohn, C. Risch, and R. Salathe, "Microwave self- modulation of a diode laser coupled to an external cavity," *IEEE J. Quantum Electron.*, vol. 6, pp. 328–334, June 1970.

[82] T. Morikawa, Y. Mitsuhashi, J. Shimoda, and Y. Kojima, "Return beam induced oscillations in self-coupled semiconductor lasers," *Electron. Lett.*, no. 12, pp. 435–436, 1976.

[83] O. Hirota and Y. Suematsu, "Noise properties of injection lasers due to reflected waves," *IEEE J. Quant. Electron.*, vol. QE-15, pp. 142–149, 1979.

[84] R. S. C. Voumard and H. Weber, "Resonance amplifier model describing diode lasers coupled to short external resonators," *Appl. Phys.*, no. 12, pp. 369–378, 1977.

[85] K. A. N. Chinone and R. Ito, "Stabilization of semiconductor laser outputs by a mirror close to a laser facet," *Appl. Phys. Lett.*, no. 33, pp. 990–992, 1978.

[86] G. van Tartwijk and G. Agrawal, "Laser instabilities: a modern perspective," *Prog. Quantum Electron.*, no. 22, pp. 43–122, 1998.

[87] G. H. M. van Tartwijk and D. Lenstra, "Semiconductor lasers with optical injection and feedback," *Quantum Semiclass. Opt.*, vol. 7, pp. 87–143, 1995.

[88] D. Larsson, K. Yvind, I.-S. Chung, and J. M. Hvam, "Optimization of vcsels for self-mixing sensing," *IEEE Photonics Technol. Lett.*, vol. 22, no. 10, pp. 667–669, 2010.

[89] T. Taimre, M. Nikolic, K. Bertling, Y. L. Lim, T. Bosch, and A. D. Rakic, "Laser feedback interferometry: a tutorial on the self-mixing effect for coherent sensing," *Adv. Opt. Photon.*, vol. 7, pp. 570–631, 2015.

[90] F. Favre, "Theoretical analysis of external optical feedback on dfb semiconductor lasers," *IEEE J. Quant. Electron.*, vol. QE-23, pp. 81–88, Jan. 1987.

[91] K. Panajotov, M. Sciamanna, M. A. Arteaga, and H. Thienpont, "Optical feedback in vertical-cavity surface-emitting lasers," *IEEE J. Sel. Topics Quantum Electron.*, vol. 19, p. 1700312, July 2013.

[92] C. Risch and C. Voumard, "Self-pulsation in the output intensity and spectrum of GaAs-AlGaAs cw diode lasers coupled to a frequency selective external optical cavity," *J. Appl. Phys.*, vol. 48, pp. 2083–2085, 1977.

[93] D. M. Kane and K. A. Shore, *Unlocking dynamical diversity*. England: John Wiley and sons, Ltd, 2005.

[94] T. Bosch, N. Servagent, and S. Donati, "Optical feedback interferometry for sensing application," *Opt. Eng*, vol. 40, no. 1, pp. 20–27, 2001.

[95] Donati and R. Horng, "The diagram of feedback regimes revisited," *IEEE J. Select. Topics Quantum Electron*, vol. 19, no. 4, pp. 1500309–1500309, 2013.

[96] M. J. Rudd, "A laser doppler velocimeter employing the laser as a mixer-oscillator," *J. Phys. E*, vol. 1, pp. 723–726, 1968.

[97] S. Donati, "Laser interferometry by induced modulation of the cavity field," *J. Appl. Phys.*, vol. 49, pp. 495–497, 1978.

[98] R. Atashkhooei, J. Urresty, S. Royo, J. Riba, and L. Romeral, "Runout tracking in electric motors using self-mixing interferometry," *IEEE/ASME Trans. Mechatronics*, vol. 19, pp. 184–190, Feb 2014.

[99] J. Urresty, R. Atashkhooei, J. Riba, L. Romeral, and S. Royo, "Shaft trajectory analysis in a partially demagnetized permanent-magnet synchronous motor," *IEEE Trans. Ind. Electron.*, vol. 60, pp. 3454–3461, Aug 2013.

[100] R. Atashkhooei, F. Azcona, S. Royo, and L. G. Espert, "Optical feedback interferometry for measuring dynamic stress deformation of beams," *AIP Conference Proceedings*, vol. 1457, no. 1, pp. 132–138, 2012.

[101] C. Zakian and M. Dickinson, "Laser doppler imaging through tissues phantoms by using self-mixing interferometry with a laser diode," *Opt. Lett.*, vol. 32, pp. 2798–2800, 2007.

[102] E. Lacot, R. Day, and F. Stoeckel, "Laser optical feedback tomography," *Opt. Lett.*, vol. 24, pp. 744–746, 1999.

[103] E. Lacot, R. Day, and F. Stoeckel, "Laser relaxation-oscillation frequency imaging," *Opt. Lett.*, vol. 26, pp. 1483–1485, 2001.

[104] G. Giuliani and M. Norgia, "Laser diode linewidth measurement by means of self-mixing interferometry," *IEEE Photon. Technol. Lett.*, vol. 12, pp. 1028–1030, 2000.

[105] J. Xi, Y. Yu, J. Chicharo, and T. Bosch, "Estimating the parameters of semiconductor lasers based on weak optical feedback self-mixing interferometry," *IEEE J. Quantum Electron.*, vol. 41, pp. 1058–1064, 2005.

[106] Y. Yu, J. Xi, J. Chicharo, and T. Bosch, "Toward automatic measurement of the linewidth-enhancement factor using optical feedback self-mixing interferometry with weak optical feedback," *IEEE J. Quantum Electron.*, vol. 43, pp. 527–534, 2007.

[107] F. Gouaux, N. Servagent, and T. Bosch, "Absolute distance measurement with an optical feedback interferometer," *Appl. Opt.*, vol. 37, pp. 6684–6689, Oct 1998.

[108] "Distance measurement using the self-mixing effect in a three-electrode distributed bragg reflector laser diode," in *Proc. SPIE*, pp. 738–743.

[109] D. Guo and M. Wang, "Self-mixing interferometry based on a double-modulation technique for absolute distance measurement," *Appl. Opt.*, vol. 46, pp. 1486–1491, Mar 2007.

[110] M. Norgia, G. Giuliani, and S. Donati, "Absolute distance measurement with improved accuracy using laser diode self-mixing interferometry in a closed loop," *IEEE Trans. Instrum. Meas.*, vol. 56, pp. 1894–1900, October 2007.

[111] M. Norgia and S. Donati, "A displacement-measuring instrument utilizing self-mixing interferometry," *IEEE Trans. Instrum. Meas.*, vol. 52, pp. 1765–1770, Dec 2003.

[112] L. Scalise, Y. Yu, and G. G. et. al, "Self-mixing laser diode velocimetry: application to vibration and velocity measurement," *IEEE Trans. Instrum. Meas.*, vol. 53, pp. 223–232, Feb 2004.

[113] A. Magnani and M. Norgia, "Spectral analysis for velocity measurement through self-mixing interferometry," *IEEE J. Quantum Electron.*, vol. 49, pp. 765–769, Sept 2013.

[114] B. V. Hoe, E. Bosman, J. Missinne, S. Kalathimekkad, and et. al, "Photonic incremental pressure sensor based on optical feedback in a polymer embedded vcsel," *IEEE Photon. Technol. Lett.*, vol. 24, pp. 1151–1153, July 2012.

[115] F. P. Mezzapesa, A. Ancona, T. Sibillano, and F. D. Lucia, "High-resolution monitoring of the hole depth during ultrafast laser ablation drilling by diode laser self-mixing interferometry," *Opt. Lett.*, vol. 36, pp. 822–824, 2011.

[116] C. Jie and H. Hong, *Sensors and Detective Technology*. Beijing: Higher Education Press, 2002.

[117] C. Paolo, G. M. Revel, and E. P. Tomasini, *An Introduction to Optoelectronic Sensors*. Singapore: World Scientific Publishing Co. Pte. Ltd., 2009.

[118] P. J. Brannon, "Laser feedback: its effect on laser frequency," *Appl. Opt.*, vol. 15, pp. 1119–1120, 1976.

[119] E. T. Shimizu, "Directional discrimination in the self-mixing type laser doppler velocimeter," *Appl. Opt.*, vol. 26, pp. 4541–4544, 1987.

[120] P. J. de Groot, G. M. Gallatin, and S. H. Macomber, "Ranging and velocimetry signal generation in a backscatter-modulated laser diode," *Appl. Opt.*, vol. 21, pp. 4475–4480, 1988.

[121] S. Shinohara, H. Naito, H. Yoshida, H. Ikeda, and M. Sumi, "Compact and versatile self-mixing type semiconductor laser doppler velocimeters with direction discrimination circuit," *IEEE Trans. Instrum. Meas.*, vol. 38, pp. 574–577, 1989.

[122] M. H. Koelink, M. Slot, and F. F. M. de Mul et. al, "Laser doppler velocimeter based on the self-mixing effect in a fiber-coupled semiconductor laser: theory," *Appl. Opt.*, vol. 31, pp. 3401–3408, 1992.

[123] W. M. Wang, W. J. Boyle, K. T. V. Grattan, and A. W. Palmer, "Self-mixing interference in a diode laser: experimental observations and theoretical analysis," *Appl. Opt.*, vol. 32, pp. 1551–1558, 1993.

[124] R. Kawai, Y. Asakawa, and K. Otsuka, "Ultrahigh sensitivity selfmixing laser doppler velocimetry with laser diode pumped microchip linp4o12 lasers," *IEEE Photon. Technol. Lett.*, vol. 11, pp. 706–708, 1999.

[125] J. Riu, M. Sicard, S. Royo, and A. Comeron, "Silicon photomultiplier detector for atmospheric lidar applications," *Opt. Lett.*, vol. 37, pp. 1229–1231, 2012.

[126] T. Bosch, N. Servagent, R. Chellali, and M. Lescure, "Three-dimensional object construction using a self-mixing type scanning laser range finder," *IEEE Trans. Instrum. Meas.*, vol. 47, pp. 1326–1329, Oct 1998.

[127] R. L. Whitman and A. Korpel, "Probing of acoustic surface perturbations by coherent light," *Appl. Opt.*, vol. 8, pp. 1567–1576, Aug 1969.

[128] M. D. Fox, "Area heterodyne optical detection of acoustic holograms," *Appl. Opt.*, vol. 14, pp. 1476–1477, Jul 1975.

[129] R. Adler, A. Korpel, and P. Desmares, "An instrument for making surface waves visible," *IEEE Trans. Sonics and Ultrasonic*, vol. SU-15, 1968.

[130] C. Scruby and L. Drain, *Laser Ultrasonics Techniques and Applications*. Taylor and Francis Group, 1990.

[131] R. A. Noble, A. R. D. Jones, T. J. Robertson, D. A. Hutchins, and D. R. Billson, "Novel wide bandwidth micromachined ultrasonic transducers," *IEEE Trans. Ultrason. Ferroelectr. Freq. Control*, vol. 48, no. 69, pp. 1495–1507, 2001.

[132] M. I. Haller and B. T. Khuri-Yakub, "A surface micromachined electrostatic ultrasonic air transducer," *IEEE Trans. Ultrason. Ferroelectr. Freq. Control*, vol. 43, no. 69, pp. 1–6, 1996.

[133] S. R. Manalis, S. C. Minne, A. Atalar, and C. F. Quate, "Interdigital cantilevers for atomic force microscopy," *Appl. Phys. Lett.*, vol. 25, no. 69, p. 3944, 1996.

[134] N. A. Hall and L. F. Degertekin, "Integrated optical interferometric detection method for micromachined capacitive acoustic transducers," *Appl. Phys. Lett.*, vol. 80, pp. 3859–61, May 2002.

[135] H. Martinussen, A. Aksnes, and H. E. Engan, "Heterodyne interferometry for high sensitivity absolute amplitude vibrational measurements," 2006.

197

[136] A. Korpel, L. J. Laub, and H. C. Sievering, "Measurement of acoustic surface wave propagation characteristics by reflected light," *Appl. Phys. Lett.*, vol. 10, no. 10, pp. 295–297, 1967.

[137] L. L. R. Whitman and W. Bates, "Acoustic surface displacement measurements on a wedge-shaped transducer using an optical probe technique," 1968.

[138] G. Massey, "An optical heterodyne ultrasonic image converter," *IEEE Proc.*, vol. 56, pp. 2157–2161, Dec 1968.

[139] C. H. Palmer, R. . Claus, and S. E. Fick, "Ultrasonic wave measurement by differential interferometry," *Appl.Opt.*, vol. 16, pp. 1849–1856, July 1977.

[140] F. F. M. de Mul, M. H. Koelink, A. L. Weijers, J. Greve, J. G. Aarnoudse, R. Graaff, and A. C. M. Dassel, "Self-mixing laser-doppler velocimetry of liquid flow and of blood perfusion in tissue," *Appl. Opt.*, vol. 31, pp. 5844–5851, 1992.

[141] J. Hast, R. Myllyl, H. Sorvoja, and J. Miettinen, "Arterial pulse shape measurement using self-mixing effect in a diode laser," *IoP Quantum Electron*, vol. 32, pp. 975–982, 2002.

[142] A. C. L. Rovati and N. Palanisamy, "Measurement of the fluid-velocity profile using a selmixing superluminescent diode," *Meas. Sci. Techn.*, vol. 22, 2011.

[143] P. Dean, "Terahertz imaging through self-mixing in a quantum cascade laser," *Opt. Lett.*, vol. 36, pp. 2587–2589, 2011.

[144] S. Kayaozdemir, S. Takamiya, S. Ito, S. Shinohara, and H. Yoshida, "Self-mixing laser speckle velocimeter for blood flow measurement," *IEEE Trans. Instrum. Meas.*, vol. 49, pp. 1029–1035, 2000.

[145] M. Norgia, A. Pesatori, and L. Rovati, "Low-cost optical flowmeter with analog front-end electronics for blood extracorporeal circulators," *IEEE Trans. Instrum. Meas.*, vol. 59, May 2010.

[146] I. Milesi, M. Norgia, P. P. Pompilio, C. Svelto, and R. L. Dellaca, "Measurement of local chest wall displacement by a custom self-mixing laser interferometer," *IEEE Trans. Instrum. Meas.*, vol. 60, pp. 2894–2901, Aug 2011.

[147] S. Blaize, B. Berenguier, I. Stefanon, A. Bruyant, G. Lerondel, P. Royer, O. Hugon, O. Jacquin, and E. Lacot, "Phase sensitive optical near-field mapping using frequency-shifted laser optical feedback interferometry," *Opt. Express*, vol. 16, pp. 11718–11726, 2008.

[148] Y. Tan, W. Wang, C. Xu, and S. Zhang, "Laser confocal feedback tomography and nano-step height measurement," *Sci. Rep.*, vol. 3, p. 2971, 2013.

[149] Y. Gao, Y. Yu, J. Xi, and Q. Guo, "Simultaneous measurement of vibration and parameters of a semiconductor laser using self-mixing interferometry," *Appl. Opt.*, vol. 53, pp. 4256–4263, Jul 2014.

[150] Y. Gao, Y. Yu, J. Xi, Q. Guo, J. Tong, and S. Tong, "Improved method for estimation of multiple parameters in self-mixing interferometry," *Appl. Opt.*, vol. 54, pp. 2703–2709, Apr 2015.

[151] Y. Yu, G. Giuliani, and S. Donati, "Measurement of the linewidth enhancement factor of semiconductor lasers based on the optical feed-back self-mixing effect," *IEEE Photon. Technol. Lett.*, vol. 16, pp. 990âĂŞ–992, Apr 2004.

[152] J. von Staden, T. Gensty, W. Elsasser, G. Giuliani, and C. Mann, "Measurements of the α factor of a distributed-feedback quantum cascade laser by an optical feedback self-mixing technique," *Opt. Lett.*, vol. 31, September 2006.

[153] T. Taimre and A. D. Rakic, "On the nature of acket's characteristic parameter c in semiconductor lasers," *Appl. Opt.*, vol. 53, pp. 1001–1006, 2014.

[154] Y. Fan, Y. Yu, J. Xi, G. Rajan, Q. Guo, and J. Tong, "Simple method for measuring the linewidth enhancement factor of semiconductor lasers," *Appl. Opt.*, vol. 54, pp. 10295–10298, 2015.

[155] T. B. N. Servagent and M. Lescure, "Design of a phase-shifting optical feedback interferometer using an electro-optic modulator," *IEEE J. Sel. Top. Quantum Electron.*, vol. 6, pp. 798–802, 2000.

[156] G. Liu, S. Zhang, J. Zhu, and Y. Li, "Optical feedback laser with a quartz crystal plate in the external cavity," *Appl. Opt*, vol. 42, pp. 6636–6639, 2003.

[157] L. Fei and S. Zhang, "The discovery of nanometer fringes in laser self-mixing interference," *Opt. Commun.*, vol. 273, no. 1, pp. 226 – 230, 2007.

[158] N. Takahashi, S. Kakuma, , and R. Ohba, "Active heterodyne interferometric displacement measurement using optical feedback effects of laser diodes," *Opt. Eng.*, vol. 35, pp. 802–807, 1996.

[159] G. Giuliani, M. Norgia, S. Donati, and T. Bosch, "Laser diode self-mixing technique for sensing applications," *J. Opt. A: Pure Appl. Opt*, no. 4, pp. 283–294, 2002.

[160] S. Donati, "Responsivity and noise of self-mixing photodetection schemes," *IEEE J. Quantum Electron.*, vol. 47, Nov. 2011.

[161] L. Wei, J. Chicharo, Y. Yu, and J. Xi, "Pre-processing of signals observed from laser diode self-mixing intereferometries using neural networks, wisp 2007," in *IEEE International Symposium on Intelligent Signal Processing*, pp. 1–5, Oct 2007.

[162] H. P. Yuen and V. W. S. Chan, "Noise in homodyne and heterodyne detection," *Opt. Lett*, vol. 8, no. 3, p. 177, 1983.

[163] S. V. Vaseghi, *Advanced Digital Signal Processing and Noise Reduction*. John Wiley and Sons Ltd., 2000.

[164] U. Zabit, T. Bosch, and F. Bony, "Adaptive transition detection algorithm for a self-mixing displacement sensor," *IEEE Sens. J.*, vol. 9, pp. 1879–1886, 2009.

[165] Y. Yu, J. Xi, and J. F. Chicharo, "Improving the performance in an optical feedback self-mixing interferometry system using digital signal pre-processing," in *IEEE International Symposium on Intelligent Signal Processing*, pp. 1–6, Oct 2007.

[166] Y. Fan, Y. Yu, J. Xi, and J. F. Chicharo, "Improving the measurement performance for a self-mixing interferometry-based displacement sensing system," *Appl. Opt.*, vol. 50, pp. 5064–5072, Sep 2011.

[167] S. Donati, G. Martini, and T. Tambosso, "Speckle pattern errors in self-mixing interferometry," *IEEE J. Quantum Electron.*, vol. 49, pp. 798–806, Sept 2013.

[168] F. G. N. Servagent and T. Bosch, "Measurements of displacement using the selfmixing interference in a laser diode," *J. Opt.*, vol. 29, pp. 168–173, 1998.

[169] S. Merlo and S. Donati, "Reconstruction of displacement wave- forms with a single-channel laser-diode feedback interferom- eter," *IEEE J. Quantum Electron.*, vol. 33, pp. 527–531, Aug 1997.

[170] S. Wang, H. K. Choi, and I. H. A. Fattah, "Studies of semiconductor lasers of the interferometric and ring types," *IEEE J. Quantum Electron.*, vol. 18, pp. 610–617, 1982.

[171] S. T. Lau, T. Shiraishi, and J. M. Ballantyne, "Scattering matrix analysis of a triangular ring laser," *J. Lightwave Technol.*, vol. 12, pp. 202–207, Feb 1994.

[172] Q. Y. Lu, W. H. Guo, R. Phelan, D. Byrne, J. F. Donegan, P. Lambkin, and B. Corbett, "Analysis of slot characteristics in slotted single-mode semiconductor lasers using the 2-d scattering matrix method," *IEEE Photonics Technol. Lett.*, vol. 18, pp. 2605–2607, Dec 2006.

[173] L. Coldren, K. Furuya, B. Miller, and J. Rentschler, "Etched mirror and groove-coupled GaInAsP/InP laser devices for integrated optics," *IEEE J. Quantum Electron.*, vol. 18, pp. 1679–1688, Oct 1982.

[174] L. A. Coldren, K. J. Ebeling, B. I. Miller, and J. A. Rentschler, "Single longitudinal mode operation of two-section GaInAsP/Inp lasers under pulsed excitation," *IEEE J. Quantum Electron.*, vol. QE-19, pp. 1057–1062.

[175] M. C. Cardilli, M. Dabbicco, F. P. Mezzapesa, and G. Scamarcio, "Linewidth measurement of mid infrared quantum cascade laser by optical feedback interferometry," *Appl. Phys. Lett.*, vol. 108, no. 3, 2016.

[176] R.Kliese and A. Rakic, "Spectral broadening caused by dynamic speckle in self-mixing velocimetry sensors," *Opt. Express*, vol. 20, pp. 18757–18771, 2012.

[177] A. Arriaga, F. Bony, and T. Bosch, "Analytic phase retrieval of dynamic optical feedback signals for laser vibrometry," in *SENSORS, 2014 IEEE*, pp. 762–765, Nov 2014.

[178] G. Strang and T. Nguyen, *Wavelets and Filter Banks*. Wellesley-Cambridge Press, 1995.

[179] P. Goupillaud, A. Grossman, and J. Morlet, "Cycle-octave and related transforms in seismic signal analysis," *Soc. of Expl. Geophys.*, vol. 23, pp. 85–102, 1984.

[180] Y. sheng, *Wavelet Transform*. CRC Press LLC, 2000.

[181] S. Lee and P. White, "Fault diagnosis of rotating machinery using wigner higher order moment spectra," *Mech. Syst. Sig. Process.*, vol. 11, no. 4, pp. 637–650, 1997.

[182] *Mechanical Signature Analysis-Theory and Applications*. New York Academic Press, 1986.

[183] P. McFadeen, "Examination of a technique for the early detection of failure in gears by signal processing of the time domain average of the meshing vibration," *Mech. Syst. Sig. Process.*, vol. 1, no. 2, 1987.

[184] D. Guo, M. Wang, and S. Tan, "Self-mixing interferometer based on sinusoidal phase modulating technique," *Opt. Express*, vol. 13, pp. 1537–1543, Mar 2005.

[185] A. Jha, F. J. Azcona, C. Y. nez, and S. Royo, "Extraction of vibration parameters from optical feedback interferometry signals using wavelets," *Appl. Opt.*, vol. 54, pp. 10106–10113, Dec 2015.

[186] A. Jha, S. Royo, F. Azcona, and C. Yanez, "Extracting vibrational parameters from the time-frequency map of a self mixing signal: An approach based on wavelet analysis," in *IEEE SENSORS*, pp. 1881–1884, Valencia, 2014.

[187] M. C. Y. Chan, P. C. K. Kwok, and E. H. Li, "The effect of carrier-induced change on the optical properties of algaasâĂŞgaas intermixed quantum wells," *IEEE J. Sel. Topics Quantum Electron.*, vol. 4, pp. 685–694, July/August 1998.

[188] S. Kobayashi, Y. Yamamoto, M. Ito, and T. Kimura, "Direct frequency modulation in algaas semiconductor lasers," *IEEE J. Quantum Electron.*, vol. 18, pp. 582–595, Apr 1982.

[189] T. Heil, I. Fischer, and W. ElsaÃ§er, "Stabilization of feedback-induced instabilities in semiconductor lasers," *J. Opt. B: Quantum Semiclass. Opt.*, vol. 2, pp. 413–420, Mar 2010.

[190] "Oclaro.com, http://images.ihscontent.net/vipimages/vipmasteric/ic/ocla/oclas00165/oclas00165-1.pdf." Online, Accessed: 17-06-2016.

[191] C. E. Wieman and L. Hollberg, "Using diode lasers for atomic physics," *Rev. Sci. Instrum.*, vol. 62, pp. 1–21, Jan 1991.

[192] U. Zabit, R. Atashkhooei, T. Bosch, S. Royo, F. Bony, and A. D. Rakic, "Adaptive self-mixing vibrometer based on a liquid lens," *Opt. Lett.*, vol. 35, pp. 1278–1280, Apr 2010.

[193] Y. Yu, J. Xi, and J. F. Chicharo, "Measuring the feedback parameter of a semiconductor laser with external optical feedback," *Opt. Express*, vol. 19, pp. 9582–9593, May 2011.

[194] A. M. Levine, G. H. M. van Tartwijk, D. Lenstra, and T. Erneux, "Diode lasers with optical feedback: Stability of the maximum gain mode," *Phys. Rev. A*, vol. 52, pp. R3436–R3439, Nov 1995.

[195] C.Bes, G. Plantier, and T. Bosch, "Displacement measurements using a self-mixing laser diode under moderate feedback," *IEEE Trans. Instrum. Meas.*, vol. 55, pp. 1101–1105, Aug 2006.

[196] D. M. Guo, M. Wang, and S. Q. Tan, "Self-mixing interferom- eter based on sinusoidal phase modulating technique," *Opt.Express*, vol. 13, pp. 1537–1543, Aug 2005.

[197] D.Zhigang, Z.Jingxuan, and J.Chunrong, "An improved wavelet threshold denoising algorithm," in *International Conference on Intelligent System Design and Engineering Applications*, pp. 297–299, 2013.

[198] "http://simon.cs.vt.edu/sosci/converted/t-dist/activity.html." Online, Accessed: 08-08-2016.

[199] "http://es.mathworks.com/help/stats/ttest2.html." Online, Accessed: 08-08-2016.

[200] J.-P. Monchalin, "Optical detection of ultrasound," *IEEE Trans. Ultrason. Ferroelectr. Freq. Control*, vol. UFFC-33, pp. 485–499, Sep 1986.

[201] "www.airmar.com,http://www.airmar.com/productdescription.html?id=28," Accessed: 14-07-2016.

[202] "www.airmar.com,http://www.airmar.com/productdescription.html?id=92," Accessed: 14-07-2016.

[203] *electronicdesign.com*, Accessed: 04-08-2016.

[204] *Tektronix.com, www.tek.com/dl/55W_17291_6_0.pdf*, Accessed: 04-08-2016.

[205] G. Rousseau, A. Blouin, and J.-P. Monchalin, "Ultrasound-modulated optical imaging using a powerful long pulse laser," *Opt. Express*, vol. 16, pp. 12577–12590, June 2008.

[206] S. W. Smith, *The Scientist and Engineer's Guide to Digital Signal Processing.* San Diego: California Technical Publishing, 1999.